Scatter correction of 4D cone beam computed tomography images for respiratory phase-dependent proton dose calculation

Henning Peter Schmitz

München 2023

Scatter correction of 4D cone beam computed tomography images for respiratory phase-dependent proton dose calculation

Henning Peter Schmitz

Dissertation
an der Fakultät für Physik
der Ludwig-Maximilians-Universität
München

vorgelegt von
Henning Peter Schmitz
aus Trier

München, den 23.02.2023

Erstgutachterin: Prof. Dr. Katia Parodi
Zweitgutachter: Prof. Dr. Marco Riboldi
Tag der mündlichen Prüfung: 05.06.2023

Zusammenfassung

Anatomische und respiratorische Veränderungen der Patientengeometrie sind von besonderem Interesse für die Protonentherapie von Lungenkrebs, da diese hierfür sehr anfällig ist. Die rechtzeitige Erstellung von genauen täglichen intensitätskorrigierten 4DCBCT-Bildern könnte es ermöglichen, die dosimetrischen Auswirkungen der interfraktionellen Veränderungen des Patienten zu bestimmen, die somit für die Online-Behandlungsanpassung oder zur Auslösung von Offline-Behandlungsanpassungen genutzt werden könnten. Diese Bewegungsdarstellungen könnten der tatsächlichen Bewegung während der Behandlung ähnlicher sein, was möglicherweise zu einem verbessertem Behandlungserlebnis führen kann. Darüber hinaus ist aufgrund der Verfügbarkeit von in-room CBCT-Bildern, die im derzeitigen klinischen Alltag ausschließlich zur Patientenpositionierung verwendet werden, keine weitere Bildaufnahme erforderlich. Folglich bedeutet dies weder eine zusätzliche Arbeitsbelastung für das klinische Personal noch eine zusätzliche Dosisbelastung für den Patienten, wobei letzteres vom verwendeten Aufnahmeprotokoll abhängt. Bislang sind die möglichen Anwendungsfälle für 4DCBCT-Bilder von Lungenpatienten aufgrund des Fehlens einer adäquaten Streuungskorrektur begrenzt. Folglich lag der Schwerpunkt dieser Arbeit auf der Erzeugung von qualitativ verbesserten 4DCBCT-Bildern, die eine Berechnung der Protonendosis ermöglichen, die dann als Auslösemechanismus für die Notwendigkeit einer Behandlungsanpassung oder einer adaptiven Online-Strahlentherapie verwendet werden können. Ein Arbeitsablauf zur Streuungskorrektur wurde in einem phantombasierten Experiment entwickelt, dann in einer retrospektiven Patientenstudie erweitert und getestet und anschließend mit Deep Learning beschleunigt.

Zunächst wurde in einer Machbarkeitsstudie an einem Schweinelungenphantom eine neuartige projektionsbasierte Intensitätskorrekturpipeline eingeführt, die auf einem vorherigen virtuellen 4DCT (4DvCT) basiert und das streuungskorrigierte 4DCBCT ($4DCBCT_{cor}$) erzeugt. Die Durchführbarkeit einer phasenabhängigen Protonendosisberechnung auf dem 4DvCT und $4DCBCT_{cor}$, die die Änderungen des Atemmusters berücksichtigten, wurde im Vergleich zu einem "Ground Truth"-CT dosimetrisch bewertet. Die Ergebnisse dieser experimentellen Validierungsstudie zeigten eine genaue Berechnung der Protonendosis für 4DvCT und $4DCBCT_{cor}$. Folglich könnte die vorgestellte Methode von klinischem Interesse für die tägliche Abschätzung der 4D-Protonendosis sein.

Zweitens wurde die Anwendbarkeit des phantomvalidierten Arbeitsablaufs zur Streuungskorrektur an einer Kohorte von 21 Lungenkrebspatienten gezeigt. Eine hohe dosimetrische Übereinstimmung wurde zwischen 4DvCT und $4DCBCT_{cor}$ erreicht, was die Konsistenz zwischen beiden Methoden zeigt. Tägliche in-room Bilder, die Atemmusterveränderungen und anatomische Veränderungen berücksichtigen, könnten für Entscheidungen über mögliche Behandlungsanpassungen genutzt werden. Die 4DCBCT-Streuungskorrektur ist ein rechenintensives Verfahren, das zu Bilderzeugungszeiten führte, die für den klinischen Einsatz zu lang waren.

Eine Beschleunigung der Methode kann durch Deep Learning Methoden erreicht werden. Zu diesem Zweck wurde ein streuungskorrigiertes 4DCBCT ($4DCBCT_{SN}$) durch den Einsatz von ScatterNet, einer deep convolutional neural network Architektur, aus dem Lungenpatientendatensatz erzeugt. Für das Netzwerktraining wurden gemessene und korrigierte CBCT-Projektionen verwendet. Die korrigierten Projektionen stammten aus der

4DCBCT Streuungskorrektur. Das resultierende 4DCBCT$_{SN}$ hat eine vergleichbare Bildqualität und Genauigkeit der Protonendosisberechnung für das Target wie das 4DCBCT$_{cor}$. Die klinische Einführung scheint nun aufgrund der schnellen Berechnungszeiten realisierbar.

Zusammenfassend lässt sich sagen, dass die vorgestellten Studien entscheidende Schritte auf dem Weg zur klinischen Einführung von genauen täglichen phasenabhängigen streuungskorrigierten 4DCBCT-Bildern für Lungentumore in der absehbaren Zukunft sind. Dies könnte adaptive Online-Behandlungsszenarien ermöglichen.

Abstract

Anatomical and respiratory pattern changes are of particular interest for proton therapy of lung cancer, given its high susceptibility to these variations. The timely generation of accurate daily intensity corrected 4DCBCT images could allow determining the dosimetric impact of the patient's interfractional changes, which thus could be used for online treatment adaptation or to trigger offline treatment adaptations. These motion representations could be more similar to the actual motion during the treatment, which potentially leads to an improved treatment outcome. Furthermore, due to the availability of in-room CBCT images, which in the current clinical setting are solely used for patient positioning, no further image acquisition is needed. Consequently, this neither adds workload to the clinical personnel nor additional dose burden to the patient, with the latter depending on the employed acquisition protocol. Hitherto, the possible use cases for 4DCBCT images of lung patients are limited due to the lack of adequate scatter correction. Consequently, the focus of this thesis was the generation of quality improved 4DCBCT images, allowing for proton dose calculation, which could then be used as a trigger mechanism for the necessity of treatment adaptation or online adaptive radiotherapy. A scatter correction workflow was developed within a phantom-based experiment, then extended and tested in a retrospective patient study, and finally accelerated with deep learning.

Firstly, in a proof-of-concept porcine lung phantom study a novel projection-based intensity correction pipeline, based on a prior 4D virtual CT (4DvCT), was introduced, which yields the scatter corrected 4DCBCT (4DCBCT$_{cor}$). The feasibility to perform phase-dependent proton dose calculation on the 4DvCT and 4DCBCT$_{cor}$, which account for breathing pattern changes, was dosimetrically evaluated in comparison to a ground truth CT. The results of this experimental validation study showed accurate proton dose calculation for 4DvCT and 4DCBCT$_{cor}$. Consequently, the presented method could be of clinical interest for daily 4D proton dose estimation.

Secondly, the applicability of the phantom-validated scatter correction workflow was shown on a cohort of 21 lung cancer patients. A high dosimetric agreement was achieved between 4DvCT and 4DCBCT$_{cor}$, which shows consistency between both methods. Daily in-room images, which account for respiratory pattern and anatomical changes, could be potentially used for decisions on possible treatment adaptations. The 4DCBCT scatter correction method is computationally expensive, which resulted in image generation times which were too long for clinical use.

Acceleration of the method could potentially be achieved using deep learning methods. To this end, a scatter-corrected 4DCBCT (4DCBCT$_{SN}$) was generated employing ScatterNet, a deep convolutional neural network architecture, on the lung patient data set. For network training raw and corrected CBCT projections were used. The corrected projections originated from the 4DCBCT scatter correction method. The resulting 4DCBCT$_{SN}$ has an image quality and proton dose calculation accuracy for the target, which is comparable to the 4DCBCT$_{cor}$. Clinical implementation seems now viable due to fast computation times.

In conclusion, the presented studies address crucial steps towards clinical implementation of accurate daily phase-dependent scatter-corrected 4DCBCT images for lung tumours in the foreseeable future. This could pave the way for online adaptive treatment scenarios.

Contents

List of Figures

List of Tables

List of Symbols and Abbreviations

The following list is neither exhaustive nor exclusive, but may be helpful.

AI **A**rtificial **i**ntelligence

ART **A**daptive **r**adiation **t**herapy

BEV **B**eam's **e**ye **v**iew

CBCT **C**one **b**eam **c**omputed **t**omography

CC **C**ranial **c**audal

CG **C**onjugate **g**radient

CNN **C**onvolutional **n**eural **n**etwork

CPE **C**harged **p**article **e**quilibrium

CT **C**omputed **t**omography

DL **D**eep **l**earning

DIR **D**eformable **i**mage **r**egistration

DNA **D**eoxyribo**n**ucleic **a**cid

DVF **D**eformation **v**ector **f**ield

DVH **D**ose-**v**olume **h**istogram

EBCT **E**lectron **b**eam **c**omputed **t**omography

eV **E**lectron**v**olts or $1.602\,176\,634 \times 10^{-19}$ J

FOV **F**ield **o**f **v**iew

FWHM **F**ull **w**idth at **h**alf **m**aximum

GAN **G**enerative **a**dversarial **n**etworks

GTV **G**ross **t**arget **v**olume

H&N **H**ead and **n**eck

IMPT **I**ntensity **m**odulated **p**roton **t**herapy

IGRT **I**mage-**g**uided **r**adiation **t**herapy

ITV **I**nternal **t**arget **v**olume

IQR **I**nter**q**uartile **r**ange

LET **L**inear **e**nergy **t**ransfer

MAE **M**ean **a**bsolute **e**rror

MCS **M**ultiple **C**oulomb **s**cattering

MC **M**onte **C**arlo

ME **M**ean **e**rror

MRI **M**agnetic **r**esonance **i**maging

MR-linac **MR**-guided **lin**ear **ac**celerator

NIST **N**ational **i**nstitute of **s**tandards and **t**echnology

NSCLC **N**on-**s**mall **c**ell **l**ung **c**ancer

PBS **P**encil **b**eam **s**canning

pCT **p**lanning **c**omputed **t**omography

PS **P**assively **s**cattered

PT **P**roton **t**herapy

OAR **O**rgans **a**t **r**isk

QA **Q**uality **a**ssurance

RBE **R**elative **b**iological **e**ffectiveness

RDN **R**esidual **d**ense **n**etwork

ROI **R**egion **o**f **i**nterest

RT **R**adiation **t**herapy

SCLC **S**mall **c**ell **l**ung **c**ancer

SFUD **S**ingle **f**ield **u**niform **d**ose

SMEIR **S**imultaneous **m**otion **e**stimation and **i**mage **r**econstruction

SOBP **S**pread **o**ut **B**ragg **p**eak

SOP **S**tandard **o**perating **p**rocedure

SI **S**uperior **i**nferior

TPS **T**reatment **p**lanning **s**ystem

vCT **v**irtual **C**omputed **t**omography

VMAT **V**olumetric **m**odulated **a**rc **t**herapy

WEPL **W**ater **e**quivalent **p**ath **l**ength

WET **W**ater **e**quivalent **t**hickness

Chapter 1

Introduction

This thesis starts with a brief description of cancer as a disease and the different modalities for its treatment. It is followed by an introduction to radiation therapy and a historic overview showing the advancements of this field, and its modern challenges. A general description of a clinical treatment workflow concludes the introduction and leads to the specific aim and scope of this thesis, which is the use of four-dimensional cone beam computed tomography images (4DCBCTs) for respiratory phase-dependent proton dose calculation.

1.1   Cancer

Diseases affect all people regardless of their age, background, race, moral, or political persuasions. Worldwide, the leading causes of death and mortality are cardiovascular diseases followed by cancer [1, 2]. Whereas cardiovascular deaths have seen a plateau in the developed world [3], cancer, which predominately affects the elderly [1], is a continuously increasing problem in particular due to ageing populations. Extrapolating current tendencies suggest a change of the leading cause of death to cancer, first in developed countries, and eventually worldwide within the next decades.

Cancer is an umbrella term that encapsulates diseases characterised by abnormal cell growth, which can occur anywhere in the body. This uncontrolled proliferation of cells is a defect in the cells' reproduction cycle and can be initiated by external and behavioural circumstances or genetic factors. Collected data show that roughly two-fifths of cancer incidences are due to avoidable risk factors such as smoking, unhealthy diet, obesity, lack of physical activity, infectious diseases, heavy alcohol abuse, and environmental factors, while the remaining three-fifths are consequences of genetic malfunctions [4].

Most cancer types, with the prominent exclusion of leukaemia, form solid lesions called tumours. These tumours can either be benign or malignant, depending on whether they stay in their primary location or invade other parts of the body. Common symptoms for over 100 different documented types of cancer [5, 6] are pain, anorexia, weakness, anxiety, lack of energy, easy fatigue, early satiety, constipation, and dyspnea [7].

To tackle several kinds of cancer, the current state-of-the-art treatment includes isolated or combined surgery, chemotherapy, hormonal or targeted therapy, and radiation therapy (RT). Depending on the patient case and the capabilities of the treatment facilities, ideally a tumour board, consisting of physicians and other health care providers, specialised in different areas, decides individually for each patient on an optimal therapy plan. For a more in-depth study of the different treatment possibilities, the following specialist literature can be consulted [8]. Within the scope of this thesis, the focus of investigation will be solely on RT.

1.2   Radiation therapy

Radiation therapy, a non-invasive and non-pharmacological method, has been practised for decades [9]. The intention of RT can be palliative or curative. The latter aims at either completely sterilising the tumours or shrinking them to a level where surgical removal is feasible. In both cases the goal is to damage the tumour cells' deoxyribonucleic acid (DNA) irreparably, using photons, protons or other sources of ionising radiation, which finally leads to the death of the cell, meaning a failure to undergo cell division. The interaction of this ionising radiation with DNA molecules affects not only cancer cells but also healthy tissue. Consequently, the greatest possible sparing of normal tissue is highly desired, while maximising the delivery of the therapeutic dose to the tumour [10]. RT can be divided broadly into three categories of sealed source radiotherapy, unsealed source radiotherapy, and external radiotherapy. Sealed and unsealed source radiotherapy, which will not be further discussed in this thesis, place the radiation source inside the patient's body. Contrary to this, in external radiation therapy, an external source of radiation is pointed at a specific body part of the patient.

A practised procedure in treatment facilities around the world in external radiation therapy is the use of accelerators. For the most widely used form of radiation, in specially designed tubes, called waveguides, electrons are repeatedly accelerated to energies in the order of megaelectronvolts (MeV) using a potential difference. The collision of these fast electrons with an X-ray target and their following deceleration generates X-ray beams. Using photons to destroy a deeply seated tumour will additionally harm superficial cells along the path of the beam as well as those behind the tumour. Therefore, using photon therapy can lead to substantial doses to adjacent organs at risk (OAR), which in the case of lung cancer would include the lung, bronchial tree, heart, and oesophagus [11]. This can result in a considerable risk of cardiac events as well as an increase of pulmonary complications. Consequently, photon therapy treatment is conducted from different angles and with multiple fractions, between which the healthy cells can recover. The rationale for this multifractional approach is that the cell survival curve (with a logarithmic ordinate) exhibits a less pronounced shoulder for tumours than for healthy tissues. Distributing dose over several fractions can thus lead to an increased differential effect between healthy tissues and tumours. As a consequence, the total dose for the overall treatment is increased, which will result in a substantially increased tumour kill [12].

Further improvements are attained by the use of protons over photons, as protons offer a ballistic advantage. The energy deposition of charged particles, e.g., protons, in matter, increases rapidly as the particle is slowed down, which happens in energy ranges relevant for radiation therapy mostly due to Coulomb interactions [13]. In particular, a sharp dose gradient occurs, as energy loss is proportional to one over the square of the velocity. This natural phenomenon, known as the Bragg peak, was first discovered by Sir William Henry Bragg in 1903[1]. This localised energy release of protons allows substantial dose sparing in OARs and a reduced integral dose.

In addition to these theoretical considerations, proton therapy (PT), which was proposed in 1946 by the American Robert Wilson [15] and initially tested on mice in 1952 by Cornelius Tobias [16], has many subtleties, which need to be addressed. Although human trials started almost 70 years ago [17], PT, depending on the tumour entity, is not a routine procedure as it is only conducted in specialised facilities. Technical details on the production of

---

[1]This should not be confused with the Bragg diffraction peak occurring due to constructive interference while analysing crystalline structures with X-rays. This scattering condition within a crystal lattice, known as Bragg's law [14], was formulated by Sir William Henry Bragg and his son Sir William Lawrence Bragg, who shared a Nobel prize in physics for this discovery in 1915. As of 2022, William Lawrence Bragg remains the youngest Nobel laureate in Physics as he received the award at the age of 25.

beams and the acceleration of protons will be explained in detail in section 2.3. The above-mentioned sharp gradient is highly susceptible to the density, more precisely the proton stopping power and the integral water equivalent thickness (WET), between the patient's skin and the tumour. While the range of protons, defined as the depth at which half of the protons have come to rest, in homogenous materials like water is well understood, this is a scenario that never occurs within the human body. Multiple different tissues and thus different stopping powers along the beam path lead to substantial range uncertainties. The magnitude of these errors can be non-negligible, which is obviously in stark contrast to the theoretical ballistic accuracy of PT. Uncertainties are more pronounced over time due to the occurring changes in a patient and thus are categorised in terms of the timescale into inter-fractional and intra-fractional. Inter-fractional changes include weight loss and gain, stochastic motion of internal organs, and change in size of the tumour. Intra-fractional changes include respiratory and cardiac motion as well as the filling of bladder and bowel, which makes it particularly relevant for tumours within the abdominothoracic region [18]. Additionally, within intra-fractional changes, psychological aspects can be relevant as the patient's breathing and pulse patterns may differ over the course of the treatment due to anxiety or relaxation. Consequently, more static cancer entities, such as head and neck (H&N) cancer, where intra-fractional changes are limited, are already treated with protons for decades [19].

The treatment of moving tumours, e.g., lung tumour, which will be the focus of this thesis, is a challenging problem. This problem gets furthermore complicated when considering the dependency on the employed beam delivery technology. PT facilities mainly conduct their treatment with two different technologies: passively scattered (PS) or active scanning. PS broadly spreads out the beam laterally through scattering. Lately, pencil beam scanning (PBS) has become more dominant, which has enabled intensity modulated proton therapy (IMPT), a highly conformal dose shaping method, utilising a narrow pencil-like beam with a varying number of protons and energy [20–22]. The correct implementation of IMPT requires accurate characterisation of inter- and intra-fractional anatomical variations to limit range uncertainties [23]. Ideally, the treatment plan, which is generated at the start of the clinical workflow, can account for these. Section 2.3 explains the different beam delivery technologies.

1.3 Clinical treatment planning workflow

The general clinical treatment workflow in RT consists of imaging, planning, and administering the dose. Possible reassessments may or may not let this workflow restart from the beginning or an intermediate step. Different relevant imaging modalities for RT as well as the process of image acquisition will be discussed in chapter 3.

In the case of lung tumours, emphasised in this thesis, a general treatment workflow could look as follows. Respiratory motion correlated 3D computed tomography (CT) scans, so-called 4DCT scans, are acquired prior to irradiation. On each respiratory phase of these 4DCTs, trained radiation oncologists delineate, in a process called contouring, the gross target volume (GTV) and OARs. The internal target volume (ITV), which is the union of the GTVs of each phase, as well as the OARs are copied to an average image of the 4DCT, making this scan the planning CT (pCT). These pCTs are transferred to a treatment planning system, on which clinical physicists optimise a specific dose plan per patient. A more detailed description of treatment planning is given in subsection 2.4.3. The scans, as discussed above, may over time no longer be representative of the changing patient situation. Consequently, geometric fidelity is no longer given and thus the exact localisation of the tumour and OARs are no longer known. One possibility to guarantee hitting the tumour is adding

safety margins to the target volume. The downside of this standard treatment planning procedure within RT is the inclusion of large volumes of healthy tissue that will be irradiated. This is why adaptive radiation therapy (ART) is of interest, as it allows multiple treatment plan modifications with the goal of improving the patient's dose distribution by reducing the margin component used to cover inter- and intra-fractional changes. Generally, avoiding harming healthy tissue as much as possible while ensuring target coverage is one of the central aspects of RT. A detailed description of a clinically employed treatment workflow for PT of lung tumours and potential alternatives are presented in chapter 5.

1.4   Objective and scope of this thesis

To address the problem of harming healthy tissue in the context of lung cancer, one idea would be the acquisition of 4DCT scans each time the patient is at the treatment site. However, this is not feasible as most facilities only have gantries equipped with cone beam CT (CBCT) scanners [24]. The initial purpose of these CBCT scanners is to ensure at each treatment fraction the correct positioning of the patient on the couch and thus make the planning treatment volume (PTV) margin smaller. The images acquired by CBCT scanners show poor quality compared to CT images, which is sufficient to position the patient, but not suitable for treatment planning.

Necessary image quality enhancements to use CBCTs for dose calculations require the correction of artefacts, that occur due to scatter detection [25], detector lag and ghosting [26], beam hardening [27], and scatter glare [28]. An explanation of those artefacts and mitigation techniques will be presented in sections 3.7 and 3.9.

Groups at the Ludwig Maximilian University of Munich from the campus in Garching as well as from the university hospital have previously developed the ability to compute proton dose distributions on intensity-corrected 3D CBCT images, which enables addressing inter-fractional uncertainties [29, 30]. Enhancing this correction method, which will be outlined in chapter 4, to 4D to potentially tackle intra-fractional changes is the main goal of this thesis. This includes working on image registration, reconstruction and scatter correction so that time-resolved proton dose calculation is feasible on CBCT data. However, one should keep in mind that this CBCT data will never be exactly representative of the motion during treatment. The idea is to have a motion pattern closer to treatment than the one used at the time of planning. In summary, this thesis works towards the ultimate overarching objective of ART.

The thesis is structured as follows: chapter 2 provides the necessary theoretical background for RT, with emphasis on the interactions of photons and protons with matter and the resulting clinical implications. Subsequently, chapter 3 gives a concise overview of different imaging modalities with a focus on CT and CBCT. Additionally, image reconstruction, artefacts, their mitigations, and image registration will be discussed. Chapter 4 introduces image guided radiotherapy (IGRT) and ART. Chapter 5 presents a clinical PT workflow for lungs and alternative methods to this workflow. Chapter 6 motivates the use of 4DCBCT for dose calculation. Chapter 7 divides investigations on the newly implemented 4DCBCT scatter correction workflow of this PhD thesis into two parts. Firstly, a proof-of-concept phantom study is presented, which after successful implementation and promising results led to the retrospective study of lung patients, which is the second part of this chapter. Chapter 8 tackles the long computation time needed for the scatter correction workflow, by employing artificial intelligence (AI) approaches for the 4DCBCT correction, in order to make the results of this thesis applicable for ART. Finally, in chapter 9 a conclusion merges the results of the three main topics (phantom study, patient study and AI implementation) into cohesive research findings and leads to future perspectives.

Chapter 2

Fundamentals of radiation therapy

"All of physics is either impossible or trivial. It is impossible until you understand it, and then it becomes trivial." This famous quote by Ernest Rutherford, who discovered the proton, sums up the intention of this chapter, which is to outline basic knowledge for understanding the physics discussed in this thesis. For a more systematic approach, this chapter is subdivided into interactions of photons and protons with matter. Additionally, a brief overview of clinical aspects within the scope of radiation therapy, which also provides some needed medical terminology, is given.

2.1 Interactions of photons with matter

This section starts with a brief review of photon physics to describe its characteristics, which is then followed by an explanation of the different interaction mechanisms with matter.

In the 1860s, Maxwell's equations, that model interference and polarisation effects seemed to have settled a decades-long debate about the nature of light, as they describe light as an electromagnetic wave. The discovery of the photoelectric effect by Heinrich Hertz and Wilhelm Hallwachs in 1887 was, however, a clear sign of particle-like behaviour of light. In 1900 Max Planck outlines a quantised energy transfer with the electromagnetic field describing the thermal radiation of black bodies [31]. This led to the theory of quantised electromagnetic radiation by Albert Einstein in 1905 [32]. Today quantum electrodynamics, a relativistic quantum field theory of electrodynamics, which was formulated in the 1970s, describes the photon as an elementary particle and force carrier of the electromagnetic force. The photon, which is denoted as γ, has no charge and no mass[1]. However, it has energy and momentum, which are proportional to its frequency and additionally it has angular momentum.

2.1.1 Photon interaction mechanisms

Photon interactions with matter are stochastic in nature. The fluence Φ [33] describes the number of photons dN on a sphere of the cross-sectional area dA:

$$\Phi = \frac{dN}{dA} \qquad [\Phi] = \mathrm{m}^{-2}. \tag{2.1}$$

For thin enough absorbers a certain fraction of photons will propagate without interaction, while the rest will either be absorbed or scattered. This attenuation of the fluence can be described by the differential equation:

$$d\Phi = -\mu\Phi dx \qquad [\mu] = \mathrm{m}^{-1}, \tag{2.2}$$

---

[1]A distinction between invariant mass (rest mass) and relativistic mass for the photon, is considered outdated. According to this concept, the photon would have an invariant mass of 0 and a relativistic mass that is proportional to its frequency.

where μ is the attenuation coefficient and x is the thickness of the absorber. Integration leads to Lambert-Beer's law:

$$\Phi(x) = \Phi_0 \cdot \exp(-\mu x), \tag{2.3}$$

where Φ_0 is the original fluence. The probability for a particular process to occur is proportional to the cross section σ:

$$\sigma = \frac{N_{\text{int}}}{\Phi} \qquad [\sigma] = \text{barn} = 10^{-28}\,\text{m}^2, \tag{2.4}$$

where N_{int} is the number of interaction photons for a given fluence Φ. The total attenuation coefficient can be expressed in terms of the cross section as follows [34]:

$$\mu_{\text{tot}} = \rho \frac{N_A}{A} \sigma_{\text{tot}}, \tag{2.5}$$

where ρ is the mass density of the material, N_A is the Avogadro number, and A is the atomic mass number of the material. The total attenuation coefficient can be split into the sum of individual contributions related to the different physical processes, namely Rayleigh scattering (RS), photoelectric effect (PE), Compton scattering (CS), and pair production (PP):

$$\mu_{\text{tot}} = \mu_{\text{RS}} + \mu_{\text{PE}} + \mu_{\text{CS}} + \mu_{\text{PP}}. \tag{2.6}$$

The contributions and mechanisms of these different processes are shown in figure 2.1 and are briefly summarised below. A more comprehensive explanation can be found in [33, 35]. It should be noted that energies for X-ray photons are very different for imaging (typically 25 keV-150 keV) and photon radiotherapy (typically up to 6 MeV-15 MeV). Consequently, the photoelectric effect and Compton scattering are the most important mechanisms for imaging. Rayleigh scattering impacts image quality solely at low energies and thus the overall contribution is little. Compton scattering is the most important for photon therapy. Pair production is present for normal therapeutic energies of 6 MeV but becomes more relevant for very high therapeutic energies of typically 15 MeV. A sketch of the three most relevant mechanisms is shown in figure 2.2.

Rayleigh scattering   Rayleigh scattering occurs if the photon's wavelength is small relative to the dimension of the interacting nucleus. In this situation, the energy of the photon can be absorbed by a shell electron. After absorption, an immediate emission of a photon with the same wavelength at a random direction makes this an elastic scattering process, as the photon loses no energy. Neither energy is transferred nor is any ionisation or excitation produced and thus Rayleigh scattering does not add to a patient's dose. Rayleigh scattering becomes more dominant for low energies mainly due to the increase of the scattering angle, which can worsen the quality of imaging. However, regarding the used energies for imaging and radiation therapy as well as the attenuation coefficient figure 2.1 it is not a dominant process.

Photoelectric effect   In 1905 Einstein first theoretically described the photoelectric effect [32], for which he was awarded the Nobel prize in 1921. A photon with sufficiently high energy ionises atoms in the traversed material by removing one of the shell electrons. This so-called photoelectron leaves the atom with the kinetic energy [33]:

$$T_{e^-} = E_\gamma - E_b - T_a \approx E_\gamma - E_b, \tag{2.7}$$
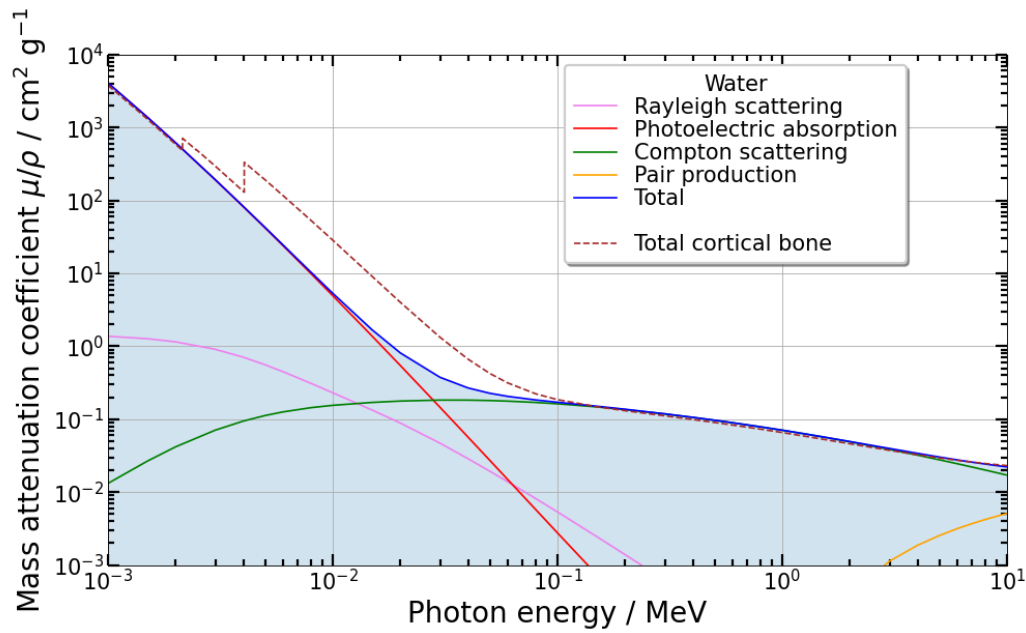
FIGURE 2.1: Contributions of mass attenuation coefficient for different interaction processes of X-ray photons in water. Additionally, the total mass attenuation coefficient for cortical bone is shown. It should be noted that imaging is performed between 25 keV-150 keV, whereas the energy for photon therapy is up to 6 MeV-15 MeV. *Data source:* XCOM database of the National Institute of Standards and Technology (NIST) [36]

where E_γ is the photon energy, E_b is the binding energy of the electron, and T_a is the kinetic energy, which is transferred to the atom. As T_a is negligibly small one can conclude that the process can only occur if the photon energy is larger than the binding energy. The resulting electron vacancy is filled by an electron falling from an outer shell. In this case, characteristic fluorescence X-ray emissions follow. Alternatively to this process, the atom can eject one of its electrons in a mechanism that is called Auger effect.

Electrons in different elements and shells have different binding energies and thus the photoelectric effect can be dominant at different energies. Figure 2.1 shows that for water the photoelectric effect is dominant at energies below 20 keV. For these energies, the proportionalities of the attenuation coefficient for the photoelectric effect can be approximated by:

$$\mu_{\text{PE}} \propto \rho \frac{Z^3}{E^3}, \tag{2.8}$$

where Z is the atomic number of the absorber material. A schematic diagram of the photoelectric effect along with the Compton scattering and pair production process described below is shown in plot 2.2.

Compton scattering Electrons in atoms where their binding energy is small compared to the energy of the photon can be regarded as quasi-free [33]. The inelastic scatter of photons on those weakly bound electrons is called Compton scattering [37], which led to the Nobel prize for Arthur Compton in 1927. In this process, the energy of the incident photon is partly transferred to the electron. As a consequence, the photon's wavelength is shifted by [38]:

$$\Delta\lambda = \frac{h}{m_e c}(1 - \cos\vartheta) = \lambda_{\text{C}}(1 - \cos\vartheta), \tag{2.9}$$

where h is Planck's constant, m_e the rest mass of the electron, c the speed of light in vacuum, ϑ the angle relative to the incident photon's direction, and λ_C the Compton wavelength. To fulfil energy and momentum conservation the scattering angle of the photon ϑ, and the recoil electron ϕ are linked in the following way:

$$\cot \phi = \left(1 + \frac{E_\gamma}{m_e c^2} \right) \tan \left(\frac{\vartheta}{2} \right), \text{with } \vartheta \in [0°, 180°] \text{ and } \phi \in [0°, 90°]. \qquad (2.10)$$

At energies of around 1 MeV Compton scattering is the dominant effect. For these energies, the attenuation coefficient for Compton scattering decreases with increasing photon energy. An exact expression can be derived from the Klein-Nishina formula [39].

Pair production   In the Coulomb field of an atomic nucleus[2], a photon with an energy above two times the rest mass of an electron, i.e. 1.022 MeV, is converted to an electron-positron pair with kinetic energies T_{e^-} and T_{e^+} [33]. The energy of the incident photon can be described as:

$$E_\gamma = 2 m_e c^2 + T_{e^-} + T_{e^+} = 1.022 \, \text{MeV} + T_{e^-} + T_{e^+}. \qquad (2.11)$$

The kinetic energy transferred to the nucleus is negligible. Analogously to Compton scattering, momentum conservation considerations lead to the angle ϕ between the photon direction and the outgoing electron and positron direction:

$$\phi \approx \frac{2 m_e c^2}{T_{e^-} + T_{e^+}} = \frac{2 m_e c^2}{E_\gamma - 2 m_e c^2} \qquad [\phi] = \text{rad}. \qquad (2.12)$$

The created electron deposits its energy in the absorber. The created positron deposits its energy, as it is slowed down by the Coulomb force, and will eventually annihilate with an electron. The photons that are created in this process can again have interactions with the absorber material [35, 38]. The first experimental detection of pair production, while investigating cosmic rays, was performed by Blackett and Occhialini in 1933 [40]. In 1948 Blackett received the Nobel prize for his works in nuclear physics and cosmic radiation. Pair production is the dominant effect at energies of above 20 MeV. For these energies, the proportionalities of the attenuation coefficient for pair production can be approximated by:

$$\mu_{\text{PP}} \propto \rho Z \log(E). \qquad (2.13)$$

2.1.2   Depth-dose curve of photons

The dose deposition of monoenergetic photons in matter is a two-step process. Firstly, secondary electrons are created, which primarily are forward directed. Secondly, these electrons deposit their energy. Consequently, the dose along the beam path increase until the point of charged particle equilibrium (CPE). After the CPE the dose follows an exponential decay.

A physically measurable quantity that is linked to the energy deposition is the absorbed energy dose D:

$$D(\vec{r}) = \frac{\mathrm{d}E}{\mathrm{d}m} = \int_0^\infty \mathrm{d}E \, \Phi_e(E, \vec{r}) S_{\text{mass}}(E, \vec{r}) \qquad [D] = \text{Jkg}^{-1} = \text{Gy}, \qquad (2.14)$$

---

[2]A special case of pair production, called triplet production, occurs in the vicinity of electrons. A minimum energy of four times the rest mass of an electron is needed in this case, which makes this process irrelevant for photon therapy.
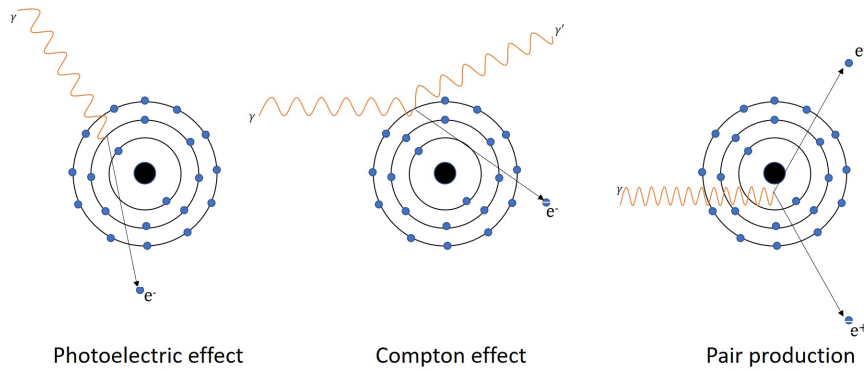
FIGURE 2.2: Sketch of the three most relevant X-ray photon interaction mechanisms in the context of imaging and radiation therapy: photoelectric effect, Compton scattering, and pair production (e^-: electron, e^+: positron, γ: photon).
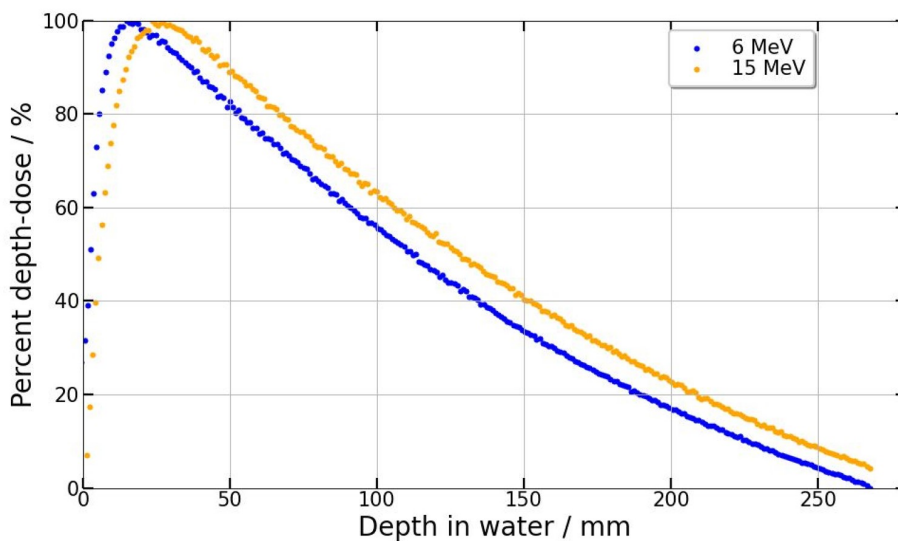
FIGURE 2.3: Depth-dose curves for 6 MeV and 15 MeV photon beams in water. The values, which are plotted relative to their maximum as a function of depth in water, were measured, using a water phantom with a plexiglas shell and ionisation chambers as detectors, in a regular QA measurement at the Department of Radiation Oncology at the University Hospital of the LMU for an Elekta Synergy linear accelerator.

where dE is the energy that is absorbed by a medium per unit mass dm. E is the energy of the electrons in the differential electron fluence spectrum $\Phi_e(E, \vec{r})$, and $S_{\mathrm{mass}}(E, \vec{r})$ is the mass stopping power at point $\vec{r}$.

Figure 2.3 shows relative depth-dose curves for two clinically relevant energies. The depth-dose values, which are normalised to their maximum, were acquired using a water phantom with a Plexiglas shell and ionisation chambers as detectors in a quality assurance (QA) measurement at the Department of Radiation Oncology at the University Hospital of the LMU for an Elekta Synergy linear accelerator (Linac, Elekta, Stockholm, Sweden).

In RT, the photon energy spectrum depends on the geometry of the accelerator, the final energy of the electrons before they hit the X-ray target, the treatment head, and the distance to the target. Additionally, the beams penetrate different tissues in a patient, which is why the shown dose deposition of this water phantom is oversimplified. During treatment planning (2.4.3) the complexity of the patient's body is modelled.

2.2 Interactions of protons with matter

Similar to the above described photons this section starts with an introduction to protons. Testing the accuracy of Thomson's plum pudding model of the atom [41], Rutherford used radium to shoot alpha particles onto a gold foil. The detected results showed that only a few particles were deflected, if however at large angles. Interpreting this outcome, Rutherford concluded that most of the atom has to be empty space with a dense and positively charged centre. Unaware of the neutron, Rutherford in 1920 called this new particle proton (Greek for first) [42].

In a modern description, the proton, which is denoted as p^+, is a baryon containing two up and one down quark. The positive electric charge of $+1e$ elementary charge is the sum of its composites as each up quark has a charge of $+\frac{2}{3}e$ while the down quark has one of $-\frac{1}{3}e$. Analogously, the spin of the proton is the sum of the spin of its quarks ($\frac{1}{2} + \frac{1}{2} - \frac{1}{2} = \frac{1}{2}$). Consequently, the proton is a fermion, following Fermi-Dirac statistics and the Pauli exclusion principle.

Additionally to electric charge and spin the three quarks making a proton, which are also called valence quarks, determine the momentum and mass of the proton. The naming is based on valence electrons, which determine the chemical properties of an atom. The rest masses of the valence quarks only contribute a small proportion to the mass of the proton (1.67×10^{-27} kg). The majority can be attributed to quantum chromodynamics binding energy with the gluons and the surrounding Dirac sea, containing virtual quark-antiquark pairs, which form from the vacuum and are immediately destroyed again (vacuum fluctuation).

The proton is the lightest baryon, as up and down quarks are the lightest and second lightest quarks. Consequently, spontaneous break up is not observed, which is in accordance with the standard model. This stability has been validated by numerous particle physics experiments, which suggest 6.6×10^{33} years [43] as a lower bound for the mean lifetime of a proton. In comparison, the estimated age of the universe is only 1.38×10^{10} years [44].

The proton has no definite boundaries and thus analogous to the atomic radius the proton is modelled as a positively charged sphere. The radius of that sphere, the proton radius, is 0.8×10^{-15} m, which is roughly 100,000 times smaller than an atomic radius.

2.2.1 Proton interaction mechanisms

Conceptually the interactions of charged particles differ from the interactions of photons. This is shown in figure 2.4, which displays the different energy deposition behaviours of photons and protons in tissue. The characteristic Bragg peak of an initial proton with its sharp fall-off as well as the superposition of multiple proton beams with a different energy to form the so-called spread-out Bragg peak (SOBP) are shown. A different behaviour to the displayed photon dose deposition can be observed.

Protons interact in matter either with the Coulomb field of atomic electrons and protons from the nucleus or directly with the nucleus. Depending on the tumour site, initial proton beam energies in the range of 70 MeV (e.g. eye irradiation) to 250 MeV (e.g. large male pelvis irradiation) are used in PT [46]. Figure 2.5 shows the relation between initial proton energy and depth of the Bragg peak in water, which explains the used energy range. High energies in PT correspond to velocities[3] $\beta \approx 0.6 - 0.7$, which makes those protons moderately relativistic [47].

---

[3] In the Lorentz transformation, a generalisation of the Galilean transformation, β is defined as the ratio of the velocity to the speed of light.
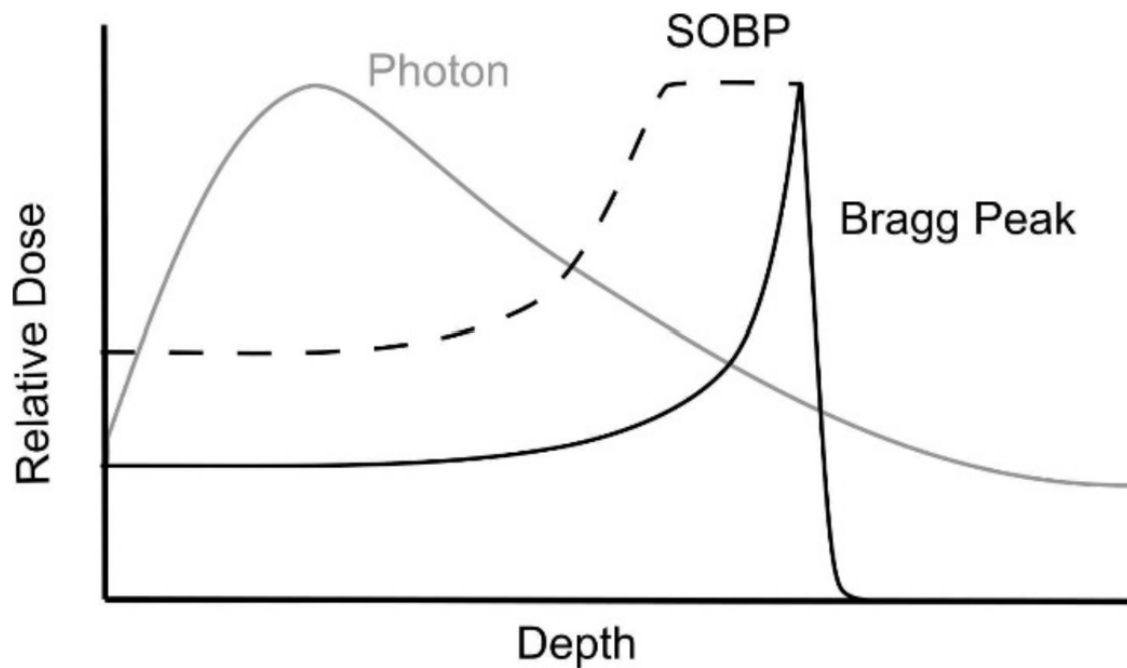
FIGURE 2.4: Depth-dose curves for a monoenergetic proton beam, showing its characteristic Bragg peak and a superposition of multiple proton beams, showing a spread-out Bragg peak (SOBP), in tissue. For comparison, the familiar behaviour of a photon beam (cf. figure 2.3) is shown as well. Figure adapted from [45].
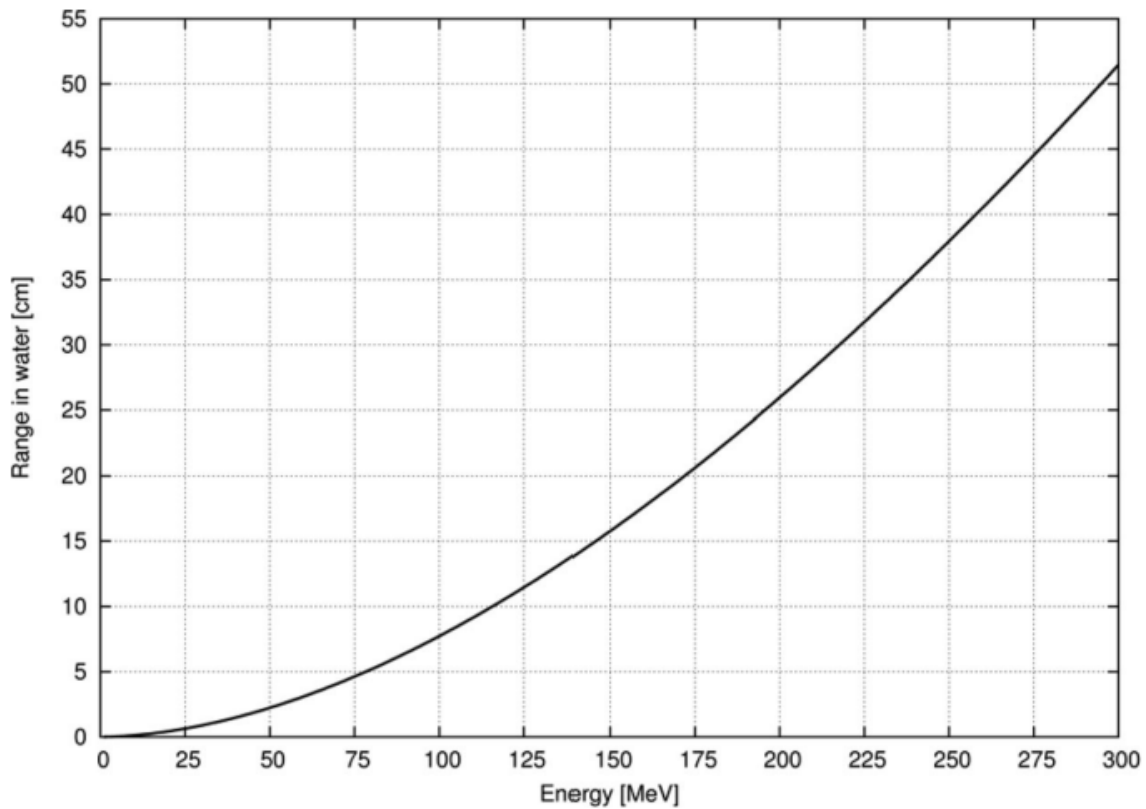
FIGURE 2.5: Depth of break peak position is shown as a function of the initial proton beam energy in water. Figure adapted from [46].
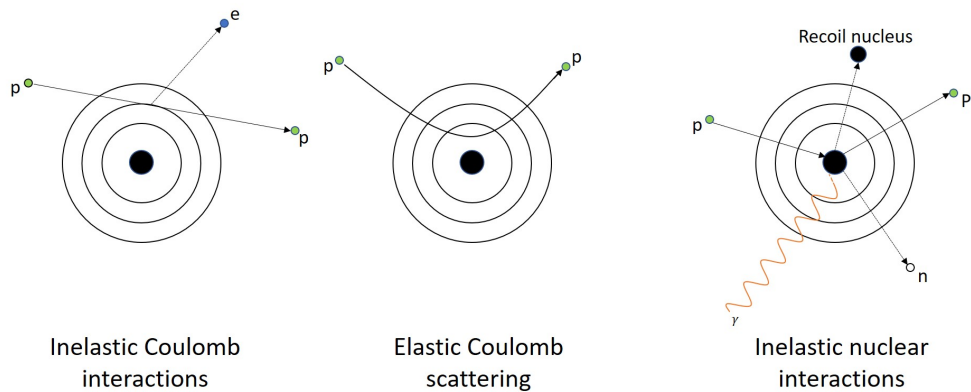
FIGURE 2.6: Sketch of the three dominant proton interaction mechanisms, inelastic Coulomb interaction, elastic Coulomb scattering, and inelastic nuclear interactions (p: proton, e: electron, n: neutron, γ: photon).

The different mechanisms, inelastic Coulomb interaction, elastic Coulomb scattering, and nuclear interactions are shown in figure 2.6 and are summarised in the following. A more comprehensive explanation can be found in [48, 49].

Inelastic Coulomb interaction   Protons, which are near to an atom, interact with the Coulomb field of an electron of the atom's shell. As protons have roughly 1,800 times the mass of electrons the deflection of the proton is negligible. However, in these interactions energy is transferred to the electron, which can lead to excitation and ionisation processes or to a scenario where the electron gets catapulted away from the atom. The proton loses a tiny amount of energy in this process. Consequently, only repeated inelastic Coulomb interactions result in a significant stopping of the proton. However, the stopping rate (=rate of energy loss) increases substantially with decreasing proton energy. This is the most frequent proton interaction process in matter.

Elastic Coulomb scattering   Protons in the vicinity of the Coulomb field of a nucleus experience a repulsive force, resulting in elastic scattering of the proton. Contrary to the inelastic interaction of the proton-electron case, the nucleus is more massive than the proton, which leads to a deflection of the proton, which is however in most cases extremely small. Consequently, only multiple Coulomb scattering (MCS) events, lead to a spread distribution of the proton beam. The spatial distribution of this spread can be modelled with a Gaussian. This type of scatter is stronger in high-Z materials.

Inelastic nuclear interactions   Occasionally a proton has a direct impact with a nucleus. In this case, the projectile proton enters the nucleus and one or more protons, neutrons, or light nucleon clusters are ejected. These secondary particles have much lower energy than the incident proton. The nucleus can be excited and in a successive de-excitation process photons can be emitted.

Elastic nuclear interactions and bremsstrahlung   In the scope of PT elastic nuclear interactions are not considered, as they are insignificant in the regarded energy range. Bremsstrahlung, which is generated when charges are decelerated, depends on the electrostatic

forces between the particle and the target. The deceleration of a proton is negligible due to its high mass and thus bremsstrahlung is irrelevant for the considered energies of PT[4].

2.2.2 Stopping power and range

The linear stopping power or energy loss rate of ions, which is defined for a beam and not a single particle [48], can be described as

$$\frac{S}{\rho} = -\frac{\mathrm{d}E}{\rho \mathrm{d}x} \tag{2.15}$$

where $-\frac{\mathrm{d}E}{\mathrm{d}x}$ is the mean energy loss (i.e. negative energy variation) per distance x. For convenience, the stopping power is normalised to the density of the absorbing material ρ. Enhancing previous works by Bohr [50] with quantum mechanical considerations a physically more precise description is given by the Bethe[13]-Bloch[51] formula, which is valid in the energy region above $\approx 1\,\mathrm{MeV/u}$:

$$\frac{S}{\rho} = -\frac{\mathrm{d}E}{\rho \mathrm{d}x} = 4\pi N_A r_e^2 m_e c^2 \frac{Z}{A} \frac{z^2}{\beta^2} \left(\ln \frac{2 m_e c^2 \gamma^2 \beta^2}{I} - \beta^2 - \frac{\delta}{2} - \frac{C}{Z} \right) \tag{2.16}$$

where N_A is Avogadro's number, r_e is the classical electron radius, z is the charge of the projectile, Z is the atomic number of the absorbing material, A is the atomic weight of the absorbing material, $\gamma = (1 - \beta^2)^{-\frac{1}{2}}$, I is the mean excitation potential of the absorbing material, δ and C are correction terms for the density effect and the shell. The density or shielding effect describes a reduction of energy loss due to the shielding of remote electrons by close electrons, which is important at high particle energies. Shell corrections arise if the assumption that the shell electrons are at rest is no longer valid. This scenario occurs at low energies where the particle velocity is in the same range as the velocity of the shell electron.

The energy loss is proportional to the inverse square of the projectile's velocity $(1/\beta^2)$ and the square of the ion charge $(z^2; z = 1$ for protons$)$. Another proportionality is to the density of the electrons in the absorber $(N_A Z/A)$. Comparing the different contributions of the proton energy loss rate, the material density, and the projectile's velocity are of particular importance. The material density in a clinical setting can vary from air in the lung to cortical bone by three orders of magnitude. The projectile's velocity for proton energies between $1\,\mathrm{MeV}$ to $250\,\mathrm{MeV}$ can change the stopping power in water by a factor of 60 [48].

The material's stopping power is related to the projectile's range, which is defined as the depth at which half of the protons from an impinging parallel beam have come to rest. Assuming an accelerator produces a perfect monoenergetic beam - typically beams have an energy spectrum that ranges around 1% of the initial energy of the beam - particles with the same energy would still not have the same range due to the stochastic nature of the described proton interactions. This range straggling spreads the Bragg peak in water by about 1% of its range [46].

2.2.3 Depth-dose curve of protons

The depth-dose curve of protons is dependent on the interaction mechanisms, range straggling, the initial energy spectrum, and the initial beam width size. Only the latter two can be directly influenced, while the other factors depend on physical laws. Figure 2.7 shows the dose deposition for protons of different energies penetrating water. The plot displays

---

[4]For electrons, which are roughly 1,800 times lighter than protons, the deceleration is substantial, as the electrostatic forces between the particle and the target are similar for protons and electrons. Consequently, bremsstrahlung must be considered in electron therapy.
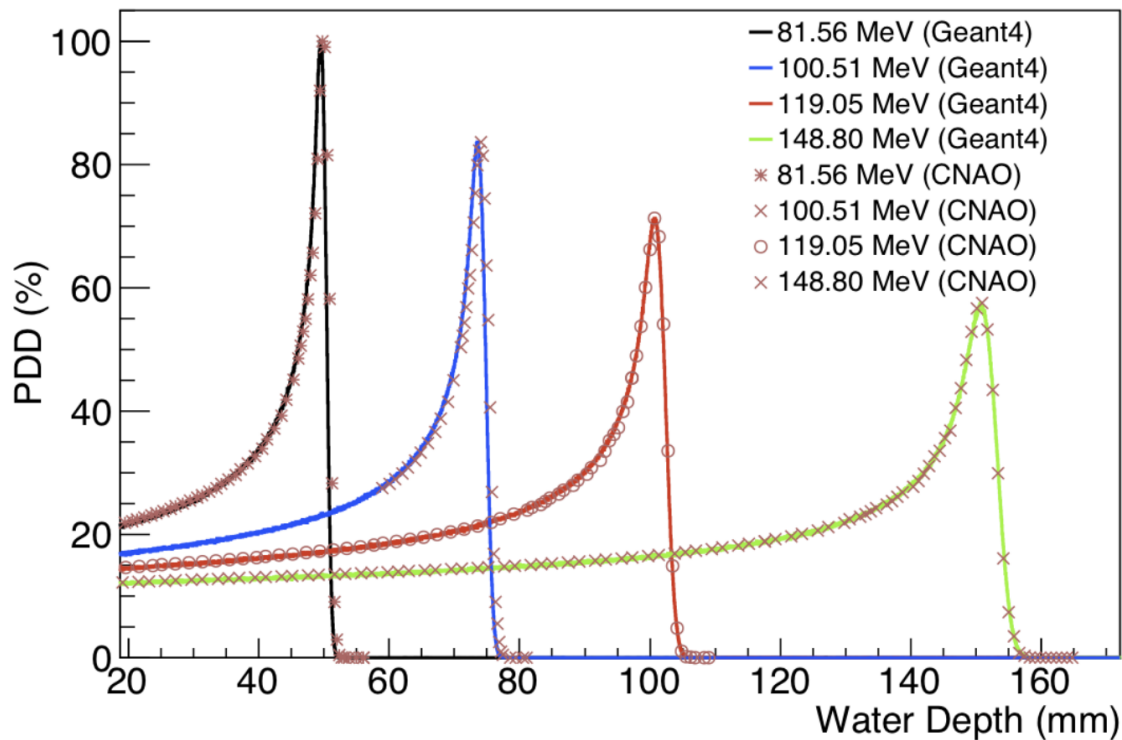
FIGURE 2.7: Depth-dose curves for four different proton energies in water. The plot shows a comparison of Geant4 [52] simulated as well as measured curves against the water depth. All values are normalised by the lowest shown energy of 81.56 MeV. Figure adapted from [53].

normalised simulated as well as measured values. The Bragg peak, which mainly happens due to the characteristics of proton energy loss[5], is observable at well-defined ranges. The higher the initial energy of a beam the more the beam is laterally spread out at the Bragg peak depth due to an increasing amount of deflections, which statistically happen for longer penetration depths.

2.3 Proton therapy

This section introduces the two main beam delivery technologies of passive scattering and active scanning. The latter led to the development of pencil beam scanning, enabling the state-of-the-art technique IMPT. Additionally, it explains technical details on the production of beams and the acceleration of protons.

2.3.1 Passive scattering vs. active scanning

Modern accelerators produce proton beams with a narrow cross sectional area. For different treatment sites the field sizes vary from 1 cm to 25 cm in diameter [38]. Consequently, the narrow, almost monoenergetic beam with a lateral FWHM of about 1 cm must be spread in beam direction and orthogonal to the beam direction. Passive scattering and active scanning are two techniques, which are used to broaden the beam and then shape it to the treatment field.

In the past, the majority of PT centres use passive scattering as their beam delivery technology. Orthogonal to the beam direction the beam is spread by a single scattering foil or

---

[5]The Bragg peak is also a result of nuclear reactions, which is why not all protons reach the peak.

a double scattering system, depending on whether a small or a large field is needed. The additional use of a range modulator ensures that the field is flattened, i.e., the centre must be scattered more than the periphery. The range modulator also generates a SOBP, which is necessary as otherwise most of the treatment volumes would not be fully covered. Aperture and compensator are then used to patient-specifically shape the treatment fields to a targeted tumour profile. The drawback of passive scattering is the need for patient-specific hardware, the constraints in the dose adaptation of the proximal edge of the tumour as well as the generation of secondary particles like neutrons due to interactions with the beam shaping elements.

The alternative to passive scattering, active scanning, which also overcomes the listed limitations, uses the fact that protons, which are subject to Lorentz forces, can be deflected magnetically to generate a quasi monoenergetic pencil beam and to scan across the target volume. Thus the proton beam is no longer broadened but scanned across the tumour. The method, which was suggested in 1980 [54], is chosen for most of the recently built treatment centres. It does not need a collimator or a compensator. The idea is to split the tumour into slices of same energy in the beam's eye view (BEV). Typically, the method starts at the deepest depth (highest energy) and reduces the employed energy for each slice. Each layer of same energy is scanned most commonly in a zigzag manner perpendicular to the beam direction, using a set of dipole magnets in the horizontal and vertical direction. These layers are usually not on the same plane, as a patient has multiple tissues with different densities. The advantages of active scanning are the variety of fine shapes of high-dose regions that can be realised as well as a significant reduction in neutron contamination. Active scanning can be used for the treatment planning methods of single field uniform dose (SFUD) and IMPT.

SFUD applies a homogeneous dose to the target for each beam direction, which is very similar to the passive scattering delivery. Multiple SOBP, which have the same size as the target in beam direction, are delivered. SFUD is more flexible and efficient than passive scattering, as it individually optimises the fluence of each beam to an arbitrarily shaped target. Adding up these individual fields generates the full treatment plan.

The concept of IMPT is to optimise all Bragg peaks from all directions simultaneously. IMPT no longer has the uniformity constraint of SFUD per field, and thus it intentionally delivers non-uniform dose distributions per beam direction. The final target dose, which is achieved by superposition of the individual fields, can have arbitrary forms as long as it achieves the desired total dose. The upside of this method is that additionally to the intensity of a single pencil beam its energy can be modulated, which immensely increases the number of possible dose shapes. Figure 2.8 shows the advantage of IMPT over SFUD, as it spares critical structure, while it ensures the dose coverage. IMPT can however be less robust to treatment uncertainties, e.g., anatomical changes.

2.3.2 Technical details

There are different ways proton beams with clinically needed energies can be produced. One uses a cyclotron, which consists of two main components. The first component is a hollow disk that is separated to form two "dees" with a gap in between them. A voltage, applied across the "dees" sets up an electric field, which accelerates any charge that is placed within that field. The second component is a magnet, whose magnetic field is applied perpendicular to the electric field. If protons, which mostly originate from ionised ion sources, are injected to the centre of the cyclotron they are accelerated by the electric field to the plate (="dee"), which is negatively charged. If the protons are within that negative cavity they are no longer in between two differences of potentials, thus they only experience a force due to the magnetic field. This force directs the protons onto a semicircle path, which causes the
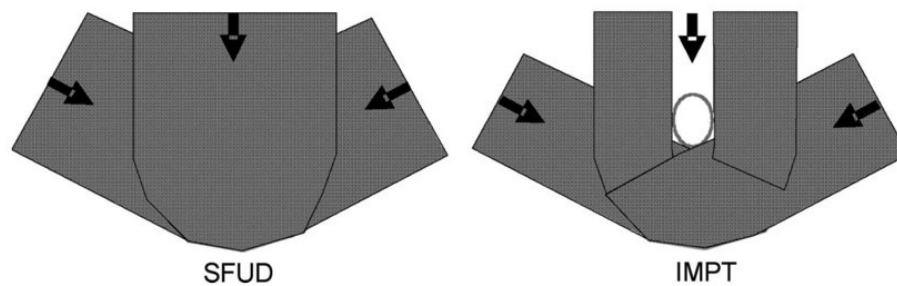
FIGURE 2.8: Three-field SFUD and IMPT plans are shown. In the SFUD plan each field delivers a homogeneous dose to the target. For the IMPT plan the posterior field (from the top) is modified so that the beams passing through the OAR are switched off. As a consequence, both lateral beams must be modified as well to guarantee the desired dose to the target. Figure adapted from [55].

protons to turn their direction. The cyclotron frequency defines the rotation frequency of the proton in a homogeneous magnetic field. In the moment the protons are leaving the cavity the polarity of the electric field is changed resulting in an acceleration of the protons to the other "dee". This change in sign of the electric field is realised by an oscillating voltage. This process is repeated and due to the increasing energies at each turn, the protons will follow a path with increasing radius. The limiting factor for energies, which can be produced in cyclotrons, is the size of the magnets and their fields. The cyclotron was invented by Lawrence in 1930 in Berkeley [56], for which he was awarded the Nobel prize in 1939.

Higher energies and the thus arising relativistic effects set another limit to the achievable energy within a cyclotron. Consequently, modern cyclotrons account for relativistic effects. Relativistic particles, approaching the speed of light, have an increasing relativistic mass, which decreases the cyclotron frequency. Thus in a synchrocyclotron, the frequency of the oscillating electric field is continuously decreased to match the cyclotron frequency. This is done with a constant magnetic field. Alternatively, in an isochronous cyclotron relativistic compensation is achieved by varying the magnetic field, while keeping the frequency of the oscillating electric field constant.

The acceleration time needed to have clinically usable proton beams is in the order of tenths of milliseconds. Consequently, the beam can be switched on and off quickly, which ensures the safety of the patient and allows very fast modifications during treatment delivery.

In synchrotrons[6], which were invented to reach energies beyond those attainable with cyclotrons, the accelerated proton beam travels on a fixed path. This is achieved by synchronising the magnetic field strength and the electric field strength at each turn of the particles in a ring. Consequently, the generation of proton beams with different energies is possible in synchrotrons. This is different to cyclotrons, where a proton beam at one energy is extracted and its energy is adjusted by traversing a so-called energy degrader, which has an adjustable thickness. Another difference between synchrotrons and cyclotrons is their size. Synchrotrons are much larger than cyclotrons however less shielding is needed.

After acceleration of the proton, a beam line, using magnets for focusing and guiding, transports the beam to a treatment room. A fixed beam line would only offer one angle

---

[6]The most famous synchrotron-like accelerator, the Large Hadron Collider (LHC) was built by the conseil européen pour la recherche nucléaire (CERN) near Geneva. It reaches energies in the order of tera electronvolts, which is 10,000 times higher than the energies used in PT.

at which patients could be treated[7]. In order to irradiate a patient from a coplanar angle the beam has to be deflected by magnetic fields, which are placed in large structures called gantries. A typical gantry size for protons is 10 m long and has a 5 m radius [57].

2.4 Biological implications

This section introduces margin terminology and the concept of relative biological effectiveness (RBE), which are necessary to discuss treatment planning. The subsection concludes with dose-volume histograms (DVHs), which is one of the main tools, that is used for treatment plan evaluation.

2.4.1 Terminology of target volumes

Determining target volumes is a crucial part of radiation therapy. Incorrect segmentations result in poor treatment plans, which lead to either underdosage and thus to a reduction in the probability of tumour control or to avoidable dose exposure in healthy tissue. The International Commission on Radiation Units and Measurements (ICRU) standardises the target volumes, which are schematically depicted in figure 2.9 [58].

Briefly summarised, the gross target volume (GTV) covers the visible extent of the tumour, which is clearly distinguishable from other anatomic structures in its vicinity. Microscopic extensions of the tumour are added in the clinical target volume (CTV). This is done to account for microscopic tumour spread, which cannot be seen on the planning images. The internal target volume (ITV) further expands this margin to include target motion. Consequently, the ITV is only defined for moving tumours such as lung tumours. The planning target volume (PTV) is the CTV or ITV plus an extra safety margin for external factors such as uncertainties in patient positioning or beam alignment during treatment. Organs at risk (OAR) are critical structures, which are worth protecting and thus need to be spared from as much dose as possible. The overall outcome of the treatment would otherwise be worse as serious short or long-term side effects could occur. OARs can overlap with other structures.

Segmentation has large uncertainties as it is highly susceptible to the physician who performs the delineation [59]. Consequently, semi- or fully-automated segmentations, which to some extent eliminate this arbitrariness, are more and more used, as they additionally speed up the time-consuming delineation process.

2.4.2 Relative biological effectiveness

Different particles delivering the same physical dose may yield a different biological effect. The effect of the treatment dose to cells is a complex and not fully understood task, which involves the consideration of the properties of the cell as well as the microdosimetric properties of the radiation [38]. The relative biological effectiveness (RBE) links the efficiency of ions compared to those of photons and is defined as:

$$\text{RBE} = \frac{D_{\text{ref}}}{D_{\text{ion}}}, \tag{2.17}$$

where D_{ref} is the reference dose and D_{ion} the ion dose, achieving the same biological effect. The rationale for the application of RBE is to benefit from the large pool of clinical photon

---

[7]In theory the couch could also be moved during treatment to achieve different angles. This is one of the possibilities for the hitherto purely research devices, combining PT with magnetic resonance imaging (MRI), which will be briefly discussed in chapter 9.
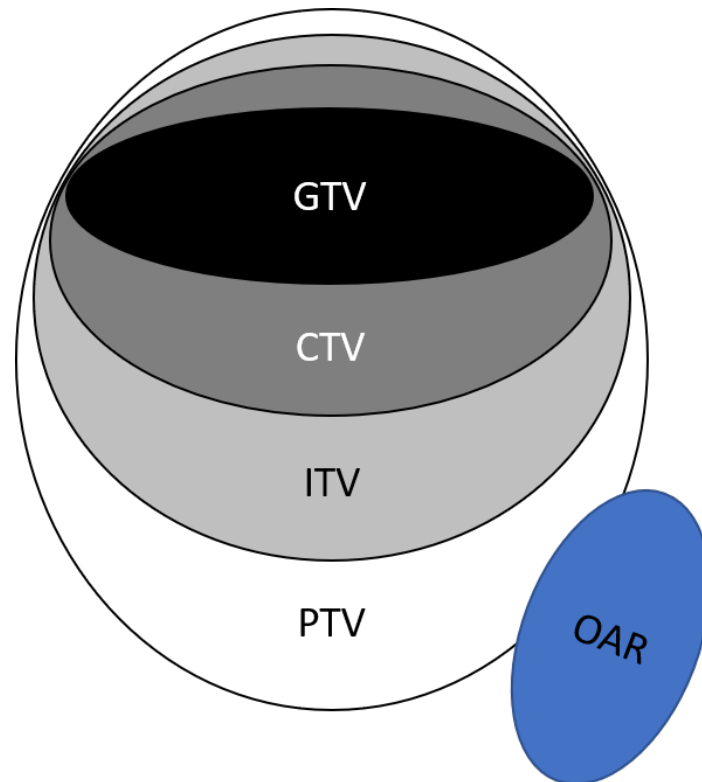
FIGURE 2.9: Hierarchical order of gross target volume (GTV), clinical target volume (CTV), internal
target volume (ITV), planning target volume (PTV) and organs at risk (OAR).

therapy results. Additionally, medically defined required doses for tumour control are given
as photon doses.

The RBE is dependent on various physical and biological properties. One important
physical factor is the linear energy transfer (LET), which is defined as

$$\text{LET}_\Delta = \frac{\text{d}E_\Delta}{\text{d}x},\tag{2.18}$$

where $\text{d}E_\Delta$ is the locally transferred energy to charged secondary particles of the stopping
medium. Energy transfers to secondary particles with an energy above the threshold Δ are
neglected.

The RBE increases for higher LET and smaller residual ranges, which means close to the
Bragg peak the LET and thus the RBE will increase (cf. figure 2.10). However, at the beam
entrance, the RBE is low. This difference between beam entrance and Bragg peak, which
is ideally positioned in the tumour, is the rationale for using heavier ions over photons.
This superior biological effectiveness is more pronounced for heavier ions than protons,
due to the z^2 dependence of the LET. For protons an approximation of a constant RBE of
1.1, which has been validated in vitro and in vivo systems, is used clinically [60]. Up to
the present, clinical data do not show that a constant RBE of 1.1, disregarding dependencies
such as proton beam energy, depth of penetration, dose per fraction, position in the SOBP,
and particular tissue, is ill-advised [49]. However, clinical data cannot confirm a RBE of 1.1,
as the effect, as well as the dose distributions, differ between proton and photon radiation
[49].
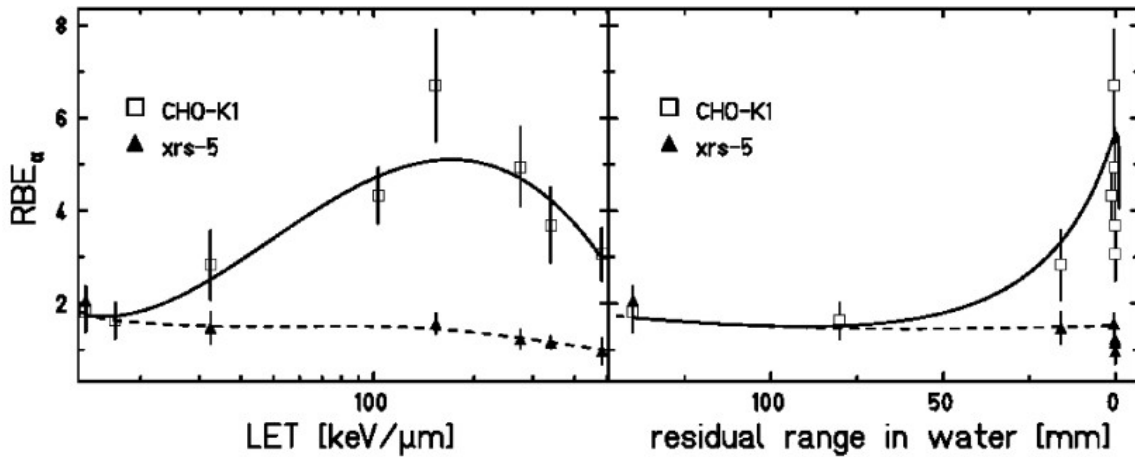
FIGURE 2.10: The RBE of ^{12}C is plotted as a function of LET (left) and residual range in water (right) for CHO-K1 Chinese hamster cells and their repair deficient mutant xrs-5. Figure adapted from [61].

2.4.3 Treatment planning

In RT treatment planning is the development of a patient specific plan to deliver the pre-scribed treatment dose to the tumour while at the same time protecting as much healthy tissue as possible. After delineation, a radiation oncologist prescribes a therapeutic dose to the lesion. This dose typically ranges between 30 Gy to 80 Gy and is delivered in daily fractions of 1.8 Gy to 2.0 Gy [46]. Medical physicists then use computer-based treatment planning systems (TPS) to generate a treatment plan. Within the TPS beam models, describing the beamline and nozzle, as well as beam parameters like the number of beams and their angles are chosen. Additionally, through objective functions, which mainly consider dose coverage, dose homogeneity, and dose exposure to OARs, clinical constraints are set. In an iterative optimisation process modifications of the treatment parameters are performed until the constraints are met and thus an acceptable plan is found. IMPT, which is suscepti-ble to small treatment uncertainties, often uses the minimax robust optimisation approach, which is defined as [62]:

$$\min_{x \in X} \max_{s \in S} \Sigma_{i=1}^{n} w_i f_i(d(x,s)) \tag{2.19}$$

where x is a spot weight of the feasible set X, s a scenario of the set of scenarios S, w is the importance weight, f is the optimisation function, and d is the dose. Minimax discretises uncertainties into a set of scenarios against which the plan should be robust. Choosing clinical robustness settings of 3% range and 6 mm setup uncertainty [63], leads to a total number of 45 scenarios. These scenarios include three possible density shifts (-3%; 0%; 3%) and 15 possible patient shifts in the direction right-left (R-L), inferior-superior (I-S), and posterior-anterior (P-A) (R-L: 0 cm, I-S: 0 cm P-A: 0 cm; R-L: 0.6 cm, I-S: 0 cm, P-A: 0 cm; ...; R-L: 0.35 cm, I-S: 0.35 cm, P-A: −0.35 cm; ...). Minimax then minimises the penalty of the worst-case scenario and provides a bound on how much the plan can deteriorate. Optimisation processes for ions account for the respective RBEs.

Up to present, most TPS solely use CT images for range calculation. To account for the different anatomy and tissue compositions along the beam path, it is not ideal to use the stopping power due to its strong dependence on the particle energy. Thus the relative stopping power, which is defined as

$$\text{RSP} = \frac{S_m}{S_w}, \tag{2.20}$$
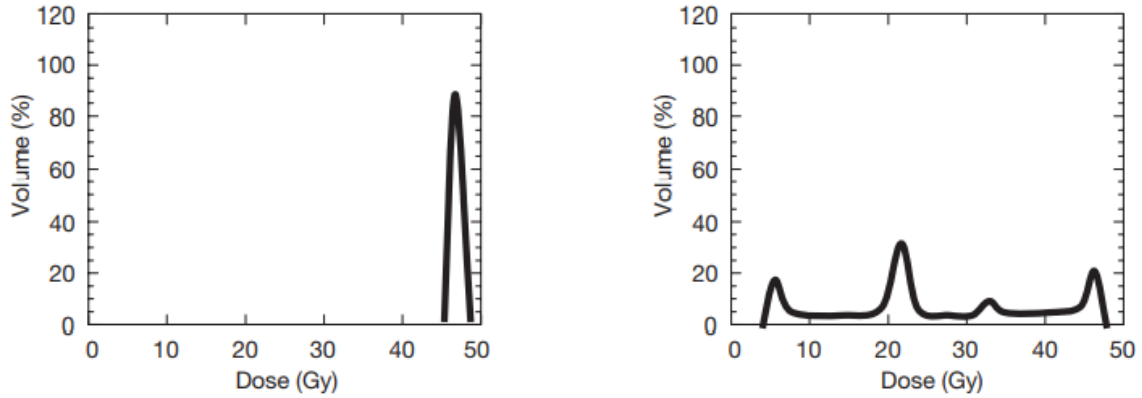
FIGURE 2.11: *Left:* Differential DVH for a target volume of a prostate treatment plan. *Right:* Differential DVH for the rectum (OAR) within the same treatment plan. Figure adapted from [64].

where S_m and S_w are the stopping powers for the material and water, is introduced. Using the RSP the WET can be calculated

$$\text{WET} = t_m \text{RSP}, \tag{2.21}$$

where t_m is the thickness of the material. The behaviour of the beam in water is well known through many experiments. The idea of the WET is to express each individual layer of tissue in the beam path in terms of water so that they are comparable and thus a calculation of the proton range is feasible.

For actively scanned proton beam delivery the TPS calculations result into a set of machine instructions that overlaps between 20,000 to 50,000 pencil beams to generate the optimal patient specific dose pattern. Each of those pencil beams is linked to a distinct pencil beam-spot and energy.

2.4.4   Dose-volume histograms

DVHs display dose statistics of the target or OAR volume, which makes them a useful quantitative tool for the evaluation of treatment plans. DVHs show a distribution of dose on the abscissa for a percentage of the considered volume on the ordinate. There are two different types of DVHs.

Differential DVHs   A differential DVH or direct DVH sums up the number of voxels for a dose within a certain range and plots the resulting percentage of the total volume. Figure 2.11 depicts a differential DVH for a prostate treatment plan of a target volume and the rectum as an OAR.

Cumulative DVHs   In a clinical environment it is important to know how much of the structure is at least covered by a certain percentage of dose, e.g. 98%. In a differential DVH this information can be retrieved by calculating the area under the curve for all doses above or equal 98%. Consequently, the cumulative DVH, which is an integration on a structure-based level is defined as [65]:

$$\text{DVH}(D) = 1 - \frac{1}{V} \int_0^D \frac{dV(D')}{dD'} \, dD'. \tag{2.22}$$
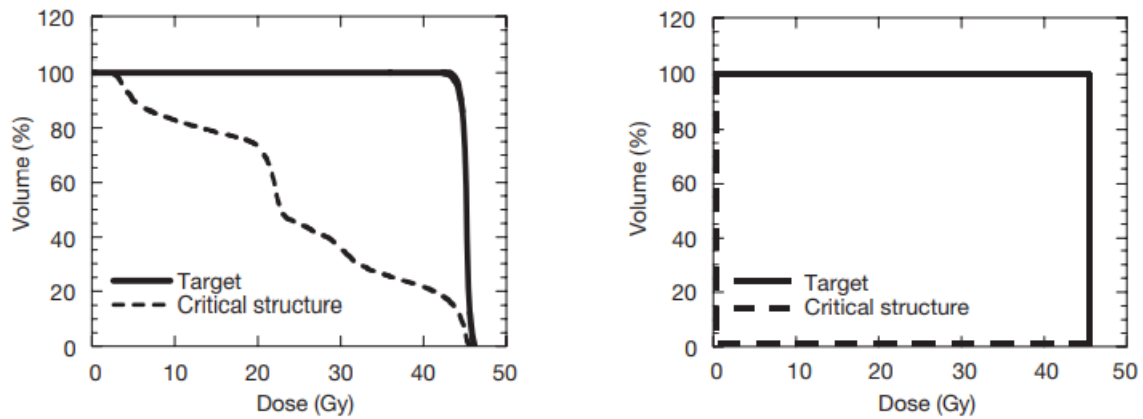
FIGURE 2.12: *Left:* Cumulative DVH for the same treatment plan shown in figure 2.11. *Right:* An ideal cumulative DVH is shown. Figure adapted from [64].

Cumulative DVH plots show the volume that at least gets a certain dose and thus all cumulative DVH has 100% at 0 Gy, because the total volume at least gets no dose. An example for a cumulative DVH, presenting the same prostate treatment plan, as in the case of the differential DVH, is shown in figure 2.12. Additionally, a perfect cumulative DVH is shown, which is only a theoretical consideration.

Chapter 3

Fundamentals of CT imaging

This chapter describes the physical aspects and the technical implementations for X-ray computed tomography and cone beam computed tomography, as those are the relevant imaging modalities for this thesis. Additionally, different image processing steps from acquisition to registration are elaborated. The chapter concludes with an overview of different CBCT intensity correction methods.

3.1 X-ray production

In 1985 Wilhelm Conrad Röntgen experimented with accelerated electrons, leading to the discovery of a high-energy radiation [66], which is capable of penetrating optically opaque objects. For this discovery of Röntgen radiation or more commonly known as X-rays, Röntgen was awarded the first Nobel prize in 1901. On the electromagnetic spectrum X-rays are more energetic than ultraviolet radiation. Figure 3.1 schematically shows an X-ray tube, which is used to generate X-ray photons for, e.g., CT and CBCT. A filament of the cathode is heated to temperatures of about 2400 K, causing the emission of electrons, as they overcome their binding energy. These thermal electrons are then accelerated towards the anode. The acceleration depends on the applied tube voltage, which for imaging is between 25 kV to 150 kV. The deceleration of fast electrons due to their interaction with the anode material causes a transfer of kinetic energy:

$$eU_a = \frac{1}{2}m_e v^2,$$
(3.1)

where e is the elementary charge, U_a the voltage between anode and cathode, and v the velocity of the electron. Consequently, the radiation energy depends on the velocity, which itself is dependent on the voltage. The deceleration of the electrons is a multitude of different slowing down processes due to their interactions with the Coulomb field of the atoms of the anode material. This deceleration, which is called bremsstrahlung, creates electric dipoles and thus electromagnetic waves are emitted. In the deceleration process, a single electron usually generates multiple photons. It is however also possible, that the entire electron energy is transferred to a single photon, which results in a corresponding minimum wavelength of

$$\lambda_{min} = \frac{hc}{eU_a} = \frac{1.24\,\text{nm}}{U_a/\text{kV}}.$$
(3.2)

X-rays can originate from two different sources. One of them is bremsstrahlung, which has a continuous spectrum, and occurs if electrons are deflected by the Coulomb field of heavy nuclei. Alternatively, electrons interact with the electrons bound by the atoms of the anode and lose their energy in several steps. While this energy is partly converted into heat, it also causes the excitation of electrons from inner shells. When electrons of a higher shell fall back onto the free holes characteristic radiation, which is specific for the anode material, is
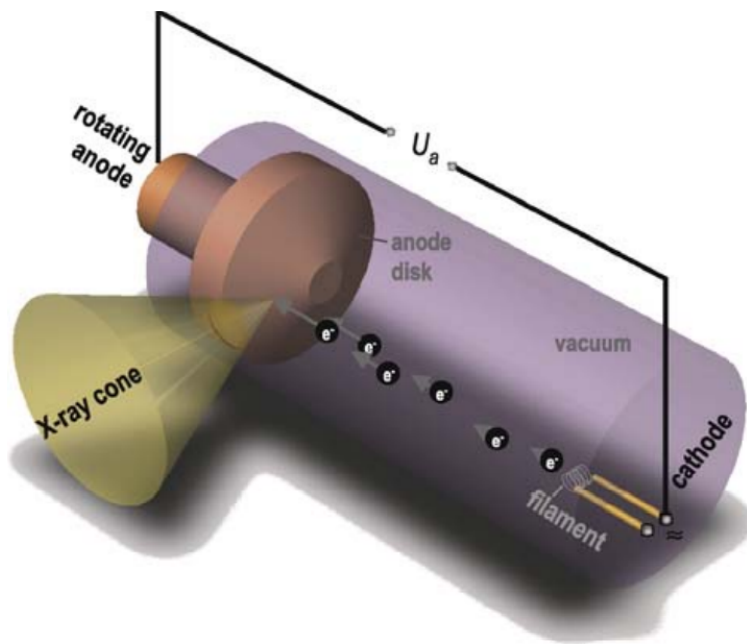
FIGURE 3.1: Sketch of an X-ray tube is shown. Thermal electrons are accelerated between cathode and anode. The deceleration due to their interaction with the anode results in X-ray emission. Figure adapted from [35].

emitted[1]. Figure 3.2 shows an X-ray spectrum, which is the superposition of the continuous bremsstrahlung as well as the characteristic emission of a tungsten photon spectrum.

X-ray production in the imaging regime can be considered very inefficient as only about 1% of the initial kinetic energy is converted. The rest is transferred to the lattice of the anode and thus dissipates as heat. As a consequence, the anode, which is usually made out of Tungsten ($_{74}$W) [68] due to its high melting point ($T_m = 3422\,^\circ$C) and thermal conductivity ($k = 173\,\text{W}/(\text{mK})$), is constantly rotated and cooled down (air or water cooling) to evenly distribute the thermal load.

The size of the X-ray focus on the detector determines, among others, the quality of the image. The smaller the angle of the anode surface normal with respect to the beam, the smaller the projection of the focus onto the detector. For small projections of the focus, the image gets sharper, however, it also causes more concentration of heat. Additional to this effect, anode effects, such as the Heel effect, must be considered. The Heel effect describes an intensity variation of the emitted X-rays due to their different directions and thus paths through the anode material to the detector.

The image quality is also directly impacted by attenuation effects in the imaged object, which depend in a non-trivial way on the wavelength. Low energy X-rays experience a larger attenuation than high energy X-rays. In order to filter out low energy photons, which would not traverse the patient completely and thus only deposit unnecessary dose to the patient, aluminium and copper sheets are added along the beam path [68].

---

[1]Instead of emitting characteristic radiation, in an alternative process, the Auger process, the atom absorbs the photon while emitting another electron (=Auger electron). This process, which is not dominant in high-Z atoms (typical for anode materials), is not considered to be radiation.
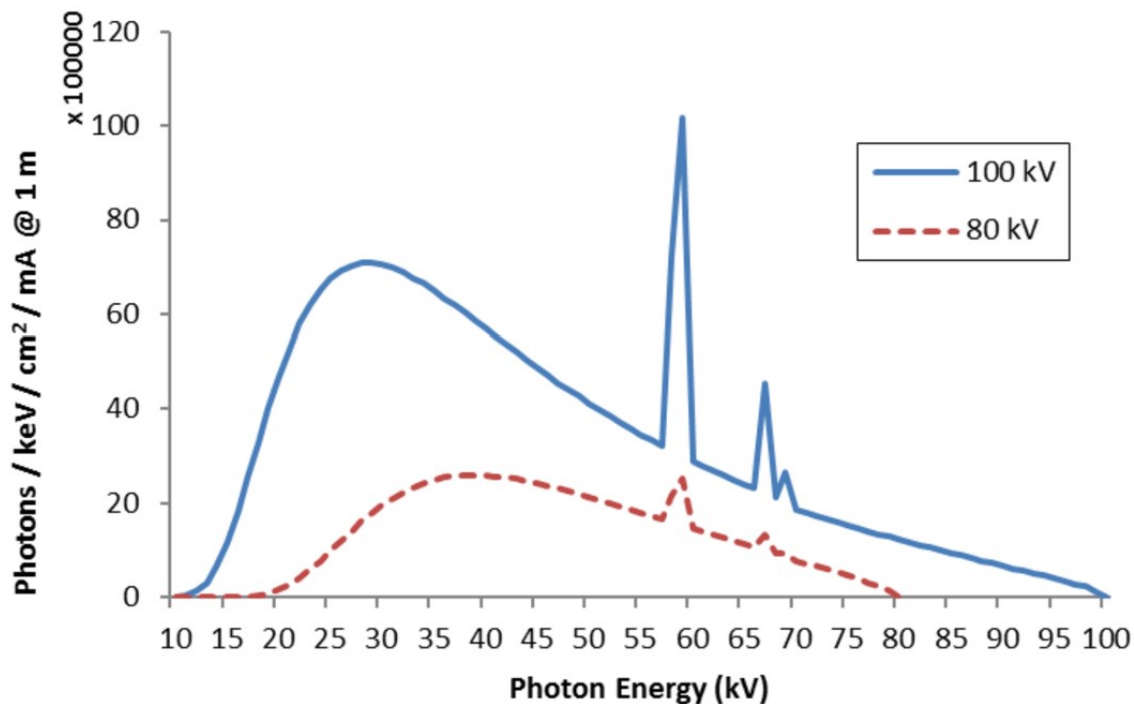
FIGURE 3.2: X-ray spectrum of tungsten including a low energy filter shows the continuous bremsstrahlung and the superimposed characteristic emission lines, which are unique for the anode material. The plot is shown for two different tube voltages. Figure adapted from [67].

3.2 Computed Tomography

Computed tomography is an imaging technique used in materials science [69] and medicine [70]. It uses a computer to calculate digital sectional images from the attenuation values of X-rays, which pass from different directions through the body of interest. Stacking the individual slices together yields a 3D map, containing morphological information on the imaged object.

In the early days of X-ray imaging, the object was X-rayed and imaged on a X-ray film. The result is a projection of the volume onto a plane. Consequently, object parts lying behind each other in the direction of the beam overlap. Due to this averaging process, it is not possible to distinguish, whether a signal on the image was caused by a material with higher absorption or by a greater thickness.

In the 1920s, Grossman overcame these limitations, by moving the X-ray source and the X-ray film synchronously in opposite directions during the imaging process. This eliminated the averaging, as it caused the single slice in the centre of rotation to be sharp, whereas all other slices above and below were blurred. Grossmann also popularised the word tomography, which is a composite word out of the Greek words tomos (=slice) and graphein (=draw).

Since these early days, the development of CT scanners, from their first realisation roughly 50 years ago [71] to now, can be categorised into four generations, which are shown schematically in figure 3.3. The different innovations affect all areas from the design of the machine to the algorithms used for reconstruction (cf. section 3.5). The primary development goals were and are the reduction of the examination time, patient dose, and costs while improving image quality.
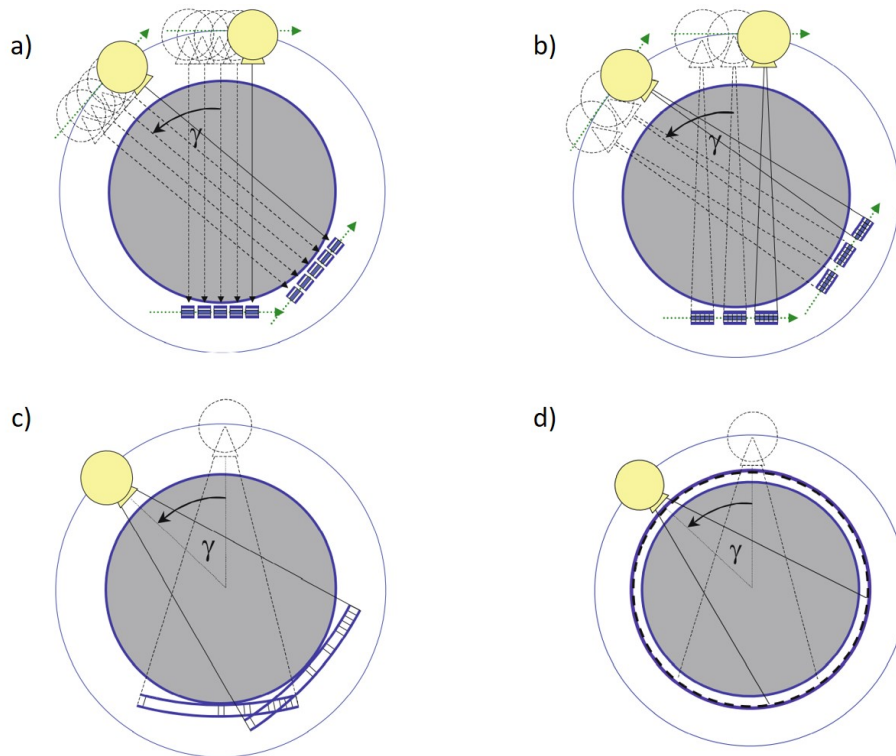
FIGURE 3.3: Different tube and detector constructions of four CT generations (a: first generation = rotation-translation of a pencil beam, b: second generation = rotation-translation of a narrow fan beam, c: third generation = rotation of a wide aperture fan beam, d: fourth generation = rotation-fix with closed detector ring). Figure adapted from [35].

First generation: rotation-translation of a pencil beam   First generation CTs used a pinhole collimator to emit a pencil beam X-ray, which was detected by a single detector. Detector and tube moved translationally at a fixed distance from each other to scan an individual layer. After one of these recordings, which yields a one-dimensional projection, detector and tube were rotated. Different projection angles are needed as otherwise no spatial information would be obtained. The projection angle was gradually changed from $0°$ to $180°$ to view the object from all sides. In 1972 Godfrey Hounsfield first built such a CT [71], for which he was awarded the Nobel prize in medicine in 1979. For the first time, an image without averaging or blurring outside of the centre slice could be acquired, yet its reconstruction needed nine days.

Second generation: rotation-translation of a narrow fan beam   Second generation devices scanned the subject in the same way but used an X-ray source with a narrow fan beam, which was projected onto ten to thirty detector cells. The linear translation, before the projection angle was varied, remained a necessity due to the very small fan angle. Acquisition times, although reduced to the order of minutes per slice, were still long. These acquisition times in combination with small measuring fields of view limited the application of all devices of the second generation (just like the first generation) to only image skulls. This was due to the fact that the cranium can be fixed and no movement inside of it on the timescale of the acquisition with regards to the achievable image resolution was observed.

Third generation: rotation of a wide aperture fan beam   Third generation devices no longer perform a translational movement of the tube, since the fan beam is wide enough

to X-ray the entire object. The only movement of the tube is its rotation around the patient. A circular and significantly larger segment of detector cells, attached to the opposite side of the tube, moves in synchrony to detect the fan beam. The fan angle was increased from around 10° to between 40° and 60°. Consequently, the acquisition time for an entire slice was substantially decreased to about 20 seconds. For the first time, acquisitions of the chest (if the patient was in breath-hold) and abdominal area were possible. A disadvantage of third generation CTs is the creation of ring artefacts, which will be explained in section 3.7.

The majority of currently used CTs are third generation types [35]. Additionally, modern CTs are often multi-slice scanners, which use a similar technique as in-room CBCTs, presented in section 3.3. The difference to CBCTs is that multi-slice scanner CTs use curved detectors. They are also equipped with anti-scatter grids, which are only used in some CBCTs. Anti-scatter collimator grids are used to reduce the number of scattered photons, leading to improved imaging quality. Anti-scatter grids, however, come at the cost of a reduction in detected photons and spatial detector resolution, as a minimum lamella thickness of 0.1 mm is required [35].

Fourth generation: rotation-fix with closed detector ring Forth generation devices have stationary detectors mounted in a full circle around the patient. The X-ray tube either rotates outside or inside the detector ring (Figure 3.3 d shows a rotation outside of the detector ring). This fourth generation, which provides an even faster scanning time, failed to catch on and soon disappeared from the market.

Up to now, the same fate happened to electron beam computed tomography (EBCT), which probably due to its high technical complexity and high price, did also not find its way into everyday medical practice. EBCT has no more moving mechanical components. In addition to a full circle detector there is a ring made of a material such as tungsten, which is used as a target for the electron beam. This electron beam is directed to the desired position on the target ring using electromagnetic fields. Wherever the electron beam hits the target X-rays are produced. EBCT currently allows the fastest acquisition times, which are in the order of milliseconds.

3.3 Cone beam computed tomography

Cone beam computed tomography is an imaging method using divergent X-rays, which form a cone. Similarly to CT, the technique is used in materials science [72, 73] and medicine [74].

Contrary to the use of fan beams in conventional modern CTs, the cone beam geometry in CBCTs exploits the X-ray source more efficiently. This leads to the simultaneous acquisition of multiple slices, which reduces scan time. In conventional CTs with fan beams, slit collimators reshape the original cone-shaped X-ray intensity profile to a planar geometry, generating a lot of heat. In CBCTs the beam is only collimated slightly to typically generate a rectangular cone. Heat production within the X-ray tube and gantry rotation speed are the limiting factors regarding measuring time. Scan time, heat, and cost reduction can be considered the main drivers for the invention of CBCTs.

A realisation of CBCTs could however only be accomplished by an accompanying improvement of detectors, which transitioned from arrays of up to four rows to truly two-dimensional detectors with around 2000×2000 pixels. These so-called flat-panel detectors, which are used in today's CBCTs [75], are based on solid-state scintillation detectors. Figure 3.4 shows a building block of a flat-panel detector. Photons, reaching a detector, interact with scintillating crystals, which are mostly out of caesium iodide (CsI), bismuth germanate ($Bi_4Ge_3O_{12}$) or cadmium tungstate ($CdWO_4$) [35]. The scintillation process occurs due to
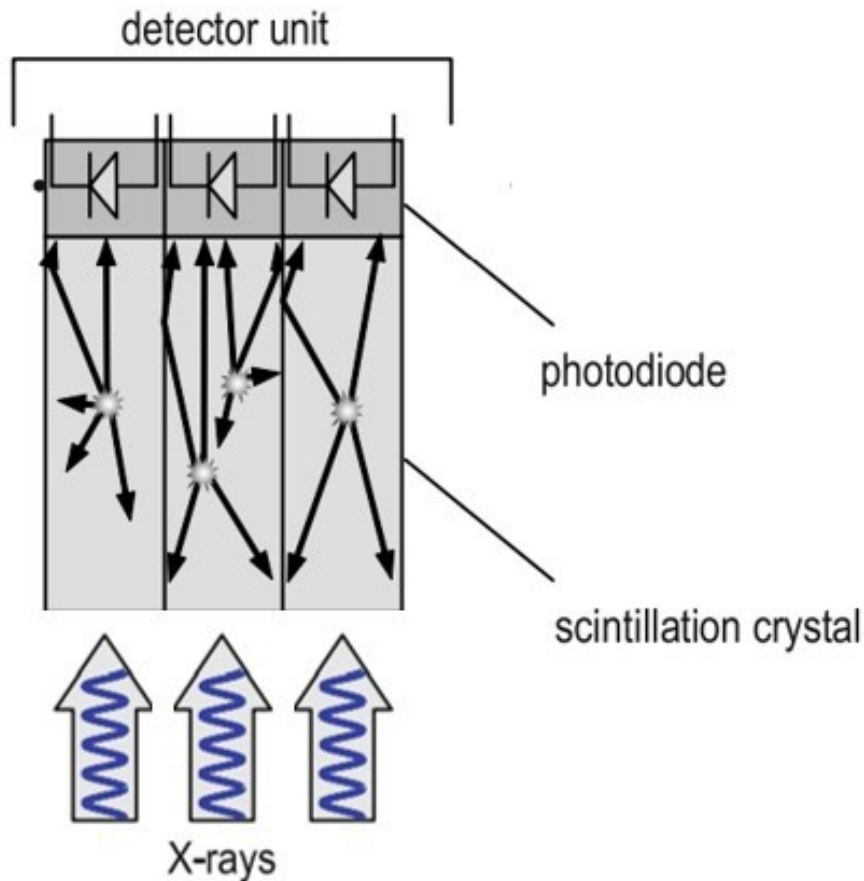
FIGURE 3.4: Sketch of a detector unit, containing photodiode and scintillation crystal used in a flat-panel detector. Figure adapted from [35].

a transition between different energy states. The photon, created in the scintillator, is absorbed by the photodiode, a semiconductor device, generating electron-hole pairs. In the depletion zone between differently doped semiconductors, the two opposite charges of the electron-hole pair quickly drift against the diffusion voltage to opposite directions (holes towards anode and electrons towards cathode), which leads to a current. This current is proportional to the intensity of the photons. Thin film transistors read out the integrated charge.

During imaging the patient couch does not move as the cone beam acquires the volumetric information in a single gantry rotation. The reconstruction of this data differs from the reconstruction used in CTs and will be explained in section 3.5.

CBCTs, which are often linac-mounted [24], allow image acquisition of patients in treatment position, and thus a set-up alignment of the patient in three dimensions. This reduces interfractional positional variations before each treatment [74, 76].

The image quality of CBCTs is in general poorer than that of CTs, which is mainly due to an increase of scatter on the detector. This leads to multiple artefacts, which will be addressed in section 3.7. Additionally, CBCTs, which have inaccurate CT numbers, require further image processing steps to be usable for more sophisticated tasks such as dose calculation. Dose calculation on CBCTs will be discussed in more detail in chapter 7.

3.4 Image acquisition

During a CT or CBCT acquisition, the machines operate according to a certain set of instructions, the scanning protocol. Multiple parameters, which cause different imaging results, are defined in that protocol by the operator before scanning. The following section presents a selection of parameters, their typical values, and their implications for the image.

Tube voltage The tube voltage, which has typical values between 80 kV to 140 kV [38], specifies the X-ray spectrum. For smaller objects small values are used and vice versa. Larger tube voltages lead to lower image contrast at the expense of increased dose, whereas lower tube voltages yield a higher contrast at the expense of a lower penetration depth.

mAs product The mAs product is proportional to the number of photons. It is a product of scan time, which for sequential scans equals the rotation time and the tube current. Typical values range from 10 mAs to 500 mAs [38]. The count of photons per slice determines the image quality in terms of noise. High mAs values result in reduced image noise, but also an increased dose burden for the patient.

Rotation time The rotation time balances the opposing goals of image quality and scan time. Less rotation time leads to a faster overall scan, yet poorer image quality. It is important to note that motion artefacts (cf. section 3.7) are decreased for low rotation times. Typical values for CTs are between 0.33 s to 2 s [38].

Slice thickness The slice thickness provides the resolution in longitudinal direction. Typical slice thicknesses vary between 0.5 mm to 3 mm. In modern third generation CT devices (cf. section 3.2) the patient couch is moved with a constant speed during acquisition, causing a helical trajectory of the X-ray tube with respect to the patient [77]. The pitch p, which is defined as [38]:

$$p = \frac{d}{W_{tot}},$$ (3.3)

where d is the travelled distance of the table during on gantry rotation and W_{tot} is the total collimation, which is the number of slices times their thickness, quantifies the path of the couch. Larger slice thicknesses or lower pitch values improve the image noise, while they prolong scan time. Typically, pitch values vary between 0.3-1.5 [38].

Bow-tie filter The bow-tie filter is used to compensate for inhomogeneities within the X-ray intensity distribution at detector level. Consequently, it can be inserted between the source and imaged object to minimise intensity fluctuations, which originate from the varying attenuations due to the different tissues of the patient, across the detector [74].

The parameter described below is CBCT specific, with a focus on Elekta machines, as those are the ones used within the scope of this thesis.

Panel position Three different field of views (S $\stackrel{\wedge}{=}$ small, M $\stackrel{\wedge}{=}$ medium, L $\stackrel{\wedge}{=}$ large), which can be thought of as the intersection of all X-ray cones, can be set by a different laterally offset panel position [74].

3.5   Image reconstruction

Image reconstruction is the mathematical multidimensional inverse problem of calculating volumetric maps of an imaged object from line integrals of different projection angles[2]. In 1917, long before the invention of the first scanning devices, Johann Radon described the theoretical basis for tomographic reconstruction [79].

The inverse problem tries to obtain the distribution of attenuation coefficients μ of an object from a set of projections p. Defining the projection function as [38]

$$P : p = P(\mu) \tag{3.4}$$

the inverse

$$\mu = P^{-1}(p) \tag{3.5}$$

has to be found. Using the ansatz of an ideal detector and monoenergetic photons, the object's photon beam intensity attenuation can be described by the Lambert-Beer law (cf. equation 2.3)

$$I = I_0 \exp\left(-\int_L \mu(x)\mathrm{d}x\right), \tag{3.6}$$

where I_0 is the initial intensity before penetrating the object. The integral is along the line L passing through the object, which connects the X-ray tube and the detector. The projection value can then be rewritten as

$$p = -\ln\frac{I}{I_0} = \int_V \mu(x,y,z)u(x,y,z)\mathrm{d}x\mathrm{d}y\mathrm{d}z, \tag{3.7}$$

where the integral is now over the full volume V and u is the contribution of each infinitely volume element. Discretising the volume, this can be expressed in vector notation as

$$\vec{p} = U\vec{\mu}, \tag{3.8}$$

with $p_j = \sum_i \mu_i u_{ij}$, which describes all possible rays of n projections of size m^2. $(U)_{ij} = u_{ij}$, defines the contribution of volume element i to the projection of ray j. Inverting this equation yields

$$\vec{\mu} = U^{-1}\vec{p}. \tag{3.9}$$

For certain conditions, the direct calculation of U^{-1} is feasible, yet computationally very demanding. More efficient inversion processes, that rely either on analytical equations or an iterative optimisation process, are discussed below. A more comprehensive explanation of each of the reconstruction methods can be found in [35, 38].

3.5.1   Parallel beam geometry

For CTs of the first generation (cf. section 3.2), parallel beam reconstruction was necessary, which is the simplest reconstruction case. Let f be the image of spatial distribution of attenuation values in the patient coordinate system (x, y). It is handy to define a coordinate system (ξ, η), which rotates with the X-ray source and detector. The relation between the two systems is

$$\xi = x \cos\gamma + y \sin\gamma \tag{3.10}$$

---

[2]The inversion process can also be performed optically, however in the scope of this thesis only numerical solutions are presented, as their results are superior. For optical reconstruction, the interested reader is referred to [78].
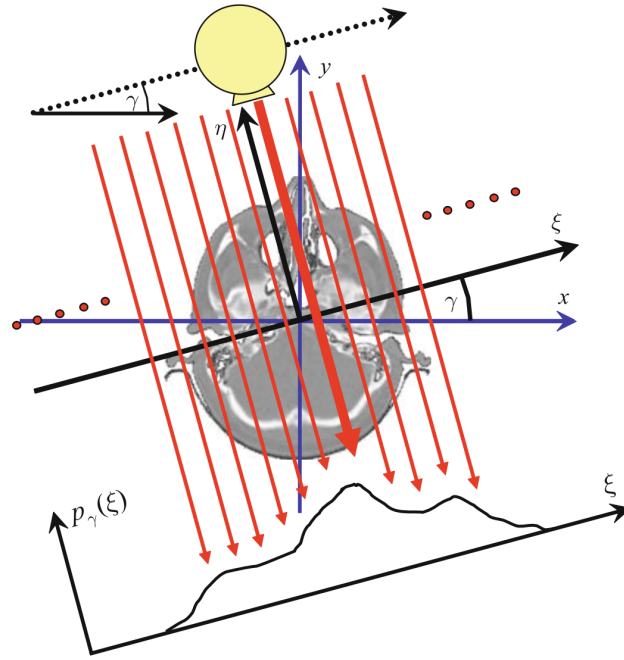
FIGURE 3.5: The relation of the two different coordinate systems (x, y) and (ξ, η) is shown. Additionally, the stepwise shift of the X-ray source at a fixed projection angle γ is displayed. Figure adapted from [35].

and

$$\eta = -x \sin \gamma + y \cos \gamma \tag{3.11}$$

with the projection angle γ. Figure 3.5 shows the relation of the two different coordinate systems. The stepwise shift of the X-ray source can be described as a sampling process of a continuous signal. Let L be a δ-line in the sectional plane, the measured projection can be expressed as [35]:

$$f * \delta(L) = \int_{r \in L} f(r) \mathrm{d}r \tag{3.12}$$

$$f * \delta(L) = \int_{\mathbb{R}} \int_{\mathbb{R}} f(x, y) \delta(x \cos \gamma + y \sin \gamma - \xi) \mathrm{d}x \mathrm{d}y = p(\xi, \gamma), \tag{3.13}$$

where δ is the Dirac delta distribution, which represents a ray line intersecting with the detector element ξ. Equation 3.13 is known as the two-dimensional Radon transform. All measurements $p(\xi, \gamma)$ combined are called sinogram, as the projection values, which belong to one feature in the spatial domain, form a sinosoidal line in the projection. Acquiring projection data for more than $180°$ is redundant as due to symmetry considerations the X-ray path backwards has the same information as the path forwards.

As stated above in the discussion of the inverse problem, the interest lies in the spatial distribution of the attenuation values $f(x, y)$. Thus the one-dimensional Fourier transform w.r.t. the coordinate ξ is applied to equation 3.13

$$
\begin{aligned}
P(q, \gamma) &= (\mathcal{F}p)(q, \gamma) \\
&= \int_{\mathbb{R}} p(\xi, \gamma) \exp\left(-2\pi i q \xi\right) \mathrm{d}\xi \\
&= \int_{\mathbb{R}} \int_{\mathbb{R}} f(x, y) \exp\left(-2\pi i q(x \cos \gamma + y \sin \gamma)\right) \mathrm{d}x \mathrm{d}y,
\end{aligned}
\tag{3.14}
$$

with the spatial frequency q. It is convenient for a later comparison with $P(q, \gamma)$, which is in polar coordinates, to calculate the two-dimensional Fourier transform in the same coordinates. So let

$$u = q \cos \gamma \qquad (3.15)$$

and

$$v = q \sin \gamma. \qquad (3.16)$$

The two-dimensional Fourier transform of the image f(x,y) can be written as

$$F(u(q, \gamma), v(q, \gamma)) = \int_{\mathbb{R}} \int_{\mathbb{R}} f(x, y) \exp\left(-2\pi i(xu + yv)\right) \mathrm{d}x \mathrm{d}y, \qquad (3.17)$$

Comparing the last line to the last line of equation 3.14 yields the identity

$$P(q, \gamma) = F(q \cos \gamma, q \sin \gamma) = F(u, v). \qquad (3.18)$$

This identity, which states that the one-dimensional Fourier transform of the measured projections $p(\xi, \gamma)$ is equal to a slice (=radial line) of the two-dimensional Cartesian Fourier spectrum $F(u, v)$ of f(x,y) at the angle γ, is known as Fourier slice theorem. The relation between the different spaces is shown below:
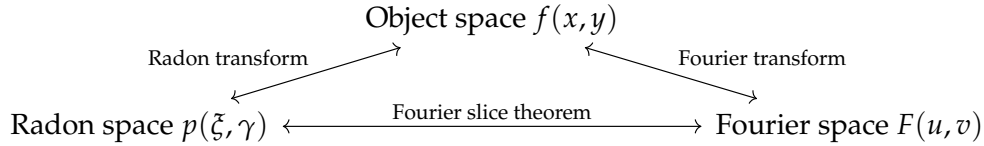
Theoretically, a reconstruction of the image $f(x, y)$ starting from the projections $p(\xi, \gamma)$ is possible. For this a resampling to Cartesian coordinates before the inverse Fourier transform is applied has to be done. This method causes artefacts and is very inefficient, which is why a workaround is needed.

A simple backprojection does not yield the correct attenuation distribution, as the projections $p(\xi, \gamma)$ are non-negative functions. Non-negative values would be "smeared" back over the complete image, resulting in positive pixel values outside of the object. The simple backprojection of a single point causes a blurring on the image, which can be described by a point spread function. Therefore an enhancement to the backprojection method is required.

This enhancement, filtered backprojection, starts with calculating the inverse Fourier transform

$$f(x, y) = \int_{\mathbb{R}} \int_{\mathbb{R}} F(u, v) \exp\left(2\pi i(ux + uv)\right) \mathrm{d}u \mathrm{d}v. \qquad (3.19)$$

The same coordinate transform as in equation 3.15 and 3.16 is used. The differential $J \mathrm{d}u_x \mathrm{d}u_y$ with the Jacobian

$$J \equiv \det\left(\frac{\partial(u, v)}{\partial(q, \gamma)}\right) = q(\sin^2 \gamma + \cos^2 \gamma) = q \qquad (3.20)$$

yields

$$f(x, y) = \int_0^{2\pi} \mathrm{d}\gamma \int_{\mathbb{R}} F(q \cos \gamma, q \sin \gamma) \exp\left(2\pi i q(x \cos \gamma + y \sin \gamma)\right) q \mathrm{d}q. \qquad (3.21)$$

Splitting the integral into a sum of two integrals where the limit for the angle interval is $[0, \pi]$ and $[\pi, 2\pi]$, shifting the second limit to the first by a phase shift in the sin and cos

terms of the integrand, and using Fourier symmetry properties yields

$$\int_0^\pi d\gamma \int_{\mathbb{R}} F(q\cos\gamma, q\sin\gamma) \exp\left(2\pi i q(x\cos\gamma + y\sin\gamma)\right)|q|dq. \tag{3.22}$$

Applying equation 3.10 and 3.18 gives

$$\int_0^\pi d\gamma \int_{\mathbb{R}} P(q, \gamma) \exp\left(2\pi i q\xi\right)|q|dq, \tag{3.23}$$

where $|q|$ is called the ramp kernel, which is renamed to $K(q)$. Using the convolution theorem the reconstruction kernel can be expressed as

$$k(\xi) = \mathcal{F}^{-1}K(q) = \int_{\mathbb{R}} \exp\left(2\pi i q\xi\right)|q|dq = \frac{-1}{(2\pi\xi)^2}. \tag{3.24}$$

This finally gives the formula for filtered backprojection

$$f(x, y) = \int_0^\pi d\gamma\, p(\gamma, \xi) * k(\xi)\Big|_{\xi = x\cos\gamma + y\sin\gamma} \tag{3.25}$$

Equation 3.25 shows that a convolution of the measured projection with the kernel reconstructs the image.

For fan beam geometries it is possible to find parallel X-ray beams within the projections. Consequently, a transition from fan beam to pencil beam (parallel beam) can be achieved by rebinning corresponding beams of different fans (different projection angles) and combining them again. After this process is done, a synthetic parallel beam geometry is obtained, which can be reconstructed as explained above.

Hounsfield scale This section concludes with a digression on the conversion of linear attenuation values to CT numbers in Hounsfield units (HU). In clinical practice CT numbers are expressed in terms of HU, a linear scaling of attenuation values, which is defined as

$$\text{CT} = \frac{\mu - \mu_{\text{water}}}{\mu_{\text{water}}} \cdot 1000\text{HU}, \tag{3.26}$$

with the attenuation values μ of a generic tissue and μ_{water} of water.

The Hounsfield scale covers a large range from air, which has a CT value of $-1000\,\text{HU}$ to cortical bone with CT values from $300\,\text{HU}$ to more than $1000\,\text{HU}$, as shown in figure 3.6.

In order to show an ideal contrast for the region of interest (ROI) within the tomographic image, the greyscale map, which is used to show the image on a monitor, is re-scaled for displaying purposes. Instead of scaling the possibly displayable grey values to the minimum and maximum intensity value of the image, two values, level l and window w, determine the scaling for the used grey map. Level should have a value, which is in the centre of the CT number range of the ROI. Window controls the range of the steps in CT numbers in correspondence to the displayed grey values. Consequently, the used interval to scale the available grey values ranges from $l - w/2$ to $l + w/2$.
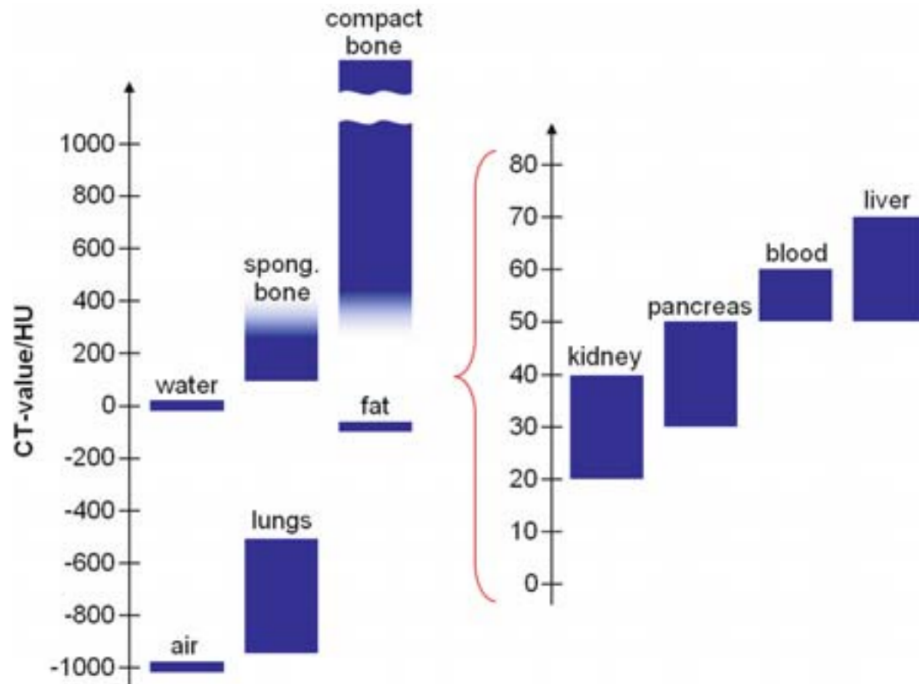
FIGURE 3.6: The range of different CT values from air to bone is displayed. Figure adapted from [38].

3.5.2   Cone beam geometry

The following section describes specific cone beam reconstruction mechanisms, which can be regarded as enhancements of the method for a parallel beam geometry. An implementation of the reconstruction operations was done by Rit et al. within their Reconstruction Toolkit (RTK) [80], which is based on the Insight Toolkit (ITK) by McCormick et al. [81]. All performed reconstructions presented in this thesis use this framework.

Feldkamp-Davis-Kress (FDK)   The reconstruction of a cone beam geometry can be done directly from the projection data. In 1984 Feldkamp, Davis, and Kress, who worked in materials testing at Ford Motors, proposed an approximation method for cone beam reconstructions [73]. An approximation is needed as in practice a full set of Radon data is never available for any circular trajectory, which can be shown by the Tuy-Smith sufficiency condition [82]. The condition states that only if trajectories of the X-ray source at least once intersect all surfaces, which intersect the object, an exact reconstruction is feasible. However, planes parallel to the trajectory of the X-ray source exist and never intersect with them. Consequently, there is an incompleteness in circular cone beam acquisitions [3].

The FDK algorithm, which uses incomplete Radon data, is based on pre-weighting of the measured projections, filtering, and backprojecting. Consequently, it is an enhancement of filtered backprojection. The idea is to partition the cone beam into fan-shaped surfaces, which will be treated independently.

Therefore, the rays are split into parts along the X-rays beams and along the direction of the detector. Additionally, a virtual detector is placed parallel to the real detector at the iso-centre. Regarding figure 3.7 each detector row (constant b) combined with the source defines a fan beam out of the complete cone beam. This simplifies the cone beam geometry problem into many fan beams.

---

[3]Acquisitions following a saddle trajectory no longer have this problem and are currently investigated.
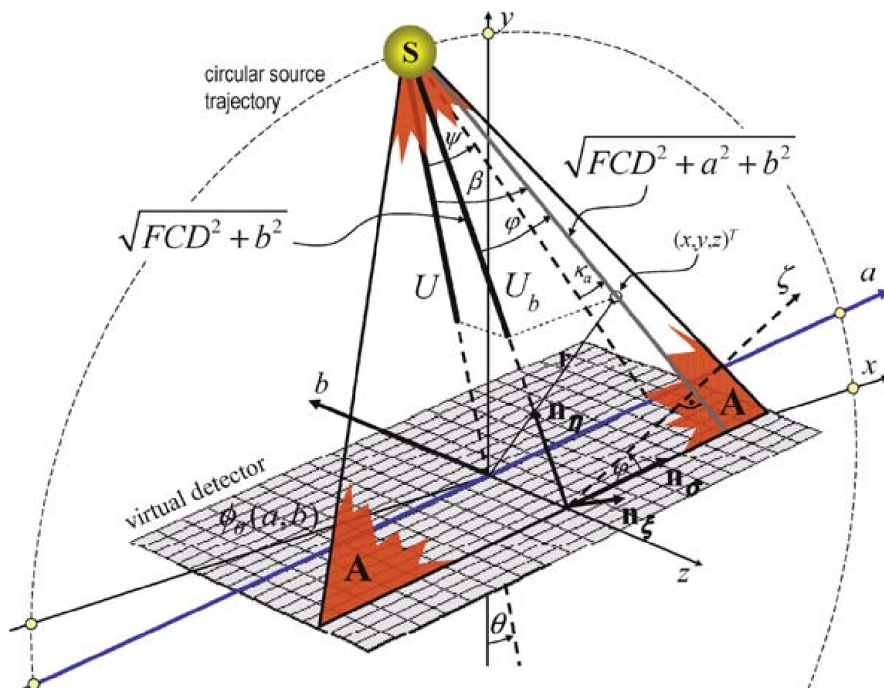
FIGURE 3.7: Overview of the geometrical quantities used in the FDK algorithm. A virtual detector with coordinates (a, b) is placed at the iso-centre. θ is the projection angle between the y-axis and the source position. The virtual measured projection values are denoted with ϕ. Within this thesis all presented calculations do not differentiate between virtual and "real" projection values and thus use p. Figure adapted from [35].

Accounting for different distances, to correct for the increased attenuation of photons along the periphery is called pre-weighting. The weighting factor can be determined as

$$w = \frac{\text{FCD}}{\sqrt{\text{FCD}^2 + a^2 + b^2}}, \tag{3.27}$$

where FCD (focus center distance) is the distance between the centre of rotation and the source and a, b are detector coordinates. Geometrically, the weighting factor is $\cos\beta$ where β is the angle with respect to the detector normal (cf. figure 3.7).

The measured projections $p(a, b, \theta)$ with the projection angle θ are weighted and convolved with a filter h(a)

$$\tilde{p} = (w \cdot p(a,b,\theta)) * h(a) \tag{3.28}$$

Using backprojection the final image can be expressed as

$$f(x,y,z) = \int_0^{2\pi} \frac{1}{U^2} (w \cdot p(a,b,\theta)) * h(a) \mathrm{d}\theta, \tag{3.29}$$

where U is a geometrical factor. FDK was originally developed for flat panel detectors, which are used in in-room CBCTs. Consequently, further adaptations of the algorithm are required, if FDK is used for multi-slice CTs, which have curved detectors.

The FDK algorithm is easy to implement, yet due to insufficient data not exact. Radon transforms from discrete data as well as approximations for the line integrals result in inaccuracies. These inaccuracies get worse for larger cone angles, which leads to artefacts (cf. section 3.7). To overcome these limitations iterative reconstruction algorithms, which increase CBCT image quality, were developed.

MA-ROOSTER   FDK, a 3D reconstruction method, shows substantial motion artefacts and thus poor image quality if moving entities, such as the lungs, are reconstructed. To mitigate motion artefacts improvements such as respiration-correlated FDK [83] and motion-compensated FDK [84] have been developed. This thesis solely focuses on motion-aware reconstruction based on spatial and temporal regularisation (MA-ROOSTER), an iterative reconstruction algorithm, which combines motion-estimation and motion-compensated reconstruction methods with regularised 4D reconstruction methods [85]. MA-ROOSTER is the used reconstruction algorithm for the pipeline presented in chapter 7.

It seeks an optimum between respiration-correlated techniques, which provide high contrast however only in combination with streaks, and motion-compensated techniques, which show fewer streaks with the drawback of fully relying on a motion prior or estimate to reconstruct a single 3D image.

MA-ROOSTER, which is based on ROOSTER, uses a 4D conjugate gradient (CG) approach for its optimisation. In 4D CG the goal is the minimisation of the cost function

$$\sum_{\alpha} ||R_{\alpha} S_{\alpha} f - p_{\alpha}||_2^2, \tag{3.30}$$

where R is a forward projection operator, S is an interpolator along the time dimension, f is a vector containing the 3D image volumes $f_1, f_2, ... f_N$, N is the number of phases, p is the measured projection, α is the projection index, and $||.||_2$ is the $\ell 2$ norm. 4D CG reconstructions show accurate motion information, yet they are blurry and contain streak artifacts [85].

For ROOSTER [86], regions, where motion is expected, are segmented to generate a motion mask. The application of this motion mask is a crucial part of ROOSTER as it removes all motion outside of the segmented region by averaging along the time dimension. Additionally, ROOSTER applies a total variation (TV) denoising on the image volumes, which is defined as

$$f_{\text{denoised}} = \arg\min_u ||u - f||_2^2 + \gamma_{\text{space}} TV_{\text{space}}(u) + \gamma_{\text{time}} TV_{\text{time}}(u), \tag{3.31}$$

where

$$TV_{\text{space}}(u) = ||\sqrt{(\nabla_x u)^2 + (\nabla_y u)^2 + (\nabla_z u)^2}||_1 \tag{3.32}$$

and

$$TV_{\text{time}}(u) = ||\nabla_t u||_1. \tag{3.33}$$

∇_x, ∇_y, ∇_z and ∇_t are gradient operators along the spatial axes x, y, z, and time axis t. $||.||_1$ is the $\ell 1$ norm. γ_{space} adjusts the denoising of the image by controlling the spatial 3D total variation. Images with less noise or lower spatial total variation are favoured when setting larger γ_{space} values. γ_{time} analogously affects the time dimension by controlling the weight given to the temporal 1D total variation.

The enhancement step to MA-ROOSTER is the additional bending of temporal regularisation to follow moving structures. This is done with the help of motion information obtained in the form of deformable vector fields (DVFs). The DVFs are determined from a 4DCT, which is available for lung patients, mapping an extremal phase in the breathing cycle to all other phases of the breathing cycle. The method by which the DVFs are determined is irrelevant for MA-ROOSTER, however within this thesis deformable image registration (DIR), which will be explained in section 3.8, is used. This additional step of MA-ROOSTER helps preserving small structures so that they are not smoothed away. It also hinders the spreading of high-intensity structures to adjacent phases. The extent of the warping of the images according to the DVFs is adjusted by the chosen value for γ_{time}. In summary, ROOSTER can be regarded as a special case of MA-ROOSTER with null DVFs.

Within this thesis MA-ROOSTER in its RTK implementation, which is GPU optimised to guarantee low computation times, is used.

3.6 4D imaging

4D imaging describes a type of medical imaging that additionally to its three spatial dimensions has a time dimension. With the help of these images internal motion can be observed, which can be useful for diagnosis, treatment planning, and as a controlling tool during and in between radiation treatments.

The acquisition of 4DCBCT projections does not differ technically from 3DCBCT projections, as the chosen reconstruction method determines the outcoming image. Nevertheless, acquisitions for 4DCBCT, which use a slower gantry motion and a higher number of projections, are longer. This is needed to prevent undersampling and thus ensure a similar image quality [87].

A respiratory signal is extracted from the 4DCBCT projections, using the Amsterdam shroud algorithm [88]. Thereby, the features on the projections, which are in the superior-inferior (SI) direction like the diaphragm, are enhanced by performing a derivative in SI and a logarithmic transform. A concatenation of transversely summed pixels generates a 2D Amsterdam Shroud image. This image is cropped so that only the main oscillatory signal is visible. The breathing phases can then be determined using the analytical signal. This retrospective binning is usually done into 10 phases. As a consequence, 3D images with reduced motion artefacts at different times within the breathing cycle, showing different tumour positions, can be reconstructed. 4DCBCT, which is a crucial part of this thesis, is up to now mostly used in research studies [89].

The difference between 3DCT and 4DCT acquisition is the additionally obtained correlated surrogate signal. This additional signal is recorded, so that a correspondence between image slice and a respiratory phase, which is needed for 4DCT, is available [90]. The additional information, a record of the external respiratory signal, can be obtained in multiple ways. For the data used within this thesis an Anzai belt (Anzai, Japan) attached to a pressure sensor, which is strapped around the chest of the patient, was used to record the breathing signal. Other possibilities to obtain a breathing signal are optical tracking of markers, which are put onto the patient's skin, or the use of spirometry devices [91].

The signal information, which contains multiple breathing cycles, is used to sort the CT slices into bins. Two different sorting methods, phase sorting and amplitude sorting are used [92]. Phase sorting is a time-based method, which specifies a percentage (e.g., 0%, 10%, 20%, ..., 90% if 10 phases are generated) of the period of each breathing cycle. For amplitude sorting constant amplitudes on the breathing cycle are chosen for the sorting.

3.7 Image artefacts

The following section discusses image artefacts. The provided, alphabetical list may not be exhaustive, but the most dominant artefacts are covered. Artefacts, structures in the image which are not present in reality, are caused by the discrepancies between physical measurement conditions and mathematical simplifications used for the reconstruction [93].

The flat panel detector design for cone beams is the main reason for scatter artefacts as it collects all scattered photons from the patient's body. With increasing size of those detectors more scatter will be detected. Additionally, the larger FOV in one rotation of a cone beam compared to a fan beam leads to a larger amount of scattered radiation. Scatter causes a deviation of the photons from their original trajectory. Primary (wanted) radiation on the detector is thus topped by scattered radiation, which leads to relatively low values in
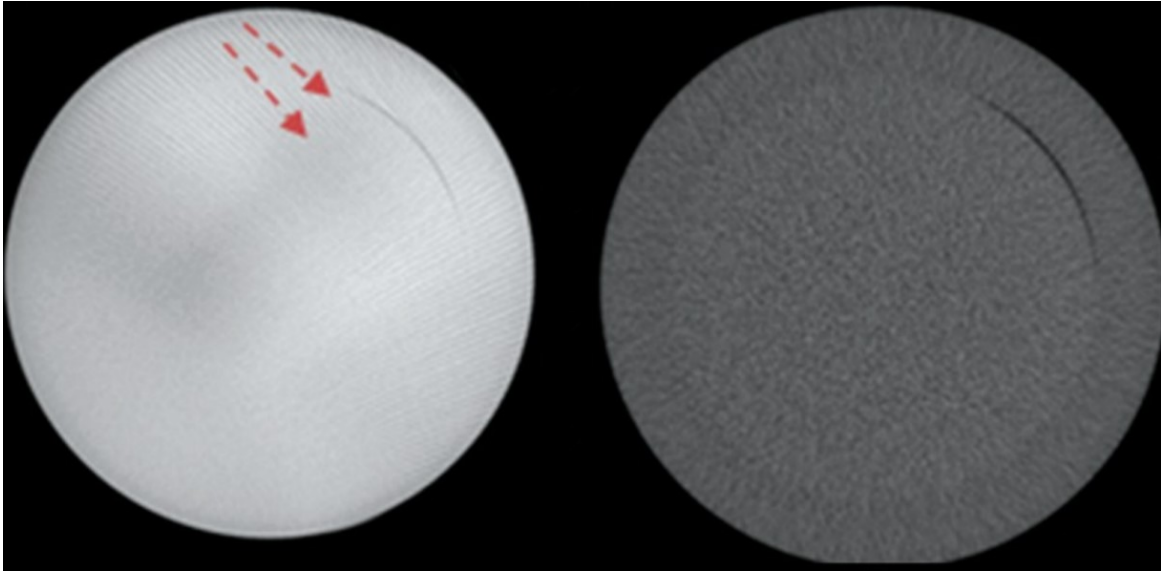
FIGURE 3.8: Aliasing patterns are visible on the left plot with the help of the red arrows. The right plot shows an aliasing corrected image. Figure adapted from [74]. Additionally, in both plots a ring artefact can be seen (cf. figure 3.14).

the middle of the reconstructed image. Scatter causes artefacts, which affect homogeneity, contrast, noise and consequently the overall image quality [74].

Noise is a random or non-random signal, which is not wanted. Regarding a ROI, noise can be described in a homogeneous section as the standard deviation relative to the mean value of that section [77]. If the number of detected photons is low, noise is high. This condition occurs for combinations of high attenuations, low mAs and small slice thicknesses (cf. section 3.4). High noise levels cause inconsistent linear attenuation values during reconstruction, which leads to lower contrast to noise ratio.

3.7.1   Aliasing

The further away a voxel is from the source the fewer rays reach it. Consequently, voxels near the source collect more rays than those near the detector. This undersampling causes line patterns in CBCT datasets, that are called aliasing artefacts. Expressed in mathematical terms the Nyquist sampling theorem is violated. Additionally, aliasing artefacts can occur due to a too coarse interpolation between backprojected lines and voxels. The aliasing artefact is visible in figure 3.8.

3.7.2   Beam hardening

Real X-ray beams have a polychromatic spectrum. Equation 3.6 however assumes monochromatic beams. If the true spectrum has more low energy rays than the detected spectrum (low energies are favourably absorbed), a non-linear error is introduced into the projection data. This causes either dark streaks or cupping artefacts in the reconstruction. Dark streaks are produced between two high attenuation objects. Cupping artefacts, which are displayed in figure 3.9, appear in homogeneous objects.

3.7.3   Detector lag and ghosting

Flat-panel detectors show high resistance to radiation damage [95], and are thus chosen for readout in tomographic devices. Detector lag describes the situation that a signal is still
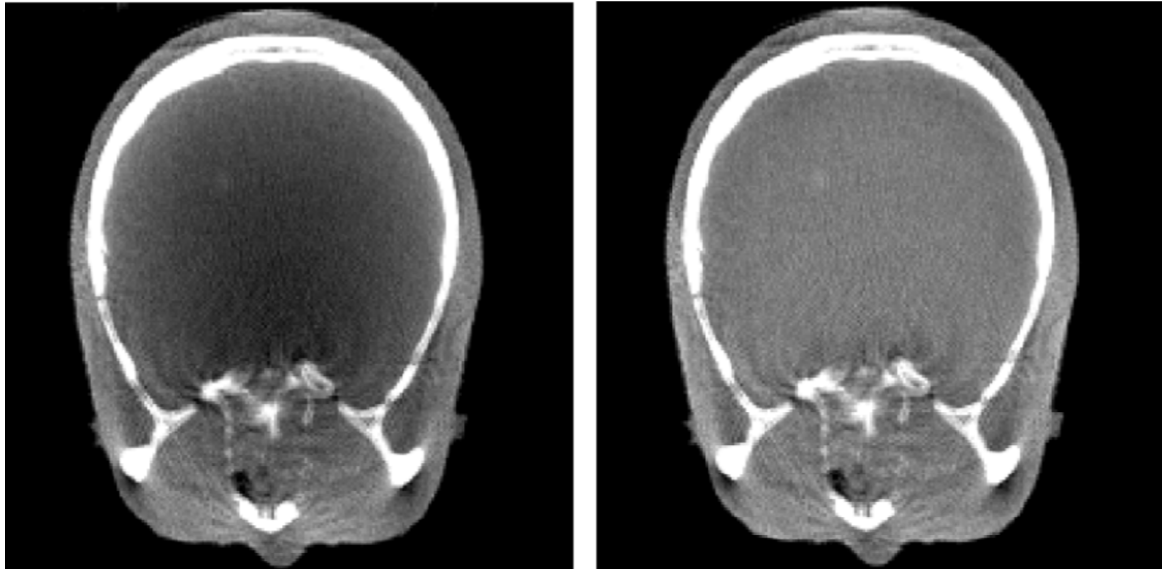
FIGURE 3.9: Axial view of a reconstructed skull phantom. The left plot shows the original image with cupping. The right plot shows a cupping corrected image. Figure adapted from [94].

present in the detector pixel frames subsequent to the frame in which the signal was generated [26]. This image information, which is carried to successive projections causes a bias in each pixel, which results in artefacts in the reconstructed image. The main causes of detector lag are threefold: the charge is not transferred completely between the capacitance of the sensor elements and that of the readout electronics, the decay time in optical emission from the X-ray converter is finite, and the signal collection is inefficient as charge gets trapped and released in sensor elements [26].

Ghosting is the long-term persistence of images up to 1 h following an exposure [26]. The sources of ghosting are similar to those of detector lag. Figure 3.10 exemplarily shows detector lag artefacts as well as ghosting artefacts.

3.7.4 Exponential edge gradient effect (EEGE)

The exponential edge gradient effect (EEGE) appears if adjacent structures vary significantly in their absorption (e.g. bone to soft tissue transition). Reconstruction algorithms such as FDK (cf. section 3.5) assume theoretical beams with zero width, whereas the true width is determined by the pixel size. Consequently, on these steep transitions an average intensity is measured. The EEGE error, which is shown in figure 3.11, always reduces and thus underestimates the real density value.

3.7.5 Extinction

The detected value can be close to zero if the object contains high absorbing material. As a result absorption calculations are not feasible and artefacts (zero entries) are produced. This problem arises often in images for dentistry as patients can have golden teeth. However, it can also occur in all other body parts, e.g., radiotherapy patients could have metal hip implants.
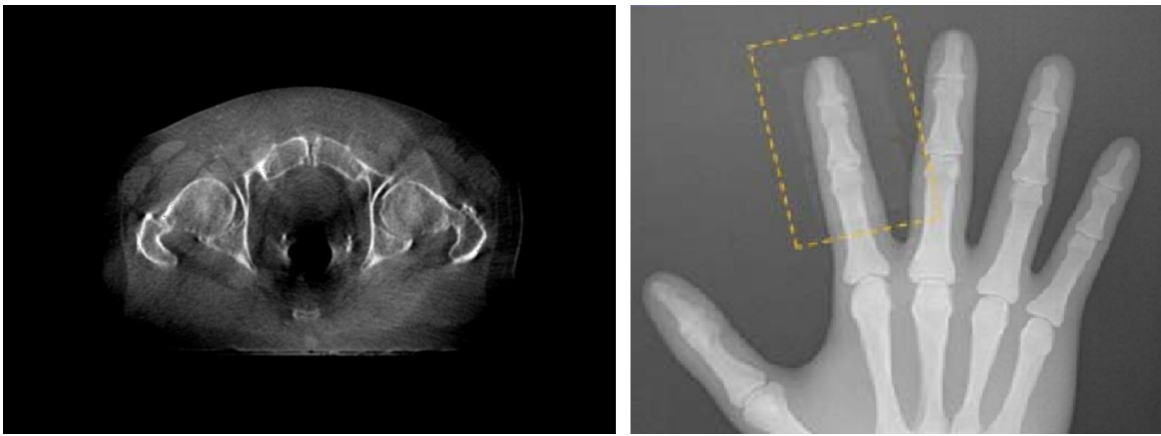
FIGURE 3.10: The left plot shows an example of detector lag artefact and its corresponding grayvalue reduction on the right side of the patient, which results in an apparent left-right contrast. Figure adapted from [96]. The right plot shows a typical ghosting artefact for a hand phantom. Figure adapted from [97].
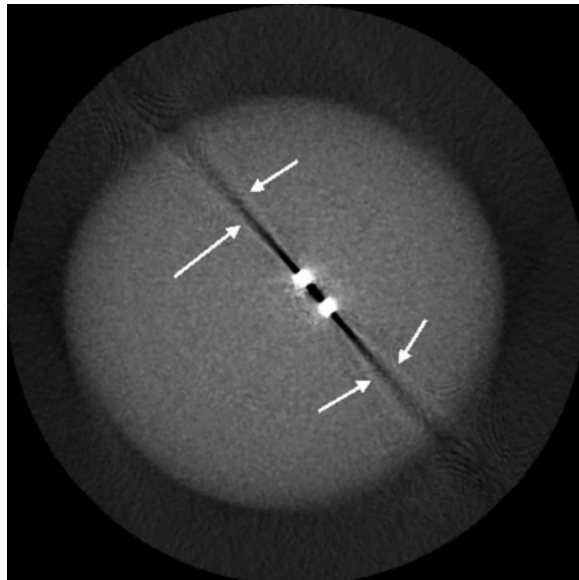
FIGURE 3.11: The EEGE causes thin lines tangent to steep transitions in beam direction, which are indicated with the white arrows. Figure adapted from [93].
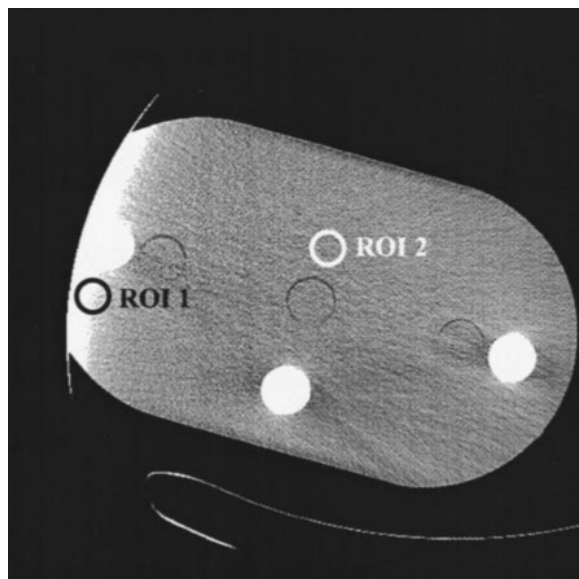
FIGURE 3.12: The plot shows a typical FOV truncation. Figure adapted from [98].

3.7.6 FOV truncation

This artifact is encountered when parts of the imaged body part remain outside the field of view (e.g. due to patient body habitus), which results in inaccurate measurement of attenuation along the edge of the image. On the left side of figure 3.12 a typical FOV truncation is displayed. The artifact can be reduced - if possible - by using an extended FOV reconstruction within the affected region.

3.7.7 Motion and misalignment

Misalignment of source, object, and detector leads to blurring in the backprojected image. A misalignment is given if the object moves during the acquisition process. These movements can be "internal" such as breathing or "external" as the patient could move on the couch during acquisition. Backprojection assumes a stationary geometry and thus reconstructions like FDK (cf. section 3.5) do not account for motion. Motion artefacts can lead to isolated or combined effects of blurring, streaks, and double images. Different motion artefacts are displayed in figure 3.13.

3.7.8 Ring

Concentric rings around the rotation axis can be caused by either defective or not correctly calibrated detector elements. This is a problem that can arise during the manufacturing process [74] or due to wear and tear, which can cause pixels to die. These inconsistencies, which are called ring artefacts, are dominant in beam direction, i.e., on axial slices. A ring artefact is shown in figure 3.14.

3.7.9 Scatter glare

Reconstruction algorithms assume a straight line for the trajectory of the photons from source to detector. In reality the X-ray trajectory is disturbed by scattering processes (cf. section 2.1). Scattered photons contribute to the intensity of a "wrong" pixel, which leads
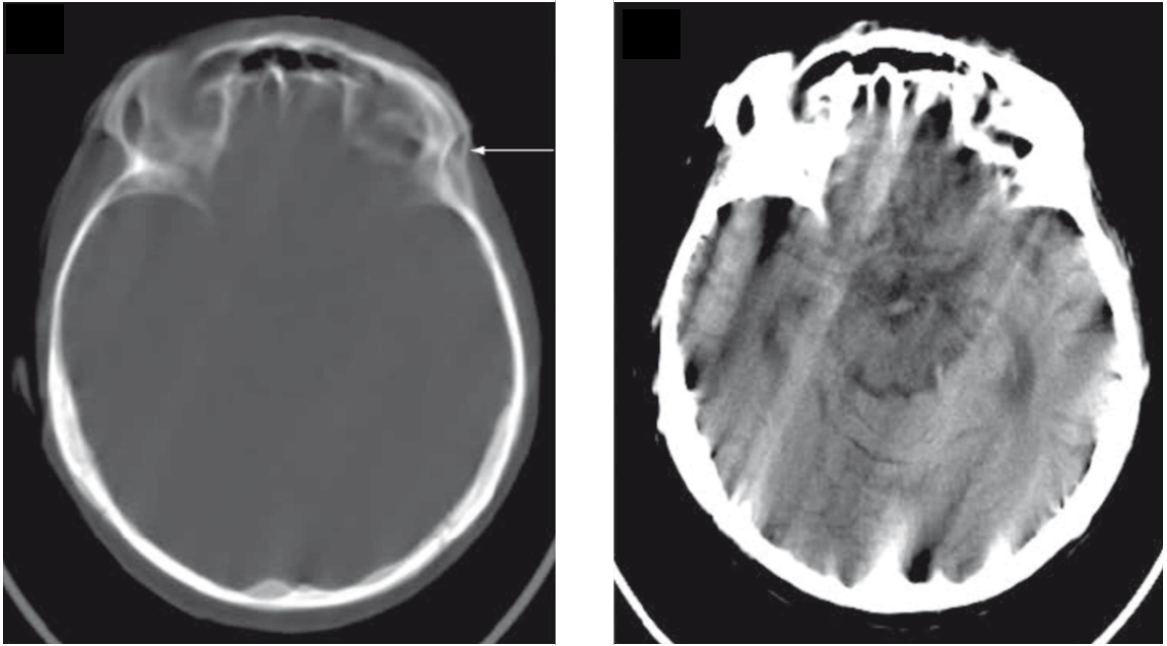
FIGURE 3.13: The two plots show different outcomes due to motion artefacts: blurring (left), double images (left), and streaks (right). Figure adapted from [99].

FIGURE 3.14: A ring artefact in the centre of this head scan is clearly visible. Figure adapted from [100].
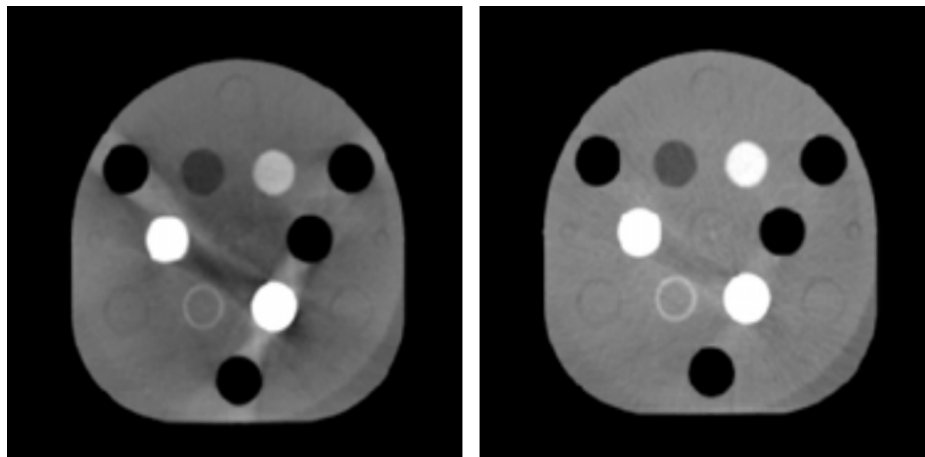
FIGURE 3.15: The left plot shows scatter glare artefacts in a CBCT scan with no corrections applied. The right plot shows the same CBCT scan with scatter glare corrections. Both plots additionally show ghosting artefacts (cf. figure 3.10) in the bottom right part of the phantom, which is shaded. Figure adapted from [28].

to a false underestimated absorption coefficient. Scatter glare originates largely from scattering of photons in the detector panel and its housing. Typical scatter glare artefacts cause streaks, shading, cupping, and reduced image contrast, which can be seen in figure 3.15.

3.8 Image registration

In a clinical radiation therapy setting many different imaging modalities are used. Among these the most prominent are CT (cf. section 3.2), CBCT (cf. section 3.3), magnetic resonance imaging (MRI) [101], and positron emission tomography (PET) [102]. To benefit from the different information provided by these different modalities, the images must be mapped to a joint coordinate system and patient anatomy. This process, image registration, has a wide field of applications in radiotherapy including patient positioning, virtual CT generation (cf. section 3.9), and transfer of contours between images.

Image registration maps one image (called moving or target image) to another image (called fixed or reference image). In mathematical terms, image registration quantifies the spatial transformation between two images of similar objects. The choice out of numerous existing image registration methods depends on the involved modalities and the considered region of the body. Two image registration types exist: affine registration and deformable registration. The goal for both types is to find the transformation Δ with which the moving image m gets warped. This is done by optimising an energy functional that consists of a metric M, which takes the warped image $m \circ \Delta$ and the fixed image f as input and returns a real value quantifying the similarity of the images [103]. The energy functional can be written as

$$\tilde{\Delta} = \text{argmin}_{\Delta} M(f, m \circ \Delta) + R(\Delta), \tag{3.34}$$

where R is a regularisation term, which hinders physically unreasonable solutions and $\circ$ is the function composition.

3.8.1 Metrics

Metrics are chosen depending on the kind of modality and whether they differ (multimodal registration) between fixed and moving image or not (monomodal registration). The simplest metric is geometry-based, which tries to minimise the Euclidean distance between

geometrical features such as points, lines, planes, and regions. These features need to be either accurately defined, which is not always feasible, or in a cumbersome pre-processing step manually determined. This is a drawback of geometry-based metrics.

Alternatively, image similarities can be determined by comparing their intensity values. A selection of so-called image similarity metrics are presented below:

Sum of square differences (SSD)   This metric is solely suitable for monomodal registration, as it depends on image intensity. It is defined as

$$M_{\text{SSD}}(f, m \circ \Delta) = \int_X (f - m \circ \Delta)^2 \tag{3.35}$$

with $X \in \mathbb{R}^3$. This metric is also often expressed in a sum notation and then called mean squared error (MSE)

$$M_{\text{MSE}}(f, m \circ \Delta) = \frac{1}{N} \sum_X (f(X) - m(X) \circ \Delta)^2, \tag{3.36}$$

where N is the number of pixels.

Cross-correlation (CC)   Cross-correlation can be used if the intensities of both images are linked in a linear way. The CC metric is defined as [104]

$$M_{\text{CC}}(f, m \circ \Delta) = \frac{\int_X f \cdot (m \circ \Delta)}{\sqrt{\int_X f^2 \cdot \int_X (m \circ \Delta)^2}} \tag{3.37}$$

Mutual information (MI)   The MI metric is used for multimodal registration with different intensity scales. The mutual information I is defined as

$$I(f, m \circ \Delta) = H(f) + H(m \circ \Delta) - H(f, m \circ \Delta), \tag{3.38}$$

with the Shannon entropy H, a measure derived from information theory, which describes the diversity in the considered data and takes into account the number of different categories and the number of individuals per category. It is defined as [105]

$$H(f) = - \sum_{i=I_{\text{min}}}^{I_{\text{max}}} h_f(i) \log(h_f(i)) \tag{3.39}$$

and the joint entropy is defined as

$$H(f, g) = - \sum_{i=I_{\text{min}}}^{I_{\text{max}}} \sum_{j=I_{\text{min}}}^{I_{\text{max}}} h_f(i, j) \log(h_f(i, j)), \tag{3.40}$$

where I_{min} and I_{max} are the extrema of the intensity values in the images and $h_f(i)$ is the ith entry in the intensity histogram of f. $h_f(i, j)$ is a joint histogram, i.e., a joint probability of pairs of intensity values.

In order to implement the MI metric it needs to preserve metric properties (positive-definite, symmetric, triangle inequality, and identity of indiscernibles). Consequently, the

MI metric is defined as [104]

$$M_{\mathrm{MI}}(f, m \circ \Delta) = 1 + \frac{I(f, m \circ \Delta)}{\max(H(f), H(m \circ \Delta))} \tag{3.41}$$

Local phase difference (LPD) The Morphons registration algorithm [106] does not rely on intensity differences but on phase differences. It assumes that images can locally be considered as a sum of periodic signals and the computation of the local phase difference is equivalent to the estimation of the local displacement between images [107]. The downturn of the local phase consideration is that there is no easy definition of a scalar metric M.

In an initial step a quadrature filter is applied to detect lines and edges within the image. Then the local phase at frequency ω in direction η is calculated. This filter, a so-called loglet, is defined as

$$H_\eta(\omega) = \chi_+(\eta^\mathsf{T}\omega)(n^\mathsf{T}\hat{\omega})^2 R(||\omega||) \tag{3.42}$$

with the frequency vector $\omega \in \mathbb{R}$, the Heaviside step function $\chi_+(\lambda) = 1$ if $\lambda > 0$ and 0 else, $||\omega|| = \omega^\mathsf{T}\omega$ and $\hat{\omega} = \frac{\omega}{||\omega||}$, and the radial function

$$R(r) = \exp\left(-\ln^2\left(\frac{2}{\rho}\right) / \ln 2\right), \tag{3.43}$$

which is centred on $\rho > 0$ and defined for $r > 0$. The angle between η and ω is defined as ϕ. For the whole 2D frequency plane only 4 directions η, which means four ϕ angles, are needed ($\phi_k = k\pi$ for $0 \le k \le 3$). In 3D six 6 directions, i.e., 6 ϕ angles are sufficient ($\phi_k = k\pi$ for $0 \le k \le 5$). The filtering operation on an image is defined by the convolution

$$q_f(x, k) = (f * h_k)(x). \tag{3.44}$$

Filtering the image f and the warped image w, the local phase difference can be determined

$$\Delta\phi_k(x) = \arg(q_f(x; k)q_w^\star(x; k)), \tag{3.45}$$

where $(.)^\star$ is the complex conjugation and $\Delta\phi_k(x) = \phi_f(x; k) - \phi_w(x; k)$ is the local dephasing between f and w in direction η_k.

The LPD is defined for a specific direction and thus no global definition of this metric is available. Its advantage is its applicability to images with different intensities (e.g. CT and CBCT), as it stresses on lines and edges instead of intensities.

3.8.2 Affine image registration

Affine transformations map parallel lines to parallel lines, using homogeneous 4x4 matrices for a 3D to 3D mapping [103]. Consequently, the image can be rotated, translated, scaled, and sheared. In rigid registration, a subclass within affine registrations, which is of particular interest in medical images, only rotations and translations are allowed. Consequently, it forbids unphysical global shearing and scaling operations. The transformation is defined as

$$\Delta = (\vec{r}, \vec{t}), \tag{3.46}$$

where $\vec{r}$ is the rotation vector and $\vec{t}$ is the translation vector. In matrix notation this would be

$$\Delta = \begin{bmatrix} r_{11} & r_{12} & r_{13} & t_1 \\ r_{21} & r_{22} & r_{23} & t_2 \\ r_{31} & r_{32} & r_{33} & t_3 \\ 0 & 0 & 0 & 1 \end{bmatrix} \tag{3.47}$$

Rigid transformations have six degrees of freedom to match the moving image to the fixed image.

3.8.3 Deformable image registration (DIR)

In contrast to affine registrations, deformable registrations can map straight lines to curves. On an individual voxel level a displacement is performed. This increases the degrees of freedom significantly. Complex motions, especially in the abdominothoracic region, can now be modelled more accurately.

   DIR methods can be categorised into parametric techniques (B-splines [108], thin-plate splines [109], radial basis functions [110], linear elastic FEM [111]) and non-parametric techniques (viscous fluid [112], optical flow [113], Demons [114]).

   For multimodal registrations non-intensity-based metrics are needed [107]. This is where the Morphons algorithm [106], which is a non-parametric method, matching transitions from dark to bright regions instead of intensities, becomes interesting. The comparison is done by investigating spatial oscillations in the intensities. The enhancement of this algorithm, the diffeomorphic Morphons [107] is used in chapter 7. A motivation for diffeomorphism is given below.

   The diffeomorphic algorithm is introduced by giving a general overview of the principle of a non-parametric registration algorithm. Specific details for the diffeomorphic Morphons algorithm are explained afterwards.

Diffeomorphism   Diffeomorphism is a branch of differential geometry, which describes bijective, continuously differentiable functions mapping a differential manifold. The inverse of this function, performing the inverse geometrical transformation, is also continuously differentiable. Diffeomorphism is a necessary condition to guarantee physically sound results. Figuratively speaking this means that body parts such as organs can be compressed and deformed, however non-invertible spatial transformations such as mirror effects or local folding are not possible.

   Let the displacement field be defined as a vectorial field [107]

$$D \in \mathcal{V} = V : \mathbb{R}^3 \to \mathbb{R}^3 \tag{3.48}$$

and the transformation

$$\Delta = \mathrm{Id} + D, \tag{3.49}$$

where Id is the identity matrix. The transformation Δ is diffeomorphic if its Jacobian is positive. The aim of the Morphons algorithm, as for all registration algorithms, is to find a D so that $f \approx m \circ \Delta$. The necessity of diffeomorphism is illustrated in figure 3.16.

Generic multiscale, non-parametric, deformable registration algorithm   Before presenting a generic pipeline for a multiscale, non-parametric, deformable image registration, the three building blocks of this algorithm, field computation Θ, field accumulation Φ, and field regularisation Ψ, will be introduced.
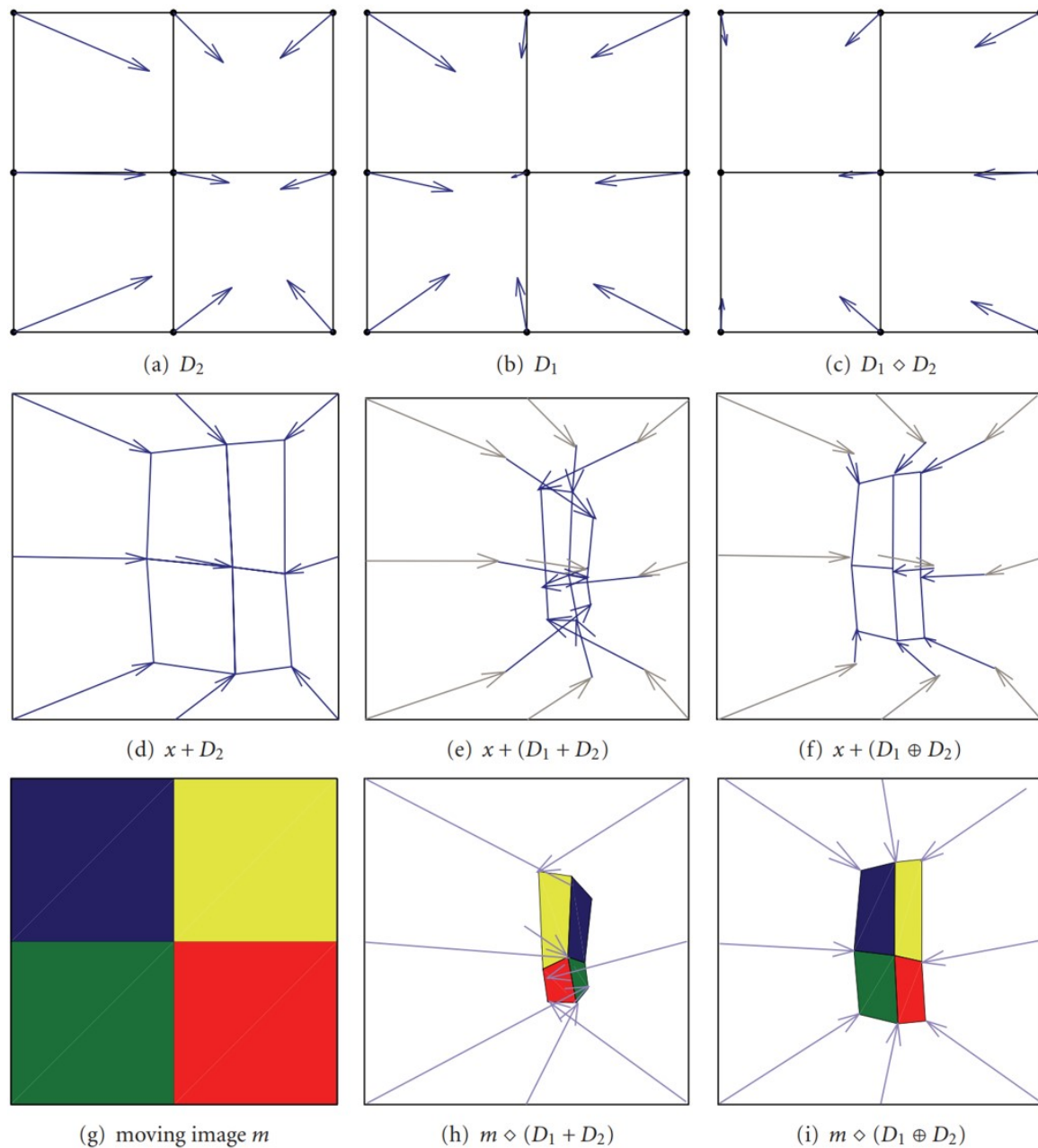
FIGURE 3.16: Plot (a) and (b) show different displacement fields. Plot (c) shows the displacement field D_1 warped by D_2, that is, $D_1 \circ \Delta_2$. Plot (d) shows the application of field D_2 to the grid. Plot (e) shows the application of an addition-based (= non-diffeomorphic) accumulation of D_1 and D_2 to the grid. Plot (f) shows the application of a composition (= diffeomorphic) of D_1 and D_2 to the grid. The definition of $D_1 \oplus D_2 = D_2 + D_1 \circ D_2$. Consequently, the vectors in (f) correspond to those in (a) and (c). Plot (g) shows a moving image m, which has four differently coloured quadratic regions of the same size. Plot (h) shows the unwanted (unphysical) mirror effect (check the positions of the colours), as the moving image m is warped by the sum of the displacement fields. Plot (i) shows the wanted (location-conserved) result, as the moving image m is warped by the composition of the displacement fields. Figure adapted from [107].

At each iteration step of the registration algorithm field computation is performed. That means that the displacement field D_u is updated by a function Θ of the fixed image f and the moving image m, warped by the displacement field resulting from the previous iteration D_a

$$D_u \leftarrow \Theta(f, m \circ \Delta_a), \tag{3.50}$$

where Δ_a is the transformation corresponding to D_a.

Following the field computation, the total displacement D_a is increased by the updated field D_u

$$D_a \leftarrow \Phi(D_a, D_u) \tag{3.51}$$

This field accumulation is done by the composite accumulation explained in figure 3.16.

To guarantee smooth transitions and to reduce noise the field is regularised at each iteration step

$$D_a \leftarrow \Psi(D_a) \tag{3.52}$$

The smoothing operation is performed by applying a low-pass filter on each component of the displacement field.

The generic multiscale, non-parametric, deformable registration algorithm takes as input a fixed image f, a moving image m, the number of scales J, and a stopping criterion s. The pipeline starts on a coarse grid, where $j = J$ and with each iteration performs the computations on a finer one until $j = 0$. The corresponding grid at each step is denoted as G_j. The algorithm starts with an initialisation step, where it sets the scale $j = J$ and initialises $D_a = 0$ on G_{J+1}. The second step, which starts the outer loop, downsamples the images f and m to the grid G_j. This generates $m_j = \text{Down}_j(m)$ and $f_j = \text{Down}_j(f)$. Additionally, upscaling is used to transfer the displacement fields used on grid G_{j+1} to the finer grid G_j. Within this loop which sets $j \leftarrow j - 1$ at each step, a while loop is performed until the stopping criterion s is met. The while loop contains of a warping $w = m_j \circ \Delta_a$, a field computation $D_u \leftarrow \Theta(f_j, w)$, an accumulation $D_a \leftarrow \Psi(D_a, D_u)$, and a regularisation $D_a \leftarrow \Psi(D_a)$ step. The output of this algorithm is the total displacement field D_a, which yields the transformation.

Diffeomorphic Morphons   The diffeomorphic Morphons algorithm uses this general idea with a few specifications. It calculates a certainty map, which is used to estimate the confidence in the computed displacement vectors. Therefore a certainty measure, which is derived from the magnitude of the phase difference, for one filter H_k is defined as

$$c_k(x) = A_f(x;k) A_m(x;k). \tag{3.53}$$

with the amplitude of the filtered image f with h_k

$$A_f(x;k) = |(f * h_k)(x)|. \tag{3.54}$$

In the field computation step Θ the updated deformation field D_u is computed by solving the weighted least square optimisation for the local phase difference

$$\Theta_D(f, w) = \operatorname*{argmin}_{d \in \mathbb{R}^3} \Sigma_k (c_k(\rho \eta_k^\mathsf{T} d - \Delta \phi_k))^2 \tag{3.55}$$

The certainty map is defined as the sum of all certainty measures

$$\Theta_c(f, w) = \Sigma_k c_k(x). \tag{3.56}$$

The field accumulation Φ uses the proper compositive accumulation to ensure diffeomorphism. Euclidean operations on elements of the Lie group of diffeomorphism can produce displacement fields, which are not within this Lie group [115]. Stationary velocity fields, which can be computed in the log-domain, are by definition Euclidean and thus they are interesting to perform operations. The log operation and its inverse, the field exponentiation, are defined as

$$V = \log(D + \mathrm{Id}) \Leftrightarrow D = \exp(V) - \mathrm{Id}. \tag{3.57}$$

Field accumulation in the diffeomorphic Morphons algorithm, which uses the certainty map for weighting, is defined as

$$\Phi_D(D_a, D_u, c_a, c_u) = D_a \oplus \left(\exp\left(\frac{c_u}{c_a + c_u} D_u \right) - \mathrm{Id} \right) \tag{3.58}$$

Field regularisation Ψ in the diffeomorphic Morphons algorithm uses a normalised Gaussian filter, which accounts for the certainty map. The normalised convolution of a scalar function s by a filter g, which is typically a Gaussian kernel of variance $\sigma_\Psi > 0$, is defined as

$$s *_h g = \frac{(hs) * g}{h * g} \tag{3.59}$$

with the normalisation h. This normalising filter never increases the maximum amplitude. The regularisation of the displacement field D_a and the certainty map c_a can be calculated as

$$\Psi_D(D_a, c_a) = D_a *_{c_a} g \tag{3.60}$$

and

$$\Psi_c(c_a, c_a) = c_a *_{c_a} g. \tag{3.61}$$

Regularisation reduces noise as its effect is similar to a low-pass filter. The weighting increases the resolution in regions with a higher certainty and blurs regions with a smaller certainty.

Further explanations regarding the diffeomorphic Morphons algorithm with more rigorous mathematical details can be found in [107].

3.9 CBCT intensity correction methods

Scatter correction is a crucial aspect of this thesis. Within this section, a motivation to use CBCTs and a broad overview of scatter mitigation methods for CBCTs are presented. Chapter 7 provides details on the correction methods used within the scope of this thesis.

In RT CBCTs are routinely acquired for patient positioning. It would be beneficial to use these already available images for more complicated tasks. In this case no additional acquisition is needed, which is important regarding the required time in a tightly scheduled clinical workflow, and also favourable for the patient, as there is no additional dose burden. Consequently, CBCTs have seen considerable interest in recent years, specifically in PT. PT with is high sensitivity to inter- and intra-fractional changes [116] could especially benefit from daily imaging.

Rit et al. proposed a reconstruction for scanners with independent source and detector rotations [117]. The advantage of such a CBCT scanner, as realised in the ImagingRing (medPhoton, Austria), is its high flexibility, as it is independent of the treatment room. This is in contrast to gantry-fixed CBCT systems, which have slow rotation speeds and can perform only partial revolutions. Other in-room CBCT realisations include nozzle, C-arm, and

couch-mounted CBCTs [24]. In order to use CBCTs for more than patient positioning scatter correction has to be performed.

Scatter correction methods are manifold and can be categorised into two different groups, scatter reduction applications and software-based corrections.

The first group contains mechanical applications such as anti-scatter grids (cf. section 3.2). The idea of these applications is the reduction of scatter so that the projections are less erroneous.

Anti-scatter grids are placed before the scintillation crystal to filter out all photons, which are not travelling in a straight line between X-ray source and detector. Scatter grids decrease the number of detected photons, which is why the dose is often increased when using a scatter grid. However, this is not necessarily the case as there are also studies showing image quality improvements using an anti-scatter grid, without increasing tube mAs [118]. The anti-scatter grid relies on a geometrical effect, which only works for a certain configuration of source and panel as desired. In this case the anti-scatter grid matches the divergence of the source. Scattered photons are either not let through or to a lesser extent. Consequently, if the panel is shifted laterally the anti-scatter grid is no longer working.

The second group, software-based corrections, covers besides different reconstruction methods, which can eliminate certain artefacts (cf. section 3.5), a wide range of different techniques. Multiple studies show correction methods for specific artefacts. Siewerdsen and Jaffray quantified lag and ghosting artefacts [26]. They tried two mitigation methods, scanning at maximum frame rate and flood-field exposure of the detector, which both did not show satisfactory results. Further increases in scanning speed or iterative correction methods were proposed as a solution. A follow-up study by Siewerdsen and Jaffray investigated CBCT scatter, which led to cupping, streak artefacts, and reduced accuracy in reconstruction values [25]. The modification of acquisition (increase of dose and slice thickness), as well as reconstruction (transaxial resolution length and filters) parameters, led to a contrast-to-noise ratio comparable to the predictions of an analytical model.

Mainegra-Hing and Kawrakow used Monte-Carlo (MC) calculations, a statistical procedure to numerically solve hard analytical problems, in which random samples of a distribution are repeatedly drawn using random experiments, to estimate CBCT scatter [119]. For their voxelised cubic phantom irradiated with a 120 kV X-ray beam, they could show substantial CBCT scatter reductions. Thing et al. investigated five lung patients to study image lag, detector scatter, and beam hardening [27]. Their best mitigation approach had multiple correction steps prior to the reconstruction. These correction steps included MC calculations to simulated scatter, which they then subtracted to correct the images. Their scatter correction improved CBCT images and showed a better CBCT-CT HU correspondence.

A different method to improve CBCT image quality was performed by Peroni et al., who introduced the concept of a virtual CT (vCT) in a retrospective H&N patient study [120]. For the generation of the vCT, they first did a coarse alignment of a planning CT with the CBCT using a rigid registration. In a second step, they performed a multistage B-spline deformable registration between the two coarsely registered images. The resulting image is an intensity improved CBCT, which is called vCT.

Landry et al. applied this vCT approach to proton dose calculation. For six H&N cancer patients, they registered a pCT with a CBCT, using diffeomorphic Morphons, a deformable image registration, to generate the vCT, which showed correct CT values [29]. Analysing DVH statistics they could show that proton dose distributions of replanning CTs were comparable to those of the vCT. Kurz et al. investigated nine H&N cancer patients [30]. They used a similar technique to generate their vCTs. Additionally, they did a second intensity correction method, a population-based CBCT intensity rescaling, where they used the alignment from the vCT generation. On these aligned image pairs, they determined CT number pairs, at multiple points in different tissues. Those paired numbers were used to generate a
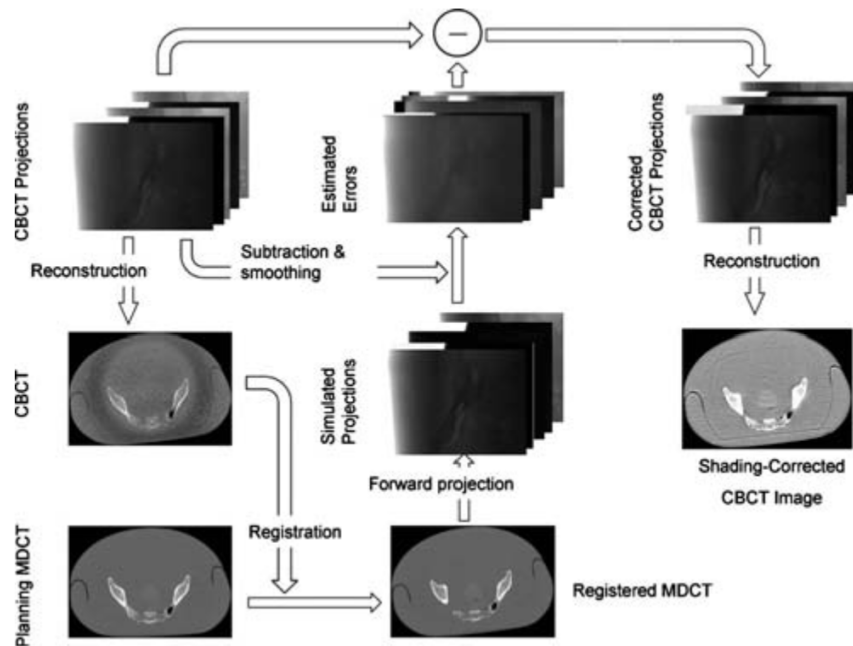
FIGURE 3.17: Projection level scatter correction workflow, which uses a pCT as a prior. Figure adapted from [124].

CBCT to pCT Hounsfield lookup table. With the help of this lookup table, CBCT intensities were scaled to the diagnostic CT HU range. Their results showed that with both methods adaptive intensity-modulated photon radiation was feasible. For adaptive intensity-modulated PT only the vCT method was suitable. Wang et al. showed in a proof-of-concept study for one H&N patient, that this vCT concept can be used to generate a WET plot and virtual proton depth radiographs (PDRs) with which the impact of anatomical changes in proton therapy can be assessed [121]. This information could be used for online decisions in an adaptive PT treatment plan.

Veiga et al. proposed the first workflow for proton therapy of the lung, using a 3DvCT [122]. The deformation could not model all anatomical changes accurately in the thorax. Thus a correction step consisting of an algorithm, which identified regions with significant intensity mismatch between vCT and CBCT, was applied. Large deviating vCT intensity values were then replaced by the bulk value of lung or tissue. Investigating clinical indicators, based on WET and dose, they could show that, for 20 lung patients with considerable anatomical changes over the course of the treatment, the CBCT-based workflow provided similar results as a workflow based on replanning CTs. A companion study validates these results by evaluating in detail the uncertainties related to WET and dose [123].

Niu et al. proposed a scatter correction workflow, which works on a projection level [124]. Figure 3.17 shows the idea. A CBCT is registered to the pCT. This pCT is forward projected to simulate projections, which are assumed to be scatter-free. These simulated projections are subtracted from the measured CBCT projections, yielding the estimated error. Subtracting the estimated error from the measured projections generates corrected projections, which are then reconstructed to the scatter corrected CBCT ($CBCT_{cor}$). The methods showed effective shading correction and accurate CT numbers. Park et al. investigated in a proton study for different phantoms and one prostate patient this method and compared it to uncorrected CBCTs and a uniform scatter correction [125]. With the Niu method they could show significantly reduced water equivalent path length (WEPL) errors and a 96% pass rate (2%, 2 mm) in a gamma analysis.

Kurz et al. combined the vCT approach and the Niu method in a proton study, where they investigated multiple phantoms as well as four H&N and four prostate patients [126]. They first generated a vCT, which they then used as a prior for the scatter correction workflow. Comparing the vCT to the $CBCT_{cor}$, showed similar qualitatively good results with gamma pass rates (2%, 2 mm) of about 96% for the different patients. Additionally, $CBCT_{cor}$ and vCT contours of PTV, CTV, bladder, and rectum to reference contours made on the initial 3DCBCT were analysed. A higher anatomical fidelity for $CBCT_{cor}$ over vCT was demonstrated. Also using the vCT as a prior, Hofmaier et al. investigated in the context of photon therapy two H&N cases with a total of 39 CBCTs for potential advantages of dose guided patient positioning [127]. They could show advantages for the $CBCT_{cor}$ compared to the clinical situation.

Comparing the Niu method to a MC simulation of scatter and beam hardening correction, Zöllner et al. could reconstruct the scatter [128]. Additionally, with an agreement of better than 3% they could show that the Niu method corrects all low frequency deviations.

Kim et al. applied in a proton study the Niu method on 13 H&N patients and calculated water equivalent path lengths to assess delivery uncertainties [129]. They could show that the dosimetric change due to anatomical changes and setup error was accounted for using $CBCT_{cor}$ images. In a follow-up study with the same patient cohort reduced by two patients, they investigated the impact of anatomical changes and setup errors to the angular sensitivity of proton range variations [130]. They could show angular dependency, which was largest for posterior oblique angles. This could lead to overdosing of normal tissues at a distal angle.

Botas et al. used $CBCT_{cor}$ images as inputs for an online plan adaptation algorithm for IMPT [131]. For ten H&N patients with an average of six CBCTs, vector fields between CT and CBCTs were determined. These vector fields were used to shift beams and adjust their energies in the adapted plan. The adapted plans improved the treatment, as they accounted for inter-fractional changes. In a phantom study Andersen et al. investigated CBCT-based proton range and dose calculations for CBCT projections acquired in a photon and a proton gantry [132]. They could show that CT numbers for $CBCT_{cor}$ were improved compared to clinical reconstructions. Additionally, WEPL errors were lower and gamma pass rates (2%, 2 mm) were improved for the $CBCT_{cor}$.

The presented methods show that proton dose calculation is feasible for scatter corrected CBCTs for tumour sites unaffected by motion. The necessary extension for lung cancer of the vCT method to 4D [133, 134], which then led to the 4DCBCT scatter corrected workflow investigated in this thesis will be presented in section 7.1.

For clinical use, the presented methods have a common bottleneck, which is a relatively large computation time. Recent advancements in AI methods seem to address this issue by providing promising scatter-reduced results in combination with clinically acceptable computation times [135–143]. The relevant studies, which led to the third topic of this thesis, an AI implementation of the scatter correction, will be presented in chapter 6.

Chapter 4

IGRT and ART

The intention of this chapter is to outline basic knowledge for understanding the concepts of image guided radiotherapy (IGRT) and adaptive radiation therapy (ART), which are explained in section 4.1 and 4.2.

4.1 IGRT

IGRT, which can nowadays be considered clinical standard, is used to assess the patient's anatomy either just before or during beam delivery. Its main goal is the accurate positioning of the patient on the treatment couch, which results in accurate positioning of the target volume.

Multiple imaging modalities, such as CBCT, CT, ultrasound imaging, planar kV X-ray imaging, MV portal imaging, and surface scanners, depending on the tumour site, are used for IGRT. With the recent clinical introduction of the MR-guided linear accelerator (MR-linac), an additional device and imaging modality with high potential for IGRT is available. The variety of imaging devices results in the use of different image types, which range from static 2D and 3D to real-time imaging during the treatment.

Modern IGRT methods, which result in high patient positioning accuracy, allow smaller PTV margins. The PTV covers random displacements, set-up errors and systematic inaccuracies, which can occur, e.g., during contouring. Additionally, over the course of the entire treatment, which is typically a few weeks, the initially defined CTVs might no longer be accurate. The PTV tries to account for the shape and position uncertainties that occurred by applying a so-called margin recipe. A widely used formula defines the PTV margin as [144]

$$m_{\mathrm{PTV}} = \alpha\Sigma + \beta\sigma - \beta\sigma_P, \tag{4.1}$$

where Σ describes systematic preparation uncertainties, σ statistical execution uncertainties, and σ_P is the width of the treatment beam penumbra. The factors α and β are parameters, which are obtained from a probability distribution. Accurate positioning due to IGRT reduces the PTV, which can lead to a better treatment outcome. The full potential of using the images for treatment adaptation will be discussed in the next section.

4.2 ART

A treatment plan, which is administered to the patient over several weeks, is usually based on CT images acquired pre-treatment. Over the course of the patient's therapy, inter- and intra-fractional changes are often observed. The idea of ART is to respond to these changes to generate an updated treatment plan, which improves the overall RT and thus the likelihood of treatment success. Consequently, ART is used to identify and compensate for potential changes with respect to the planning images. The observed deviations due to

anatomical changes can lead to substantial errors in the dose delivery to the target as well as to overdosage of OARs. The treatment plan, calculated pre-treatment, can only be seen as an estimate of the true situation during the actual irradiation. Recent technological advancements change the prevalent view on ART, which was already discussed in 1997 [145], from a purely academic topic to a concept which has clinical relevance.

ART can be performed after the dose of the treatment fraction was delivered, which is called offline ART, or right before the treatment, which is called online ART. Independent of online or offline, a generic ART workflow can be divided into verification, evaluation, and adjustment. Verification assesses all kinds of variations that occurred during or after treatment via volumetric image acquisition. In the evaluation step, the significance of potential anatomical changes and their resulting dosimetric consequences is checked considering the newly obtained information. The adjustment step then changes the treatment accordingly. This workflow can happen multiple times during the course of the fractionated treatment. In an ideal online ART scenario, this workflow is applied at each treatment session. ART is generally based on in-room IGRT modalities. For photon therapy currently two commercial solutions, the Elekta Unity MR-linac [146] (Elekta, Stockholm, Sweden) and the Varian Ethos [147] (Varian Medical Systems, Palo Alto, California, United States), are available for online adaptive workflows.

Chapter 5

Proton treatment planning and delivery for lung cancer

Clinical implementations of treatment planning and delivery largely depend on the tumour entity. This chapter solely focuses on lung tumours, as it is the body site of focus within this thesis. For multiple different tumour sites and their treatments, the interested reader is referred to [148].

5.1 Clinical workflow

The following section presents the clinical PT workflow implemented for lung patients at the Department of Radiation Oncology at the University Medical Centre Groningen (UMCG) in the Netherlands as described by Meijers et al. [63] and Ribeiro et al. [149]. The treatment planning for the phantom as well as the patient study (cf. chapter 7) was inspired by this workflow, because the UMCG is an experienced proton centre, which has treated many patients and among those many lung cases.

On a planning 4DCT a medical doctor and medical physicist define the extremal breathing phases, i.e., maximum inhale and maximum exhale phase. On those two images the medical doctor delineates the CTVs. A union of those two CTVs yields the ITV, which accounts for the target motion. DIR between the two phases yields a deformation vector field, which is used to quantify the range of the target motion. This information is used to adjust planning (field selection and design) and delivery (enlargement of the spot size, rescanning strategy).

An average CT of the planning 4DCT is used to generate 3D robustly optimised plans (cf. section 2.4). Muscle tissue with a density of $1.05\,\mathrm{gcm^{-3}}$ is used for a density override of the ITV. The use of the average CT as well as the density override minimises IMPT plan degradation to mobile lung tumours as they account for motion effects within the target structure. Clinical robustness settings of $\pm 3\%$ range error and $\pm 6\,\mathrm{mm}$ setup error are used [150]. A 3-field arrangement with specific angles depending on the target and OARs location is used.

The spot size of the clinical beam at the Groningen facility ranges from $3\,\mathrm{mm}$ to $6.5\,\mathrm{mm}$, depending on the proton energy, which varies from $230\,\mathrm{MeV}$ to $70\,\mathrm{MeV}$. During plan optimisation spot spacing as a function of the spot full width at half maximum (FWHM) in water with a ratio of 0.8-1 is used. For all plans 5-times layered rescanning is used. Rescanning is a method to address the interplay effect, which describes the interference between the dynamic pencil beam delivery and the tumour motion. The idea of rescanning is to deliver the dose in multiple scans with a reduced spot weight [151]. The addition of all reduced spot weights equals the original spot weight. These repeated irradiations of the target volume lead to a statistical averaging effect. In layered rescanning or slice-by-slice rescanning, each energy layer is rescanned to the prescribed dose before moving to the next iso-energy slice.

Subsequently, robustness evaluation is performed. A set of 28 scenarios (14 directions) with predefined setup and range errors is simulated. The assessment of the robustness of the plan is made by voxel-wise worst-case minimum and maximum dose distributions.

5.2   Alternative generation of planning images and target volumes

Different planning images and thus different target definitions can be used for a clinical workflow. An overview is presented below.

5.2.1   Mid-ventilation volume (midV)

The definition of the ITV substantially increases the irradiated volume, which leads to an increased radiation burden for the patient. Consequently, non-blurred images at average positions can be generated out of a 4DCT, which aim at eliminating the motion during planning. These motion-reduced average images are then used to define a new and ideally smaller target volume.

The mid-ventilation volume approach determines a mean position and a mid-ventilation time-percentage [152]. The mean position is defined as the time-weighted centre of gravity of a structure in all three spatial dimensions. The mid-ventilation time-percentage within a breathing cycle is where the structure is closest to the time-weighted mean position. A 3DCT scan from a 4DCT data set close to the mean position is reconstructed, which is called the mid-ventilation CT scan. The target structure within this image is the mid-ventilation volume.

5.2.2   Mid-position volume (midpV)

The mid-position volume [153] can be seen as an alternative to the midV. Due to its high reproducibility, the maximum expiration phase is often used as a reference phase to which the other phases are registered, yielding deformable vector fields (DVFs). The DVFs are averaged, yielding the mean motion vector field. The inverse of this mean motion vector is composed with each of the original DVFs, yielding new DVFs relative to the mean position. These new DVFs are applied to their corresponding phase of the 4DCT. The median of the set of deformed 4DCT phases generates the motion-compensated midp image. The target structure within this image is the mid-position volume (midpV).

5.3   Alternatives during beam delivery

Similarly to the previous section the used methods during the beam delivery can also vary. The most common ones are presented below.

5.3.1   Breathing control techniques

In order to limit intrafractional motion the breathing motion is controlled to have the lowest possible amplitude. This can be regulated voluntarily by the patient, who has been trained and instructed to do so by clinical personnel, or with the use of an occlusion valve [154], which temporarily blocks the patient's airflow and thus immobilises breathing motion [155].

5.3.2 Jet-ventilation

Going one step further, which means to almost completely eliminate any breathing motion, radiation treatment can be performed with anaesthesia and jet-ventilation [156]. Jet-ventilation is a special mechanical ventilation, which is commonly used for surgical interventions on the respiratory system.

5.3.3 Rescanning

Rescanning, which is used in the described Groningen workflow, comes in different types: layered (used in Groningen), volumetric and breath-sampled [151]. In volumetric rescanning the whole target volume is scanned at once and the rescans are applied continuously. In layered rescanning or slice-by-slice rescanning, each energy layer is rescanned to the prescribed dose before moving to the next iso-energy slice. Breath-sampled rescanning is similar to volumetric rescanning, however the rescans are evenly spaced in time with regards to the breathing cycle and thus they are no longer continuously applied.

5.3.4 Beam gating

During beam gating, the patient is typically actively in breath-hold. The idea is to irradiate the target volume only within a specific part of the breathing cycle, the gating window [157]. The target motion is monitored either directly or by - ideally well-correlated - surrogates using, e.g., X-ray imaging of implanted markers, optical tracking of markers, which are put on the patient's skin, pressure belts (similar to the methods used in 4DCT acquisitions; cf. section 3.6), or real-time imaging such as cine MRI, which is currently only available for photon therapy. The gating window is a predefined, mostly symmetric tolerance region around an extremal phase of the breathing cycle, as those are the most stable positions. If the patient's breathing is within the gating window, it triggers the radiation. If the breathing motion leaves the tolerance region, radiation is immediately turned off.

5.3.5 Beam tracking

In beam tracking the beam follows the target motion. For particle therapy, lateral tracking is achieved with magnets, while the depth can be adapted by different energy modulations. The parameters, defining the beam, are calculated and stored beforehand using the 4D pCT [158]. With the help of target motion forecasting, online adaptation to the detected motion phase is feasible. Beam tracking can be regarded as an enhancement of beam gating, as the beam is more efficiently used and does not have to be constantly switched on and off. For photon therapy tracking has been realised clinically in systems, such as the Cyberknife Synchrony [159, 160]. Beam tracking for proton therapy is so far not clinically implemented and remains a part of scientific research [161].

Chapter 6

Using 4DCBCT for dose calculation

This chapter compares the different planning and delivery methods and lists their challenges. It is important to mention that all of the presented methods are constantly re-examined and thus continue to be part of scientific research. The chapter concludes with a motivation for the use of 4DCBCTs.

6.1 Challenges

In general, the first goal before radiation delivery is to ensure that the position of the patient during irradiation is as close as possible to the patient's position during the acquisition of the pCT. This is usually complicated due to the fact that CT scanners are rarely available in-room. Consequently, more often in-room CBCTs acquire images, which, registered to the pCT, are used to minimise the patient's setup error. This however completely ignores changes due to breathing motion and patient anatomy.

The application of the ITV and additional safety margins increase the overall target volume, which guarantees the irradiation of the target during all different breathing phases, yet it leads to unnecessary irradiation of healthy tissue. Approaches like midpV can reduce the treated volumes and thus lead to dose sparing in healthy tissues. However, they require lengthy DIR calculations and more importantly these smaller volumes might not necessarily lead to sufficient target coverage [162].

Besides the few centres with in-room CT capabilities, most proton facilities solely have CBCT scanners in their treatment rooms. In these cases repeated CT imaging, which is conducted in a different room, always leads to a setup error, which is why an in-room CBCT scan is still necessary. Furthermore, repeated CT imaging increases the overall workload, which is inefficient and thus in contrast to the tightly scheduled clinical workflows.

Breathing control techniques largely depend on the patient's ability to hold a breath and its reproducibility, which cannot be ensured and thus makes them not ideal. The use of narcotics to reduce the breathing amplitude, as done within jet-ventilation, can cause different complications, which is why an anaesthetist needs to be present. This further complicates the radiation therapy workflow and is the reason why this should be avoided.

In rescanning the dose distribution is dependent on scanning parameters, which is why a fast energy switching time is needed [163]. Rescanning relies on the idea that for a large number of scans local over- and underdosages will statistically average out. However, if beam delivery and target motion are correlated this will not be the case [163]. In rescanning the dose is "smeared out" over the motion, which leads to a compromised target dose conformity [164].

Gating depends on how well the patient can perform the breath-holds as well as the quality of the motion surrogate. Additionally, residual target motion within the gating window can lead to interplay effects between the beam delivery and the target motion. This can result in local over- or underdosages [165]. Another disadvantage of gating is the prolonged

treatment time due to the inefficient usage of the treatment beam. Tracking eliminates this problem, however an already complicated gating workflow gets further complicated by, e.g., the additional motion estimation.

Rescanning in combination with breath-hold methods or gating could possibly lead to a better target coverage and thus to an improved outcome. An ideal solution in the future could be the combination of rescanning and tracking, which is called retracking [166].

6.2   4DCBCT adaptive radiation therapy

The use of 4DCBTs for adaptive radiation therapy can address some of the challenges described above. A large advantage is the in-room availability of CBCT scanners [24], which are already used for IGRT of lung cancer treatments. CBCTs, which can be used daily, mostly ensure the three-dimensional setup of the patient.

The CBCT's lack in image quality prohibits their further usage, which is why repeated CT imaging is a still more widely used ART option. Improving the quality of CBCTs to a level, which makes dose calculations feasible, could remove the necessity of repeated CT imaging. This would reduce avoidable dose to the patient as well as workload, because no additional acquisition has to be done. It would further eliminate registration errors, as the CBCT acquisition is done in treatment position.

Using 4DCBCTs over 3DCBCTs could furthermore improve the patient's setup, as the tumour can be better visualised [167]. Additionally, with the use of 4DCBCTs the breathing information would be available on the scan close in time to irradiation. Consequently, daily 4DCBCTs could visualise changes in breathing motion.

A quality-improved 4DCBCT, which can be generated in a clinically acceptable time, could thus be used to obtain an updated target definition, which could be interesting for rescanning, gating or tracking during the beam delivery and also for retrospective time-correlated dose reconstruction. With respect to the latter, a quality-improved 4DCBCT would enable phase-dependent proton dose calculation, which could be used to determine the delivered dose within a given fraction.

However, it should also be stated that breathing motion assessment based on a single or few cycles for CBCT is questionable. It can be doubted that this single cycle represents all actual target motion positions during the treatment. The interested reader is referred to the following study [162], which is one of many that investigates this topic.

Nevertheless, the mentioned reasons motivated many studies to utilise the CBCT scan for more than just patient setup. Many of these studies are discussed in section 3.9. The advancement of these 3D CBCT ideas to 4D is introduced in chapter 7, which then outlines the first and second project of this thesis, a 4DCBCT feasibility study using a porcine lung phantom and a retrospective 4DCBCT lung patient study. Both studies investigate corrections techniques, which enable proton dose calculation.

Chapter 7

Validation of proton dose calculation on scatter corrected 4D cone beam computed tomography

This chapter presents the efforts to achieve proton dose calculation on scatter corrected 4DCBCT images. It starts by summarising work done before this thesis, which led to the 4DCBCT scatter correction workflow. Subsequently, the first project of this thesis, a feasibility study using a porcine lung phantom, is elaborated. The results of that study are presented in detail and were first published in Physics in Medicine & Biology [168]. These results led to a retrospective lung patient study, the second project within this thesis, which is also presented in this chapter. The sections, describing the studies, each end with a discussion and a conclusion.

7.1   4D extension of an existing proton dose calculation framework

The treatment of lung cancer with radiotherapy has been significantly improved over the last two decades. Starting as an almost purely palliative treatment it is now an established curative treatment too [169]. Nevertheless, the prognosis, if diagnosed with non-small cell lung cancer (NSCLC) or small cell lung cancer (SCLC), remains dire.

   The favourable ballistics of protons over photons due to their complete stopping in matter at therapeutic energies have led to a substantial interest in PT treatments. Therapeutic results are expected to improve with modern PT facilities, which use IMPT, having better dose conformity than passive beam scattering [20, 21]. Protons have been used for different tumour sites such as head and neck (H&N) [170], oesophageal [171], paediatric brain [172], gastrointestinal [173], meningioma [174], and NSCLC [175].

   PT is highly susceptible to anatomical changes, which occur over the patient's treatment due to inter- and intra-fractional variations. In order to benefit from the superior ballistics of proton beams, these changes need to be accounted for to prevent target under- or OAR overdosage [176]. Consequently, PT is mostly used for static tumours with no or negligible motion, i.e., no or negligible intra-fractional changes. Nevertheless, the better conformity of PT is expected to be also beneficial to moving tumour entities such as lung cancer.

   Veiga et al. accounted for inter-fractional changes in their proton lung study by calculating dose distributions on vCTs using 3D averaged images [122, 123]. However, this does not consider changing respiratory patterns, which can vary substantially between fractions [177, 178]. Therefore daily 4D imaging, which would detect variations linked to the tumour motion, is highly desired [179–182]. This would enable daily dose reconstructions, which could lead to a better knowledge of the delivery dose. It could also be used for offline adaptations for which current clinical approaches mostly rely on weekly 4DCT acquisitions [63].
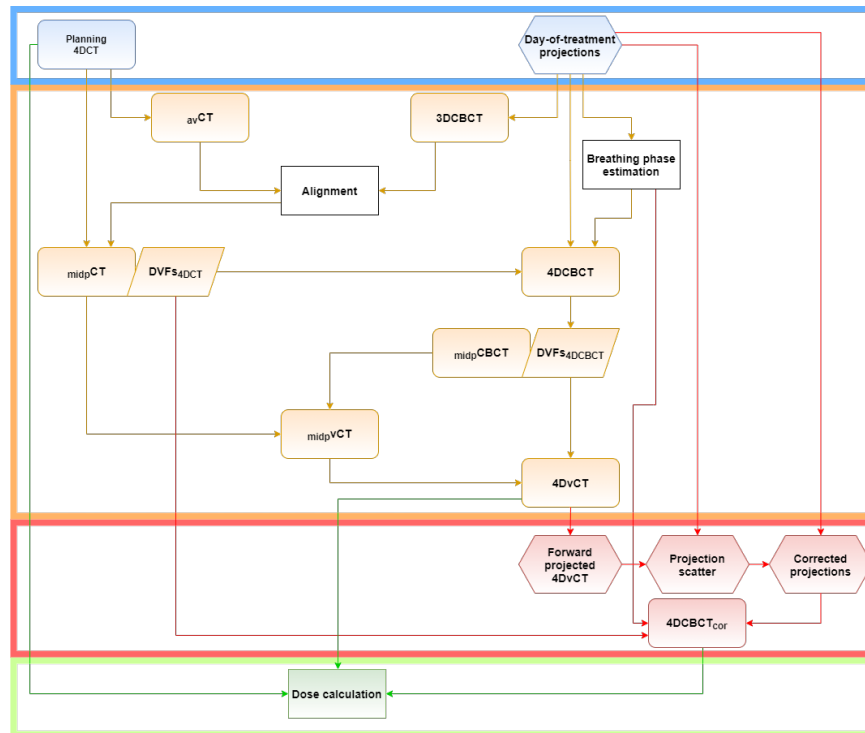
FIGURE 7.1: Overview of the workflow used in the porcine lung phantom study and the retrospective patient study. The input is shown in the blue box. The steps of 4DvCT generation are shown in the orange box and the steps of the 4DCBCT$_{cor}$ are bounded by the red box. The green arrows show the images on which proton dose calculation is performed. Images are expressed by rounded rectangles, projections by hexagons, DVFs by parallelograms, and actions by rectangles. Figure reprinted from [168].

The 3DvCT approach was extended to 4DvCT by Niepel et al. [133], who registered a 4DCT to a 4DCBCT. For the 4DCBCT acquisition, they used linac mounted CBCT scanners. In their phantom study, the 4DCBCT reconstruction was performed iteratively using a method described by Hansen and Sørensen [183]. Bondesson et al., using data acquired from a PT CBCT scanner, generated a 4DvCT with a similar method [134]. The main difference in their phantom study was the use of MA-ROOSTER (cf. section 3.5) for the 4DCBCT reconstruction. Both studies obtained ground truth data using a phantom and thus showed the feasibility of proton dose calculations. An alternative 4DCBCT workflow was performed by Shresta et al. in a study, which simulated for each phase of an acquired 4DCT CBCT projections [184]. They used simultaneous motion estimation and image reconstruction (SMEIR) [185] for their 4DCBCT reconstruction and showed that carbon ion dose calculation was feasible on their generated images.

Combining the 4DvCT approaches of Niepel and Bondesson with the Niu scatter correction method (cf. section 3.9) led to the 4DCBCT scatter-correction (4DCBCT$_{cor}$) workflow for the porcine lung phantom study as well as for the retrospective lung patient study within this thesis. Figure 7.1 shows the complete workflow, which can be divided into a 4DvCT generation part and a scatter correction part. As an input, a planning 4DCT equidistantly separated into 10 breathing phases, and day-of-treatment CBCT projections are used. The data acquisition in the phantom study as well as the data cohort of the retrospective lung study will be discussed in more detail in sections 7.2 and 7.3.
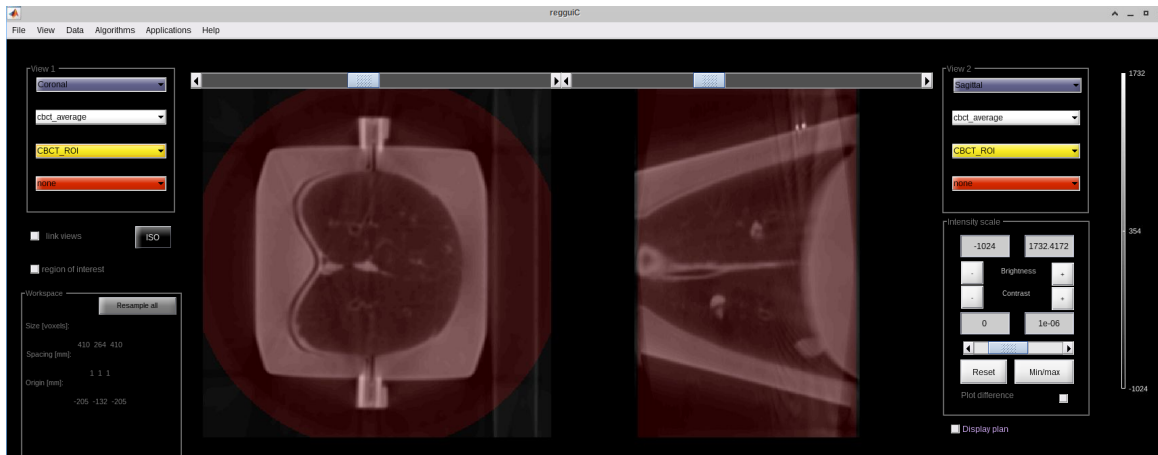
FIGURE 7.2: The OpenREGGUI interface is shown. A 3DCBCT image of the porcine lung phantom and corresponding ROI, superimposed in red, in two different views are selected. The description of the views is not correct as OpenREGGUI is designed for the IBA coordinate system, which is different to the Elekta coordinate system in which the data for the phantom, as well as the patient study, is acquired. Consequently, the Elekta images are displayed in a rotated and transposed way.

7.1.1 4D scatter correction workflow

The 4DvCT generation is implemented in OpenREGGUI (Registration Graphical User Interface; `https://openreggui.org/`), which is a medical image processing software with a graphical user interface that is based on MATLAB (MathWorks, Natick, Massachusetts, USA). All steps such as mid-positioning or registration can be visualised and thus immediately checked, which makes OpenREGGUI a powerful tool. Additionally, in OpenREGGUI individual commands can be strung together to create workflows. A predefined workflow for 4DvCT creation for CBCT data acquired with IBA scanners [1] was adjusted to the porcine lung data set, which is acquired by an Elekta XVI 4.5.1 scanner. Figure 7.2 shows the OpenREGGUI interface. The different coordinate systems between IBA data and Elekta data are immediately visible as the description of views is incorrect and the images are displayed in a rotated and transposed way.

   The 4D workflow starts by creating an average CT ($_{av}$CT) from the planning 4DCT and a static FDK-reconstructed (cf. section 3.5) 3DCBCT from the day-of-treatment projections, for which the function rtkfdk of RTK is used. A Mattes Mutual information rigid registration algorithm, implemented in ITK, is used for the coarse alignment of $_{av}$CT and 3DCBCT.

   For a few patients, this initial registration was not sufficient. Consequently, for these patients a two-step rigid registration was used. The first step uses the same rigid registration as described above. On this coarse alignment in a second step a box is drawn manually at a static body region such as the spine. An additional rigid registration then specifically focuses on this box region. A composition of the transformation matrices out of both rigid registrations is then applied to reach an improved alignment between $_{av}$CT and 3DCBCT. With the alignment information from either of the two rigid registration methods, each of the 10 planning 4DCT phases are moved to the CBCT space. The same registration was used to move the pCT and the corresponding structures, which are not used specifically within the 4DCBCT$_{cor}$ workflow, to the CBCT space.

   In the next step, a mid-position CT ($_{midp}$CT; cf. section 5.2) is generated from the planning 4DCT using DIR (cf. section 3.8). The DVFs, obtained from the mid-position step

---

[1] `https://openreggui.org/git/open/REGGUI/blob/master/plugins/clinical_indicators/workflows/Virtual_4DCT_creation.m` accessed:16-11-2022
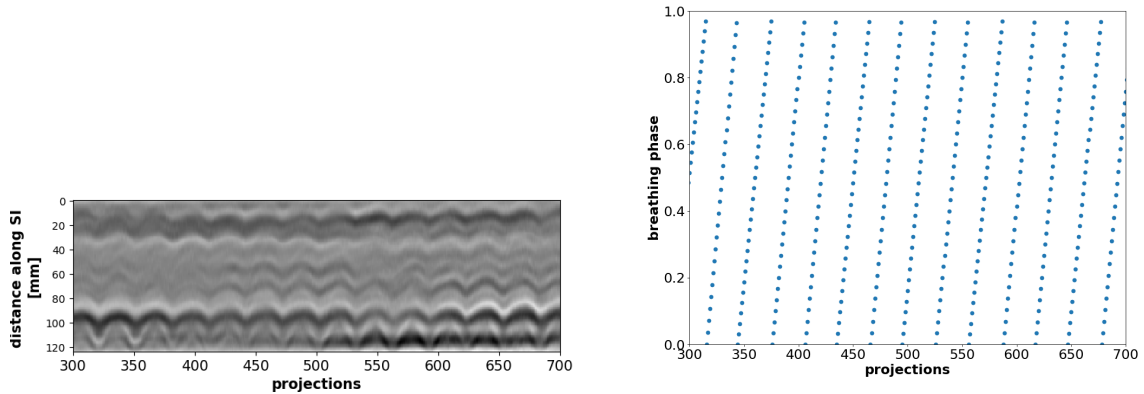
FIGURE 7.3: The left plot shows an example Amsterdam Shroud image for projections 300 to 700 of the porcine lung phantom scan. The plot on the right shows the extracted breathing curve for the same projections. The repetitive breathing character of the porcine lung phantom can be seen in both plots. Figure reprinted from supplementary materials of [168].

(DVFs$_{4DCT}$), and the breathing phase estimation are the two prerequisites for the 4DCBCT reconstruction.

The breathing phase estimation is extracted from the day-of-treatment projections using the Amsterdam Shroud algorithm [88] (cf. section 3.6). Figure 7.3 shows the result of the Amsterdam Shroud algorithm for the porcine lung phantom.

Subsequently, using the function rtkfourdrooster of RTK, the 4DCBCT is reconstructed with MA-ROOSTER (cf. section 3.5) using the day-of-treatment projections, the breathing phase estimation, and the 4DCT DVFs, from the mid-positioning, as input. Additionally, MA-ROOSTER takes two regularisation parameters γ_{space} and γ_{time} (cf. section 3.5) as input. Different combinations for those two values were tried iteratively and the reconstructed image was qualitatively assessed. The chosen values for the reconstruction in the phantom as well as in the patient study are $\gamma_{\text{space}} = 5 \cdot 10^{-4}$ and $\gamma_{\text{time}} = 6.5 \cdot 10^{-4}$.

In the porcine lung phantom study an initial line profile analysis between planning 4DCT and 4DCBCT showed a mismatch at the diaphragm position, attributed to a breathing phase shift, which can be seen in the line profile figure 7.4. The plot shows CT numbers in Hounsfield unit versus pixel numbers. To obtain Hounsfield units within this thesis the following formula for conversion from attenuation values is used [125]

$$\text{CT} = \mu \cdot 65536 - 1024. \tag{7.1}$$

This formula eliminates the need to determine a reference value for μ_{water} (cf. section 3.5).

For the inhale phase (phase 0) and the phases close to the inhale position the misalignment is substantial whereas there is almost no mismatch in the exhale phase (phase 6) and nearby phases. The sigmoidal function

$$f(z) = a \cdot -\text{erf}(\frac{z - c}{b}) + d \tag{7.2}$$

where

$$\text{erf}(x) = \frac{2}{\sqrt{\pi}} \int_0^x e^{-t^2} dt \tag{7.3}$$

was fitted to the line profiles. For a normal distributed random variable Y with mean 0 and variance 0.5 the function $\text{erf}(x)$ represents the probability that Y is between $[-x, x]$.
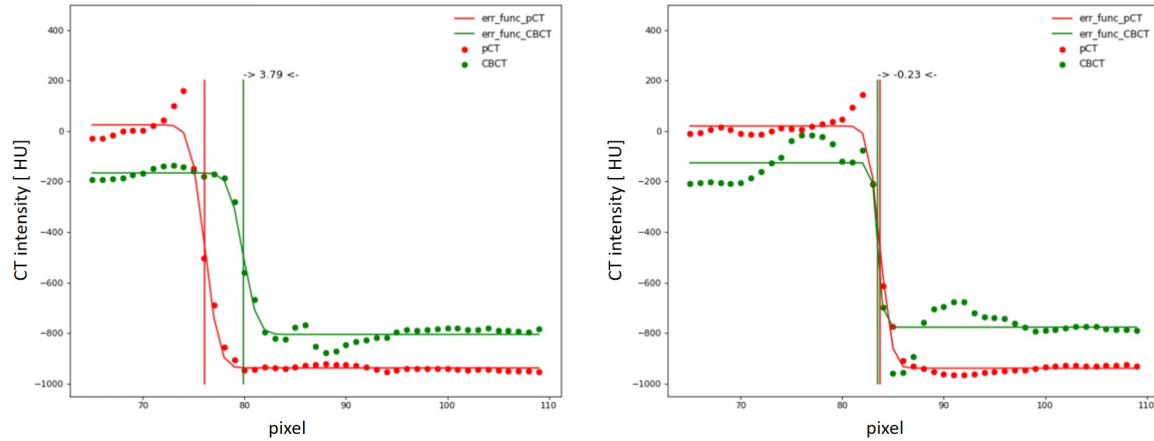
FIGURE 7.4: Line profile in inferior superior direction around the diaphragm position of planning 4DCT and 4DCBCT for inhale phase 0 (left) and exhale phase 6 (right). The values are shown as dots. Error functions, shown as solid lines, are fitted to the values. The difference of the shifting parameter Δc for one phase is shown by the difference between the vertical lines.

The position of the shifting parameter c was plotted against the 10 breathing phases. The difference in the shifting parameter Δc for each phase was averaged so that for one applied breathing curve one total difference in the shifting parameter Δc_{tot} value existed.

$$\Delta c_{\text{tot}} = \frac{1}{10}\Sigma_{i=1}^{10}\Delta c_i = \frac{1}{10}\Sigma_{i=1}^{10}|c_{\text{4DCT},i} - c_{\text{4DCBCT},i}| \qquad (7.4)$$

The breathing curve, extracted within the Amsterdam Shroud algorithm, was iteratively adjusted by a small constant shift. This shift changed the total difference in the shifting parameter c. The process was repeated until the total difference in the shifting parameter Δc_{tot} was minimised.

For the patient cohort, the breathing curves are not as regular as in the phantom case. Thus the cropped Amsterdam Shroud images (cf. section 3.6) were manually checked whether they contained the main oscillatory signal and if necessary the cropping was adapted. The adjustment of the shifting parameter was not conducted per patient.

With the new adjusted breathing curves in the phantom case as well as for the patients, an improved 4DCBCT was generated. Analogously to the 4DCT a mid-position operation is applied to the 4DCBCT, yielding mid-position CBCT ($_{\text{midp}}$CBCT) and corresponding vector fields (DVFs$_{\text{4DCBCT}}$). Using the diffeomorphic Morphons algorithm (cf. section 3.8) $_{\text{midp}}$CT and $_{\text{midp}}$CBCT are registered yielding the mid-position vCT ($_{\text{midp}}$vCT). For the patient cases the intensities outside the CBCT FOV in the $_{\text{midp}}$CBCT and $_{\text{midp}}$CT were replaced by the minimum value of the $_{\text{midp}}$CBCT and $_{\text{midp}}$CT so that the focus of the Morphons algorithm was within the CBCT FOV.

Subsequently applying the inverted vector fields from the 4DCBCT mid-positioning step to the $_{\text{midp}}$vCT, the image is propagated to 4D and is now called 4DvCT. The workflow up to this point, which generates the 4DvCT is implemented for IBA (Ion Beam Applications SA, Louvain-la-Neuve, Belgium) CBCT machines in OpenREGGUI and was used by Bondesson et al. [134].

For the patients, the CBCT field of view (FOV) did not always cover the contralateral lung as the isocentre is located at the tumour. Consequently, the 4DvCT was stitched using the 4DCT outside of the CBCT FOV. For the 4DCT all values inside the CBCT FOV were set to zero and for the 4DvCT all values outside the CBCT FOV were set to zero. The addition of these modified 4DCT and 4DvCT images generated the stitched 4DvCT. Figure 7.5 shows
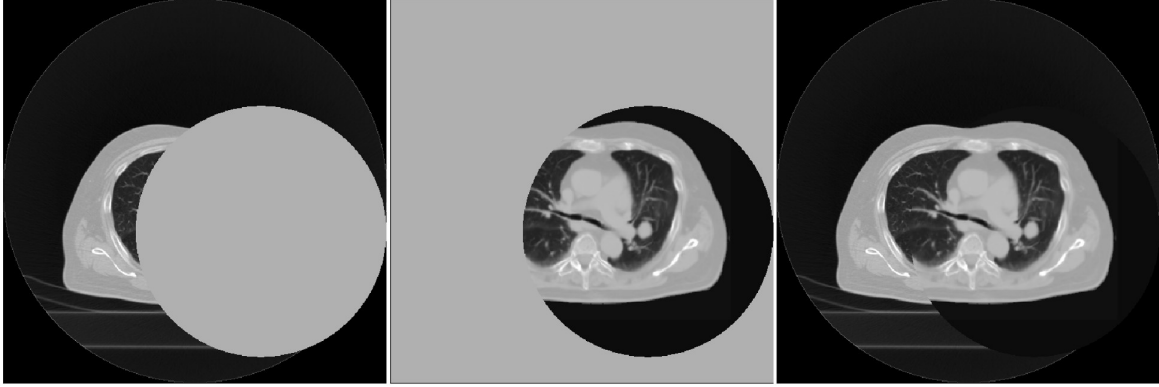
FIGURE 7.5: For a single breathing phase for patient 14 the individual steps of the stitching process are shown. Left: CT with values inside the CBCT FOV set to zero. Middle: vCT with values outside the CBCT FOV set to zero. Right: The addition of both modified CT and vCT, which yields the stitched vCT. A couch removal step in the scatter correction workflow leads to an initial CBCT, vCT, and CBCT$_{\text{cor}}$, that do not show the couch.

the individual images for one exemplary patient.

The scatter-correction is based on works by Park et al. [125] and Niu et al. [124]. It is conducted on a per-phase level, meaning that a single phase of the 4DvCT and corresponding CBCT day-of-treatment projections are the input. The day-of-treatment projections are defined as

$$p_{\text{raw},\alpha} = -\ln \frac{I_{\text{raw},\alpha}}{I_0} \tag{7.5}$$

where $I_{\text{raw},\alpha}$ is the total measured intensity and I_0 is the open field intensity. $I_{\text{raw},\alpha}$ is the sum of a scatter component $I_{\text{sca},\alpha}$ and a primary component $I_{\text{pri},\alpha}$, which can be calculated by forward projecting the 4DvCT phase according to the CBCT geometry. The index α indicates the breathing phase. Without the stitching operation incorrect forward projections are generated. The 4DvCT is assumed to be scatter-free and thus the simulated projections are also assumed to be scatter-free.

A correction factor CF, accounting for the tube current-exposure time mAs (cf. section 3.4), defined as the ratio between a reference value mAs and the measured mAs, was determined (phantom case: reference tube current = 64 mA, reference exposure time = 40 ms, measured tube current = 32 mA, measured exposure time = 20 ms $\longrightarrow$ CF = 4.0). Subsequently, the projections were subtracted from each other and convolved with a generous smoothing filter F described by Kurz et al. [126]. This led to the projection scatter

$$I_{\text{sca},\alpha} = F(I_{\text{raw},\alpha} \cdot \text{CF} - I_{\text{pri},\alpha}) \, . \tag{7.6}$$

Subtracting $I_{\text{sca},\alpha}$ from the measured $I_{\text{raw},\alpha}$ finally yields the corrected projections ($I_{\text{cor},\alpha}$)

$$I_{\text{cor},\alpha} = I_{\text{raw},\alpha} \cdot \text{CF} - I_{\text{sca},\alpha} \, . \tag{7.7}$$

Analogously to the 4DCBCT the log-transformed corrected projections ($p_{\text{cor},\alpha} = -\ln I_{\text{cor},\alpha}/I_0$) are reconstructed using MA-ROOSTER with the same settings, vector fields, and breathing curves, yielding the 4DCBCT$_{\text{cor}}$.

In the final step of the 4D workflow proton dose distributions were recalculated on each phase of the 4DCBCT$_{\text{cor}}$, 4DvCT, and 4DCT. The results for the respective studies will be individually described in sections 7.2 and 7.3.

7.2 Porcine lung phantom

This section presents a porcine lung phantom-based validation study, which was performed by the author as his initial project of this dissertation. The study was published in Physics in Medicine & Biology in 2021 [168]. The research article included figures 7.1, 7.7, 7.9, 7.10, 7.11, 7.12, 7.13, 7.14 and tables 7.1, 7.2. In the supplementary material figure 7.3 was shown. Figures 7.6 and 7.8 were added to this section. This as well as an adapted text improves the readability of the study within this thesis.

Additionally, this work was presented at the AAPM 63rd Annual Meeting & Exhibition, which was a virtual conference, under the title "Scatter Correction of 4D Cone Beam Computed Tomography for Time-Resolved Proton Dose Calculation: Porcine Lung Phantom Validation" and at the Joint Conference of the ÖGMP, DGMP and SGSMP (2021), which was a virtual conference, under the title "Experimental lung phantom based validation of scatter corrected 4D cone beam computed tomography for proton dose calculations".

The goal of this study was to introduce and validate a novel CBCT-based tool for phase-dependent dose calculation in proton therapy using a realistic movable porcine lung phantom, which can be programmed to perform specific breathing patterns. Two motion patterns of different amplitude (planning and day-of-treatment) were used. The validation of the daily 4D images 4DvCT and 4DCBCT$_{cor}$ was performed by comparing their accuracy qualitatively and quantitatively to an acquired ground truth 4DCT. For a more systematic approach, this section is subdivided into Material and Methods, Results, Discussion, and Conclusion.

7.2.1 Material and Methods

Porcine lung phantom 4DCT and CBCT imaging was performed using an ex-vivo porcine lung phantom (Artichest, PROdesign GmbH, Heiligkreuzsteinach, Germany) [186], which could emulate user-defined breathing patterns. Consequently, the phantom allowed reproducible breathing motion measurements of lungs in a human-like thorax geometry, which is crucial for this ground-truth study.

Figure 7.6 shows the porcine lung phantom, consisting of two double-walled shells filled with water, which resemble a human thorax. Inside the shell an inflatable lung and artificial silicone diaphragm are placed. To reduce friction between shell, lung, and diaphragm the surfaces are coated with ultrasound gel. Via tubes and hoses the porcine lung phantom is connected to vacuum and pressure pumps as well as a control system.

Multiple ex-vivo porcine lungs were bought from a local butcher that slaughters. The pigs were checked for diseases by a veterinarian, who allowed their sale. The location of the biopsy, taken by the veterinarian for the disease check, turned out to be crucial as only airtight lungs were of interest for the study. Consequently, the lungs were checked for tissue damages by manually inflating them with a pair of bellows. The best lung, staying inflated for the longest time, was chosen for the study. A gelatin-water mixture (TreeHouse Foods, Inc., Oak Brook, IL, USA) with a mass concentration of $0.3\,\mathrm{g\,ml^{-1}}$ was heated until it was a homogeneous mixture, which could be drawn into a syringe. Injecting this gelatin-water mixture into the lung mimicked tumour lesions, as the mixture solidified upon contact with the cold lung tissue. With this method, four tumours, which ranged in size from $16\,\mathrm{cm^3}$ - $20\,\mathrm{cm^3}$, a range comparable to stage T1 or T2 NSCLC lesions [188], were artificially generated.

The trachea was connected via a tube to ambient pressure, so that outside pressure was established within the bronchi. Mounting the upper shell sealed the phantom, which allowed the creation of negative pressure in the surroundings of the lung. This passively inflated the lung. Different breathing patterns, i.e., frequencies and amplitudes, could be
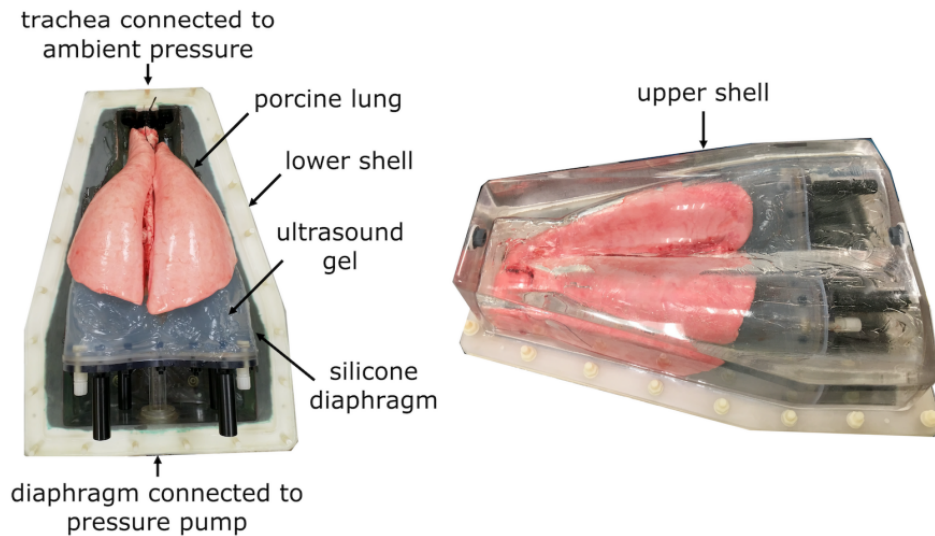
FIGURE 7.6: The porcine lung phantom is shown with the upper shell removed (left) and closed (right). The arrows and corresponding labels indicate the main components. The vacuum pump, which is used to evacuate the volume surrounding the lung so that the lung can be passively inflated is not depicted. Figure adapted from [187].

generated by applying pressure to the water-filled silicone diaphragm, which consequently changed its volume. The specifics of this motion was set by a computer control system. The employed settings in this study emulated a respiration rate of 11 breaths per minute. Two different periodical diaphragm movement simulations were run by the control system to obtain a large amplitude for the planning motion images and a smaller one for the day-of-treatment motion (cf. figure 7.9).

During the measurement, which was conducted in a single session of 3.5 h, two 4DCTs (planning motion and day-of-treatment motion) and one CBCT projection with day-of-treatment motion were acquired. Figure 7.7 shows a scheme, which relates the different data sets to each other.

CT data acquisition   The images were acquired with the scanning devices of the Department of Radiation Oncology in the University Hospital of the LMU. The left plot of figure 7.8 shows the porcine lung phantom inside of the Toshiba Aquilion LB (Canon Medical Systems, Otawara, Japan) CT scanner.

Projection data for 4DCT, which covered the complete porcine lung phantom, were acquired during constant couch movement. Using an Anzai load cell (Anzai, Tokyo, Japan) the diaphragm pressure signal was measured as a surrogate signal of the breathing pattern. The 4DCT was reconstructed with ten breathing phases (reconstruction grid of 1.074 mm × 1.074 mm × 2 mm, X-ray tube voltage: 120 kV) using the vendor's algorithm.

Figure 7.9 shows the extremal phases of the two acquired 4DCTs with different motion. Additionally, three of the mimicked tumours are visible.

CBCT data acquisition   The CBCT projection acquisition was conducted with an on-board CBCT imaging system of an Elekta Synergy linac (XVI 4.5.1, Elekta, Stockholm, Sweden) shown in the right plot of figure 7.8. For a 4 min acquisition with a shifted detector the following settings were used: tube voltage = 120 kVp, tube current = 32 mA, exposure time = 20 ms, collimator = M20, filter = F1, #frames = 1320, 512 × 512 pixels, and pixel size of 0.8 mm. In order to avoid saturation and loss of object edge the exposure time and tube current were adjusted according to findings in Niepel et al. [133].
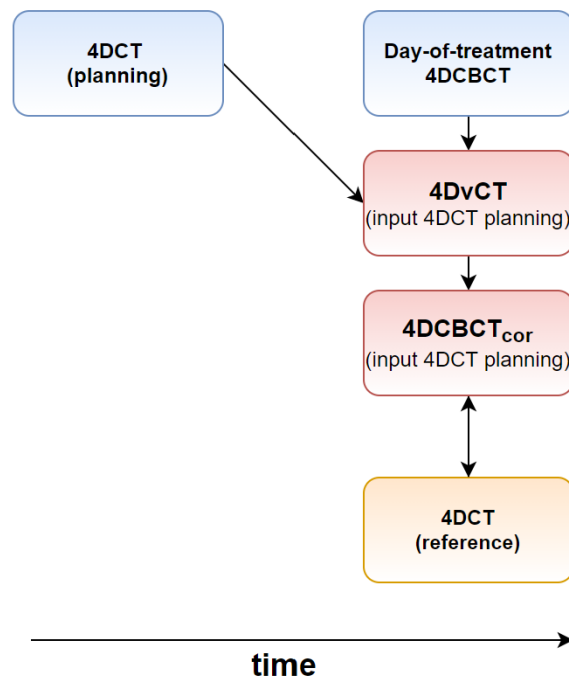
FIGURE 7.7: Overview linking the different data sets. The blue boxes show the data sets, which would be acquired in a clinical setting. In red the generated images are shown. The ground truth image, which is purely used for validation purposes in this study, is displayed in orange. Figure reprinted from [168].
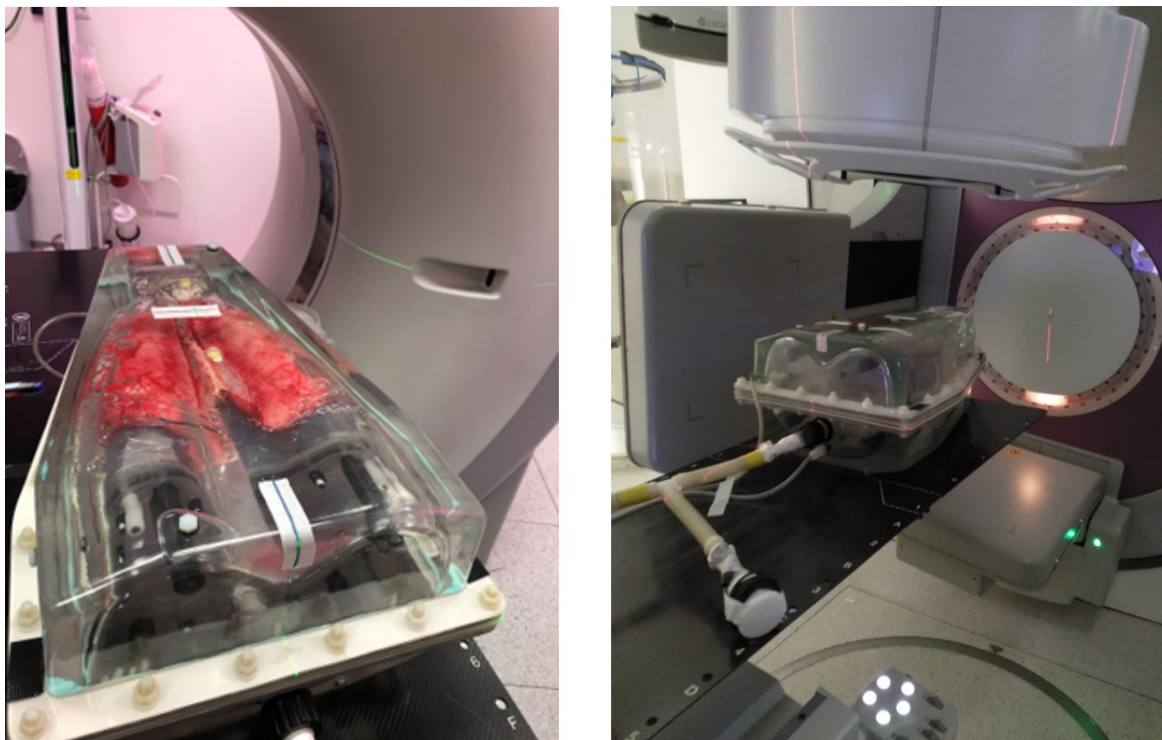
FIGURE 7.8: Porcine lung phantom acquisition with CT scanner (left) and CBCT scanner (right).

| (a) ph0 plan | (b) ph0 ref | (c) ph6 plan | (d) ph6 ref |
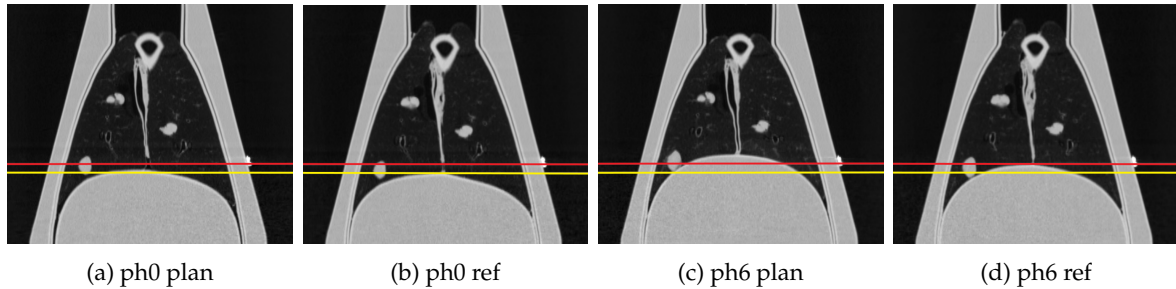
FIGURE 7.9: 4DCT images of the porcine lung phantom in the two different motions, planning and day-of-treatment (called reference), shown for the inhale (phase 0) and exhale (phase 6) phases. Three of the four injected lesions are clearly visible on this slice. For improved comparability, the yellow (red) horizontal line indicates the diaphragm position of the inhale (exhale) reference motion. Inhale phases show similar motions (7.9a, 7.9b), whereas a larger amplitude for the planning motion can be seen in the exhale phases (7.9c, 7.9d). All images are displayed with level = -300 and window = 1600. Figure reprinted from [168].

Treatment planning Treatment planning was performed in the research version 8.99 of the commercial TPS RayStation (RaySearch Laboratories, Stockholm, Sweden). The treatment plan is inspired by the clinically used PT treatment at the UMCG (cf. section 5.1) [63, 149].

The day-of-treatment 4DCT or reference 4DCT along with the 4DvCT and 4DCBCT$_{cor}$ using the same generic CT density calibration curve were transferred to the TPS. On all phases of the 4DCT the four simulated tumours were contoured to create four ITVs, which were subsequently copied to the $_{av}$CT. The density of the ITV was overridden by muscle tissue. Pencil beam scanning proton treatment plans, which administer 60 Gy in 30 fractions with a 3-field arrangement, set to avoid screws and sharp edges of the phantom, were created for each of the four ITVs on the $_{av}$CT. The optimisation of the beams was simultaneous. Clinical robustness settings of range error = $\pm3\%$ and setup error = ±6 mm were applied [63]. With a statistical error of 1% the Monte Carlo dose engine was used during plan optimisation.

Robust plans were created using the minimax method (cf. section 2.4) [62]. A constant RBE of 1.1 was used [60]. The clinical goal of at least 95% volume above 57 Gy was fulfilled by each IMPT plan.

Eventually, the doses of each of the four plans were recalculated on the 10 phases of reference 4DCT, 4DvCT, and 4DCBCT$_{cor}$.

Computer hardware The most demanding computation aspects of the workflow are the DIR and the filtering, which were calculated on a computer with two Intel Xeon E5-2630 v3 processors at 2.4 GHz with each having 8 physical cores and hyper-threading enabled, resulting in a total of 32 threads. An Nvidia Quadro P6000 with 24 GB was used as GPU.

Data analysis The data analysis was twofold. In an image quality analysis containing difference plots, line profiles and mean error calculations in terms of CT numbers in Hounsfield unit (HU), the 4DvCT and 4DCBCT$_{cor}$ were compared to the reference 4DCT.

Additionally, a dose analysis which again compared 4DvCT and 4DCBCT$_{cor}$ to the reference 4DCT was conducted. Dose difference plots were generated for a qualitative analysis. For a quantitative dose analysis DVH parameters ($D_{2\%}$, $D_{98\%}$, $D_{mean, ITV}$, $D_{mean, lung}$) and global gamma pass rates (PR) with two different criteria (3%, 3 mm and 2%, 2 mm) were determined. This was done for single phases and accumulated doses, which were calculated for each ITV of each 4D image. Applying the DVFs$_{4DCT}$ to the respective 4DCT phase and

the DVFs$_{4DCBCT}$ to the respective phase of 4DvCT and 4DCBCT$_{cor}$ and averaging the results yielded the accumulated doses.

7.2.2 Results

Image quality analysis Sagittal views of reference 4DCT, 4DCBCT, 4DvCT, and 4DCBCT$_{cor}$ are shown in figure 7.10 for phase 0 (inhale), phase 3, and phase 6 (exhale). A comparison of 4DvCT with 4DCBCT as well as 4DCBCT$_{cor}$ with 4DCBCT shows clear quality enhancements as the images are substantially less blurred. The 4DvCT shows a similar low noise level as the 4DCT, which is expected and crucial for the assumption of a scatter-free 4DvCT in the scatter correction part of the workflow. The bottom two rows show difference plots for 4DvCT-4DCT and 4DCBCT$_{cor}$-4DCT. In homogeneous regions, such as the lung, tumour, diaphragm, and shell a good agreement is visible as differences are close to 0 HU. At each boundary between homogeneous regions, such as the tumour-lung or diaphragm-lung interfaces, differences of more than 100 HU are observed.

Figure 7.11 shows line profiles displaying CT numbers in HU versus distance in mm for 4DCT, 4DCBCT, 4DvCT, and 4DCBCT$_{cor}$ for the two extremal breathing phases. The chosen path in inferior-superior direction, which traverses the diaphragm, lung, tumour, and phantom shell is shown with a yellow line in the thumbnails. An additional arrow indicates the direction. Both plots for all modalities show three plateaus for diaphragm, tumour, and phantom shell. In between there are two valleys for the lung. The behaviour in CT numbers of 4DCT, and 4DCBCT$_{cor}$ is very similar. Especially for the lung the difference in CT numbers is very little. There is one spike shown in 4DCT and 4DCBCT$_{cor}$ in the inhale plot (phase 0) at around 60 mm, which is missing in the 4DvCT. Within the lung the 4DvCT shows a constant mean CT number versus the breathing phases.

It should be noted that at the edge of the diaphragm, inside the tumour, and the outer shell of the phantom the 4DCBCT$_{cor}$ consistently shows larger values. The overall good agreement of 4DCT, 4DvCT, and 4DCBCT$_{cor}$ is in stark contrast to the original 4DCBCT with non-corrected CT values. The 4DCBCT systematically overestimates the lung values by around 200 HU and systematically underestimates the diaphragm, tumour, and shell values by roughly the same amount.

Figure 7.12 displays mean error (ME) plots in HU versus the breathing phase for 4DCBCT-4DCT, 4DvCT-4DCT, and 4DCBCT$_{cor}$-4DCT. The chosen contours in each ME plot are shown in the top left plot additionally to a CT image of the lung phantom. The body contour is the union of the lung and the shell contour. The comparison of initial 4DCBCT to reference 4DCT shows substantial differences, which is expected and one of the reasons triggering this study. The ME for the lung is larger than 150 HU and the ME for the shell is almost -150 HU. The ME for the body is at around -25 HU.

The two bottom ME plots, displayed with a smaller ordinate range, show reduced deviations. Here the shell ME is about 10 HU for the 4DvCT and about 15 HU for the 4DCBCT$_{cor}$. The lung shows ME of around 10 HU for the 4DvCT. However, in the exhale phase and the adjacent phases to the exhale phase the ME drops to almost 0 HU. The 4DCBCT$_{cor}$ shows a similar behaviour for the ME in the lung contour however with smaller absolute ME values than the 4DvCT. For the body contour, which contains the lung contour, the ME consequently shows a similar behaviour with overall values of about 20 HU for the 4DvCT and reduced values around the exhale phase. The behaviour is analogous for the body in the 4DCBCT$_{cor}$ case with slightly larger values.
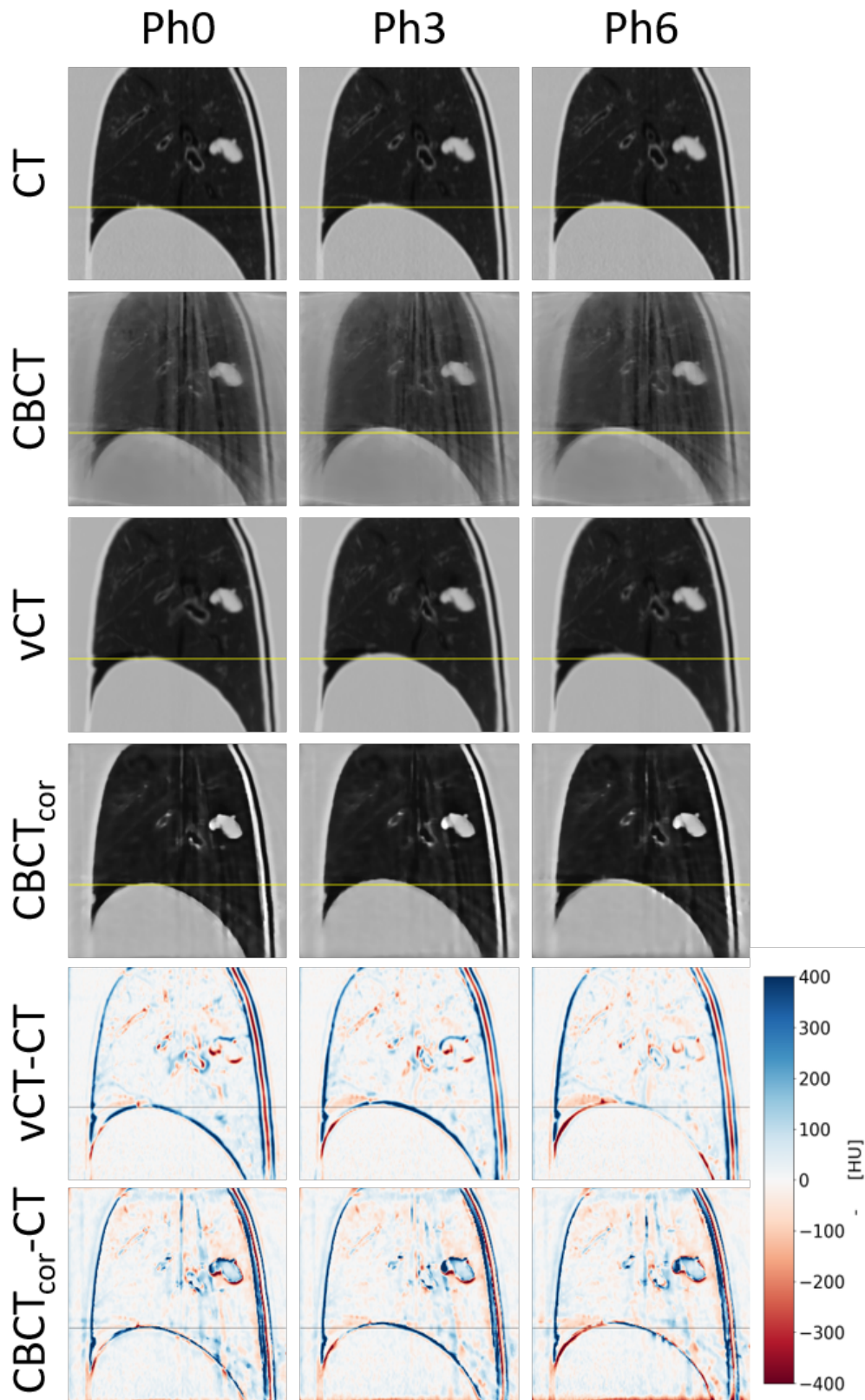
FIGURE 7.10: In the top four rows the four 4D images 4DCT, 4DCBCT, 4DvCT, and 4DCBCT$_{cor}$ are displayed in phase 0 (inhale), phase 3, and phase 6 (exhale) with level = -300 and window = 1600. The bottom two rows show difference images of 4DvCT and 4DCBCT$_{cor}$ to the reference 4DCT. All images are shown in a sagittal view. The horizontal lines indicate the diaphragm position at inhale. Figure reprinted from [168].
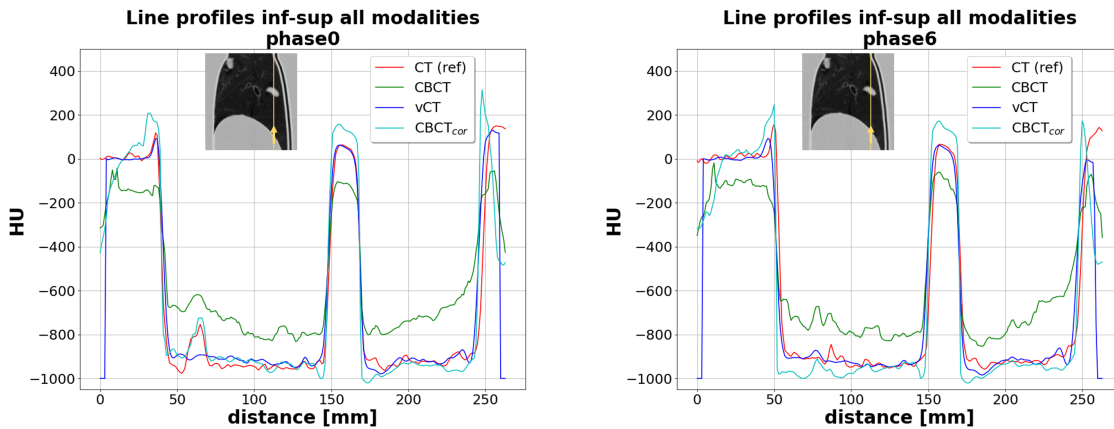
FIGURE 7.11: Inferior-superior line profiles for two extremal phases of 4DCT, 4DCBCT, 4DvCT, and 4DCBCT$_{cor}$. The thumbnails, which are displayed with level = -300 and window = 1600 show the regarded path of the line profile. The direction is indicated with a yellow arrow. Figure reprinted from [168].
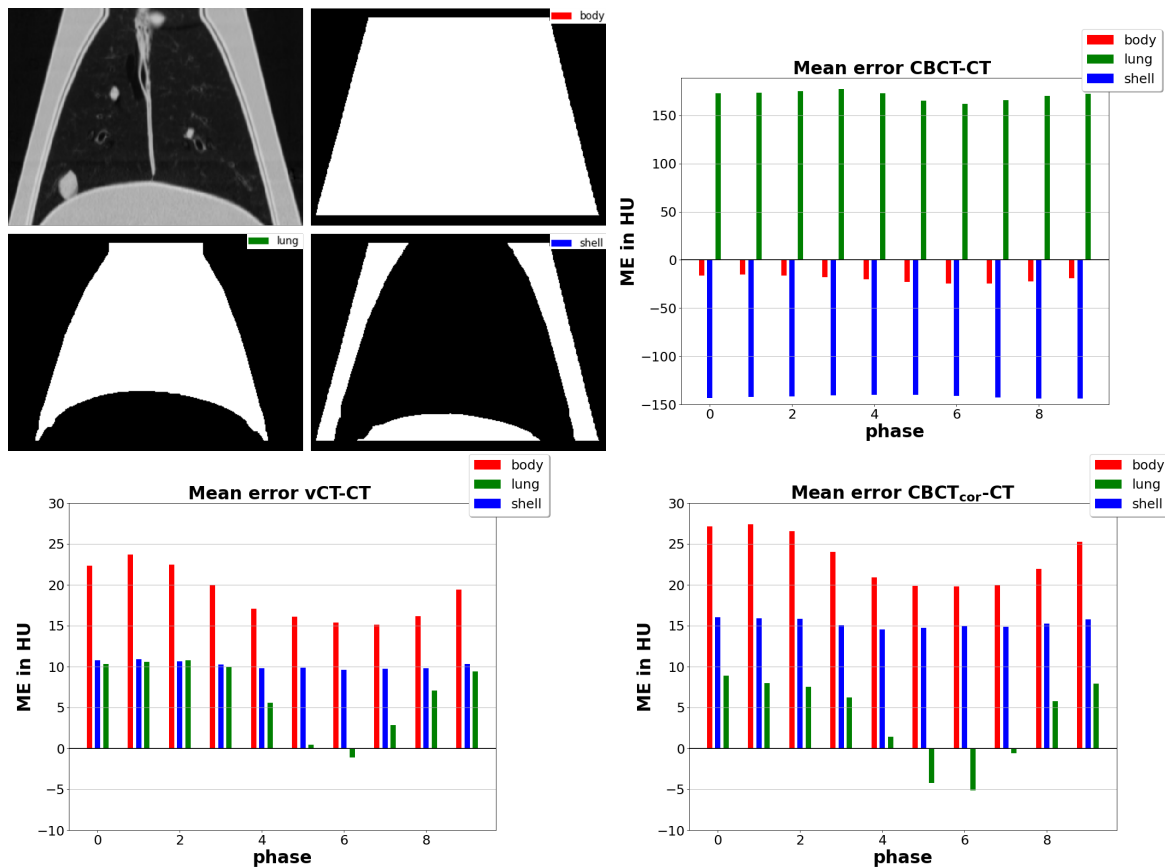
FIGURE 7.12: The top left plot shows the considered contours for the mean error analysis next to a CT image of the phantom. The three other plots display mean error plots in HU versus breathing phases for CBCT-CT, vCT-CT, and CBCT$_{cor}$-CT. Note the substantially larger range of the ordinate in the CBCT-CT case. Figure reprinted from [168].

Proton dose distribution analysis   Figure 7.13 shows axial slices of 4DCT, 4DvCT, and 4DCBCT$_{cor}$ with superimposed proton dose distributions for the ITV$_4$ plan. The first three rows, which display absolute doses, show good tumour coverage in all modalities for phase 0 (inhale), phase 3, and phase 6 (exhale). The two bottom rows show dose difference plots, expressed as a percentage of the prescribed dose. There is an overall good agreement as only minor deviations of a few percent for the 4DvCT and 4DCBCT comparison with the reference 4DCT are observed.

For ITV$_4$ and the lung DVH plots of 4DCT, 4DvCT, and 4DCBCT$_{cor}$ are shown in figure 7.14. These plots are presented for the inhale and exhale phase as well as the accumulated dose. The good agreement visible in figure 7.13 is validated. The zoomed-in right tail of the ITV$_4$ shows slightly larger values for 4DvCT and 4DCBCT$_{cor}$ in the extremal phases. This is not observed in the accumulated dose. The lung shows in all scenarios almost no deviation between the different modalities. The 4DvCT-4DCT differences for the DVH parameters $\Delta D_{2\%}$, $\Delta D_{98\%}$ of plan ITV$_4$ are for phase 0 -1.0%, -1.0%, for phase 6 0.1%, -0.5% and for the accumulated dose 0.2%, 0.1%, respectively. The corresponding DVH parameter differences for the comparison 4DCBCT$_{cor}$-4DCT are for phase 0 -0.7%, -0.5%, for phase 6 -0.2%, -0.7% and for the accumulated dose 0.0%, 0.8%, respectively.

For the accumulated doses the relative difference in the characteristic DVH parameters $D_{2\%}$, $D_{98\%}$, $D_{\text{mean, ITV}}$, $D_{\text{mean, lung}}$ for all plans (ITV$_1$, ITV$_2$, ITV$_3$, ITV$_4$) are presented in table 7.1. The good agreement is validated as for both comparisons (4DvCT-4DCT, 4DCBCT$_{cor}$-4DCT) no more than 2% deviations for $D_{2\%}$ and $D_{98\%}$ are found. For the DVH parameters mean ITV and mean lung the differences have a maximum value of 1.3%.

TABLE 7.1: Relative difference in percent of the accumulated dose for the comparisons of 4DvCT and 4DCBCT$_{cor}$ to reference 4DCT. For all four plans the DVH parameters $D_{2\%}$, $D_{98\%}$, $D_{\text{mean, ITV}}$ and $D_{\text{mean, lung}}$ are regarded. Table reprinted from [168].

vCT		CBCT$_{cor}$		vCT		CBCT$_{cor}$	
ITV$_1$	ITV$_2$	ITV$_1$	ITV$_2$	ITV$_1$	ITV$_2$	ITV$_1$	ITV$_2$
ITV$_3$	ITV$_4$	ITV$_3$	ITV$_4$	ITV$_3$	ITV$_4$	ITV$_3$	ITV$_4$
$\Delta D_{2\%}$				$\Delta D_{98\%}$			
1.7%	-0.1%	2.0%	-0.2%	1.3%	1.2%	1.6%	1.4%
0.4%	0.2%	-0.1%	0.0%	0.8%	0.1%	0.9%	0.8%
$\Delta D_{\text{mean, ITV}}$				$\Delta D_{\text{mean, lung}}$			
0.9%	0.4%	1.0%	0.4%	1.1%	1.3%	1.0%	1.2%
0.3%	-0.1%	0.4%	0.0%	-1.2%	1.0%	-0.5%	0.6%

Table 7.2 shows gamma-index PR of the accumulated doses for the comparison 4DvCT-4DCT and 4DCBCT$_{cor}$-4DCT for two global criteria of all four plans. For a 3%, 3 mm criterion the gamma-index PR for vCT and CBCT$_{cor}$ is between 97% and 100%. The corresponding values for a 2%, 2 mm criterion are between 93% and 98%.

7.2.3   Discussion

The porcine lung phantom study successfully introduced a novel 4DCBCT correction algorithm, which uses a 4DvCT as prior. A successful evaluation was achieved with a comparison to a ground truth 4DCT image. This was feasible due the usage of an anthropomorphic porcine lung phantom, which allowed reproducible breathing motion in a geometry similar
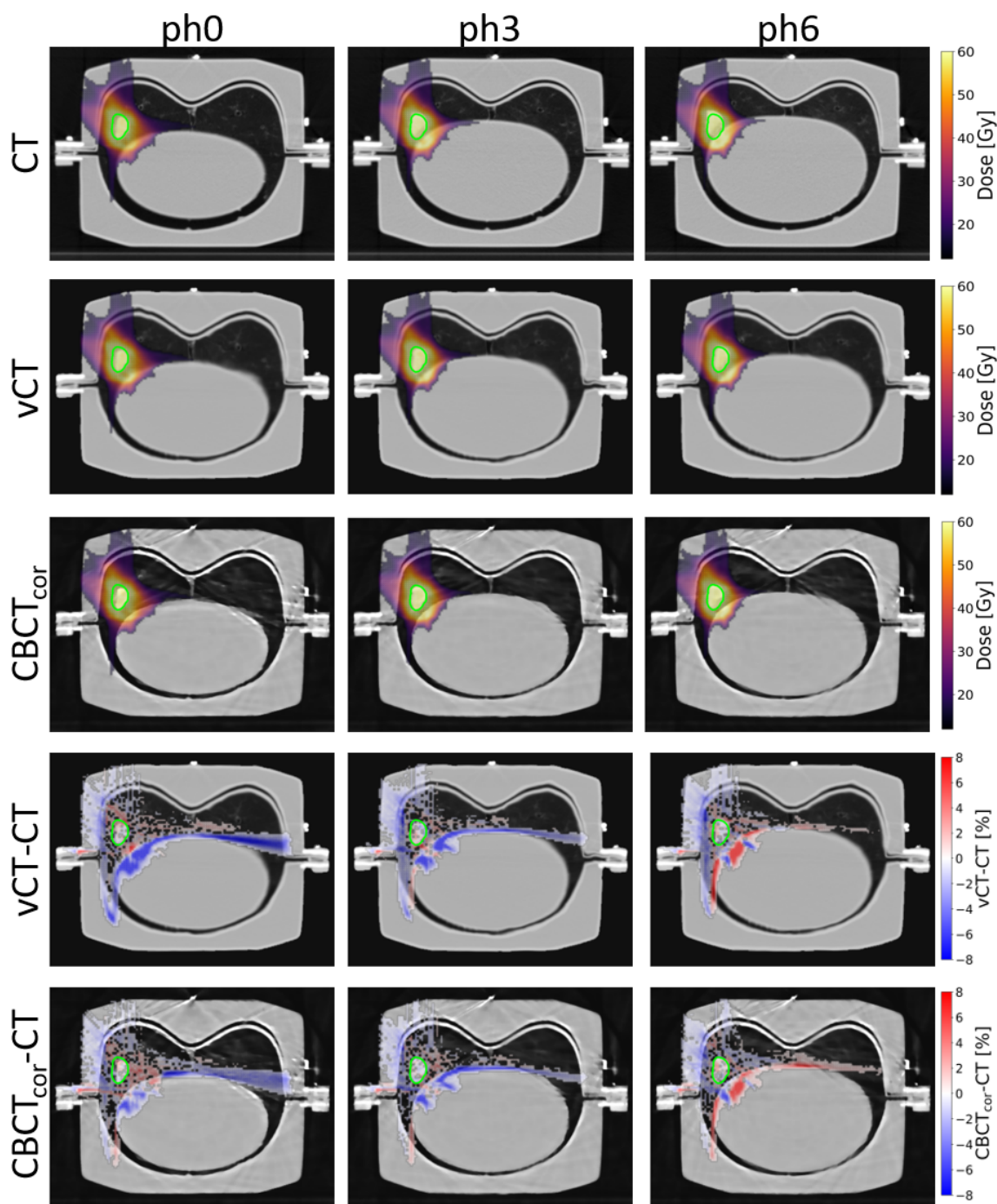
FIGURE 7.13: The first three rows show proton dose calculations for ITV$_4$ for three different phases of 4DCT, 4DvCT, and 4DCBCT$_{cor}$. Dose values below 15 Gy are masked to improve clarity. The two bottom rows display dose differences, which are expressed as percentages of the prescribed dose. To improve clarity in the dose difference images dose differences smaller than 0.4% are not shown. The images are displayed with level = -300 and window = 1600. Figure reprinted from [168].
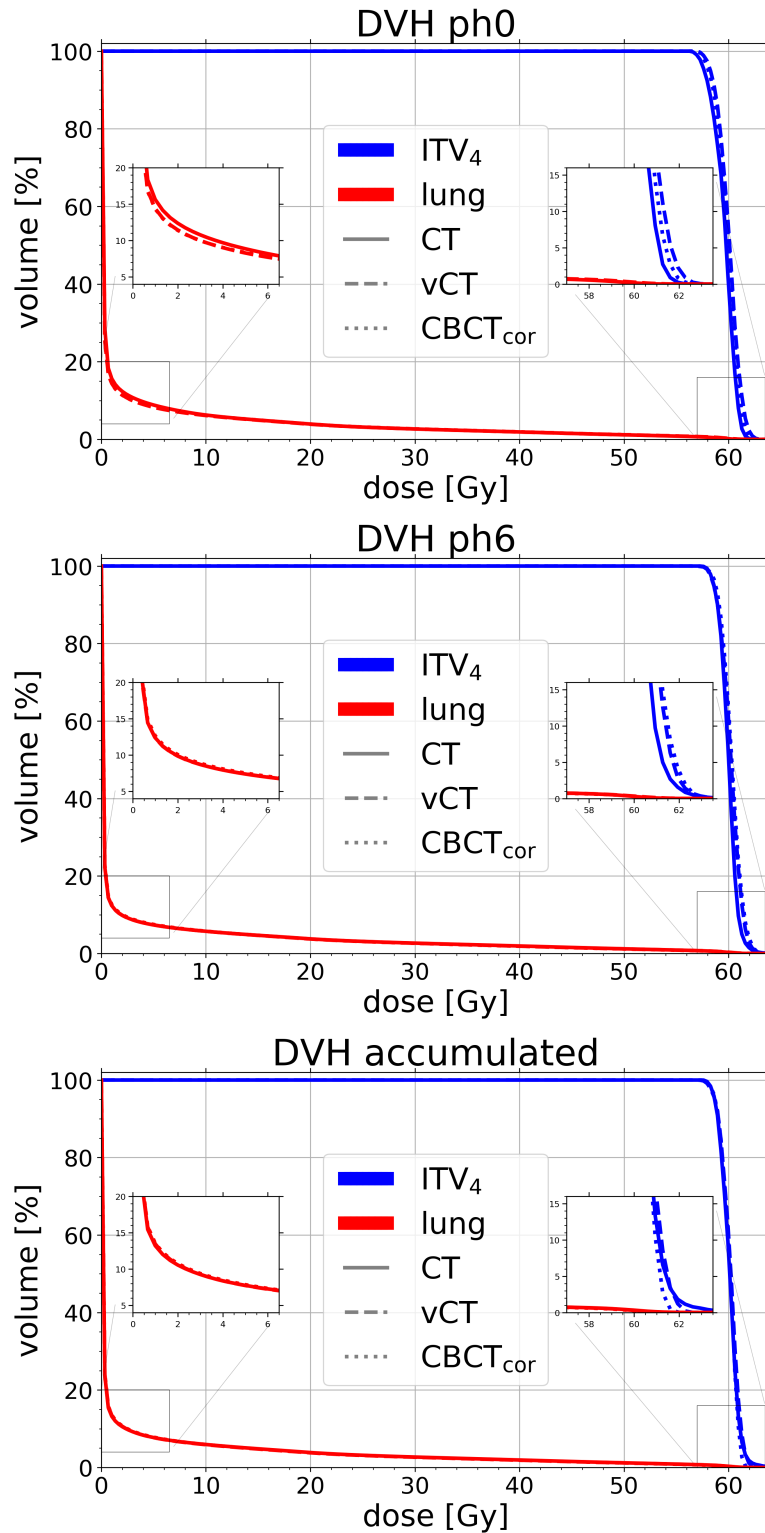
FIGURE 7.14: DVHs of ITV$_4$ and lung for phase 0 (inhale), phase 6 (exhale) and the accumulated dose of 4DCT, 4DvCT, and 4DCBCT$_{cor}$. Figure reprinted from [168].

TABLE 7.2: Results of the gamma-index PR analysis for a 3%, 3 mm and a 2%, 2 mm global criterion with a fixed threshold of 10%. For each of the four plans accumulated doses of 4DvCT and 4DCBCT$_{cor}$ were compared to corresponding accumulated dose values of the reference 4DCT. Table reprinted from [168].

plan	vCT	CBCT$_{cor}$	vCT	CBCT$_{cor}$
	(3%, 3 mm)		(2%, 2 mm)	
ITV$_1$	97.3	98.3	93.4	94.2
ITV$_2$	98.7	99.3	93.2	95.5
ITV$_3$	97.6	98.4	94.7	95.7
ITV$_4$	99.7	99.7	97.5	97.9

to the human thorax. The acquired CT and CBCT images were used to generate a day-of-treatment 4DCBCT$_{cor}$ image and a day-of-treatment 4DvCT image. Those two 4D images and thus those two generation methods were compared to the reference 4DCT. Accurate proton dose calculation was feasible on the 4DvCT and the 4DCBCT$_{cor}$ image of the porcine lung phantom. For the first time the 4DCBCT$_{cor}$ was evaluated for proton dose distributions. Overall good agreement between 4DvCT and 4DCBCT$_{cor}$ to the reference 4DCT was found as for accumulated doses investigated DVH parameters differed at most 1.7% and 2.0% for the 4DvCT and 4DCBCT$_{cor}$ case, respectively. Gamma PR for a 3%, 3 mm criterion with a fixed threshold of 10% of the prescribed dose were at least 97.3% in the 4DvCT and at least 98.3% in the 4DCBCT$_{cor}$ case.

Typical cranial-caudal (cc) ranges observed in clinical routine for tumour centroid positions between the extremal breathing phases of the motion amplitude are similar to those of the simulated lesions, which were between 2.3 mm and 10.8 mm [189]. The four mimicked lesions, which had different extents of motion as they were distributed within the lung [190], showed no difference in proton dose calculation accuracy.

A dose measurement would offer interesting insights, however due to the setup of the porcine lung phantom, which can only operate with a closed shell, it remains challenging. The same phantom using a dosimetric gel was investigated in an MRI study by Mann et al. [191]. Their measurement showed a high agreement between measured and calculated doses while maintaining a homogeneous coverage of the PTV. Additionally, they conducted a gamma analysis for a 3%, 3 mm criterion and reported values between 87.4% and 94.4%.

Lung tissue with its low density is very susceptible to small differences, which is why no range analysis was conducted.

Shresta et al. presented comparable gamma analysis values in their carbon-ion CBCT study, which used SMEIR for the reconstruction, ranging from 96.1% to 99.1% for a 3%, 3 mm criterion.

In general, the DVH and gamma PR analysis of this porcine phantom study is in a similar range to previous 4DvCT studies. Niepel et al. showed for a two-field plan gamma PR with a 3%, 3 mm criterion of at least 95% [133]. They investigated doses on a phase-by-phase level and did not consider accumulated doses. Bondesson et al. who investigated accumulated doses reported gamma PR of above 95% [134]. Niepel et al. and Bondesson et al. used residual tissues as a tumour surrogate, which is different to the injected gelatin-water mixture lesions used in the phantom study.

The DVH parameter differences for the 4DCBCT$_{cor}$ were often slightly larger than those of the 4DvCT, hinting at a slightly better performance of the latter. For the gamma PR the opposite was true as in this case slightly larger values for the 4DCBCT$_{cor}$ were observed, which suggests a better performance of the 4DCBCT$_{cor}$. It should be noted that this is not a

contradiction of this study but can be explained by the difference in regions of interest. The gamma PR evaluates the dose volume covered by a fixed threshold, whereas the DVH parameters relate to voxels inside specific organs. This makes the observed minor differences of a few tenths of a percent likely.

The anthropomorphic porcine lung phantom was perfectly suited to investigate realistic different breathing motions. However, it should be noted that anatomical changes cannot be simulated. Therefore, a demonstration of higher anatomical fidelity for CBCT$_{cor}$ over vCT as reported in a 3D case by Kurz et al. [126] cannot be investigated in the experimental setup. They compared the contours of PTV, CTV, bladder, and rectum to reference contours made on the initial 3DCBCT to those on the 3DCBCT$_{cor}$ and 3DvCT. The latter showed a lower agreement as they resulted from inaccurate DIR. Consequently, further investigation of this topic in a 4D setting with patient data remains necessary.

This is also important for tumour shrinkage and pleural effusion, which cannot be simulated and are not accurately modelled by DIR. Veiga et al. proposed cavity corrections, addressing these limitations [122, 123]. Consequently, adding these correction steps to the 4DCBCT$_{cor}$ could be beneficial.

Visual improvements presented in this study are similar to those reported in static 3D studies [30, 125]. It should be noted that those studies relied on FDK reconstructions. Nevertheless, these two studies reported gamma PR in the same order of magnitude as the values of this phantom study. Kurz et al. investigated different regions, which makes a direct comparison impossible. However, Park et al. showed for lung 98.6% (3%, 3 mm) and 93.0% (2%, 2 mm).

The constant overshoot of CT numbers for the lung in the 4DCBCT image could have their origin in different X-ray spectra, beam hardening and spectral response of the CT and CBCT. The overshoot for the diaphragm, tumour, and shell in the 4DCBCT$_{cor}$ are potentially a weakness of this scatter correction approach as they could be caused by inaccuracies within the DIR and the resampling steps. This could lead to a blurred vCT image, which was used as a prior for the CBCT$_{cor}$. However, both assumptions remain speculative and cannot be answered within the study setup.

The feasibility of DIR of 4DCT and 4DCBCT with different breathing motions, which led to a 4DvCT with updated motions was successfully employed. This 4DvCT was suitable for use as a prior of the 4D scatter correction workflow, which yielded the 4DCBCT$_{cor}$. Nevertheless, minor misalignments of the DIR are still perceptible especially at boundaries, such as the diaphragm-lung interface. Consequently, differences occur in these regions due to residual mismatches.

The anthropomorphic porcine lung phantom, which can be programmed to constant breathing patterns is ideally suited for proof-of-concept studies like the presented one. This was also demonstrated in the studies by Niepel et al. [133] and Bondesson et al. [134], as well as in an MR motion tracking study by Rabe et al. [187] or a range uncertainty assessment based on radiography for protons by Meijers et al. [150]. As the phantom has a non-varying anatomy, the newly presented 4D workflow has to be tested with clinical data in a next step. The clinical data should consist of lung patients with changing breathing patterns as well as changing tumour sizes over the course of their treatment.

Patient studies cannot have ground truth information as the breathing patterns between different acquisitions would differ. Consequently, a thorough investigation of the 4D workflow before applying it to patient cases is only feasible with a phantom with programmable breathing motion. Therefore, proof-of-principle studies, using a phantom, should be conducted as they provide valuable insight [192].

A remaining limitation of the 4D workflow is the needed computation time of roughly

4 h for the entire workflow. Possible accelerations of the computation were not investigated in this proof-of-concept study. Consequently, neither the runtime of 4DvCT workflow, which takes about 3.5 h, nor the subsequent 4DCBCT scatter correction workflow, which takes about 30 min are optimised. DIR using the Morphons algorithm as well as filtering processes during the scatter correction, which need to be conducted separately for each phase, are the most computationally demanding tasks. These bottlenecks could be addressed with further overall parallelisation and filtering functions, which are GPU-implemented. Another promising approach is the use of deep learning (DL) for 4D images, which will be described in chapter 8.

7.2.4 Conclusion

This porcine lung phantom study successfully implemented a novel 4DCBCT$_{cor}$ workflow, which is based on a per phase-level scatter correction, using a 4DvCT as a prior. The generated 4DvCT and 4DCBCT$_{cor}$ showed an improved quality compared to the initial 4DCBCT so that accurate proton dose calculation was feasible. Consequently, the method can be used for up-to-date in-room image generation, which accounts for breathing motion and is thus of clinical interest. Nevertheless, this has to be validated in a study containing clinical lung data, which led to the retrospective lung patient study, which is explained in the next section.

7.3   Patient application

This section describes a retrospective patient study conducted by the author, which is a follow-up study to the presented porcine lung phantom study.

This work was presented at the 4D treatment workshop on particle therapy in 2021 in Delft under the title "Scatter correction of 4D conebeam computed tomography for time-resolved proton dose calculation: first patient application", at the 2022 AAPM Annual Meeting in Washington, D.C. under the title "Scatter correction of 4D cone beam computed tomography images for time-resolved proton dose calculation: first patient application", and at the Jahrestagung der Deutschen Gesellschaft für Medizinische Physik in Aachen under the title "Intensitätskorrektur von 4D-Conebeam Computertomographie Bildern zur Berechnung zeitaufgelöster Protonendosisverteilungen: erste Anwendung am Patienten". Additionally, the study was accepted for publication in Medical Physics.

The goal of this retrospective patient study was the verification of a projection-based 4DCBCT scatter-correction algorithm on a cohort of lung cancer patients for proton dose calculation and its comparison to a 4DvCT approach, which is based on CT-to-CBCT DIR. Furthermore, the 4DvCT and 4DCBCT$_{cor}$ were evaluated for their potential for triggering treatment adaptation. For a more systematic approach, this section is subdivided into Material and Methods, Results, Discussion, and Conclusion.

7.3.1   Material and Methods

Patient cohort The retrospective patient study used imaging data from 21 lung cancer patients, who were treated with photon radiotherapy at the Department of Radiation Oncology at the University Hospital of LMU Munich. Patients were included if their tumour was clearly visible on the pCT and if they had a large target motion in cc direction of at least 6 mm. Patients with collapsed lungs or metal artefacts were excluded. For each of the 21 lung patients, a free-breathing 4DCT scan, equidistantly separated into 10 breathing phases, a free-breathing 3D pCT, and corresponding measured CBCT projections of an arbitrary treatment fraction were available. On the pCT, contours were delineated by a trained

radiation oncologist. The pCT and 4DCT were successively acquired in the same session. CBCT scans with more than 600 projections (number of projections per patient listed in table 7.3) were chosen among the several clinical acquisition protocols in use. The images were acquired on the same machines used in the porcine lung phantom study. Consequently, pCT and 4DCT acquisition was performed with a Toshiba Aquilion LB (Canon Medical Systems, Otawara, Japan) CT scanner using a reconstruction grid of $1.074 \times 1.074 \times 3 \, \text{mm}^3$ and the CBCT acquisition with the on-board CBCT imaging system of an Elekta Synergy or VersaHD linac (XVI 4.5.1, Elekta, Stockholm, Sweden) with a shifted detector (collimator = M20, M panel position, tube current = 40 mA, tube voltage = 120 kVp, exposure time = 40 ms).

TABLE 7.3: Characteristics of patients of the cohort: ITV size and cc motion, number and angles of simulated proton treatment beams, number of CBCT projections, and time between 4DCT and CBCT projections acquisition Δ_t are shown.

patient	size ITV [cm^3]	cc motion [mm]	# beams	beam angles [°]	# projections	Δt [d]
1	7.9	9	3	5, 60, 195	687	6
2	16.3	9	3	10, 170, 280	667	5
3	298.9	12	3	180, 240, 350	690	8
4	228.5	9	3	0, 180, 210	665	12
5	2.4	10	3	220, 270, 350	672	14
6	17.6	6	3	0, 160, 200	682	9
7	3.4	6	3	0, 180, 280	678	12
8	35.0	15	3	0, 90, 180	701	15
9	23.2	6	3	20, 90, 150	681	7
10	14.0	6	3	5, 60, 220	675	13
11	2.1	6	3	0, 180, 270	658	10
12	14.0	6	3	0, 180, 245	647	11
13	26.5	9	2	155, 210	654	14
14	20.4	6	2	80, 175	681	20
15	64.9	12	3	0, 160, 270	663	16
16	17.1	6	3	0, 70, 190	695	9
17	1.1	6	3	0, 180, 230	685	11
18	8.0	12	3	180, 230, 270	675	11
19	92.7	21	3	80, 150, 190	662	14
20	7.5	6	3	25, 150, 200	663	8
21	62.7	8	3	15, 80, 160	682	10
median	17.1	8	3		675	11

Treatment planning   Treatment planning was performed in the research version 10.1.100.0 of the commercial TPS RayStation (RaySearch Laboratories, Stockholm, Sweden). Similar to the porcine lung phantom study the treatment plans were inspired by the clinically used PT treatment at the UMCG (cf. section 5.1) [63, 149].

The pCT as well as all ten phases of 4DCT, 4DvCT, and 4DCBCT$_{\text{cor}}$ were imported to the TPS. All transferred images used the same generic CT number to density calibration curve. "RSL_PBS_CYC" was used as a beam model, which emulates a generic pencil beam scanning beamline and nozzle (available energy range: 70-230 MeV; nominal spot size (1σ) at isocenter: 7.0 mm (70 MeV) / 2.7 mm (230 MeV); Bragg peak width at 80% dose level: 1.7 mm (70 MeV) / 8.5 mm (230 MeV); hexagonal spot scanning pattern with automatic spot

spacing of 1.06 times 1σ of the lateral Bragg peak spread; automatic energy layer spacing corresponding to the width at 80% dose level of the more distant Bragg peak). The outer contours of the patients were automatically generated using a threshold of $-500\,$HU. If it was considered necessary the outer contours were manually adapted.

The ITV, which is the union of the GTV delineation performed by a physician on each phase of the 4DCT, was overridden on the pCT. Similar to the phantom study muscle tissue with a density of $1.05\,\mathrm{g\,cm^{-3}}$ [63, 149] was used. On the pCT, robustly optimised 3D pencil beam scanning IMPT plans, which administered 8 times 7.5 Gy were created. Each plan used a range shifter of 7.5 cm. Optimisation of the beams was done individually, which results in SFUD plans (cf. section 2.3).

Table 7.3 shows the wide range in investigated tumour volume from $1.1\,\mathrm{cm^3}$ to $298.9\,\mathrm{cm^3}$ with a median of $17.1\,\mathrm{cm^3}$. Additionally, relevant patient specific information for the treatment planning such as cc motion, number of beams, and beam angles are listed in the table.

A statistical error of 1% during plan optimisation was used for the Monte Carlo dose engine. For each plan an RBE of 1.1 was chosen [60]. Similar to the phantom study clinical robustness settings of 3% range and 6 mm setup uncertainty [63], used at the UMCG, were applied. Consequently, a total number of scenarios or optimisation dose computations of 45 (3 range scenarios times 15 setup scenarios) were considered. The minimax optimisation method (cf. section 2.4) [62] was used for robust optimisation. Objectives for the ITV were a minimum dose of 60 Gy, a maximum dose of 70 Gy, and a uniform dose of 60 Gy. The objectives for the considered OARs oesophagus, heart, and bronchi were a maximum dose of 43 Gy, 65 Gy, and 46 Gy, respectively.

Eventually, on all ten phases of the planning 4DCT, day-of-treatment 4DvCT, and day-of-treatment 4DCBCT$_\mathrm{cor}$ the proton dose distribution was recomputed without a density override.

Computer hardware The 4D scatter correction workflow was calculated on a computer with two Intel Xeon Gold 6254 (Cascade Lake-EP) 18-Core CPU at 3.1 GHz. Enabling of hyper-threading resulted in a total of 72 threads. An Nvidia Quadro P6000 with 24 GB was used as GPU.

Data analysis The analysis of the retrospective lung patient study was twofold. An image quality analysis investigated the differences between the different modalities 4DCT, 4DvCT, and 4DCBCT$_\mathrm{cor}$. To this aim a mean absolute error (MAE) and a mean error (ME) analysis was conducted. Only values inside the union of the CBCT FOV with the CT body outline were considered.

Proton dose distributions were recalculated on each phase of the 4DCT, 4DvCT, and 4DCBCT$_\mathrm{cor}$. This enabled a pairwise comparison between the different modalities on a phase-level. Interplay effects were not considered. DVH parameters (bronchi D$_{2\%}$, ITV D$_{98\%}$, lung D$_\mathrm{mean}$) and global gamma PR using a 2%, 2 mm criterion with a fixed dose threshold of 10% of the prescribed dose were evaluated. All contours, needed for this analysis, were rigidly copied from the pCT.

The results of the DVH and gamma PR analysis were compared to results, obtained in the ground truth study using the porcine lung phantom, which are listed in table 7.1 and 7.2. Using extreme values from the phantom study the expected accuracy of the 4DvCT and 4DCBCT$_\mathrm{cor}$ method can be estimated. Consequently, patient study values were compared to accuracy thresholds based on the phantom results, which were 1.6% for the ITV D$_{98\%}$ and 90% for the gamma PR (2%, 2 mm). Differences exceeding these thresholds are considered clinically relevant and indicate changes that would be detectable with the suggested methodology to trigger, e.g., an offline treatment adaptation.
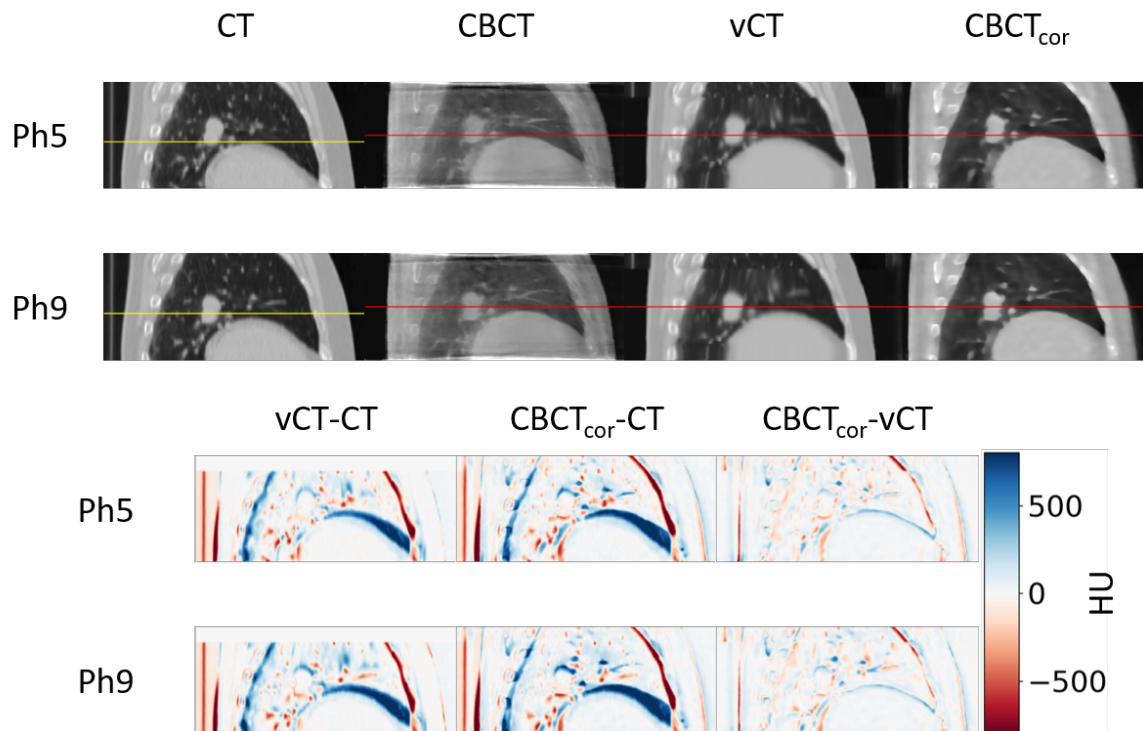
FIGURE 7.15: 4DCT, 4DCBT, 4DvCT, and 4DCBCT$_{cor}$ of patient 14 are shown using level = -300 and window = 1600 for phase 5 (exhale) and phase 9 (inhale) in the first two rows. The exhale diaphragm position is indicated by a horizontal line (yellow $\hat{=}$ CT and red $\hat{=}$ CBCT). The two bottom rows show difference images of vCT-CT, CBCT$_{cor}$-CT, and CBCT$_{cor}$-vCT. Deviations are expressed in Hounsfield units. The vCT is stiched with the CT (top part in this view). Consequently, the difference vCT-CT in this area is 0.

When discussing phases of the 4DCT, 4DCBCT, 4DvCT, and 4DCBCT$_{cor}$, the 4D prefix is omitted. CT should not be confused with pCT.

7.3.2   Results

Image quality analysis   Figure 7.15 shows phase 5 (exhale) and phase 9 (inhale) in sagittal view for 4DCT, 4DCBCT, 4DvCT, and 4DCBCT$_{cor}$ of patient 14. The horizontal lines in the top two rows indicate the exhale diaphragm position, which is different in the 4DCT case to all other modalities. This hints at interfractional changes. A clear quality improvement in 4DvCT and 4DCBCT$_{cor}$ over 4DCBCT is observable. The 4DCBCT$_{cor}$ has a higher anatomical fidelity than the 4DvCT as the lung appears less distorted. Additionally, the 4DCBCT$_{cor}$ appears sharper than the 4DvCT.

The two bottom rows of figure 7.15 display difference images. In the cases vCT-CT and CBCT$_{cor}$-CT differences of more than 500 HU are observed at the diaphragm-lung interface. For the comparison CBCT$_{cor}$-vCT the deviations are very small. The top part of the vCT is stitched with the CT. Consequently, for the vCT-CT comparison the difference image is zero in that area.

Figure 7.16 shows in the top row a ME analysis for all patients for the three different comparisons vCT-CT, CBCT$_{cor}$-CT, and CBCT$_{cor}$-vCT. For each of the patients the data is averaged over the 10 breathing phases. The bottom row shows a MAE analysis for the same patients and comparisons. Average values for the comparisons over all patients were 8.4 HU, 19.7 HU, and 11.3 HU for ME and 73.0 HU, 91.0 HU, and 60.7 HU for MAE, respectively.
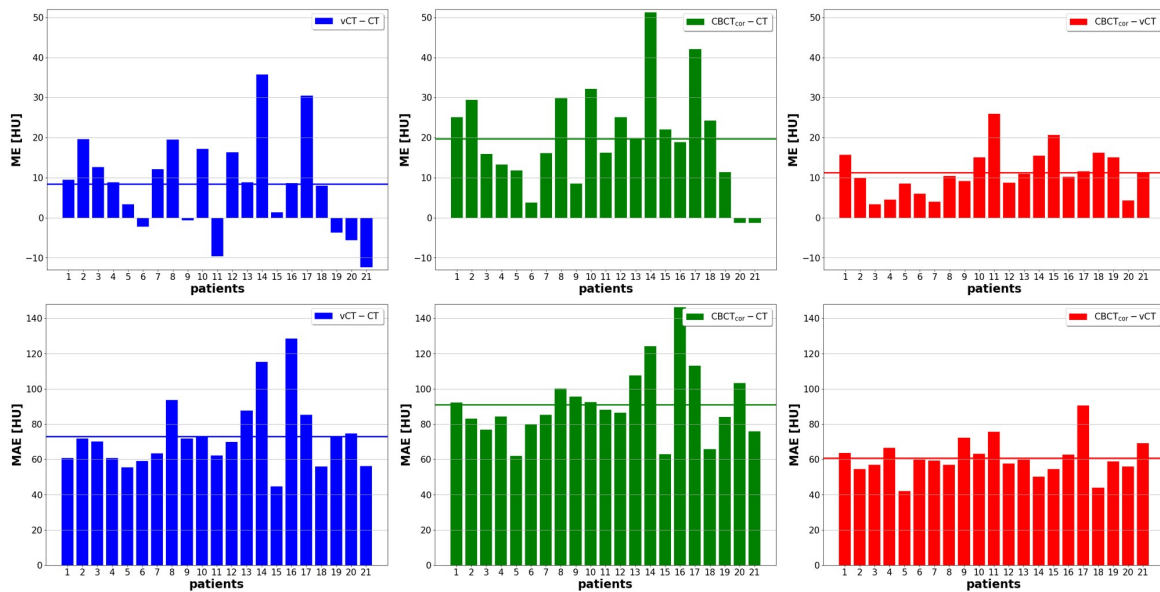
FIGURE 7.16: ME and MAE for all patients averaged over the 10 breathing phases are shown for the comparisons vCT-CT, CBCT$_{cor}$-CT, and CBCT$_{cor}$-vCT. For each case the mean value over all patients is shown with a horizontal line.

Proton dose distribution analysis   Figure 7.17 shows for 4DCT, 4DvCT, and 4DCBCT$_{cor}$ on axial slices the extremal breathing phases of patient 14. Absolute proton dose distributions and dose differences are superimposed on the images. The two top rows, displaying the absolute dose, show overall good target coverage for all modalities. Based on the gamma PR analysis (cf. table 7.4) anatomical or breathing pattern differences can be suspected between 4DCT and 4DCBCT for patient 14.

The results of the dose difference plots are twofold. Large deviations of more than 8% are observed for the differences vCT-CT and CBCT$_{cor}$-CT, which is a comparison between images acquired on different days. Minor deviations of less than 4% are observed between CBCT$_{cor}$-vCT. This excludes the bronchi area where differences are larger. Unlike the vCT the contralateral lung of the CBCT$_{cor}$ was not stitched, as it was not relevant for any subsequent step including dose calculation. Among the investigated patient cohort the time between 4DCT and CBCT projections acquisition Δt was the largest for patient 14 with 20 days.

Figure 7.18 displays a similar dose and dose difference plot for patient 1, showing substantially smaller dose deviations between 4DvCT-4DCT and 4DCBCT$_{cor}$-4DCT. Patient 1 was selected based on the gamma PR analysis since we suspect almost no anatomical changes between 4DCT and 4DCBCT. Patient 1 has the second smallest Δt with 6 days.

Figure 7.19 shows the differences in the DVH parameters ITV D$_{98\%}$ and bronchi D$_{2\%}$ for the comparisons vCT-CT, CBCT$_{cor}$-CT, and CBCT$_{cor}$-vCT of all patients and all phases in violin and box plots. The highest similarity for both DVH parameters is observed for the comparison of CBCT$_{cor}$ and vCT as their distribution is the narrowest around 0. The medians of all DVH differences, shown as white horizontal lines, are centred around zero. The mean lung dose, which is not displayed in this plot, was additionally investigated. It showed for all image comparisons median dose differences below 0.1 Gy.

Figure 7.20 displays absolute dose values of ITV D$_{98\%}$ of all patients for individual phases of the three modalities 4DCT, 4DvCT, and 4DCBCT$_{cor}$. The qualitative impression of a good dose coverage shown for two phases of a single patient in the top two rows of figures 7.17 and 7.18 is validated. This can be seen as the recalculations on the individual phases mostly yield dose values around 60 Gy (distributions are widest here), which is the dose target.
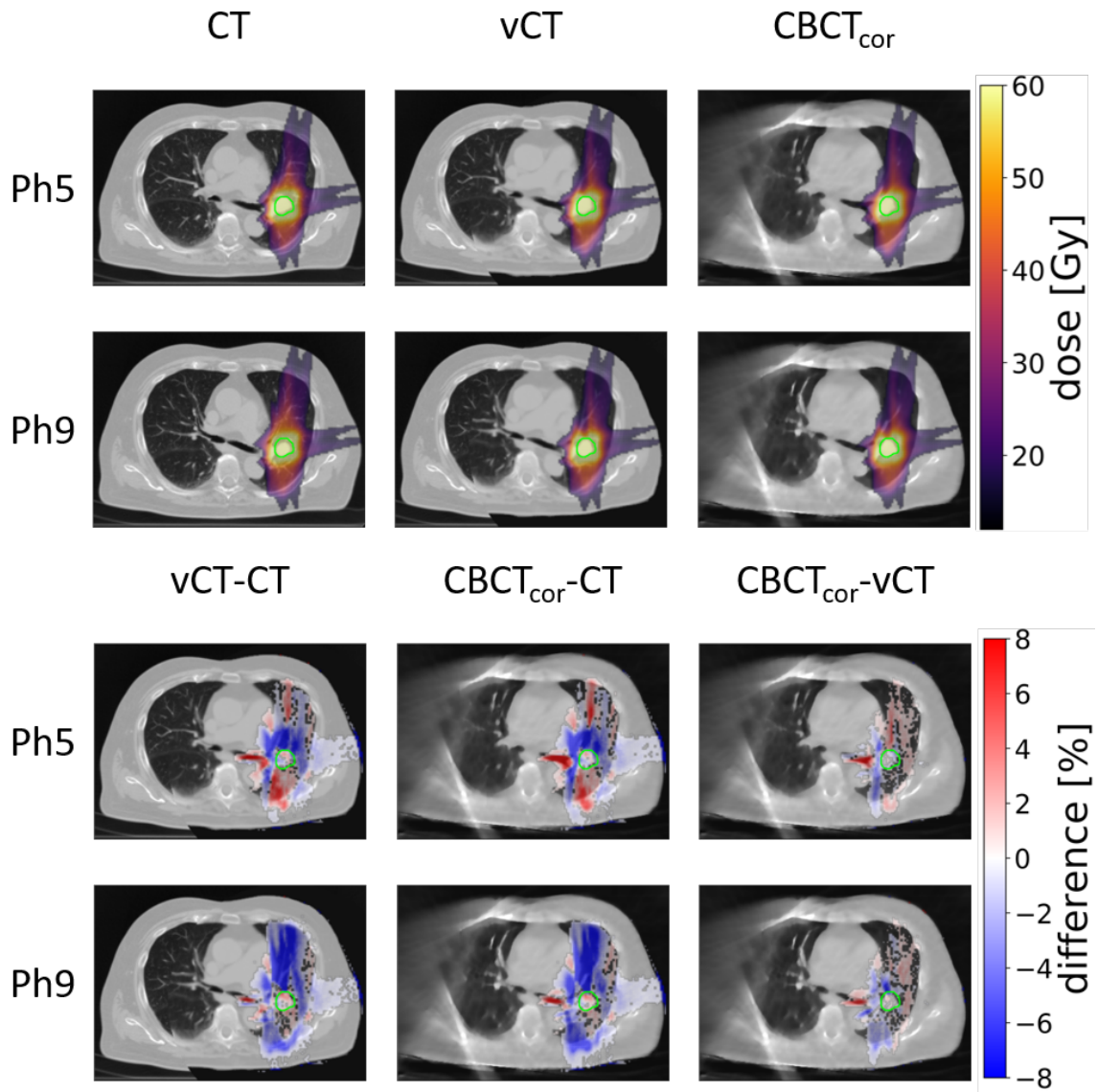
FIGURE 7.17: Recalculated proton dose distribution on extremal phases of 4DCT, 4DvCT, and 4DCBCT$_{cor}$ of patient 14 are shown in the top two rows. The bottom two rows display dose difference plots, which are expressed as a percentage of the prescribed dose. To improve the clarity of the plot dose difference values smaller than 0.4% are masked. The vCT is stitched with the CT in areas outside of the CBCT FOV.
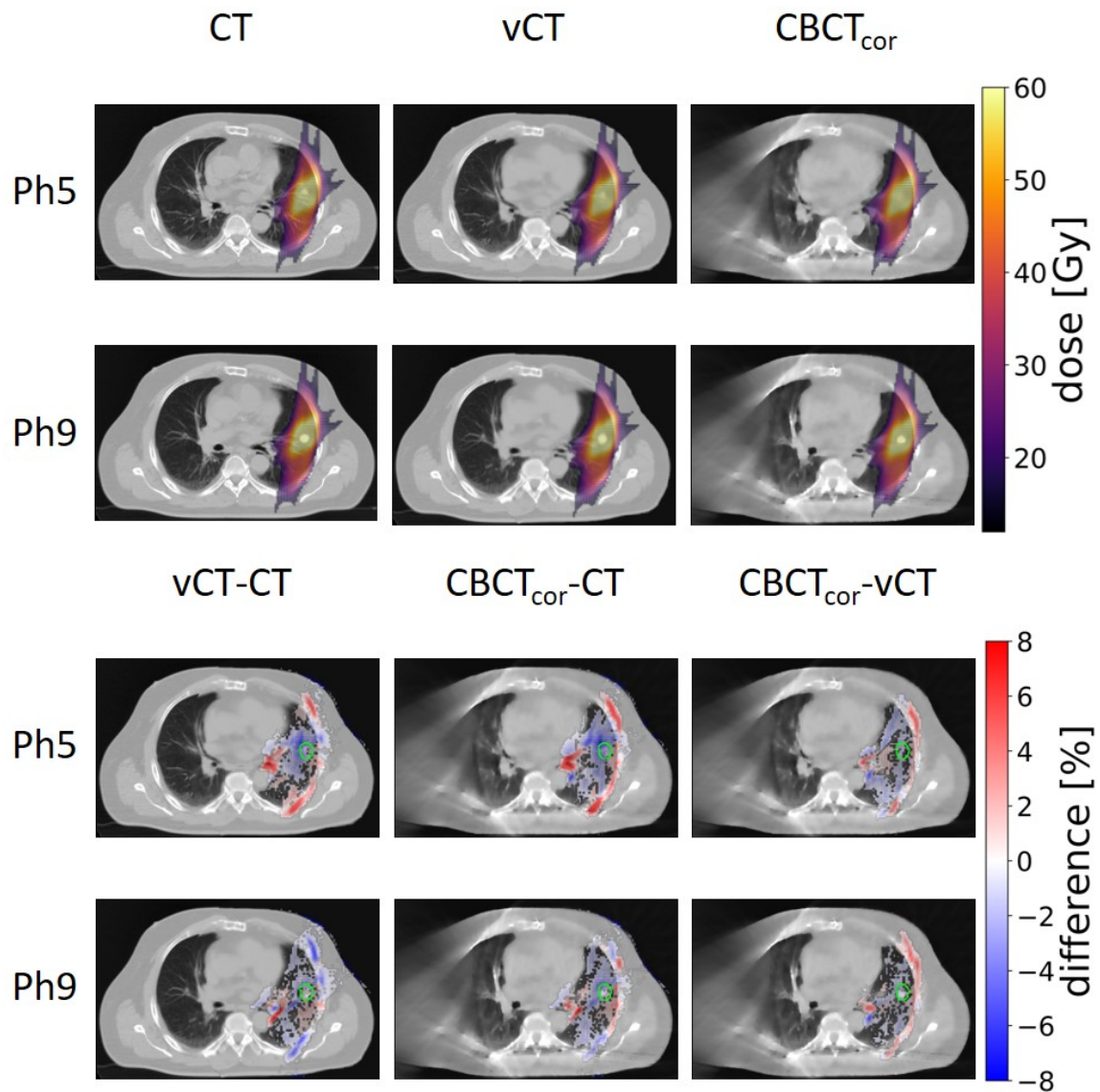
FIGURE 7.18: Analogous to figure 7.17 the recalculated proton dose distribution on extremal phases of 4DCT, 4DvCT, and 4DCBCT$_{cor}$ of patient 1 are shown in the top two rows and dose difference plots are shown in the bottom two rows. This patient shows small dose differences.
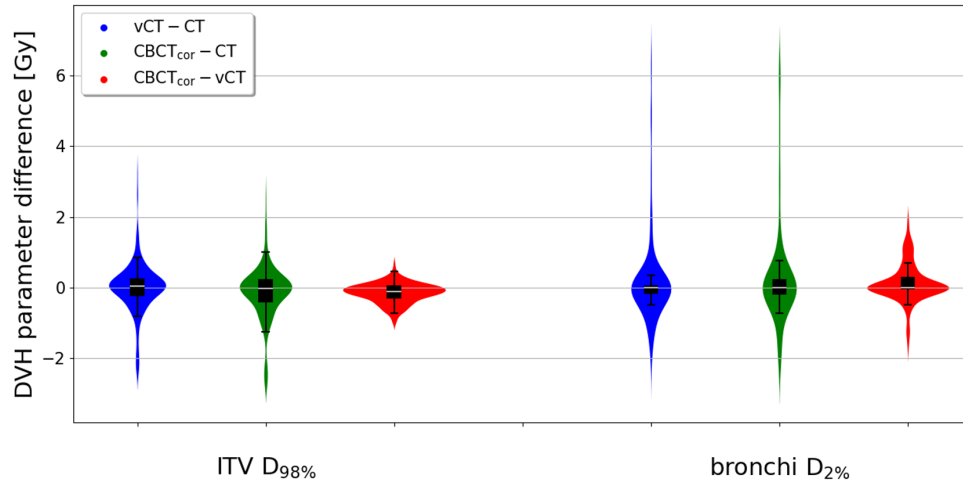
FIGURE 7.19: DVH parameter differences of the complete patient cohort with each patient having 10 breathing phases for ITV $D_{98\%}$ and bronchi $D_{2\%}$ are shown in violin plots for vCT-CT, $CBCT_{cor}$-CT, and $CBCT_{cor}$-vCT. Box plots with the median value shown as a white horizontal line and a whisker length of 1.5 times the interquartile range (IQR; range from Q1 to Q3 $\stackrel{\wedge}{=}$ length of the box) are superimposed. Outliers of the box plots are masked.
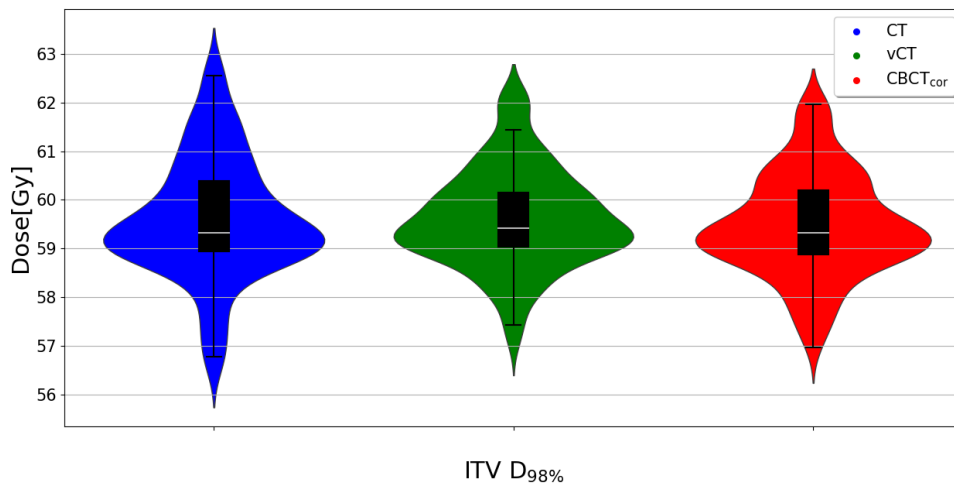
FIGURE 7.20: For the complete patient cohort violin plots show the absolute dose of ITV $D_{98\%}$ for all phases of CT, vCT, and $CBCT_{cor}$. Box plots with the median value shown as a white horizontal line and a whisker length of 1.5 times the IQR (25th to 75th percentile), are superimposed.
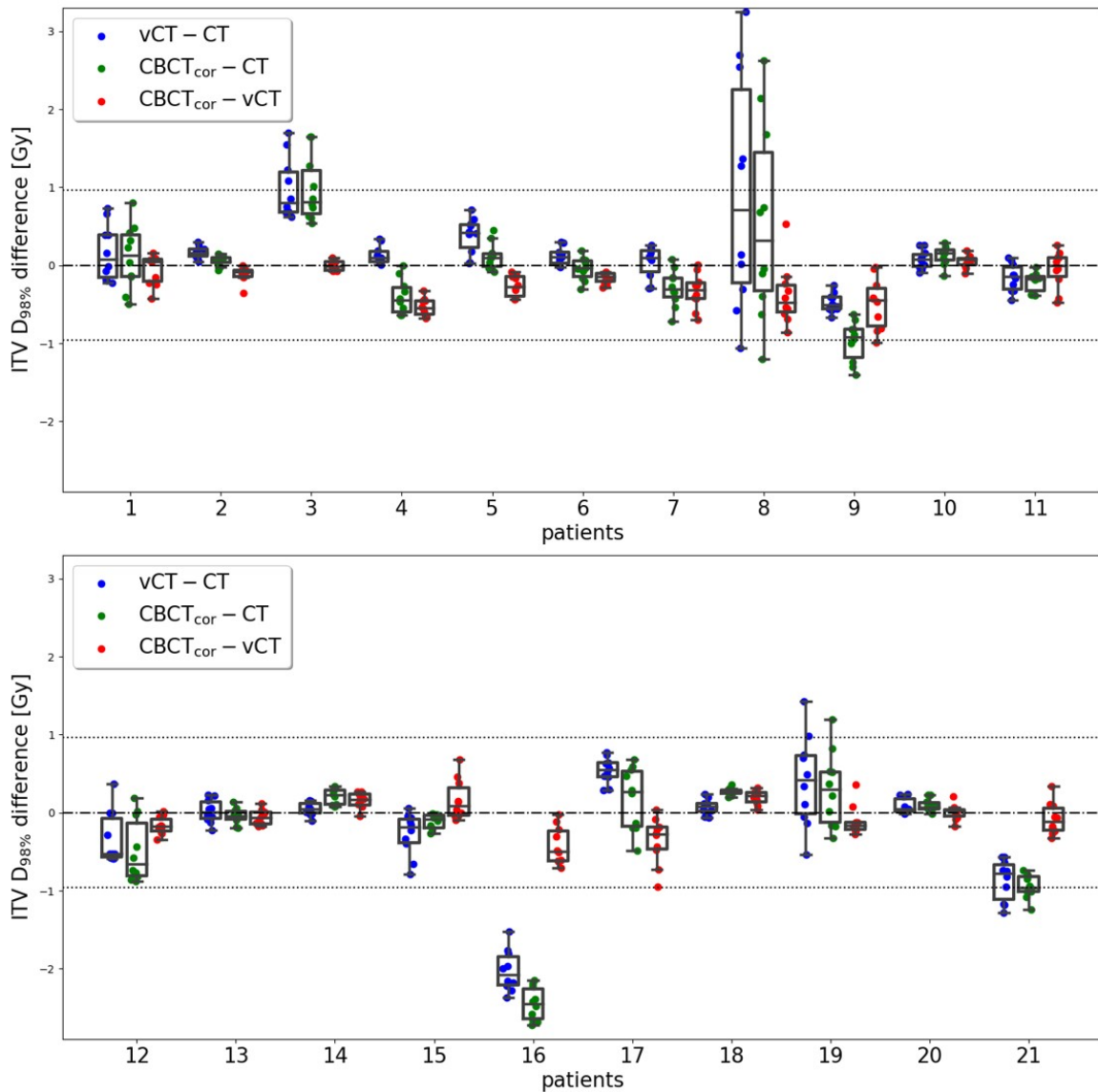
FIGURE 7.21: Differences in the DVH parameter ITV $D_{98\%}$ are shown as box plots for the comparisons vCT-CT, $CBCT_{cor}$-CT, and $CBCT_{cor}$-vCT at individual patient level. The box plots show the median values as a black horizontal line and have a whisker length of 1.5 times the IQR. Additionally, the individual data points of each breathing phase are displayed. To compare these results with the porcine lung phantom study, horizontal lines at $\pm 1.6\% \cdot 60\,\text{Gy}$ are drawn. 1.6% was the largest relative deviation detected for the DVH parameter ITV $D_{98\%}$ in the phantom study (cf. table 7.1).
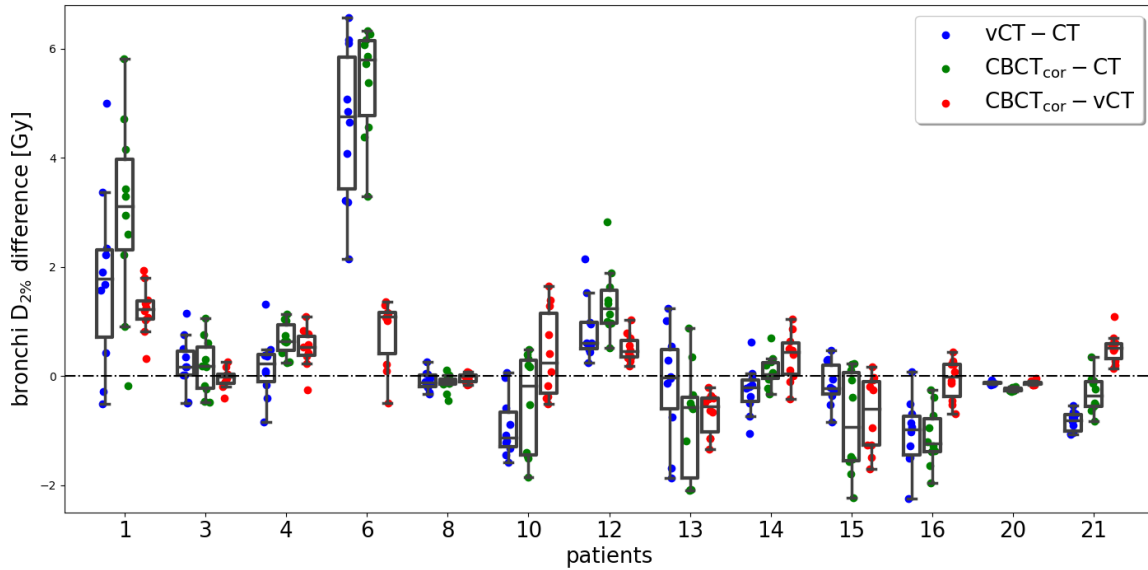
FIGURE 7.22: Analogous to figure 7.21 differences in the DVH parameter bronchi $D_{2\%}$ are shown in box plots for the comparisons vCT-CT, $CBCT_{cor}$-CT, and $CBCT_{cor}$-vCT at individual patient level. For a few patients no bronchi structure was contoured. Those patients are omitted in the plot.

Figure 7.21 shows differences in the DVH parameter ITV $D_{98\%}$ for all patients individually. Detected differences are small for most of the patients and comparisons as they are centred around 0. Horizontal lines at $\pm 1.6\% \cdot 60\,\mathrm{Gy}$, which was the largest observed deviation in the phantom case (cf. table 7.2), are drawn to help compare the results with the previous porcine lung phantom study. For patients 3, 8, 9, 16, 19, and 21 the differences for the comparisons vCT-CT and $CBCT_{cor}$-CT are larger than the largest differences detected in the phantom study. The differences between $CBCT_{cor}$-vCT are mostly centred around 0 and never exceed the maximum difference of the phantom study.

Figure 7.22 shows differences in the DVH parameter bronchi $D_{2\%}$ for all patients individually. For a few patients the bronchi structures were sufficiently far away from the target and thus they were not contoured. Those patients are not shown in the plot. As the phantom did not have segmented bronchi structures a direct comparison to the patients is not possible. For most patients the detected differences are small and centred around $\pm 0\,\mathrm{Gy}$. If larger deviations are observed those occur mostly for the cases vCT-CT and $CBCT_{cor}$-CT. Table 7.4 presents the gamma PR for a 2%/2mm criterion of all patients for the comparisons vCT-CT, $CBCT_{cor}$-CT, and $CBCT_{cor}$-vCT. The median of $CBCT_{cor}$-vCT is larger than the median of either vCT-CT or $CBCT_{cor}$-CT. This is true for all patients individually and thus this can also be observed in the median values of all patients which are 98%, 92% and 91%, for $CBCT_{cor}$-vCT, vCT-CT, and $CBCT_{cor}$-CT, respectively. Values below 90%, which only occur for the cases vCT-CT and $CBCT_{cor}$-CT are shown in bold to highlight the largest deviations. These low gamma-index PR values of the patients 3, 6, 7, 8, 9, 13, 14, 16, and 21 are all lower than the smallest value observed in the phantom study, which was 93.2% (cf. table 7.2). Patients 8 and 14 show the lowest PR for the comparison of vCT-CT and $CBCT_{cor}$-CT with minimum values of 75% and 74%. However, the same patients show median values for the comparison $CBCT_{cor}$-vCT of 99% and 98%. Patient 1 shows the overall largest agreement with median values of 98%, 97%, and 100% for vCT-CT, $CBCT_{cor}$-CT, and $CBCT_{cor}$-vCT, respectively.

TABLE 7.4: On a single patient level, gamma-index PR in percent for a global criterion of 2%/2mm with a fixed dose threshold of 10% of the prescribed dose are shown. For the 10 breathing phases the median, minimum, and maximum values are shown. Values below 90%, which is less than the smallest values observed in the phantom study, are in bold.

patient	vCT-CT median [min, max]	CBCT$_{cor}$-CT median [min, max]	CBCT$_{cor}$-vCT median [min, max]
1	98 [97, 99]	97 [95, 98]	100 [99, 100]
2	97 [96, 98]	97 [97, 97]	99 [99, 100]
3	**81 [80, 83]**	**82 [81, 84]**	97 [95, 99]
4	91 [87, 91]	91 [89, 92]	94 [91, 97]
5	96 [93, 99]	95 [90, 97]	97 [95, 98]
6	93 [90, 94]	**88 [85, 91]**	98 [96, 99]
7	**88 [84, 92]**	91 [89, 93]	97 [96, 97]
8	**87 [75, 96]**	**86 [78, 93]**	99 [92, 100]
9	**78 [76, 83]**	**77 [73, 84]**	98 [98, 99]
10	96 [91, 97]	97 [94, 98]	99 [98, 100]
11	90 [84, 94]	94 [89, 96]	96 [93, 99]
12	93 [84, 97]	91 [82, 95]	99 [98, 99]
13	**86 [84, 94]**	**87 [83, 94]**	96 [94, 98]
14	**80 [75, 83]**	**79 [74, 81]**	98 [98, 99]
15	97 [96, 98]	97 [96, 98]	98 [95, 99]
16	**85 [83, 87]**	**83 [81, 85]**	99 [99, 99]
17	92 [90, 94]	93 [92, 96]	97 [95, 97]
18	96 [91, 99]	97 [92, 99]	98 [97, 99]
19	97 [93, 98]	95 [93, 98]	99 [96, 100]
20	93 [90, 95]	91 [89, 93]	99 [99, 100]
21	**89 [88, 95]**	**87 [86, 94]**	99 [99, 99]
median	92 [88, 95]	91 [89, 94]	98 [96, 99]

7.3.3 Discussion

A 4DCBCT correction workflow previously validated using porcine lung phantom data, generating 4DvCT and 4DCBCT$_{cor}$ images, was successfully applied to a lung cancer patient cohort, which was clinically treated with photon radiation. In a proton dose comparison between 4DCT, 4DvCT, and 4DCBCT$_{cor}$ good agreement was found between 4DvCT and 4DCBCT$_{cor}$. The evaluation of the presented technique can be considered as a next step, after the initial proof-of-concept phantom study, towards a potential clinical application.

The investigated patient cohort with tumour sizes ranging from $1.1\,cm^3$ to $298.9\,cm^3$ is comparable to values of an NSCLC study, analysing volume changes, which reported sizes between $4\,cm^3$ and $776\,cm^3$ [193]. A study by Wolthaus et al. reported GTV volumes between $2\,cm^3$ and $200\,cm^3$ [194], which again is in a similar range. The same study investigated patients with target motion in cc ranging from $0.8\,mm$ to $24\,mm$, which is slightly smaller than the motions investigated in this patient study, which were between $6\,mm$ and $21\,mm$. Liu et al. investigated a lung cohort in which about 40% showed cc motion of more than $5\,mm$ [195]. Additionally, for 95% of the patients the cc motion was lower than $13.4\,mm$, which again indicates that motion amplitudes in this study are within a normal clinical range. In general, respiratory target motion, which is highly patient-specific and thus irregular, changes from fraction to fraction [162, 196, 197].

Similar to Ribeiro et al. the presented 4DCBCT$_{cor}$ method could be used to split the dose plan into different phases [149]. This would allow accounting for interplay effects and could thus be used in the future for daily dose reconstruction or online adaptation.

Similar to the porcine lung phantom study the qualitative image analysis for the patient study shows improved image quality for 4DvCT and 4DCBCT$_{cor}$ over the initial 4DCBCT. Additionally, the patient's breathing motion as well as changed anatomy was displayed correctly, which can be observed in the difference images (cf. figure 7.15) at the lung-diaphragm interface. For vCT-CT as well as CBCT$_{cor}$-CT large baseline shifts occurred. The higher geometric fidelity of the CBCT$_{cor}$ to the vCT and thus an improved image adaptation to changes that occurred in a patient, which was reported by Kurz et al. for the 3D case [126], is also true for 4D images. This can be seen for the tumour outline and ribs.

The recalculation of the dose plans, which were optimised on 3D pCTs, on the phases of 4DCT, 4DvCT, and 4DCBCT$_{cor}$ can be considered robust as the median values of ITV D$_{98\%}$ were slightly above 59 Gy (cf. figure 7.20). Consequently, the dose values are close to the prescribed 60 Gy. This high robustness was only achieved for the presented planning settings if the beams were optimised individually, resulting in SFUD plans. Clinical goals, such as sparing of OARs, were met for 4DCT, 4DvCT, and 4DCBCT$_{cor}$ as, e.g., medium values for bronchi D$_{2\%}$ were below 10 Gy.

Large dose differences for 4DvCT-4DCT and 4DCBCT$_{cor}$-4DCT indicate that inter-scan breathing and anatomy changes are accounted for in the 4DvCT and 4DCBCT$_{cor}$ case. 4DvCT and 4DCBCT$_{cor}$ values are close to each other, which shows consistency of these methods, even though there is no ground truth available like in the porcine lung phantom study. This indicates that those generated images show the same day-of-treatment breathing motion and anatomy as the 4DCBCT, which is different to the 4DCT and thus the pCT.

The shown violin and box plots (cf. figure 7.19) support this statement, as the distribution for both ITV D$_{98\%}$ and bronchi D$_{2\%}$ are narrower around 0 for the comparison 4DCBCT$_{cor}$ and 4DvCT than in the two other comparisons. This conclusion is further validated by comparing dose differences of 10 breathing phases on a single patient level. The dose difference is in the 4DCBCT$_{cor}$-4DvCT case closer to zero than in the other two cases.

A similar conclusion can be drawn from the gamma PR analysis. For 4DvCT-4DCT and CBCT$_{cor}$-CT the median values are substantially lower with 92% and 91% than for the comparison of CBCT$_{cor}$-vCT with 98%. Kurz et al. reported similar results as they also showed high similarity between CBCT$_{cor}$ and vCT [126]. Consequently, the gamma PR analysis is another indication that anatomical or breathing pattern changes are accounted for in the 4DvCT and 4DCBCT$_{cor}$ images.

Nevertheless, gamma PR median values for all considered cases are within a range of less than 3% for patients 1, 2, 5, 10, 15, and 18, which leads to the assumption that for those patients almost no changes occurred between the acquisitions on the planning and the selected fraction day.

Large differences in target coverage, which can be observed for patients 3, 8, 9, 16, 19, and 21, could potentially be used as an indicator for the necessity of replanning. Large differences are defined as the maximum deviation observed in the porcine lung phantom study, which demonstrated small image and dose differences between the generated vCT and CBCT$_{cor}$ to a ground truth CT. Consequently, large differences hint at breathing pattern or anatomical changes. An additional indicator with respect to replanning could be gamma PR values below 90%, which is less than the minimum value observed in the phantom study. Those occurred for patients 3, 6, 7, 8, 9, 13, 14, 16, and 21, respectively. The intersection of these two sets, which would be patients 3, 8, 9, 16, and 21, could be a more robust and reliable indicator and thus be suggested for a decision tool on replanning.

Thing et al., who compared a clinically used corrected CBCT and an improved version of the corrected CBCT to a replanning CT in a lung study reported gamma PR results of 93.1%

and 99.4% [198] for a 2%, 2 mm criteria, which is in a similar range to the reported results of this patient study. It should be pointed out that a higher agreement would be anticipated for their 3D study compared to this 4D study. This is because of the lack of motion effects, which are no longer there due to the averaging. Additionally, they are comparing a replanning CT to their generated images, which have almost the same anatomy.

As breathing patterns change between the different image acquisitions, a ground truth analysis, as performed in the porcine phantom study, is not feasible. Nevertheless, there is high confidence in the accuracy of the presented results especially due to the phantom validation.

Wrong deformations could potentially originate from large volume changes in the lung. This would necessitate a post processing step of the 4DvCT in which the cavities are either filled or emptied [122]. This was not observed in our lung patient data set and thus the potential limitation in the presented method could not be investigated.

As already mentioned in the discussion of the porcine lung phantom study, the long computation time for the 4D workflow of roughly 4 h per patient is an issue that needs to be tackled for a possible clinical application. AI approaches, which recently also include 4DCBCT image generation [142], could potentially solve the time issue.

7.3.4 Conclusion

This retrospective lung patient study verified a 4DCBCT$_{cor}$ workflow, which was previously tested on a porcine lung phantom. Similar to the results of the phantom study, both generated images, the 4DvCT and 4DCBCT$_{cor}$, in all of the 21 lung tumour patient cases could be used for accurate proton dose calculation. Among 4DvCT and 4DCBCT$_{cor}$ there is a high agreement. More pronounced differences to the 4DCT, acquired on a different day, are observable in both 4DvCT and 4DCBCT$_{cor}$. The method could be used for up-to-date in-room image generation, which accounts for daily breathing motion and anatomical changes. Consequently, the method is of clinical interest as the 4DvCT and 4DCBCT$_{cor}$ images could be used for indicating the necessity of plan adaptation or even online treatment adaptation in the future.

However, the long runtime of the workflow makes it not suitable for a potential clinical implementation yet. This led to the third project, an AI implementation of the scatter correction workflow, which will be presented in chapter 8.

Chapter 8

ScatterNet

This chapter introduces the third and final project conducted by the author for this thesis. It addresses the long computation times needed for the 4DCBCT scatter correction workflow, presented in the previous chapter. The idea is to employ AI methods to speed up the generation of daily 4D images based on CBCT projections, which are suitable for proton dose calculation. As a consequence, the results of this project could be applicable for online ART (cf. section 4.2). An abstract summarising this study was accepted for an oral presentation at ESTRO 2023 in Vienna.

This chapter starts with an overview of different AI studies, which led to the one presented in this thesis. Initial findings of this study, which have been submitted to the 2023 ESTRO conference under the title "ScatterNet for 4D cone-beam CT intensity correction of lung cancer patients", are presented. An outlook on further improvements of the methods is given. Similar to the description of the previous studies in this thesis this chapter is subdivided into Motivation, Material and Methods, Results, Discussion, and Conclusion.

8.1 Motivation

As stated in chapters 6 and 7 the use of CBCT scanners in radiation therapy clinics is widely spread. CBCT images, due to their limited image quality, are mostly used for patient positioning. However, as shown in chapter 7, further usage in the field of proton dose calculation, such as providing information about interfractional changes of the patient anatomy, is feasible and thus clinically interesting. A remaining bottleneck of the presented 4D scatter correction workflow is the long computation time of more than 10 min, which makes it not applicable within tight clinical schedules, especially in the context of online treatment adaptation.

Recent studies based on deep convolutional neural networks (CNNs) [199], which are powerful techniques for image feature extraction, showed promising results addressing the issue of providing an accurate scatter-corrected CBCT image in a clinically acceptable time of a few seconds. Relevant studies for the third topic of this thesis, which mostly rely on U-shaped CNNs (Unet)[200], consisting of multiple convolutional and transposed convolutional layers in an encoding and decoding branch, are in the following summarised. CNNs learn a direct non-linear mapping of image intensities between their paired image input (CBCT and CT). This is different to conventional machine learning techniques such as random forest [201] in which decision trees are trained to predict image intensities on patches of, e.g., aligned CBCTs and CTs. A major advantage of all AI approaches is that they do not rely on a pCT or DIR after training.

In 2018, Kida et al. were among the first that showed a deep learning application that converts CBCT images into vCTs [135]. They did this for paired pCT and CBCT images of 20 prostate cancer patients. Their evaluation, which includes only image quality metrics and no dosimetric analysis, showed a clearly enhanced image quality. Maier et al. trained a Unet to predict scatter by using MC simulated scatter distributions for training. They did this on

a projection level for head [202], thorax, and abdomen [203] scans as well as in an industrial setting [204]. Similar to Kida et al. image quality improvements, more specifically intensity corrections, were shown without any dose evaluation.

Hansen et al. also trained a Unet with pairs of raw and corrected projections (Niu-method was used to generate the corrected projections; cf. section 3.9) using 30 prostate patients [136]. They evaluated the dosimetric accuracy of their corrected CBCTs by calculating VMAT and IMPT treatment plans. They showed that their intensity correction was sufficient for VMAT dose calculation, but not satisfactory for IMPT dose calculation for all patients. Landry et al. used the same network architecture as Hansen et al. with three different paired data sets (raw and corrected CBCT projections, CBCT and vCT, and CBCT and corrected CBCT using the Niu-method; cf. section 3.9) to evaluate whether it is optimal to train a Unet with projections or images [137]. In their dose evaluation, they concluded that the VMAT dose accuracy was good in all three cases and thus independent of using projections or images as network input. For proton dose calculations the approach that used paired CBCT and corrected CBCT images showed the best results.

Neppl et al. used the same ScatterNet architecture in an MRI setting [205]. They trained the 2D ScatterNet and a 3D extension of it with MRI and CT data pairs of 89 head patients aiming at generating synthetic CTs from MRIs. Their 3D network needed more time to train than the 2D network (36 h versus 6 h), but both networks had small conversion times (12 s versus 2 s). Image quality metrics showed a better performance for the 2D network over the 3D network. Evaluating VMAT and SFUD plans, a similar dose accuracy was reported for the 2D and 3D networks.

Kurz et al. used a cycle-consistent generative adversarial network (cycleGAN) [206] to convert CBCT images to CTs [138]. The advantage of cycleGANs is that they do not require paired data sets, which are not always available, for training. In general, a GAN [207] consists of a generator and a discriminator. The generator tries to create a realistic enough image, which can fool the discriminator in order to perform domain transfer. Both generator and discriminator, which are usually CNNs, are trained jointly. Kurz et al. could show for 33 prostate patients that their resulting CT was sufficient for VMAT plans, yet for SFUD plans further improvements were deemed needed.

Thummerer et al. trained a Unet with paired CBCT and CT images from 33 H&N patients. They compared this method with two different CBCT correction approaches, which are either based on DIR or on an analytical correction method [139]. The output of their network achieved the highest image quality. Proton dose evaluation showed accurate results for the network and the DIR method, while the analytical method was worse.

Lalonde et al. trained a Unet on a projection level with 48 H&N patients to reproduce MC-based CBCT scatter correction [140]. In a second step, the CNN prediction of the scatter can then be used for projection-based CBCT correction. This scatter correction method showed overall good agreement compared to the Niu scatter correction method (cf. section 3.9). Additionally, for a head phantom they compared the proton range accuracy of their network output with a ground truth CT image and could show in the central axis of the proton beam a difference on R_{80} of just 1 mm.

Madesta et al. [141] presented a deep learning approach for improving 4DCBCT reconstructions, which used a residual dense network (RDN) [208] for 20 liver and lung tumor patients. An RDN mainly consists of a residual dense block, which is described by densely connected convolutional layers (extracted features are globally available), local feature fusion (used to control output features so that it is still feasible to train deeper networks), and local residual learning (implementation of skip connection, which makes learning of the identity function in deeper networks feasible). Madesta et al. want to learn the relationships between low-quality 3DCBCTs, which are pseudo-time-averaged CBCTs of a phase, reconstructed out of a specific selection of all projections, and a high-quality 3DCBCT,

which is reconstructed using all projections. Their trained network can then be applied post-reconstruction, independent of the reconstruction method, to reduce artefacts in each breathing phase of a 4DCBCT. Dong et al. [142] trained their cycleGAN with 4DCBCT and CT slices of 20 NSCLC patients. Their network then generates a high-quality 4DCBCT from a poor-quality 4DCBCT. Both studies showed improved image quality but did not include any dose calculations.

Thummerer et al. used a Unet by Spadea et al. [209], which trains separate networks with axial, coronal, and sagittal slices individually so that each generates a corrected CBCT [143]. Each corrected CBCT is then combined into a final corrected CBCT. As network input, they used pairs of 4DCBCT and 4DCT images of 45 thoracic cancer patients. They trained their network exclusively with pairs of the 0% breathing phase of the 4DCBCT and 4DCT images. The result of this training was inferred to all breathing phases so that a total corrected 4DCBCT could be generated. They could show a high agreement in clinical target volume dose between network generated corrected 4DCBCTs and 4DCTs, which were acquired on the same day.

These presented studies as well as an existing 4D database of paired uncorrected and corrected lung CBCT projections and images, from the retrospective lung patient study (cf. section 7.3), triggered the AI study, which is presented in the following.

8.2 Materials and methods

Patient data This study used lung patients from the same database, treated with photon therapy at the LMU University Hospital, as the previously presented patient study (cf. section 7.3). For 5 additional patients, the 4D scatter correction workflow (cf. section 7.1) was conducted. Including the 21 patients of the previously presented study, a total of 26 lung patients were available for the AI study. Table 8.1 shows the characteristics of the 5 additional patients, which were used for testing. Table 7.3 shows the other 21 patients.

TABLE 8.1: Characteristics of the additional patients, which were used for testing in this AI study: ITV size and cc motion, number and angles of simulated proton treatment beams, number of CBCT projections, and time between 4DCT and CBCT projections acquisition Δt are shown. Median values among these 5 test patients are displayed.

patient	size ITV [cm^3]	cc motion [mm]	# beams	beam angles [°]	# projections	Δt [d]
22	23.3	6	3	30, 150, 190	680	17
23	1.7	10	3	90, 140, 180	669	7
24	53.6	8	3	15, 50, 200	683	7
25	53.2	6	3	70, 200, 345	697	6
26	1.6	1.2	3	150, 210, 270	732	13
median	26.7	8	3		688	10

For each of the 26 patients, paired raw and corrected CBCT projections, with the latter ones generated within the 4D scatter correction workflow (cf. section 7.3), were available. The 26 patients with a total of 17,564 2D projection pairs were split into 15, 6, and 5 for training, validation, and testing, respectively. This resulted in the data partitioning approach of 60/20/20, which is commonly used. Training data was used to train the network. With the validation data, a loss function was calculated and used to decide after which iteration to stop the training. In order to avoid bias, the testing data was only used after the network was trained and the final model was selected based on the validation data. All projections
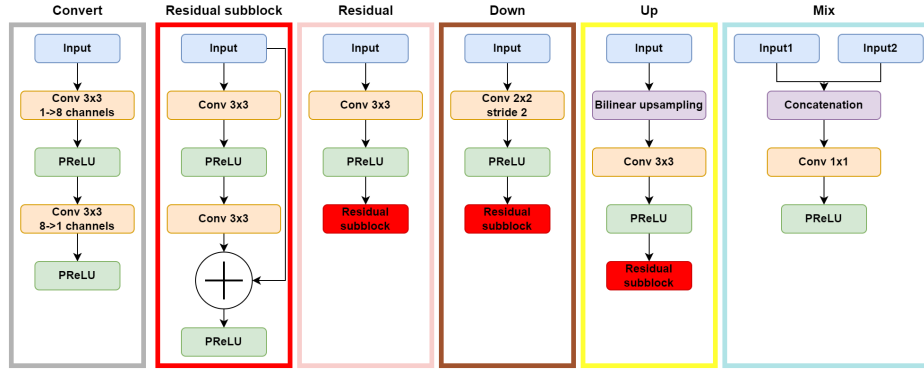
FIGURE 8.1: Building blocks used for the employed neural network (from left to right: spectrum convert (convert), residual subblock, residual (res), down, up, and mix).

from an initial size of 504×504 were zero padded to a size of 512×512. The training data set was augmented using the mixup method [210], which linearly combines two unrelated projections p_i and p_j with a certain weighting factor α sampled between 0 and 1 from a uniform distribution.

$$p_i^* = \alpha p_i + (1 - \alpha) p_j \tag{8.1}$$

This data augmentation, which is used with the intention to avoid overfitting, is applied similarly to the raw projections and the corrected projection.

Network architecture   This AI project made use of ScatterNet, which is a Unet architecture for CBCT projection correction previously introduced by Hansen et al. [136] and employed by Landry et al. [137]. Neppl et al. used the same architecture in an MRI setting [205]. Figure 8.1 displays the individual building blocks out of which the Unet itself, shown in figure 8.2, is built.

The employed network is based on the ansatz that a scatter-free projection can be expressed as

$$p_{\text{CBCT}_{\text{SN}}} = S(p_{\text{CBCT}_{\text{raw}}}) * (1 - K) \tag{8.2}$$

where $p_{\text{CBCT}_{\text{SN}}}$ are the projections after log transform, that are the output of the ScatterNet, S is a function that scatter corrects for the difference in spectrum between CT and CBCT, $p_{\text{CBCT}_{\text{raw}}}$ are the initially acquired CBCT projections after log transform, and K is a pseudo scatter kernel.

The function S is modelled as a CNN with a single hidden layer with 8 channels (cf. figure 8.1). This function is convolved with $(1 - K)$, which is modelled as a residual Unet [211]. The multiple resolution levels with 8, 16, 32, 64, 128, and 256 channels (=feature maps) model the low-frequency differences (cf. figure 8.2). Downsampling is achieved by a 2×2 convolution with a stride of 2. Upsampling is performed with bilinear upsampling. To avoid scaling of the scatter, batch normalisation, described by Zhang et al. [211], is not used. As an activation function, the parametric rectified linear unit (PReLU) is used [212]. Employing the Adam optimiser [213] the network was trained end to end with a batch size of 8 and the sum of squared differences as a loss function. The learning rate was set to $3 \cdot 10^{-4}$, $\beta_1 = 0.9$, $\beta_2 = 0.999$, and the weight_decay = 0. The network was implemented using the open-source machine learning framework PyTorch [214], developed by Meta AI (Meta Platforms, Menlo Park, California, USA).

Treatment planning   The corrected projections from the ScatterNet were reconstructed using MA-ROOSTER (cf. section 3.5) with the same settings and vector fields as in the
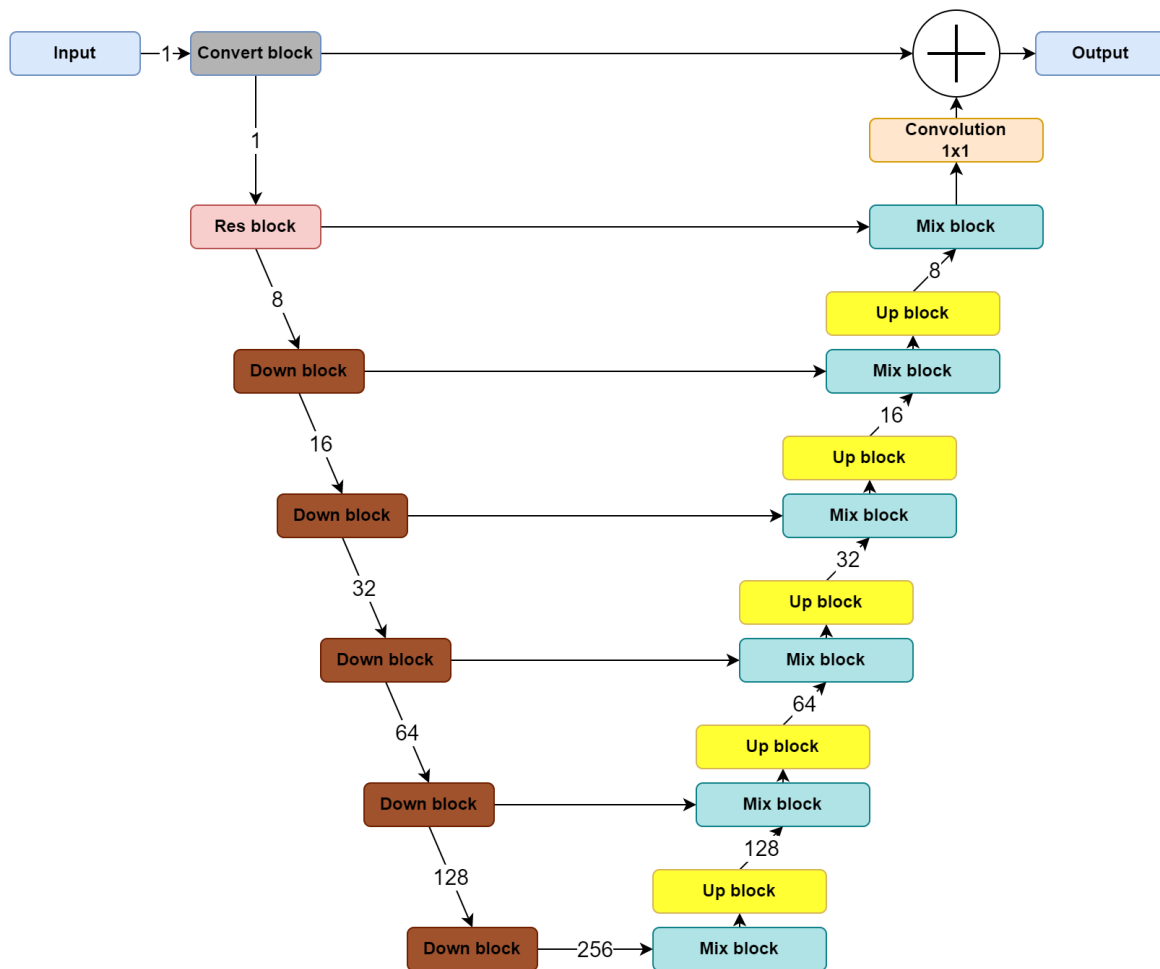
FIGURE 8.2: The full ScatterNet architecture showing the typical U-shape of a Unet. On every layer the number of channels are shown. The individual building blocks are displayed in figure 8.1.

$4DCBCT_{cor}$ case, yielding $4DCBCT_{SN}$. The pCT, 4DvCT, $4DCBCT_{cor}$, and $4DCBCT_{SN}$ were then transferred to the TPS. On each of the ten phases of 4DvCT, $4DCBCT_{cor}$, and $4DCBCT_{SN}$, the proton dose was recalculated. Recalculation used an IMPT plan on the free-breathing pCT, that administered 8 fractions of 7.5 Gy with a 3-field arrangement. This is identical to the treatment planning described in detail in section 7.3.1.

Computer hardware   The network was trained on the same computer, with two Intel Xeon Gold 6254 (Cascade Lake-EP) 18-Core CPU at 3.1 GHz, that was used for the scatter correction workflow. Hyper-threading was enabled, which resulted in a total of 72 threads. An Nvidia Quadro P6000 with 24 GB was used as GPU.

Data analysis   The initial data analysis was twofold. The image quality was quantitatively evaluated with a mean absolute error (MAE) and a mean error (ME) analysis. Only voxels inside the union of the CBCT FOV with the CT body outline were considered. The dose analysis was limited to qualitative dose difference plots between 4DvCT, $4DCBCT_{cor}$, and $4DCBCT_{SN}$ and a quantitative analysis using the DVH parameter ITV $D_{98\%}$.
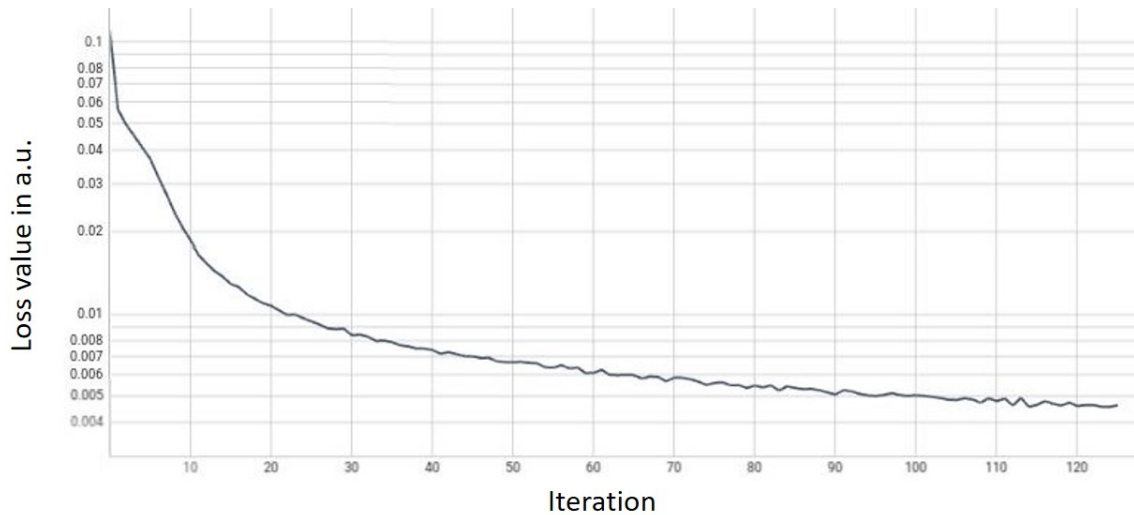
FIGURE 8.3: Training loss plotted versus the number of iterations.
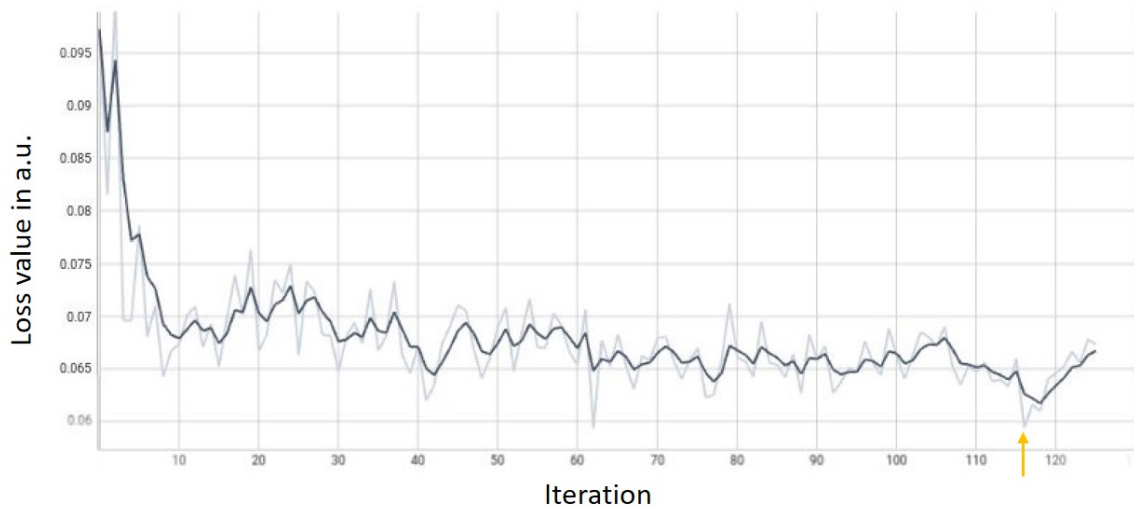
FIGURE 8.4: Validation loss plotted versus the number of iterations. For displaying purposes a smoothed curve is superimposed to a curve, shown with less opacity, connecting all real data values. The arrow indicates the iteration that was selected for the final model.

8.3 Results

Network training and timing Figure 8.3 shows the loss value in arbitrary units versus the number of iterations for the training and figure 8.4 for the validation cohort. The network was stopped after 126 iterations, as the validation loss did no longer improve. Iteration 115 was used for the final model. At iteration 115 the loss value is $4.692 \cdot 10^{-3}$ and the validation value is $5.938 \cdot 10^{-2}$. The network needed around 12 h to be trained. After training on average 3.9 s (on average 5.7 ms per projection slice) are needed for the network to correct an entire projection set (up to 732 projection slices).

Image quality analysis Figure 8.5 shows for patients 24 and 25 a fixed slice of the raw and scatter corrected projections, with the latter generated from the 4D correction workflow (cf. section 7.3), before zero padding. Additionally, the same slice of the projection generated
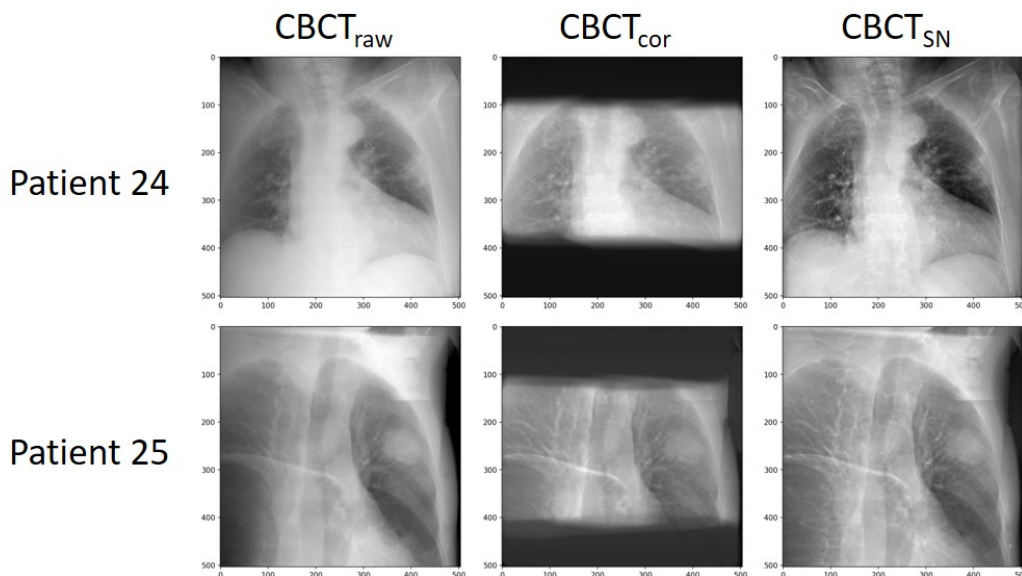
FIGURE 8.5: For patients 24 and 25 the measured projections (CBCT$_{raw}$) are shown on a fixed slice as the scatter corrected projections from the 4D scatter correction workflow (CBCT$_{cor}$) and from the ScatterNet (CBCT$_{SN}$) are shown.

by the trained ScatterNet is shown. The projections, generated by the ScatterNet show enhanced structures and less blurring compared to the measured projections. They are similar to the projections from the 4D correction workflow. The FOV of the projections generated by the 4D correction workflow is smaller (4DvCT is smaller than the initial 4DCBCT) than the FOV of the measured projections. The FOV of the projection, generated by the ScatterNet, has the same size as the measured projections.

Figure 8.6 and 8.7 show phase 5 (exhale) and phase 9 (inhale) in axial view for 4DCBCT$_{SN}$, 4DCBCT$_{cor}$, and 4DvCT of test patients 24 and 25. The 4DCBCT$_{SN}$ shows a similar image quality to the 4DCBCT$_{cor}$. Consequently, the 4DCBCT$_{SN}$ is improved over the initial 4DCBCT (cf. figures 7.10 and 7.15). The bottom rows display differences images. Differences between both scatter corrected 4DCBCT are minor for the target region. Larger differences can be observed in the lung region and for the chest wall. In general, the deviation for 4DCBCT$_{SN}$-4DvCT seems larger than for 4DCBCT$_{cor}$-4DvCT. The largest noticeable differences are observed in the stitching region for cases 4DCBCT$_{SN}$-4DvCT and 4DCBCT$_{cor}$-4DvCT. Neither of the scatter corrected 4DCBCT images was stitched.

Figure 8.8 shows in the top row a ME analysis for all testing patients for the comparisons 4DCBCT$_{SN}$-4DvCT, 4DCBCT$_{SN}$-4DCBCT$_{cor}$, and 4DCBCT$_{cor}$-4DvCT. For each of the patients, the data is averaged over the 10 breathing phases. The bottom row shows a MAE analysis for the same patients and comparisons. In both cases only voxels inside the union of the CBCT FOV with the CT body outline were considered. Average values for the comparisons over all testing patients are 22.7 HU, 3.9 HU, and 18.8 HU for ME and 102.3 HU, 86.7 HU, and 72.6 HU for MAE, respectively.

Proton dose distribution analysis Figure 8.9 shows proton dose differences of patient 24 for the comparisons 4DCBCT$_{cor}$-4DvCT, 4DCBCT$_{SN}$-4DvCT, and 4DCBCT$_{SN}$-4DCBCT$_{cor}$. For all comparisons, the two extremal breathing phases are displayed. Overall small deviations of a few percent are observed around the target structure. However, larger deviations are detected in the lung tissue when comparing 4DCBCT$_{SN}$ to either 4DvCT or 4DCBCT$_{cor}$.
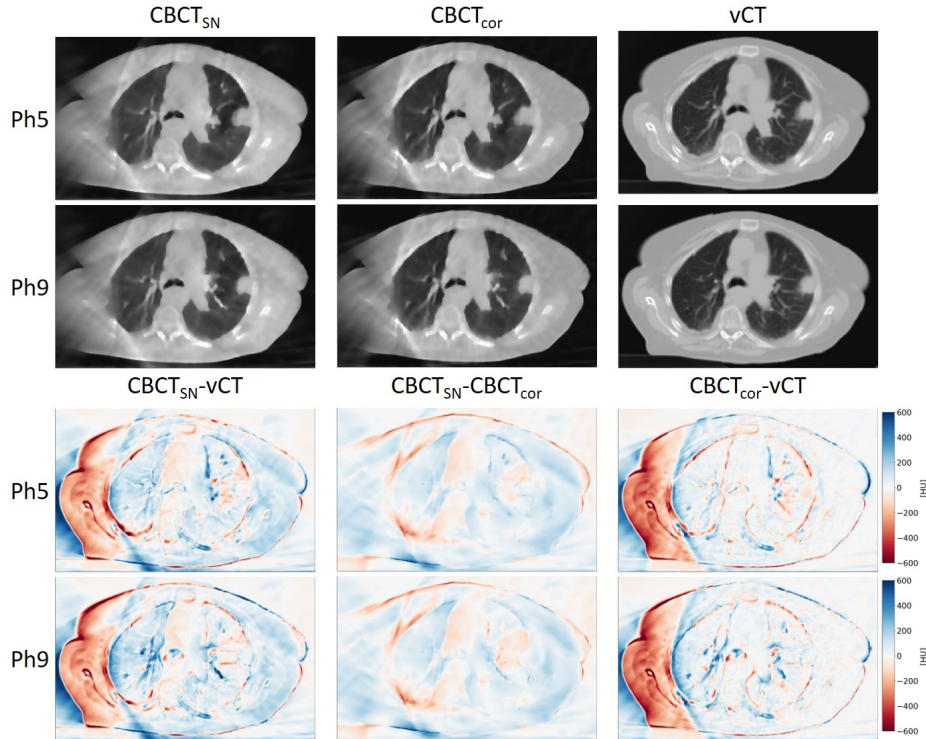
FIGURE 8.6: The top two rows show the extremal phases of the 4D images 4DCBCT$_{SN}$, 4DCBCT$_{cor}$, and 4DvCT displayed with level = -300 and window = 1600, for patient 24. The bottom two rows show difference images of 4DCBCT$_{SN}$-4DvCT, 4DCBCT$_{SN}$-4DCBCT$_{cor}$, and 4DCBCT$_{cor}$-4DvCT from the same patient. All images are shown in axial view.

Table 8.2 presents the ITV D$_{98\%}$ values for the 5 test patients. All values for 4DvCT, 4DCBCT$_{cor}$, and 4DCBCT$_{SN}$ are averaged over the ten breathing phases. Overall a high dose agreement for the different modalities in terms of ITV D$_{98\%}$ was observed. The largest median differences per patient were observed for patient 23 with 0.6 Gy, 0.7 Gy, and 1.3 Gy between 4DCBCT$_{cor}$-4DvCT, 4DCBCT$_{SN}$-vCT, and 4DCBCT$_{SN}$-4DCBCT$_{cor}$, respectively.

TABLE 8.2: ITV D$_{98\%}$ values averaged over ten breathing phases of 4DvCT, 4DCBCT$_{cor}$, and 4DCBCT$_{SN}$ in Gy for the five test patients.

	4DvCT	4DCBCT$_{cor}$	4DCBCT$_{SN}$
patient	median [min, max]	median [min, max]	median [min, max]
22	61.2 [60.2, 61.7]	60.8 [60.2, 61.2]	60.5 [60.2, 60.9]
23	64.7 [64.1, 65.3]	64.1 [62.7, 65.3]	63.4 [60.5, 66.5]
24	60.9 [60.5, 61.1]	60.7 [60.6, 61.1]	60.9 [60.7, 61.1]
25	60.9 [60.8, 61.0]	60.2 [59.8, 60.5]	60.7 [60.5, 60.8]
26	63.5 [63.1, 63.8]	63.8 [63.4, 64.4]	63.6 [63.2, 64.4]
median	62.2 [61.7, 62.6]	61.9 [61.3, 62.5]	61.8 [61.0, 62.7]

Table 8.3 presents the gamma PR for a 2%/2mm criterion of all test patients for the comparisons CBCT$_{SN}$-vCT, CBCT$_{SN}$-CBCT$_{cor}$, and CBCT$_{cor}$-vCT. The median for CBCT$_{SN}$-vCT and CBCT$_{SN}$-CBCT$_{cor}$ is substantially lower than for CBCT$_{cor}$-vCT.
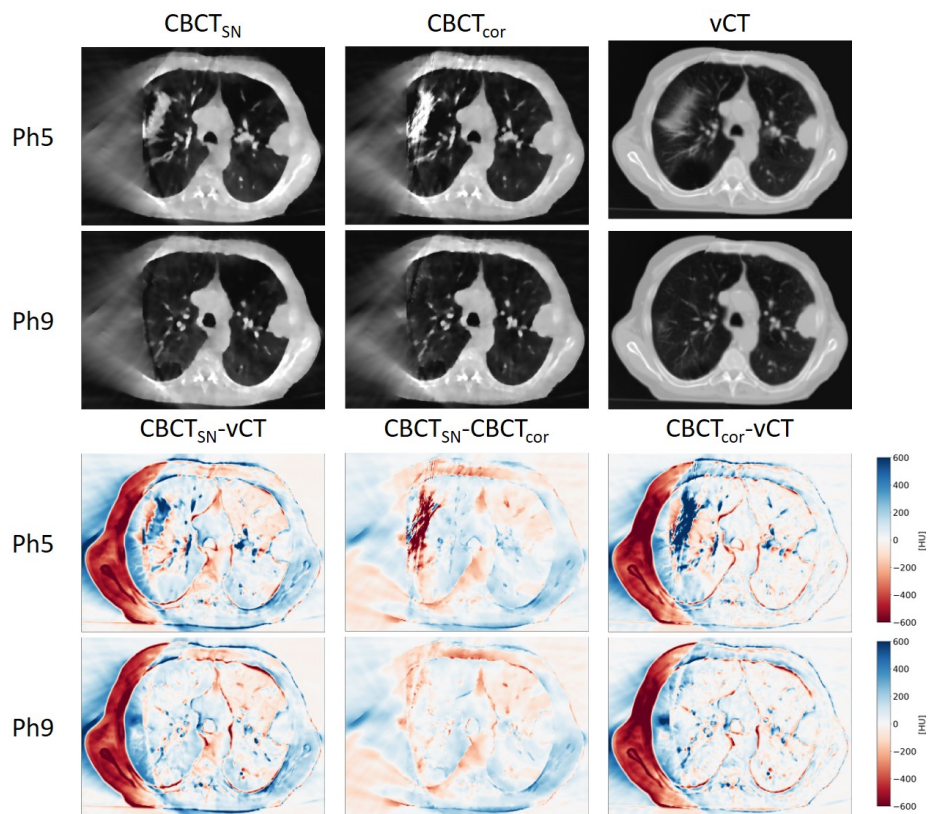
FIGURE 8.7: The top two rows show the extremal phases of the 4D images 4DCBCT$_{SN}$, 4DCBCT$_{cor}$, and 4DvCT displayed with level = -300 and window = 1600, for patient 25. The bottom two rows show difference images of 4DCBCT$_{SN}$-4DvCT, 4DCBCT$_{SN}$-4DCBCT$_{cor}$, and 4DCBCT$_{cor}$-4DvCT from the same patient. All images are shown in axial view.
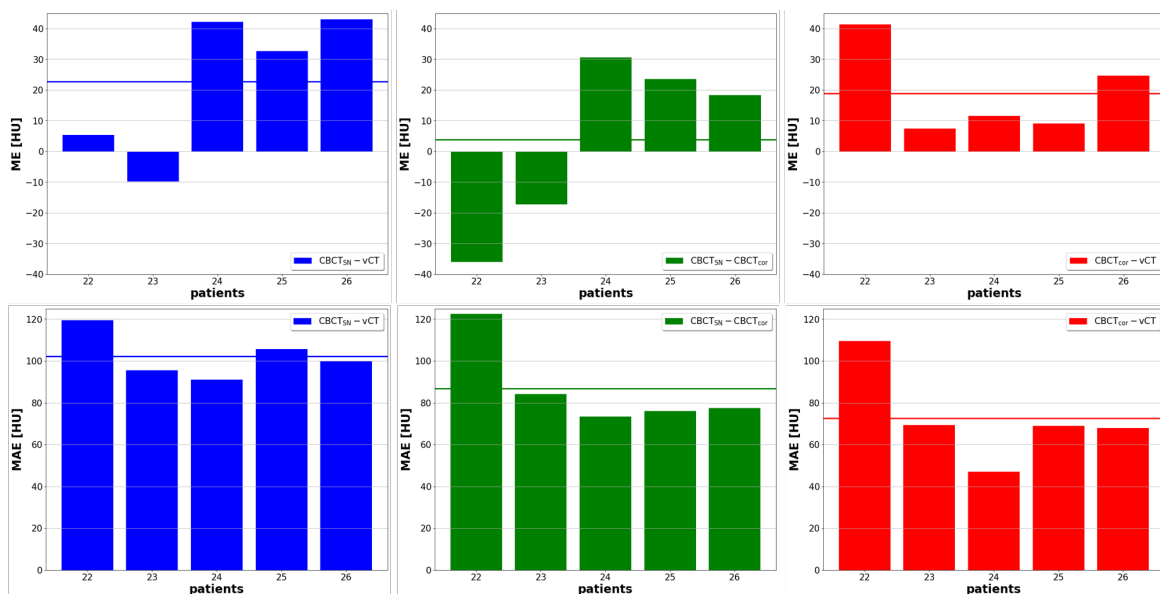
FIGURE 8.8: ME (top) and MAE (bottom) for all testing patients averaged over the 10 breathing phases are shown for the comparisons 4DCBCT$_{SN}$-4DvCT, 4DCBCT$_{SN}$-4DCBCT$_{cor}$, and 4DCBCT$_{cor}$-4DvCT. For each case, the mean value over all patients is shown with a horizontal line.
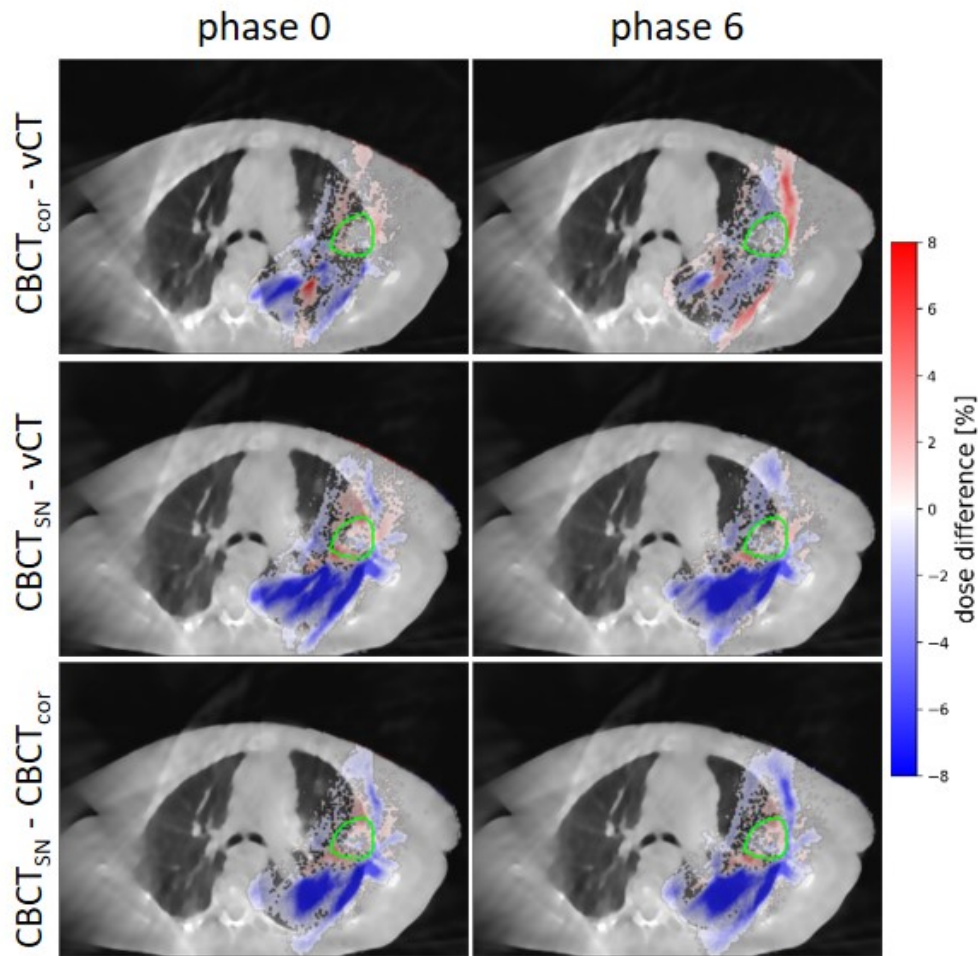
FIGURE 8.9: Deviations in percent of the prescribed dose of 60 Gy for the recalculated proton dose distribution of 4DvCT, 4DCBCT$_{cor}$, and 4DCBCT$_{SN}$ from patient 24. To improve the readability of the plot dose differences smaller than 0.4% are masked.

TABLE 8.3: On a single patient level, gamma-index PR in percent for a global criterion of 2%/2mm with a fixed dose threshold of 10% of the prescribed dose are shown. For the 10 breathing phases the median, minimum, and maximum values are shown.

	CBCT$_{SN}$-vCT	CBCT$_{SN}$-CBCT$_{cor}$	CBCT$_{cor}$-vCT
patient	median [min, max]	median [min, max]	median [min, max]
22	88 [87, 89]	90 [89, 92]	98 [97, 99]
23	85 [83, 87]	86 [85, 87]	99 [99, 99]
24	90 [87, 91]	91 [89, 92]	98 [96, 99]
25	92 [92, 93]	93 [93, 93]	98 [97, 98]
26	87 [81, 92]	85 [78, 89]	97 [96, 98]
median	88 [86, 90]	89 [87, 91]	98 [97, 99]

Computational time analysis   The computational time of the 4D scatter correction workflow (cf. section 7.3), which is not optimised, was roughly 4 h per patient. This can be broken down to more than 3.5 h needed for the 4DvCT generation with computational intensive image registrations, more than 10 min needed for the scatter correction (shown by the red box in figure 7.1) with computational intensive filtering operations, and more than 10 min needed for the final MA-ROOSTER reconstruction (cf. section 3.5) of the $4DCBCT_{cor}$. After the network is trained, which once takes a substantial amount of time (around 12 h for the ScatterNet) scatter correction is very fast as on average 5.7 ms are needed per projection slice, which results in an average conversion time for an entire projection set of 3.9 s.

8.4   Discussion

As previously demonstrated by Hansen et al. [136] and Landry et al. [137] the ScatterNet can be utilised for CBCT intensity correction. This contribution presented the first use of the ScatterNet with 4D lung patient data and an initial dosimetric evaluation of the resulting images.

The corrected projections, which are one part of the used paired data set, were obtained with the 4D scatter correction workflow (cf. section 7.1), which was previously phantom-validated [168].

The training loss value of the chosen iteration 115, being $4.692 \cdot 10^{-3}$, is similar to the value by Hansen et al. [136] and the value for Unet1 (projection-based) by Landry et al. [137]. Both did not report a specific value but judging from their plots their values should be around $5 \cdot 10^{-3}$. The validation loss value, being $5.938 \cdot 10^{-2}$, is almost twice as much compared to around $3.5 \cdot 10^{-2}$ (Hansen et al.) and around $2.15 \cdot 10^{-2}$ (Landry et al.). The latter two values are again read off the plots.

A substantial image improvement between initial 4DCBCT and $4DCBCT_{SN}$ can be observed. The image quality of the $4DCBCT_{SN}$ is comparable to the $4DCBCT_{cor}$. The ScatterNet seems to account for the same artefact corrections as the 4D scatter correction workflow.

The dose difference plots show a high agreement among the three investigated modalities 4DvCT, $4DCBCT_{cor}$, and $4DCBCT_{SN}$ in the target region. The $4DCBCT_{cor}$ and 4DvCT [168], similar to the same methods applied in 3D [125, 126], have been previously found sufficient for proton dose calculation. Nevertheless, larger dose differences can be observed in the lung tissue between $4DCBCT_{SN}$-4DvCT and $4DCBCT_{SN}$-$4DCBCT_{cor}$. These differences are less prominent within the comparison $4DCBCT_{cor}$-4DvCT. The quantitative gamma PR analysis supports this statement as values for $CBCT_{SN}$-vCT and $CBCT_{SN}$-$CBCT_{cor}$ are lower than for $CBCT_{cor}$-vCT. The origin of these differences needs to be further investigated.

An initial proof-of-principle, using the ScatterNet, has been demonstrated for a 4D lung data set. Further improvements could be achieved by testing different data augmentation methods. Those could be isolated or combining approaches of translational shifts, rotations, zooming, and intensity scaling. Regardless of the used augmentation, a larger patient data set, which could either mean adding more fractions per patient or adding more patients, could yield better results.

Similar to Landry et al. [137], the network could also be trained using reconstructed images to check whether an image- or projection-based approach yields superior results for lung patients. Additional testing could be done with data pairs that include simulated projections of the 4DvCT or the 4DvCT as an image.

Another interesting research direction is investigating potential performance differences between the presented 2D approach and 3D approaches like those published by Neppl et al. [205] and Thummerer et al. [143].

Independent of different method adaptations, a more thorough analysis is needed in all cases. This is the only way to improve confidence in the applied method in a meaningful manner.

For clinical implementation, not purely the performance, but also the stability of the method and its time consumption are dominant factors. Whereas stability needs to be investigated, a substantial reduction in computational time was observed. In comparison to the 4D scatter correction workflow, which was conducted on the same computer, scatter correction for all phases per patient decreased from more than 10 min to 3.9 s. This does not include the 4DCBCT reconstruction with MA-ROOSTER (cf. section 3.5), which is in itself with more than 10 min highly time-consuming. Thummerer et al., who also used MA-ROOSTER for reconstruction, reported an average of 45 min for their six-phase 4DCBCT reconstruction [143], which thus requires substantially more time than the method presented in this thesis. In the future, a combination of this ScatterNet approach and a reconstruction method based on AI could bring down the total time to clinically acceptable levels. Consequently, for daily clinical decisions such as the necessity of replanning the ScatterNet is a potentially interesting technique.

8.5 Conclusion

4DCBCT intensity correction is feasible for lung cancer patients using ScatterNet. Phase-dependent proton dose calculations showed comparable quality of network images to those of the non-deep learning 4D scatter correction workflow. The small and thus clinically acceptable computational time makes this CNN method potentially interesting for daily clinical decisions such as the necessity of treatment adaptation.

Chapter 9

Summary and Outlook

The timely availability of accurate daily 4D scatter corrected images based on in-room CBCT in a radiation therapy workflow can allow the detection of dosimetric changes caused by variations of the patient's breathing motion pattern and anatomy. This could be used to either reconstruct the daily applied dose or in the future even for online treatment adaptation, which then potentially leads to an improved treatment outcome. Providing daily up-to-date patient information is a clear advancement to the current standard of repeated CT imaging, which is mostly only conducted on a weekly basis and not in treatment position, as the majority of treatment rooms are not equipped with CT scanners. In-room CBCT images are in current clinical practice exclusively used for patient positioning. Their further utilisation would eliminate the issue of potential patient setup errors between CT and treatment and thus would not further increase the overall workload in an already tightly scheduled clinical workflow.

This thesis was focused on scatter corrected 4DCBCT images, allowing for accurate proton dose calculation, which accounts for interfractional changes. Such quality improved 4DCBCT images can be used to trigger daily treatment adaptations. These adaptations lead to a more accurate and precise treatment delivery of conformal proton dose distributions for lung cancer patients. Regardless of these advantages, which improve the treatment through an increased dose sparing in OARs combined with a fully covered target, daily scatter corrected 4DCBCTs can never be used in radiation therapy centres, if their generation is not achieved in a clinically acceptable time. Consequently, within the scope of this thesis three research projects, that build on one another, ranging from an experimental porcine lung phantom-based proof-of-concept study, over a computational retrospective lung cancer patient study to a deep learning study to speed up the 4D scatter correction workflow, were conducted.

Section 7.2 presented a proof-of-concept study that showed the feasibility to perform phase dependent proton dose calculation on scatter corrected 4DCBCT images. Comparing the generated up-to-date in-room images, which account for breathing pattern changes, to a ground truth 4DCT was used to evaluate the method.

Niepel et al. [133] and Bondesson et al. [134] already showed that proton dose calculation is possible on 4DvCTs. They reported similar gamma PR values for their 4DvCT to the 4DvCT and 4DCBCT$_{cor}$ described in this thesis [168]. Consequently, using 4DCBCT$_{cor}$ images for proton dose calculation could be a valuable technique to improve radiotherapeutical treatments.

Large anatomical changes cannot be modelled with our phantom. Consequently, a potential higher geometric fidelity of the 4DCBCT$_{cor}$ over the 4DvCT, as shown in a 3D case by Kurz et al. [126], could not be investigated. In this study setup, the need of generating a 4DCBT$_{cor}$, while already having a 4DvCT, could thus not be quantitatively demonstrated, since dose results between 4DCBT$_{cor}$ and 4DvCT did not differ substantially. Furthermore, the origin of the blurring within the 4DvCT (cf. figure 7.10), which potentially is either due

to inaccuracies of the DIR or a result of the resampling steps, performed due to computational reasons before the registration, cannot be answered in this study setup.

A successful implementation of a novel 4DCBCT$_{cor}$ workflow on a porcine lung phantom, which generated daily images that can be used for proton dose calculation, was shown in the first part of the thesis. This method could be of clinical interest and thus needed to be validated with a clinical lung cancer patient data set.

While the first proof-of-concept study focused on the general feasibility of the method, the topic of the second project was the application of the same method on clinical patient data. Section 7.3 could show that the generation of daily 4DvCT and 4DCBCT$_{cor}$ images for phase dependent proton dose calculation was achievable. Dose distribution results showed a good agreement between 4DvCT and 4DCBCT$_{cor}$. These daily updated images could potentially be used as an indicator for the necessity of treatment adaptation for lung cancer patients.

For the first time, a 4DCBCT$_{cor}$ was generated using a 4DvCT as prior. The anticipated higher geometrical fidelity of the 4DCBCT$_{cor}$ to the 4DvCT, as reported by Kurz et al. for a 3D case [126], could be observed for the tumour outline and ribs (cf. figure 7.15). Gamma PR values are comparable to 3DCBCT lung studies by Park et al. [125], who used the Niu method (cf. section 3.9) and Thing et al. [198], who used multiple correction steps, including MC calculations to simulated scatter, which was then subtracted to correct the images. Madesta et al. showed a promising AI method to improve 4DCBCT reconstructed images [141], which mainly focuses on the reduction of streak artefacts, caused by undersampling and not on artefacts, originating from motion. Comparing the approach presented in this thesis with and without the possible improvement due to an implementation of the Madesta et al. method could be an interesting research direction for further refinement of the method.

An intrinsic limitation of many patient studies is the lack of ground truth data and thus only a previous thorough phantom-based investigation, conducted in this case with the porcine lung phantom [168], can truly evaluate the quality of the workflow. Furthermore, volume changes in the lung, such as pleural effusion, which did not occur within the used patient cohort, could potentially lead to wrong deformations. Additional patients, having these volume changes, need to be investigated.

A successful application of the 4D scatter correction workflow on patient data generated intensity-corrected in-room images, which account for breathing pattern and anatomical changes. Those images could potentially be used for decision making on treatment adaptations, which makes them clinically valuable. Nevertheless, long computational runtimes of the workflow make the method currently inadequate for clinical use. Consequently, a speedup of the method, which could possibly be achieved using AI methods is diserable.

The AI study presented in chapter 8 demonstrated the feasibility of using the ScatterNet architecture for a 4D lung patient data set. The used paired data consisted of raw and corrected CBCT projections, with the latter ones generated within the 4D scatter correction workflow (cf. section 7.3). The image quality of the 4DCBCT$_{SN}$ was comparable to the 4DCBCT$_{cor}$. The needed time for scatter correction was reduced from over 10 min, which was needed for the 4D scatter correction workflow, to an average of 3.9 s. This leads to a method, generating fast updated daily images, which is thus potentially applicable in a clinical setting.

Thummerer et al. presented a network, which is based on a Unet, containing three separate networks training axial, coronal, and sagittal slices individually, by Spadea et al. [209], to generate corrected 4DCBCT images [143]. For training they use pairs of 4DCBCT and 4DCT images. Similar to the method presented in this thesis, their method relies on MA-ROOSTER (cf. section 3.5) as a 4DCBCT reconstruction technique. In the future, both methods could be compared in terms of performance and computational time among each other.

A limitation of the presented AI study is the data set with a modest number of patients and fractions (26 patients, 17,564 2D images). A larger number of patients or fractions could lead to an improved outcome. Another way, which could lead to better results, is trying out further data augmentation methods. The most time-consuming part of the presented method are slow 4DCBCT reconstructions, using MA-ROOSTER. In the future deep learning might also tackle the speed-up of reconstruction methods.

A fast runtime makes clinical use of this ScatterNet method possible. A more thorough proton dose analysis, exceeding our initial analysis, is however necessary to evaluate the quality of the method. A refined data augmentation approach as well as a larger data set could lead to improved performance. Besides computational time and performance, the stability of the method is important for clinical implementation. This needs to be further investigated.

Proton therapy for moving lung tumours is an active research field. Among many interesting directions, into which the field might evolve, only a few are outlined here. The selected topics, which are briefly presented here, have a clinical perspective by focusing on an immediate clinical implementation, a CBCT-based aspect by showing the development in this field, and they glance at the distant future.

From a clinical perspective research methods often seem abstract and distant until they are in actual use. The photon therapy platform HyperSight from Varian [1] (Varian Medical Systems a subsidiary of Siemens Healthineers, Erlangen, Germany) promises to substantially improve CBCT acquisition and its immediate post-processing. The vendor advertises improved image quality, which is suitable for dose calculation, in combination with reduced acquisition times of no more than 6 s for all anatomical sites. These exciting claims are only possible due to among others incorporation of CBCT scatter correction methods. Research progress, which happened over many years in the field of CBCT imaging, laid the groundwork.

The evolution of post-processing CBCT images or projections ranges from analytical over DIR to AI methods. Analytical methods, which are the most elegant and frankly from a perspective of a scientist most satisfying, are however incapable of accounting for the multitude of different aspects in complicated motions such as lung motion. Consequently, in a comparison of analytical, DIR, and AI corrected CBCT images the analytical approach performed the poorest [139]. Methods based on DIR show good performance, however, are computationally expensive (cf. section 7.3). AI methods seem to hit the optimal spot between performance and runtime. In the near future, AI methods, which combine 4DCBCT scatter correction and 4DCBCT reconstruction could be one of the most investigated research topics within CBCT imaging. Independent of the chosen method, further improvements in CBCT acquisition, through e.g. better detectors, will be beneficial for all CBCT techniques.

In the far distant future, a different technology could supersede the use of CBCT imaging in the field of PT for moving lung tumours. Combining PT with magnetic resonance imaging (MRI) [215], having superior soft tissue contrast and the capability of real-time tumour imaging, which allows for tracking during irradiation, could become the dominant method. However, this remains a topic of the future as the intrinsic incompatibility of MRI and PT leads to multiple problems for hitherto purely research devices [216], which have to be mastered first.

---

[1] `https://www.varian.com/products/radiotherapy/treatment-delivery/hypersight`
`accessed:18-12-2022`

In conclusion, the feasibility of proton dose calculation on a novel 4DCBCT scatter corrected image, generated in a workflow, which uses a 4DvCT as prior, was experimentally shown in a porcine lung phantom study and extended to a lung cancer patient data set. The successful speedup of this correction method with the use of AI as presented in this thesis marks another important step towards a potential clinical implementation, which could be beneficial for the treatment of moving lung tumours in the future.

Bibliography

[1] Hannah Ritchie and Max Roser. "Causes of Death". *Our World in Data* (2018). https://ourworldindata.org/causes-of-death.

[2] Hyuna Sung et al. "Global Cancer Statistics 2020: GLOBOCAN Estimates of Incidence and Mortality Worldwide for 36 Cancers in 185 Countries". *CA: A Cancer Journal for Clinicians* 71.3 (2021), pp. 209–249. DOI: 10.3322/caac.21660.

[3] Mensah G.A. et al. "Decline in Cardiovascular Mortality: Possible Causes and Implications". *Circulation Research* 120 (2017). DOI: 10.1161/CIRCRESAHA.116.309115.

[4] Thomas Gredner et al. "Cancers due to infection and selected environmental factors". *Deutsches Aerzteblatt Online* (Sept. 2018). ISSN: 1866-0452. DOI: 10.3238/arztebl.2018.0586. URL: http://doi.org/10.3238/arztebl.2018.0586.

[5] Z.R. Chalmers et al. "Analysis of 100,000 human cancer genomes reveals the landscape of tumor mutational burden". *Genome Medicine* 9 (2017). DOI: 10.1186/s13073-017-0424-2.

[6] *Website US National Cancer Institute.* https://www.cancer.gov/about-cancer/understanding/what-is-cancer. Accessed: 10th March 2022.

[7] S Donnelly and D Walsh. "The symptoms of advanced cancer". *Seminars in oncology* 22.2 Suppl 3 (Apr. 1995), 67—72. ISSN: 0093-7754. URL: http://europepmc.org/abstract/MED/7537907.

[8] Karl R. Aigner and Frederick O. Stephens, eds. *Onkologie Basiswissen.* Springer Berlin Heidelberg, 2016. DOI: 10.1007/978-3-662-48585-9. URL: https://doi.org/10.1007/978-3-662-48585-9.

[9] Dorothy Abshire and Matthew K. Lang. "The Evolution of Radiation Therapy in Treating Cancer". *Seminars in Oncology Nursing* 34.2 (May 2018), pp. 151–157. DOI: 10.1016/j.soncn.2018.03.006. URL: https://doi.org/10.1016/j.soncn.2018.03.006.

[10] Michael Baumann et al. "Radiation oncology in the era of precision medicine". *Nature Reviews Cancer* 16.4 (Mar. 2016), pp. 234–249. DOI: 10.1038/nrc.2016.18. URL: https://doi.org/10.1038/nrc.2016.18.

[11] Stephen G. Chun et al. "Impact of Intensity-Modulated Radiation Therapy Technique for Locally Advanced Non–Small-Cell Lung Cancer: A Secondary Analysis of the NRG Oncology RTOG 0617 Randomized Clinical Trial". *Journal of Clinical Oncology* 35.1 (2017). PMID: 28034064, pp. 56–62. DOI: 10.1200/JCO.2016.69.1378. eprint: https://doi.org/10.1200/JCO.2016.69.1378. URL: https://doi.org/10.1200/JCO.2016.69.1378.

[12] L. Moonen and H. Bartelink. "Fractionation in radiotherapy". *Cancer Treatment Reviews* 20.4 (Oct. 1994), pp. 365–378. DOI: 10.1016/0305-7372(94)90018-3. URL: https://doi.org/10.1016/0305-7372(94)90018-3.

[13] H Bethe. "Zur Theorie des Durchgangs schneller Korpuskularstrahlen durch Materie". *Ann Phys Leipzig* 5 (1930), p. 325.

[14] William H. Bragg and William L. Bragg. "The reflection of X-rays by crystals". *Proceedings of the Royal Society of London. Series A, Containing Papers of a Mathematical and Physical Character* 88.605 (July 1913), pp. 428–438. DOI: 10.1098/rspa.1913.0040. URL: https://doi.org/10.1098/rspa.1913.0040.

[15] Robert R. Wilson. "Radiological Use of Fast Protons". *Radiology* 47.5 (Nov. 1946), pp. 487–491. DOI: 10.1148/47.5.487. URL: https://doi.org/10.1148/47.5.487.

[16] Tobias C.A., Anger H.O., and Lawrence J.H. "Radiological use of high energy deuterons and alpha particles". *Am J Roentgenol Radium Ther Nucl Med.* 67.1 (Jan. 1952), pp. 1–27.

[17] Cornelius A Tobias et al. "Irradiation hypophysectomy and related studies using 340-MeV protons and 190-MeV deuterons" (1955).

[18] Paul J. Keall et al. "The management of respiratory motion in radiation oncology report of AAPM Task Group 76a)". *Medical Physics* 33.10 (Sept. 2006), pp. 3874–3900. DOI: 10.1118/1.2349696. URL: https://doi.org/10.1118/1.2349696.

[19] Pierre Blanchard et al. "Proton Therapy for Head and Neck Cancers". *Seminars in Radiation Oncology* 28.1 (Jan. 2018), pp. 53–63. DOI: 10.1016/j.semradonc.2017.08.004. URL: https://doi.org/10.1016/j.semradonc.2017.08.004.

[20] A. J. Lomax et al. "Intensity modulated proton therapy: A clinical example". *Medical Physics* 28.3 (Mar. 2001), pp. 317–324. DOI: 10.1118/1.1350587. URL: https://doi.org/10.1118/1.1350587.

[21] Antony J Lomax et al. "The Clinical Potential of Intensity Modulated Proton Therapy". *Zeitschrift für Medizinische Physik* 14.3 (2004), pp. 147–152. DOI: 10.1078/0939-3889-00217. URL: https://doi.org/10.1078/0939-3889-00217.

[22] H M Kooy and C Grassberger. "Intensity modulated proton therapy". *The British Journal of Radiology* 88.1051 (July 2015), p. 20150195. DOI: 10.1259/bjr.20150195. URL: https://doi.org/10.1259/bjr.20150195.

[23] Antje-Christin Knopf and Antony Lomax. "In vivoproton range verification: a review". *Physics in Medicine and Biology* 58.15 (July 2013), R131–R160. DOI: 10.1088/0031-9155/58/15/r131. URL: https://doi.org/10.1088/0031-9155/58/15/r131.

[24] Guillaume Landry and Chia ho Hua. "Current state and future applications of radiological image guidance for particle therapy". *Medical Physics* 45.11 (Nov. 2018). DOI: 10.1002/mp.12744. URL: https://doi.org/10.1002/mp.12744.

[25] Jeffrey H. Siewerdsen and David A. Jaffray. "Cone-beam computed tomography with a flat-panel imager: Magnitude and effects of x-ray scatter". *Medical Physics* 28.2 (Feb. 2001), pp. 220–231. DOI: 10.1118/1.1339879. URL: https://doi.org/10.1118/1.1339879.

[26] J. H. Siewerdsen and D. A. Jaffray. "A ghost story: Spatio-temporal response characteristics of an indirect-detection flat-panel imager". *Medical Physics* 26.8 (Aug. 1999), pp. 1624–1641. DOI: 10.1118/1.598657. URL: https://doi.org/10.1118/1.598657.

[27] Rune Slot Thing et al. "Hounsfield unit recovery in clinical cone beam CT images of the thorax acquired for image guided radiation therapy". *Physics in Medicine & Biology* 61.15 (July 2016), pp. 5781–5802. DOI: 10.1088/0031-9155/61/15/5781. URL: https://doi.org/10.1088/0031-9155/61/15/5781.

[28] G Poludniowski et al. "Removal and effects of scatter-glare in cone-beam CT with an amorphous-silicon flat-panel detector". *Physics in Medicine & Biology* 56.6 (Feb. 2011), pp. 1837–1851. DOI: 10.1088/0031-9155/56/6/019. URL: https://doi.org/10.1088/0031-9155/56/6/019.

[29] Landry et al. "Investigating CT to CBCT image registration for head and neck proton therapy as a tool for daily dose recalculation". *Medical Physics* 42.3 (Feb. 2015), pp. 1354–1366. DOI: 10.1118/1.4908223. URL: https://doi.org/10.1118/1.4908223.

[30] Christopher Kurz et al. "Comparing cone-beam CT intensity correction methods for dose recalculation in adaptive intensity-modulated photon and proton therapy for head and neck cancer". *Acta Oncologica* 54.9 (July 2015), pp. 1651–1657. DOI: 10.3109/0284186x.2015.1061206. URL: https://doi.org/10.3109/0284186x.2015.1061206.

[31] Max Planck. "AUS DEN VERHANDLUNGEN DER DEUTSCHEN PHYSIKALISCHEN GESELLSCHAFT (1900) S. 237: Zur Theorie des Gesetzes der Energieverteilung im Normalspectrum". *Physik Journal* 4.4 (Apr. 1948), pp. 146–151. DOI: 10.1002/phbl.19480040404. URL: https://doi.org/10.1002/phbl.19480040404.

[32] Albert Einstein. "Über einen die Erzeugung und Verwandlung des Lichtes betreffenden heuristischen Gesichtspunkt". *Annalen der Physik* 322.6 (1905), pp. 132–148. DOI: 10.1002/andp.19053220607.

[33] Frank H. Attix. "Ionizing Radiation". *Introduction to Radiological Physics and Radiation Dosimetry*. John Wiley & Sons, Ltd, 1986. DOI: 10.1002/9783527617135.ch1.

[34] John H. Hubbell. "Photon Cross Sections, Attenuation Coefficients, and Energy Absorption Coefficients from 10 keV to 100 GeV". *National Bureau of Standards Report NSRDS-NBS29, Washington DC* (1969).

[35] Thorsten M. Buzug. *Computed Tomography: From Photon Statistics to Modern Cone-Beam CT*. Springer-Verlag Berlin Heidelberg, 2008. DOI: 10.1007/978-3-540-39408-2.

[36] Martin J. Berger et al. "XCOM: Photon Cross Section Database". *NIST Standard Reference Database 8 (XGAM)* (2010). Accessed: 21st August 2022. DOI: 10.18434/T48G6X.

[37] Arthur H. Compton. "A Quantum Theory of the Scattering of X-rays by Light Elements". *Physical Review* 21.5 (1923), pp. 483–502. DOI: 10.1103/PhysRev.21.483.

[38] Wolfgang Schlegel, Christian P. Karger, and Oliver Jäkel. *Medizinische Physik: Grundlagen – Bildgebung – Therapie – Technik*. Springer Spektrum, 2018. DOI: 10.1007/978-3-662-54801-1.

[39] Oskar Klein and Yoshio Nishina. "Über die Streuung von Strahlung durch freie Elektronen nach der neuen relativistischen Quantendynamik von Dirac". *Zeitschrift für Physik* 52.11-12 (1929), pp. 853–868. DOI: 10.1007/BF01366453.

[40] Patrick M. S. Blackett and Giuseppe P. S. Occhialini. "Some photographs of the tracks of penetrating radiation". *Proceedings of the Royal Society of London. Series A* 139.839 (1933), pp. 699–726. DOI: 10.1098/rspa.1933.0048.

[41] J.J. Thomson. "XXIV. On the structure of the atom: an investigation of the stability and periods of oscillation of a number of corpuscles arranged at equal intervals around the circumference of a circle; with application of the results to the theory of atomic structure". *The London, Edinburgh, and Dublin Philosophical Magazine and Journal of Science* 7.39 (Mar. 1904), pp. 237–265. DOI: 10.1080/14786440409463107. URL: https://doi.org/10.1080/14786440409463107.

[42] "The Cardiff Meeting of the British Association". *Nature* 105.2651 (Aug. 1920), pp. 780–781. DOI: 10.1038/105780a0. URL: https://doi.org/10.1038/105780a0.

[43] Borut Bajc et al. "Threshold Corrections to Dimension-six Proton Decay Operators in Non-minimal SUSY SU(5) GUTs" (2016). DOI: 10.48550/ARXIV.1603.03568. URL: https://arxiv.org/abs/1603.03568.

[44] Planck Collaboration et al. "Planck 2018 results. VI. Cosmological parameters" (2018). DOI: 10.48550/ARXIV.1807.06209. URL: https://arxiv.org/abs/1807.06209.

[45] Sandra Nuyts et al. "Proton Therapy for Squamous Cell Carcinoma of the Head and Neck: Early Clinical Experience and Current Challenges". *Cancers* 14.11 (May 2022), p. 2587. DOI: 10.3390/cancers14112587. URL: https://doi.org/10.3390/cancers14112587.

[46] Antony J. Lomax. "Charged Particle Therapy: The Physics of Interaction". *The Cancer Journal* 15.4 (July 2009), pp. 285–291. DOI: 10.1097/ppo.0b013e3181af5cc7. URL: https://doi.org/10.1097/ppo.0b013e3181af5cc7.

[47] Marco Durante and Harald Paganetti. "Nuclear physics in particle therapy: a review". *Reports on Progress in Physics* 79.9 (Aug. 2016), p. 096702. DOI: 10.1088/0034-4885/79/9/096702. URL: https://doi.org/10.1088/0034-4885/79/9/096702.

[48] Wayne D Newhauser and Rui Zhang. "The physics of proton therapy". *Physics in Medicine and Biology* 60.8 (Mar. 2015), R155–R209. DOI: 10.1088/0031-9155/60/8/r155. URL: https://doi.org/10.1088/0031-9155/60/8/r155.

[49] Harald Paganetti. *Proton Therapy Physics*. CRC Press, 2018. DOI: 10.1201/b22053.

[50] N. Bohr Dr. Phil. "LX. On the decrease of velocity of swiftly moving electrified particles in passing through matter". *The London, Edinburgh, and Dublin Philosophical Magazine and Journal of Science* 30.178 (1915), pp. 581–612. DOI: 10.1080/14786441008635432. eprint: https://doi.org/10.1080/14786441008635432. URL: https://doi.org/10.1080/14786441008635432.

[51] F. Bloch. "Zur Bremsung rasch bewegter Teilchen beim Durchgang durch Materie". *Annalen der Physik* 408.3 (Jan. 1933), pp. 285–320. DOI: 10.1002/andp.19334080303.

[52] S. Agostinelli et al. "Geant4—a simulation toolkit". *Nuclear Instruments and Methods in Physics Research Section A: Accelerators, Spectrometers, Detectors and Associated Equipment* 506.3 (2003), pp. 250–303. ISSN: 0168-9002. DOI: https://doi.org/10.1016/S0168-9002(03)01368-8. URL: https://www.sciencedirect.com/science/article/pii/S0168900203013688.

[53] Pierluigi Piersimoni et al. "Optimization of a general-purpose, actively scanned proton beamline for ocular treatments: Geant4 simulations". *Journal of applied clinical medical physics / American College of Medical Physics* 16 (June 2015), p. 5227. DOI: 10.1120/jacmp.v16i2.5227.

[54] Tatsuaki Kanai et al. "Spot scanning system for proton radiotherapy". *Medical Physics* 7.4 (July 1980), pp. 365–369. DOI: 10.1118/1.594693. URL: https://doi.org/10.1118/1.594693.

[55] Albertini, Francesca. "Planning and optimizing treatment plans for actively scanned proton therapy: evaluating and estimating the effect of uncertainties". en. PhD thesis. 2011. DOI: 10.3929/ETHZ-A-006576001. URL: http://hdl.handle.net/20.500.11850/152818.

[56] Ernest O. Lawrence and M. Stanley Livingston. "The Production of High Speed Light Ions Without the Use of High Voltages". *Phys. Rev.* 40 (1 Apr. 1932), pp. 19–35. DOI: 10.1103/PhysRev.40.19. URL: https://link.aps.org/doi/10.1103/PhysRev.40.19.

[57] Udo Weinrich. "Gantry Design for Proton and Carbon Hadrontherapy Facilities" (2006), 5 p. URL: https://cds.cern.ch/record/1078592.

[58] V. Grégoire and T.R. Mackie. "State of the art on dose prescription, reporting and recording in Intensity-Modulated Radiation Therapy (ICRU report No. 83)". *Cancer/Radiothérapie* 15.6-7 (Oct. 2011), pp. 555–559. DOI: 10.1016/j.canrad.2011.04.003. URL: https://doi.org/10.1016/j.canrad.2011.04.003.

[59] Shalini K. Vinod et al. "Uncertainties in volume delineation in radiation oncology: A systematic review and recommendations for future studies". *Radiotherapy and Oncology* 121.2 (2016), pp. 169–179. ISSN: 0167-8140. DOI: https://doi.org/10.1016/j.radonc.2016.09.009. URL: https://www.sciencedirect.com/science/article/pii/S0167814016343316.

[60] Harald Paganetti et al. "Relative biological effectiveness (RBE) values for proton beam therapy". *International Journal of Radiation Oncology, Biology, Physics* 53.2 (June 2002), pp. 407–421. DOI: 10.1016/s0360-3016(02)02754-2. URL: https://doi.org/10.1016/s0360-3016(02)02754-2.

[61] M. Scholz W. K. Weyrather S. Ritter. "RBE for carbon track-segment irradiation in cell lines of differing repair capacity". *International Journal of Radiation Biology* 75.11 (Jan. 1999), pp. 1357–1364. DOI: 10.1080/095530099139232. URL: https://doi.org/10.1080/095530099139232.

[62] Albin Fredriksson, Anders Forsgren, and Björn Hårdemark. "Minimax optimization for handling range and setup uncertainties in proton therapy". *Medical Physics* 38.3 (Mar. 2011), pp. 1672–1684. DOI: 10.1118/1.3556559. URL: https://doi.org/10.1118/1.3556559.

[63] Arturs Meijers et al. "Evaluation of interplay and organ motion effects by means of 4D dose reconstruction and accumulation". *Radiotherapy and Oncology* 150 (Sept. 2020b), pp. 268–274. DOI: 10.1016/j.radonc.2020.07.055. URL: https://doi.org/10.1016/j.radonc.2020.07.055.

[64] Ervin B. Podgoršak. *Radiation Oncology Physics*. International Atomic Energy Agency, 2005. URL: https://www.iaea.org/publications/7086/radiation-oncology-physics.

[65] International Commission on Radiation Units and Measurements. "ICRU Report 83: Prescribing, recording, and reporting photon-beam intensity-modulated radiation therapy (IMRT)". *Journal of the International Commission on Radiation Units and Measurements* 10.1 (2010), pp. 1–112. URL: https://www.icru.org/report/prescribing-recording-and-reporting-intensity-modulated-photon-beam-therapy-imrticru-report-83/.

[66] Wilhelm C. Röntgen. "Über eine neue Art von Strahlen". *Sitzungsberichte der Physikalisch-Medicinischen Gesellschaft zu Würzburg* 137 (1895), pp. 132–141.

[67] Frikkie C De Beer. "Neutron and X-Ray tomography as research tools for applied research in South Africa". en (2018). DOI: 10.13140/RG.2.2.22287.89765. URL: http://rgdoi.net/10.13140/RG.2.2.22287.89765.

[68] Jerrold T. Bushberg et al. *The Essential Physics of Medical Imaging*. Lippincott Williams & Wilkins, 2012.

[69] Philip J. Withers et al. "X-ray computed tomography". *Nature Reviews Methods Primers* 1.1 (Feb. 2021). DOI: 10.1038/s43586-021-00015-4. URL: https://doi.org/10.1038/s43586-021-00015-4.

[70] Geoffrey D. Rubin. "Computed Tomography: Revolutionizing the Practice of Medicine for 40 Years". *Radiology* 273.2S (Nov. 2014), S45–S74. DOI: 10.1148/radiol.14141356. URL: https://doi.org/10.1148/radiol.14141356.

[71] Godfrey N. Hounsfield. "Computerized transverse axial scanning (tomography): Part 1. Description of system". *The British Journal of Radiology* 46.552 (1973), pp. 1016–1022. DOI: 10.1259/0007-1285-46-552-1016.

[72] MAREK Danczak and KLAUS Juergen-Wolter. "Cone-beam computer tomography as a new testing method for industrial application". *27th International Spring Seminar on Electronics Technology: Meeting the Challenges of Electronics Technology Progress, 2004.* Vol. 1. IEEE. 2004, pp. 105–109.

[73] Lee A. Feldkamp, Lloyd C. Davis, and James W. Kress. "Practical cone-beam algorithm". *Journal of the Optical Society of America A* 1.6 (1984), pp. 612–619. DOI: 10.1364/JOSAA.1.000612.

[74] Kavitha Srinivasan, Mohammad Mohammadi, and Justin Shepherd. "Applications of linac-mounted kilovoltage Cone-beam Computed Tomography in modern radiation therapy: A review". *Polish Journal of Radiology* 79 (2014), pp. 181–193. DOI: 10.12659/PJR.890745.

[75] David A. Jaffray et al. "Flat-panel cone-beam computed tomography for image-guided radiation therapy". *International Journal of Radiation Oncology, Biology, Physics* 53.5 (2002), pp. 1337–1349. DOI: 10.1016/S0360-3016(02)02884-5.

[76] Nima Nabavizadeh et al. "Image Guided Radiation Therapy (IGRT) Practice Patterns and IGRT's Impact on Workflow and Treatment Planning: Results From a National Survey of American Society for Radiation Oncology Members". *International Journal of Radiation Oncology, Biology, Physics* 94.4 (2016), pp. 850–857. DOI: 10.1016/j.ijrobp.2015.09.035.

[77] Willi A. Kalender et al. "Spiral volumetric CT with single-breath-hold technique, continuous transport, and continuous scanner rotation". *Radiology* 176.1 (1990), pp. 181–183. DOI: 10.1148/radiology.176.1.2353088.

[78] P Edholm, L G Hellstrom, and B Jacobson. "Transverse tomography with incoherent optical reconstruction". *Physics in Medicine and Biology* 23.1 (Jan. 1978), pp. 90–99. DOI: 10.1088/0031-9155/23/1/008. URL: https://doi.org/10.1088/0031-9155/23/1/008.

[79] Johann Radon. "Über die Bestimmung von Funktionen durch ihre Integralwerte längs gewisser Mannigfaltigkeiten". *Berichte über die Verhandlungen der Königlich-Sächsischen Gesellschaft der Wissenschaften zu Leipzig, Mathematisch-Physische Classe* 69 (1917), pp. 262–277.

[80] S Rit et al. "The Reconstruction Toolkit (RTK), an open-source cone-beam CT reconstruction toolkit based on the Insight Toolkit (ITK)". *Journal of Physics: Conference Series* 489 (Mar. 2014), p. 012079. DOI: 10.1088/1742-6596/489/1/012079. URL: https://doi.org/10.1088/1742-6596/489/1/012079.

[81] Matthew McCormick et al. "ITK: enabling reproducible research and open science". *Frontiers in Neuroinformatics* 8 (2014). DOI: 10.3389/fninf.2014.00013. URL: https://doi.org/10.3389/fninf.2014.00013.

[82] Heang K. Tuy. "An Inversion Formula for Cone-Beam Reconstruction". *SIAM Journal on Applied Mathematics* 43.3 (June 1983), pp. 546–552. DOI: 10.1137/0143035. URL: https://doi.org/10.1137/0143035.

[83] Jan-Jakob Sonke et al. "Respiratory correlated cone beam CT". *Medical Physics* 32.4 (Mar. 2005), pp. 1176–1186. DOI: 10.1118/1.1869074. URL: https://doi.org/10.1118/1.1869074.

[84] Simon Rit et al. "On-the-fly motion-compensated cone-beam CT using an a priori model of the respiratory motion". *Medical Physics* 36.6Part1 (May 2009), pp. 2283–2296. DOI: 10.1118/1.3115691. URL: https://doi.org/10.1118/1.3115691.

[85] Cyril Mory, Guillaume Janssens, and Simon Rit. "Motion-aware temporal regularization for improved 4D cone-beam computed tomography". *Physics in Medicine & Biology* 61.18 (Sept. 2016), pp. 6856–6877. DOI: 10.1088/0031-9155/61/18/6856. URL: https://doi.org/10.1088/0031-9155/61/18/6856.

[86] Cyril Mory et al. "Cardiac C-arm computed tomography using a 3D + time ROI reconstruction method with spatial and temporal regularization". *Medical Physics* 41.2 (Jan. 2014), p. 021903. DOI: 10.1118/1.4860215. URL: https://doi.org/10.1118/1.4860215.

[87] Sheeba Thengumpallil et al. "Difference in performance between 3D and 4D CBCT for lung imaging: a dose and image quality analysis". *Journal of Applied Clinical Medical Physics* 17.6 (Nov. 2016), pp. 97–106. DOI: 10.1120/jacmp.v17i6.6459. URL: https://doi.org/10.1120/jacmp.v17i6.6459.

[88] Lambert Zijp, Jan-Jakob Sonke, and Marcel van Herk. "Extraction of the Respiratory Signal from Sequential Thorax Cone-Beam X-Ray Images". *2004 International Conference on the Use of Computers in Radiation Therapy*. 2004, pp. 507–509.

[89] Chris C. Shaw, ed. *Cone Beam Computed Tomography*. CRC Press, Feb. 2014. DOI: 10.1201/b16465. URL: https://doi.org/10.1201/b16465.

[90] S S Vedam et al. "Acquiring a four-dimensional computed tomography dataset using an external respiratory signal". *Physics in Medicine and Biology* 48.1 (Dec. 2002), pp. 45–62. DOI: 10.1088/0031-9155/48/1/304. URL: https://doi.org/10.1088/0031-9155/48/1/304.

[91] Jenny Bertholet et al. "Real-time intrafraction motion monitoring in external beam radiotherapy". *Physics in Medicine & Biology* 64.15 (Aug. 2019), 15TR01. DOI: 10.1088/1361-6560/ab2ba8. URL: https://doi.org/10.1088/1361-6560/ab2ba8.

[92] Nicole M. Wink, Christoph Panknin, and Timothy D. Solberg. "Phase versus amplitude sorting of 4D-CT data". *Journal of Applied Clinical Medical Physics* 7.1 (Feb. 2006), pp. 77–85. DOI: 10.1120/jacmp.v7i1.2198. URL: https://doi.org/10.1120/jacmp.v7i1.2198.

[93] R Schulze et al. "Artefacts in CBCT: a review". *Dentomaxillofacial Radiology* 40.5 (July 2011), pp. 265–273. DOI: 10.1259/dmfr/30642039. URL: https://doi.org/10.1259/dmfr/30642039.

[94] Shipeng Xie et al. "A level set method for cupping artifact correction in cone-beam CT". *Medical Physics* 42.8 (July 2015), pp. 4888–4895. DOI: 10.1118/1.4926851. URL: https://doi.org/10.1118/1.4926851.

[95] L.E. Antonuk et al. "Development of hydrogenated amorphous silicon sensors for diagnostic x-ray imaging". *IEEE Transactions on Nuclear Science* 38.2 (1991), pp. 636–640.

[96] Uros Stankovic et al. "Clinical introduction of image lag correction for a cone beam CT system". *Medical Physics* 43.3 (Feb. 2016), pp. 1057–1064. DOI: 10.1118/1.4941015. URL: https://doi.org/10.1118/1.4941015.

[97] Won-Ji Jung and Kwon Su Chon. "Ghosting Artifacts in Digital Radiography". *Journal of the Korean Society of Radiology* 8 (2014), pp. 377–382.

[98] B. Ohnesorge et al. "Efficient correction for CT image artifacts caused by objects extending outside the scan field of view". *Medical Physics* 27.1 (Jan. 2000), pp. 39–46. DOI: 10.1118/1.598855. URL: https://doi.org/10.1118/1.598855.

[99] Franz Boas and Dominik Fleischmann. "CT artifacts: Causes and reduction techniques". *Imaging in Medicine* 4 (Apr. 2012). DOI: 10.2217/iim.12.13.

[100] *Radiology reference website Radiopedia*. https://radiopaedia.org/cases/ring-artifact-1. Accessed: 23rd August 2022.

[101] Robert W. Brown et al. *Magnetic Resonance Imaging: Physical Principles and Sequence Design*. John Wiley & Sons, Ltd, 2014. DOI: 10.1002/9781118633953.

[102] ME Phelps et al. "Application of annihilation coincidence detection to transaxial reconstruction tomography". *J Nucl Med.* 16.3 (Mar. 1975), pp. 210–24.

[103] M Holden. "A review of geometric transformations for nonrigid body registration". *IEEE Trans Med Imaging* 27.1 (Jan. 2008), pp. 111–28. DOI: 10.1109/TMI.2007.904691.

[104] L. Ibanez et al. "The itk software guide second edition updated for itk version 2.4". *Kitware* 47.49 (2003).

[105] C. E. Shannon. "Prediction and Entropy of Printed English". *Bell System Technical Journal* 30.1 (Jan. 1951), pp. 50–64. DOI: 10.1002/j.1538-7305.1951.tb01366.x. URL: https://doi.org/10.1002/j.1538-7305.1951.tb01366.x.

[106] H. Knutsson and M. Andersson. "Morphons: segmentation using elastic canvas and paint on priors". *IEEE International Conference on Image Processing 2005*. Vol. 2. 2005, pp. II–1226. DOI: 10.1109/ICIP.2005.1530283.

[107] Guillaume Janssens et al. "Diffeomorphic Registration of Images with Variable Contrast Enhancement". *International Journal of Biomedical Imaging* 2011 (2011), pp. 1–16. DOI: 10.1155/2011/891585. URL: https://doi.org/10.1155/2011/891585.

[108] D. Rueckert et al. "Nonrigid registration using free-form deformations: application to breast MR images". *IEEE Transactions on Medical Imaging* 18.8 (1999), pp. 712–721. DOI: 10.1109/42.796284.

[109] K. Rohr et al. "Point-based elastic registration of medical image data using approximating thin-plate splines". *Visualization in Biomedical Computing*. Ed. by Karl Heinz Höhne and Ron Kikinis. Berlin, Heidelberg: Springer Berlin Heidelberg, 1996, pp. 297–306. ISBN: 978-3-540-70739-4.

[110] Mike Fornefett, Karl Rohr, and H. Siegfried Stiehl. "Radial basis functions with compact support for elastic registration of medical images". *Image Vis. Comput.* 19 (2001), pp. 87–96.

[111] Matthieu Ferrant et al. "Deformable Modeling for Characterizing Biomedical Shape Changes". *Discrete Geometry for Computer Imagery*. Springer Berlin Heidelberg, 2000, pp. 235–248. DOI: 10.1007/3-540-44438-6_20. URL: https://doi.org/10.1007/3-540-44438-6_20.

[112] Gary E. Christensen, Richard D. Rabbitt, and Michael I. Miller. "Deformable templates using large deformation kinematics". *IEEE Transactions on Image Processing* 5.10 (1996), pp. 1435–1447.

[113] Berthold K.P. Horn and Brian G. Schunck. "Determining optical flow". *Artificial Intelligence* 17.1-3 (Aug. 1981), pp. 185–203. DOI: 10.1016/0004-3702(81)90024-2. URL: https://doi.org/10.1016/0004-3702(81)90024-2.

[114] J.-P. Thirion. "Image matching as a diffusion process: an analogy with Maxwell's demons". *Medical Image Analysis* 2.3 (Sept. 1998), pp. 243–260. DOI: 10.1016/s1361-8415(98)80022-4. URL: https://doi.org/10.1016/s1361-8415(98)80022-4.

[115] Guillaume Janssens. "Registration models for tracking organs and tumors in highly deformable anatomies: applications to radiotherapy". PhD thesis. Universite Catholique De Louvain, 2010.

[116] Mei Chen et al. "Anatomic change over the course of treatment for non–small cell lung cancer patients and its impact on intensity-modulated radiation therapy and passive-scattering proton therapy deliveries". *Radiation Oncology* 15.1 (Mar. 2020b). DOI: 10.1186/s13014-020-01503-9. URL: https://doi.org/10.1186/s13014-020-01503-9.

[117] Simon Rit et al. "Filtered-backprojection reconstruction for a cone-beam computed tomography scanner with independent source and detector rotations". *Medical Physics* 43.5 (Apr. 2016), pp. 2344–2352. DOI: 10.1118/1.4945418. URL: https://doi.org/10.1118/1.4945418.

[118] C S Moore et al. "Investigating the use of an antiscatter grid in chest radiography for average adults with a computed radiography imaging system". *The British Journal of Radiology* 88.1047 (Mar. 2015), p. 20140613. DOI: 10.1259/bjr.20140613. URL: https://doi.org/10.1259/bjr.20140613.

[119] Ernesto Mainegra-Hing and Iwan Kawrakow. "Variance reduction techniques for fast Monte Carlo CBCT scatter correction calculations". *Physics in Medicine & Biology* 55.16 (July 2010), pp. 4495–4507. DOI: 10.1088/0031-9155/55/16/s05. URL: https://doi.org/10.1088/0031-9155/55/16/s05.

[120] Marta Peroni et al. "Automatic Segmentation and Online virtualCT in Head-and-Neck Adaptive Radiation Therapy". *International Journal of Radiation Oncology, Biology, Physics* 84.3 (Nov. 2012), e427–e433. DOI: 10.1016/j.ijrobp.2012.04.003. URL: https://doi.org/10.1016/j.ijrobp.2012.04.003.

[121] Peng Wang et al. "Quantitative assessment of anatomical change using a virtual proton depth radiograph for adaptive head and neck proton therapy". *Journal of Applied Clinical Medical Physics* 17.2 (Mar. 2016), pp. 427–440. DOI: 10.1120/jacmp.v17i2.5819. URL: https://doi.org/10.1120/jacmp.v17i2.5819.

[122] Veiga et al. "First Clinical Investigation of Cone Beam Computed Tomography and Deformable Registration for Adaptive Proton Therapy for Lung Cancer". *International Journal of Radiation Oncology, Biology, Physics* 95.1 (May 2016), pp. 549–559. DOI: 10.1016/j.ijrobp.2016.01.055. URL: https://doi.org/10.1016/j.ijrobp.2016.01.055.

[123] Catarina Veiga et al. "A comprehensive evaluation of the accuracy of CBCT and deformable registration based dose calculation in lung proton therapy". *Biomedical Physics & Engineering Express* 3.1 (Jan. 2017), p. 015003. DOI: 10.1088/2057-1976/3/1/015003. URL: https://doi.org/10.1088/2057-1976/3/1/015003.

[124] Tianye Niu et al. "Shading correction for on-board cone-beam CT in radiation therapy using planning MDCT images". *Medical Physics* 37.10 (Sept. 2010), pp. 5395–5406. DOI: 10.1118/1.3483260. URL: https://doi.org/10.1118/1.3483260.

[125] Yang-Kyun Park et al. "Proton dose calculation on scatter-corrected CBCT image: Feasibility study for adaptive proton therapy". *Medical Physics* 42.8 (July 2015), pp. 4449–4459. DOI: 10.1118/1.4923179. URL: https://doi.org/10.1118/1.4923179.

[126] Christopher Kurz et al. "Investigating deformable image registration and scatter correction for CBCT-based dose calculation in adaptive IMPT". *Medical Physics* 43.10 (Sept. 2016), pp. 5635–5646. DOI: 10.1118/1.4962933. URL: https://doi.org/10.1118/1.4962933.

[127]   Hofmaier et al. "Multi-criterial patient positioning based on dose recalculation on scatter-corrected CBCT images". *Radiotherapy and Oncology* 125.3 (Dec. 2017), pp. 464–469. DOI: 10.1016/j.radonc.2017.09.020. URL: https://doi.org/10.1016/j.radonc.2017.09.020.

[128]   Christoph Zöllner et al. "Decomposing a prior-CT-based cone-beam CT projection correction algorithm into scatter and beam hardening components". *Physics and Imaging in Radiation Oncology* 3 (July 2017), pp. 49–52. DOI: 10.1016/j.phro.2017.09.002. URL: https://doi.org/10.1016/j.phro.2017.09.002.

[129]   Jihun Kim et al. "Water equivalent path length calculations using scatter-corrected head and neck CBCT images to evaluate patients for adaptive proton therapy". *Physics in Medicine & Biology* 62.1 (Dec. 2016), pp. 59–72. DOI: 10.1088/1361-6560/62/1/59. URL: https://doi.org/10.1088/1361-6560/62/1/59.

[130]   Jihun Kim et al. "Beam angle optimization using angular dependency of range variation assessed via water equivalent path length (WEPL) calculation for head and neck proton therapy". *Physica Medica* 69 (Jan. 2020), pp. 19–27. DOI: 10.1016/j.ejmp.2019.11.021. URL: https://doi.org/10.1016/j.ejmp.2019.11.021.

[131]   P Botas et al. "Online adaption approaches for intensity modulated proton therapy for head and neck patients based on cone beam CTs and Monte Carlo simulations". *Physics in Medicine & Biology* 64.1 (Dec. 2018), p. 015004. DOI: 10.1088/1361-6560/aaf30b. URL: https://doi.org/10.1088/1361-6560/aaf30b.

[132]   Andreas Gravgaard Andersen et al. "Evaluation of an a priori scatter correction algorithm for cone-beam computed tomography based range and dose calculations in proton therapy". *Physics and Imaging in Radiation Oncology* 16 (Oct. 2020), pp. 89–94. DOI: 10.1016/j.phro.2020.09.014. URL: https://doi.org/10.1016/j.phro.2020.09.014.

[133]   Niepel et al. "Feasibility of 4DCBCT-based proton dose calculation: An ex vivo porcine lung phantom study". *Zeitschrift für Medizinische Physik* 29.3 (Aug. 2019), pp. 249–261. DOI: 10.1016/j.zemedi.2018.10.005. URL: https://doi.org/10.1016/j.zemedi.2018.10.005.

[134]   Bondesson et al. "Anthropomorphic lung phantom based validation of in-room proton therapy 4D-CBCT image correction for dose calculation". *Zeitschrift für Medizinische Physik* (Nov. 2020). DOI: 10.1016/j.zemedi.2020.09.004. URL: https://doi.org/10.1016/j.zemedi.2020.09.004.

[135]   Satoshi Kida et al. "Cone Beam Computed Tomography Image Quality Improvement Using a Deep Convolutional Neural Network". *Cureus* (Apr. 2018). DOI: 10.7759/cureus.2548. URL: https://doi.org/10.7759/cureus.2548.

[136]   David C. Hansen et al. "ScatterNet: A convolutional neural network for cone-beam CT intensity correction". *Medical Physics* 45.11 (Oct. 2018), pp. 4916–4926. DOI: 10.1002/mp.13175. URL: https://doi.org/10.1002/mp.13175.

[137]   Guillaume Landry et al. "Comparing Unet training with three different datasets to correct CBCT images for prostate radiotherapy dose calculations". *Physics in Medicine & Biology* 64.3 (Jan. 2019), p. 035011. DOI: 10.1088/1361-6560/aaf496. URL: https://doi.org/10.1088/1361-6560/aaf496.

[138]   Christopher Kurz et al. "CBCT correction using a cycle-consistent generative adversarial network and unpaired training to enable photon and proton dose calculation". *Physics in Medicine & Biology* 64.22 (Nov. 2019), p. 225004. DOI: 10.1088/1361-6560/ab4d8c. URL: https://doi.org/10.1088/1361-6560/ab4d8c.

[139] Adrian Thummerer et al. "Comparison of CBCT based synthetic CT methods suitable for proton dose calculations in adaptive proton therapy". *Physics in Medicine & Biology* 65.9 (Apr. 2020), p. 095002. DOI: 10.1088/1361-6560/ab7d54. URL: https://doi.org/10.1088/1361-6560/ab7d54.

[140] Arthur Lalonde et al. "Evaluation of CBCT scatter correction using deep convolutional neural networks for head and neck adaptive proton therapy". *Physics in Medicine & Biology* 65.24 (Dec. 2020), p. 245022. DOI: 10.1088/1361-6560/ab9fcb. URL: https://doi.org/10.1088/1361-6560/ab9fcb.

[141] Frederic Madesta et al. "Self-contained deep learning-based boosting of 4D cone-beam CT reconstruction". *Medical Physics* 47.11 (Oct. 2020), pp. 5619–5631. DOI: 10.1002/mp.14441. URL: https://doi.org/10.1002/mp.14441.

[142] Guoya Dong et al. "A deep unsupervised learning framework for the 4D CBCT artifact correction". *Physics in Medicine & Biology* 67.5 (Mar. 2022), p. 055012. DOI: 10.1088/1361-6560/ac55a5. URL: https://doi.org/10.1088/1361-6560/ac55a5.

[143] Adrian Thummerer et al. "Deep learning–based 4D-synthetic CTs from sparse-view CBCTs for dose calculations in adaptive proton therapy". *Medical Physics* (Aug. 2022). DOI: 10.1002/mp.15930. URL: https://doi.org/10.1002/mp.15930.

[144] Marcel van Herk et al. "The probability of correct target dosage: dose-population histograms for deriving treatment margins in radiotherapy". *International Journal of Radiation Oncology, Biology, Physics* 47.4 (July 2000), pp. 1121–1135. DOI: 10.1016/s0360-3016(00)00518-6. URL: https://doi.org/10.1016/s0360-3016(00)00518-6.

[145] Di Yan et al. "Adaptive radiation therapy". *Physics in Medicine and Biology* 42.1 (Jan. 1997), pp. 123–132. DOI: 10.1088/0031-9155/42/1/008. URL: https://doi.org/10.1088/0031-9155/42/1/008.

[146] Dennis Winkel et al. "Adaptive radiotherapy: The Elekta Unity MR-linac concept". *Clinical and Translational Radiation Oncology* 18 (Sept. 2019), pp. 54–59. DOI: 10.1016/j.ctro.2019.04.001. URL: https://doi.org/10.1016/j.ctro.2019.04.001.

[147] Taeho Kim et al. "Visually guided respiratory motion management for Ethos adaptive radiotherapy". *Journal of Applied Clinical Medical Physics* 23.1 (Oct. 2021). DOI: 10.1002/acm2.13441. URL: https://doi.org/10.1002/acm2.13441.

[148] X.A. Li. *Adaptive Radiation Therapy*. Imaging in Medical Diagnosis and Therapy. CRC Press, 2011. ISBN: 9781439816356. URL: https://books.google.de/books?id=9hEPvAlgPfMC.

[149] Cássia O. Ribeiro et al. "Towards the clinical implementation of intensity-modulated proton therapy for thoracic indications with moderate motion: Robust optimised plan evaluation by means of patient and machine specific information". *Radiotherapy and Oncology* 157 (Apr. 2021), pp. 210–218. DOI: 10.1016/j.radonc.2021.01.014. URL: https://doi.org/10.1016/j.radonc.2021.01.014.

[150] A Meijers et al. "Assessment of range uncertainty in lung-like tissue using a porcine lung phantom and proton radiography". *Physics in Medicine & Biology* 65.15 (July 2020a), p. 155014. DOI: 10.1088/1361-6560/ab91db. URL: https://doi.org/10.1088/1361-6560/ab91db.

[151] Clemens Grassberger et al. "Motion mitigation for lung cancer patients treated with active scanning proton therapy". *Medical Physics* 42.5 (Apr. 2015), pp. 2462–2469. DOI: 10.1118/1.4916662. URL: https://doi.org/10.1118/1.4916662.

[152] Jochem W.H. Wolthaus et al. "Mid-ventilation CT scan construction from four-dimensional respiration-correlated CT scans for radiotherapy planning of lung cancer patients". *International Journal of Radiation Oncology, Biology, Physics* 65.5 (Aug. 2006), pp. 1560–1571. DOI: 10.1016/j.ijrobp.2006.04.031. URL: https://doi.org/10.1016/j.ijrobp.2006.04.031.

[153] J. W. H. Wolthaus et al. "Reconstruction of a time-averaged midposition CT scan for radiotherapy planning of lung cancer patients using deformable registrationa)". *Medical Physics* 35.9 (Aug. 2008a), pp. 3998–4011. DOI: 10.1118/1.2966347. URL: https://doi.org/10.1118/1.2966347.

[154] Kenneth E Rosenzweig et al. "The deep inspiration breath-hold technique in the treatment of inoperable non small-cell lung cancer". *International Journal of Radiation Oncology, Biology, Physics* 48.1 (Aug. 2000), pp. 81–87. DOI: 10.1016/s0360-3016(00)00583-6. URL: https://doi.org/10.1016/s0360-3016(00)00583-6.

[155] John W Wong et al. "The use of active breathing control (ABC) to reduce margin for breathing motion". *International Journal of Radiation Oncology, Biology, Physics* 44.4 (July 1999), pp. 911–919. DOI: 10.1016/s0360-3016(99)00056-5. URL: https://doi.org/10.1016/s0360-3016(99)00056-5.

[156] Holger Hof et al. "Stereotactic single-dose radiotherapy of stage I non–small-cell lung cancer (NSCLC)". *International Journal of Radiation Oncology, Biology, Physics* 56.2 (June 2003), pp. 335–341. DOI: 10.1016/s0360-3016(02)04504-2. URL: https://doi.org/10.1016/s0360-3016(02)04504-2.

[157] Shinichi Minohara et al. "Respiratory gated irradiation system for heavy-ion radiotherapy". *International Journal of Radiation Oncology, Biology, Physics* 47.4 (July 2000), pp. 1097–1103. DOI: 10.1016/s0360-3016(00)00524-1. URL: https://doi.org/10.1016/s0360-3016(00)00524-1.

[158] Christoph Bert et al. "Dosimetric precision of an ion beam tracking system". *Radiation Oncology* 5.1 (June 2010). DOI: 10.1186/1748-717x-5-61. URL: https://doi.org/10.1186/1748-717x-5-61.

[159] Eric W. Pepin et al. "Correlation and prediction uncertainties in the CyberKnife Synchrony respiratory tracking system". *Medical Physics* 38.7 (June 2011), pp. 4036–4044. DOI: 10.1118/1.3596527. URL: https://doi.org/10.1118/1.3596527.

[160] Yuichi Akino et al. "Evaluation of the accuracy of the CyberKnife Synchrony™ Respiratory Tracking System using a plastic scintillator". *Medical Physics* 45.8 (June 2018), pp. 3506–3515. DOI: 10.1002/mp.13028. URL: https://doi.org/10.1002/mp.13028.

[161] Ye Zhang et al. "Online image guided tumour tracking with scanned proton beams: a comprehensive simulation study". *Physics in Medicine and Biology* 59.24 (Nov. 2014), pp. 7793–7817. DOI: 10.1088/0031-9155/59/24/7793. URL: https://doi.org/10.1088/0031-9155/59/24/7793.

[162] Moritz Rabe et al. "Real-time 4DMRI-based internal target volume definition for moving lung tumors". *Medical Physics* 47.4 (Feb. 2020), pp. 1431–1442. DOI: 10.1002/mp.14023. URL: https://doi.org/10.1002/mp.14023.

[163] Eike Rietzel and Christoph Bert. "Respiratory motion management in particle therapy". *Medical Physics* 37.2 (Jan. 2010), pp. 449–460. DOI: 10.1118/1.3250856. URL: https://doi.org/10.1118/1.3250856.

[164] Antje-Christin Knopf and Antony John Lomax. "In the context of radiosurgery – Pros and cons of rescanning as a solution for treating moving targets with scanned particle beams". *Physica Medica* 30.5 (July 2014), pp. 551–554. DOI: 10.1016/j.ejmp.2014.03.010. URL: https://doi.org/10.1016/j.ejmp.2014.03.010.

[165] Christoph Bert et al. "Gated Irradiation With Scanned Particle Beams". *International Journal of Radiation Oncology Biology Physics* 73.4 (Mar. 2009), pp. 1270–1275. DOI: 10.1016/j.ijrobp.2008.11.014. URL: https://doi.org/10.1016/j.ijrobp.2008.11.014.

[166] S van de Water et al. "Tumour tracking with scanned proton beams: assessing the accuracy and practicalities". *Physics in Medicine and Biology* 54.21 (Oct. 2009), pp. 6549–6563. DOI: 10.1088/0031-9155/54/21/007. URL: https://doi.org/10.1088/0031-9155/54/21/007.

[167] Reinhart A Sweeney et al. "Accuracy and inter-observer variability of 3D versus 4D cone-beam CT based image-guidance in SBRT for lung tumors". *Radiation Oncology* 7.1 (June 2012). DOI: 10.1186/1748-717x-7-81. URL: https://doi.org/10.1186/1748-717x-7-81.

[168] Henning Schmitz et al. "Validation of proton dose calculation on scatter corrected 4D cone beam computed tomography using a porcine lung phantom". *Physics in Medicine & Biology* 66.17 (Aug. 2021), p. 175022. DOI: 10.1088/1361-6560/ac16e9. URL: https://doi.org/10.1088/1361-6560/ac16e9.

[169] Dirk De Ruysscher, Wouter van Elmpt, and Philippe Lambin. "Radiotherapy with curative intent for lung cancer: A continuing success story". *Radiotherapy and Oncology* 101.2 (Nov. 2011), pp. 237–239. DOI: 10.1016/j.radonc.2011.10.019. URL: https://doi.org/10.1016/j.radonc.2011.10.019.

[170] Manzar et al. "Comparative analysis of acute toxicities and patient reported outcomes between intensity-modulated proton therapy (IMPT) and volumetric modulated arc therapy (VMAT) for the treatment of oropharyngeal cancer". *Radiotherapy and Oncology* 147 (June 2020), pp. 64–74. DOI: 10.1016/j.radonc.2020.03.010. URL: https://doi.org/10.1016/j.radonc.2020.03.010.

[171] Welsh et al. "Intensity-Modulated Proton Therapy Further Reduces Normal Tissue Exposure During Definitive Therapy for Locally Advanced Distal Esophageal Tumors: A Dosimetric Study". *International Journal of Radiation Oncology, Biology, Physics* 81.5 (Dec. 2011), pp. 1336–1342. DOI: 10.1016/j.ijrobp.2010.07.2001. URL: https://doi.org/10.1016/j.ijrobp.2010.07.2001.

[172] Lin et al. "Radiation Therapy for Pediatric Brain Tumors using Robotic Radiation Delivery System and Intensity Modulated Proton Therapy". *Practical Radiation Oncology* 10.3 (May 2020), e173–e182. DOI: 10.1016/j.prro.2019.09.008. URL: https://doi.org/10.1016/j.prro.2019.09.008.

[173] Vivek Verma et al. "Clinical outcomes and toxicities of proton radiotherapy for gastrointestinal neoplasms: a systematic review". *Journal of Gastrointestinal Oncology* 7.4 (Aug. 2016), pp. 644–664. DOI: 10.21037/jgo.2016.05.06. URL: https://doi.org/10.21037/jgo.2016.05.06.

[174] Damien C. Weber et al. "Spot Scanning-Based Proton Therapy for Intracranial Meningioma: Long-Term Results From the Paul Scherrer Institute". *International Journal of Radiation Oncology, Biology, Physics* 83.3 (July 2012), pp. 865–871. DOI: 10.1016/j.ijrobp.2011.08.027. URL: https://doi.org/10.1016/j.ijrobp.2011.08.027.

[175] Koichiro Nakajima et al. "Clinical outcomes of image-guided proton therapy for histologically confirmed stage I non-small cell lung cancer". *Radiation Oncology* 13.1 (Oct. 2018). DOI: 10.1186/s13014-018-1144-5. URL: https://doi.org/10.1186/s13014-018-1144-5.

[176]   Abigail Berman, Sara James, and Ramesh Rengan. "Proton Beam Therapy for Non-Small Cell Lung Cancer: Current Clinical Evidence and Future Directions". *Cancers* 7.3 (July 2015), pp. 1178–1190. DOI: 10.3390/cancers7030831.

[177]   J R McClelland et al. "Inter-fraction variations in respiratory motion models". *Physics in Medicine & Biology* 56.1 (Dec. 2010), pp. 251–272. DOI: 10.1088/0031-9155/56/1/015. URL: https://doi.org/10.1088/0031-9155/56/1/015.

[178]   You Zhang, Fang-Fang Yin, and Lei Ren. "Dosimetric verification of lung cancer treatment using the CBCTs estimated from limited-angle on-board projections". *Medical Physics* 42.8 (July 2015), pp. 4783–4795. DOI: 10.1118/1.4926559. URL: https://doi.org/10.1118/1.4926559.

[179]   Lone Hoffmann et al. "Adaptation is mandatory for intensity modulated proton therapy of advanced lung cancer to ensure target coverage". *Radiotherapy and Oncology* 122.3 (Mar. 2017), pp. 400–405. DOI: 10.1016/j.radonc.2016.12.018. URL: https://doi.org/10.1016/j.radonc.2016.12.018.

[180]   Annika Jakobi et al. "Feasibility of proton pencil beam scanning treatment of free-breathing lung cancer patients". *Acta Oncologica* 57.2 (Aug. 2017), pp. 203–210. DOI: 10.1080/0284186x.2017.1355107. URL: https://doi.org/10.1080/0284186x.2017.1355107.

[181]   Yolanda D Tseng et al. "4D computed tomography scans for conformal thoracic treatment planning: is a single scan sufficient to capture thoracic tumor motion?" *Physics in Medicine & Biology* 63.2 (Jan. 2018), 02NT03. DOI: 10.1088/1361-6560/aaa44e. URL: https://doi.org/10.1088/1361-6560/aaa44e.

[182]   Francesca Albertini et al. "Online daily adaptive proton therapy". *The British Journal of Radiology* 93.1107 (Mar. 2020), p. 20190594. DOI: 10.1259/bjr.20190594. URL: https://doi.org/10.1259/bjr.20190594.

[183]   David C. Hansen and Thomas Sangild Sørensen. "Fast 4D cone-beam CT from 60s acquisitions". *Physics and Imaging in Radiation Oncology* 5 (Jan. 2018), pp. 69–75. DOI: 10.1016/j.phro.2018.02.004. URL: https://doi.org/10.1016/j.phro.2018.02.004.

[184]   Deepak Shrestha et al. "Dosimetric evaluation of 4D-CBCT reconstructed by Simultaneous Motion Estimation and Image Reconstruction (SMEIR) for carbon ion therapy of lung cancer". *Medical Physics* 46.9 (July 2019), pp. 4087–4094. DOI: 10.1002/mp.13706. URL: https://doi.org/10.1002/mp.13706.

[185]   Jing Wang and Xuejun Gu. "Simultaneous motion estimation and image reconstruction (SMEIR) for 4D cone-beam CT". *Medical Physics* 40.10 (Sept. 2013), p. 101912. DOI: 10.1118/1.4821099. URL: https://doi.org/10.1118/1.4821099.

[186]   Jürgen Biederer and Martin Heller. "Artificial Thorax for MR Imaging Studies in Porcine Heart-Lung Preparations". *Radiology* 226.1 (Jan. 2003), pp. 250–255. DOI: 10.1148/radiol.2261011275. URL: https://doi.org/10.1148/radiol.2261011275.

[187]   Moritz Rabe et al. "Porcine lung phantom-based validation of estimated 4D-MRI using orthogonal cine imaging for low-field MR-Linacs". *Physics in Medicine & Biology* 66.5 (Feb. 2021), p. 055006. DOI: 10.1088/1361-6560/abc937. URL: https://doi.org/10.1088/1361-6560/abc937.

[188]   Stephen B. Edge and Carolyn C. Compton. "The American Joint Committee on Cancer: the 7th Edition of the AJCC Cancer Staging Manual and the Future of TNM". *Annals of Surgical Oncology* 17.6 (Feb. 2010), pp. 1471–1474. DOI: 10.1245/s10434-010-0985-4. URL: https://doi.org/10.1245/s10434-010-0985-4.

[189] Jochem W.H. Wolthaus et al. "Comparison of Different Strategies to Use Four-Dimensional Computed Tomography in Treatment Planning for Lung Cancer Patients". *International Journal of Radiation Oncology, Biology, Physics* 70.4 (Mar. 2008b), pp. 1229–1238. DOI: 10.1016/j.ijrobp.2007.11.042. URL: https://doi.org/10.1016/j.ijrobp.2007.11.042.

[190] Hiroki Shirato et al. "Intrafractional tumor motion: lung and liver". *Seminars in Radiation Oncology* 14.1 (Jan. 2004), pp. 10–18. DOI: 10.1053/j.semradonc.2003.10.008. URL: https://doi.org/10.1053/j.semradonc.2003.10.008.

[191] P Mann et al. "3D dosimetric validation of motion compensation concepts in radiotherapy using an anthropomorphic dynamic lung phantom". *Physics in Medicine and Biology* 62.2 (Dec. 2016), pp. 573–595. DOI: 10.1088/1361-6560/aa51b1. URL: https://doi.org/10.1088/1361-6560/aa51b1.

[192] Landry et al. "Phantom based evaluation of CT to CBCT image registration for proton therapy dose recalculation". *Physics in Medicine & Biology* 60.2 (Dec. 2014), pp. 595–613. DOI: 10.1088/0031-9155/60/2/595. URL: https://doi.org/10.1088/0031-9155/60/2/595.

[193] Jana Fox et al. "Quantification of Tumor Volume Changes During Radiotherapy for Non–Small-Cell Lung Cancer". *International Journal of Radiation Oncology Biology Physics* 74.2 (June 2009), pp. 341–348. DOI: 10.1016/j.ijrobp.2008.07.063. URL: https://doi.org/10.1016/j.ijrobp.2008.07.063.

[194] Jochem W.H. Wolthaus et al. "Comparison of Different Strategies to Use Four-Dimensional Computed Tomography in Treatment Planning for Lung Cancer Patients". *International Journal of Radiation Oncology Biology Physics* 70.4 (Mar. 2008b), pp. 1229–1238. DOI: 10.1016/j.ijrobp.2007.11.042. URL: https://doi.org/10.1016/j.ijrobp.2007.11.042.

[195] H. Helen Liu et al. "Assessing Respiration-Induced Tumor Motion and Internal Target Volume Using Four-Dimensional Computed Tomography for Radiotherapy of Lung Cancer". *International Journal of Radiation Oncology, Biology, Physics* 68.2 (June 2007), pp. 531–540. DOI: 10.1016/j.ijrobp.2006.12.066. URL: https://doi.org/10.1016/j.ijrobp.2006.12.066.

[196] Lukas Knybel et al. "Analysis of Lung Tumor Motion in a Large Sample: Patterns and Factors Influencing Precise Delineation of Internal Target Volume". *International Journal of Radiation Oncology, Biology, Physics* 96.4 (Nov. 2016), pp. 751–758. DOI: 10.1016/j.ijrobp.2016.08.008. URL: https://doi.org/10.1016/j.ijrobp.2016.08.008.

[197] Jennifer Dhont et al. "The long- and short-term variability of breathing induced tumor motion in lung and liver over the course of a radiotherapy treatment". *Radiotherapy and Oncology* 126.2 (Feb. 2018), pp. 339–346. DOI: 10.1016/j.radonc.2017.09.001. URL: https://doi.org/10.1016/j.radonc.2017.09.001.

[198] Rune Slot Thing et al. "Accuracy of dose calculation based on artefact corrected Cone Beam CT images of lung cancer patients". *Physics and Imaging in Radiation Oncology* 1 (Jan. 2017), pp. 6–11. DOI: 10.1016/j.phro.2016.11.001. URL: https://doi.org/10.1016/j.phro.2016.11.001.

[199] Y. Lecun et al. "Gradient-based learning applied to document recognition". *Proceedings of the IEEE* 86.11 (1998), pp. 2278–2324. DOI: 10.1109/5.726791. URL: https://doi.org/10.1109/5.726791.

[200]   Olaf Ronneberger, Philipp Fischer, and Thomas Brox. "U-Net: Convolutional Networks for Biomedical Image Segmentation". *Lecture Notes in Computer Science*. Springer International Publishing, 2015, pp. 234–241. DOI: 10.1007/978-3-319-24574-4_28. URL: https://doi.org/10.1007/978-3-319-24574-4_28.

[201]   Tin Kam Ho. "Random decision forests". *Proceedings of 3rd International Conference on Document Analysis and Recognition*. IEEE Comput. Soc. Press, 1995. DOI: 10.1109/icdar.1995.598994. URL: https://doi.org/10.1109/icdar.1995.598994.

[202]   Joscha Maier et al. "Deep scatter estimation (DSE): feasibility of using a deep convolutional neural network for real-time x-ray scatter prediction in cone-beam CT". *Medical Imaging 2018: Physics of Medical Imaging*. Ed. by Guang-Hong Chen, Joseph Y. Lo, and Taly Gilat Schmidt. SPIE, Mar. 2018a. DOI: 10.1117/12.2292919. URL: https://doi.org/10.1117/12.2292919.

[203]   Joscha Maier et al. "Real-time scatter estimation for medical CT using the deep scatter estimation: Method and robustness analysis with respect to different anatomies, dose levels, tube voltages, and data truncation". *Medical Physics* 46.1 (Nov. 2018b), pp. 238–249. DOI: 10.1002/mp.13274. URL: https://doi.org/10.1002/mp.13274.

[204]   Joscha Maier et al. "Deep Scatter Estimation (DSE): Accurate Real-Time Scatter Estimation for X-Ray CT Using a Deep Convolutional Neural Network". *Journal of Nondestructive Evaluation* 37.3 (July 2018c). DOI: 10.1007/s10921-018-0507-z. URL: https://doi.org/10.1007/s10921-018-0507-z.

[205]   Sebastian Neppl et al. "Evaluation of proton and photon dose distributions recalculated on 2D and 3D Unet-generated pseudoCTs from T1-weighted MR head scans". *Acta Oncologica* 58.10 (July 2019), pp. 1429–1434. DOI: 10.1080/0284186x.2019.1630754. URL: https://doi.org/10.1080/0284186x.2019.1630754.

[206]   Jun-Yan Zhu et al. "Unpaired Image-to-Image Translation Using Cycle-Consistent Adversarial Networks". *2017 IEEE International Conference on Computer Vision (ICCV)*. IEEE, Oct. 2017. DOI: 10.1109/iccv.2017.244. URL: https://doi.org/10.1109/iccv.2017.244.

[207]   Ian Goodfellow et al. "Generative Adversarial Nets". *Advances in Neural Information Processing Systems*. Ed. by Z. Ghahramani et al. Vol. 27. Curran Associates, Inc., 2014. URL: https://proceedings.neurips.cc/paper/2014/file/5ca3e9b122f61f8f06494c97b1afccf3-Paper.pdf.

[208]   Yulun Zhang et al. "Residual dense network for image restoration". *IEEE Transactions on Pattern Analysis and Machine Intelligence* 43.7 (2020), pp. 2480–2495.

[209]   Maria Francesca Spadea et al. "Deep Convolution Neural Network (DCNN) Multiplane Approach to Synthetic CT Generation From MR images—Application in Brain Proton Therapy". *International Journal of Radiation Oncology, Biology, Physics* 105.3 (Nov. 2019), pp. 495–503. DOI: 10.1016/j.ijrobp.2019.06.2535. URL: https://doi.org/10.1016/j.ijrobp.2019.06.2535.

[210]   Hongyi Zhang et al. *mixup: Beyond Empirical Risk Minimization*. 2017. DOI: 10.48550/ARXIV.1710.09412. URL: https://arxiv.org/abs/1710.09412.

[211]   Zhengxin Zhang, Qingjie Liu, and Yunhong Wang. "Road Extraction by Deep Residual U-Net" (2017). DOI: 10.48550/ARXIV.1711.10684. URL: https://arxiv.org/abs/1711.10684.

[212]   Kaiming He et al. "Delving Deep into Rectifiers: Surpassing Human-Level Performance on ImageNet Classification". *2015 IEEE International Conference on Computer Vision (ICCV)*. 2015, pp. 1026–1034. DOI: 10.1109/ICCV.2015.123.

[213] Diederik P. Kingma and Jimmy Ba. *Adam: A Method for Stochastic Optimization*. 2014. DOI: 10.48550/ARXIV.1412.6980. URL: https://arxiv.org/abs/1412.6980.

[214] Adam Paszke et al. "Automatic Differentiation in PyTorch". *NIPS 2017 Workshop on Autodiff*. Long Beach, California, USA, 2017. URL: https://openreview.net/forum?id=BJJsrmfCZ.

[215] Aswin Hoffmann et al. "MR-guided proton therapy: a review and a preview". *Radiation Oncology* 15.1 (May 2020). DOI: 10.1186/s13014-020-01571-x. URL: https://doi.org/10.1186/s13014-020-01571-x.

[216] Trang Thanh Pham et al. "Magnetic resonance imaging (MRI) guided proton therapy: A review of the clinical challenges, potential benefits and pathway to implementation". *Radiotherapy and Oncology* 170 (May 2022), pp. 37–47. DOI: 10.1016/j.radonc.2022.02.031. URL: https://doi.org/10.1016/j.radonc.2022.02.031.

List of Publications

Peer-reviewed articles as first author in the scope of this thesis

H. Schmitz, M. Rabe, G. Janssens, D. Bondesson, S. Rit, K. Parodi, C. Belka, J. Dinkel, C. Kurz, F. Kamp, and G. Landry. "Validation of proton dose calculation accuracy on scatter corrected 4D cone beam computed tomography using a porcine lung phantom". *Physics in Medicine & Biology* (2021), *In press*. DOI: 10.1088/1361-6560/ac16e9.

H. Schmitz, M. Rabe, G. Janssens, S. Rit, K. Parodi, C. Belka, F. Kamp, G. Landry, and C. Kurz. "Scatter correction of 4D cone beam computed tomography to detect dosimetric effects due to anatomical changes in proton therapy for lung cancer". *Manuscript accepted for publication in Medical Physics.*

H. Schmitz, E. Lombardo, M. Kawula, A. Thummerer, K. Parodi, C. Belka, F. Kamp, G. Landry, and C. Kurz. "Projection-based scatter correction of 4D cone beam computed tomography images of lung patients for proton therapy using a convolutional neural network". *Manuscript in preparation.*

Peer-reviewed articles as co-author

M. Rabe, C. Paganelli, **H. Schmitz**, G. Meschini, M. Riboldi, J. Hofmaier, J. Dinkel, M. Reiner, K. Parodi, C. Belka, G. Landry, C. Kurz, and F. Kamp. "Continuous time-resolved estimated synthetic CTs for dose reconstruction of lung tumor treatments at the low field MR-Linac". *Manuscript in preparation.*

Conference contributions as first author

H. Schmitz, M. Rabe, G. Janssens, J. Dinkel, S. Rit, K. Parodi, C. Belka, C. Kurz, F. Kamp, and G. Landry. "Scatter Correction of 4D Cone Beam Computed Tomography for Time-Resolved Proton Dose Calculation: Porcine Lung Phantom Validation". Oral presentation at the *Virtual AAPM 63rd Annual Meeting & Exhibition* (2021), virtual conference.

H. Schmitz, M. Rabe, G. Janssens, D. Bondesson, S. Rit, K. Parodi, C. Belka, J. Dinkel, C. Kurz, F. Kamp, and G. Landry. "Experimental lung phantom based validation of scatter corrected 4D cone beam computed tomography for proton dose calculations". ePoster presentation at the *Joint Conference of the ÖGMP, DGMP and SGSMP* (2021), virtual conference.

H. Schmitz, M. Rabe, G. Janssens, J. Dinkel, S. Rit, K. Parodi, C. Belka, F. Kamp, G. Landry, and C. Kurz. "Scatter correction of 4D cone beam computed tomography for time-resolved proton dose calculation: first patient application". Poster presentation at the *4D treatment workshop on particle therapy* (2021), in Delft.

H. Schmitz, M. Rabe, G. Janssens, S. Rit, K. Parodi, C. Belka, F. Kamp, G. Landry, and C. Kurz. "Scatter correction of 4D cone beam computed tomography images for time-resolved proton dose calculation: first patient application". Oral presentation at the *AAPM 64th Annual Meeting & Exhibition* (2022) in Washington D.C. .

H. Schmitz, M. Rabe, G. Janssens, S. Rit, K. Parodi, C. Belka, F. Kamp, G. Landry, and C. Kurz. "Intensitätskorrektur von 4D-Conebeam Computertomographie Bildern zur Berechnung zeitaufgelöster Protonendosisverteilungen: erste Anwendung am Patienten". Poster presentation at the *53. Jahrestagung der DGMP* (2022) in Aachen

H. Schmitz, E. Lombardo, M. Kawula, K. Parodi, C. Belka, F. Kamp, G. Landry, and C. Kurz. "ScatterNet for 4D cone-beam CT intensity correction of lung cancer patients". Oral presentation at the *ESTRO* (2023) in Vienna .

Conference contributions as co-author

M. Rabe, C. Paganelli, **H. Schmitz**, G. Meschini, M. Riboldi, J. Hofmaier, J. Dinkel, M. Reiner, K. Parodi, C. Belka, G. Landry, C. Kurz, and F. Kamp. "Time-resolved estimated synthetic CTs based on orthogonal cine MRI for low-field MR-Linac treatments". Oral presentation at the *Virtual AAPM 63rd Annual Meeting & Exhibition* (2021), virtual conference.

M. Rabe, C. Paganelli, **H. Schmitz**, G. Meschini, M. Riboldi, J. Hofmaier, J. Dinkel, M. Reiner, K. Parodi, C. Belka, G. Landry, C. Kurz, and F. Kamp. "Experimental validation of time-resolved estimated synthetic CTs at 3.65 Hz for MR-guided lung tumor treatments". Oral presentation at the *Joint Conference of the ÖGMP, DGMP and SGSMP* (2021), virtual conference.

J. Albrecht, S. Rit, P. Steininger, F. Ginzinger, P. Huber, I. Messner, M. Kraihamer, **H. Schmitz**, S. Corradini, C. Belka, C. Kurz, M. Riboldi, G. Landry. "Cone-Beam CT from complete data using saddle trajectories on a mobile robotic CBCT scanner". Oral presentation at the *AAPM 64th Annual Meeting & Exhibition* (2022) in Washington D.C.

J. Albrecht, S. Rit, P. Steininger, F. Ginzinger, P. Huber, I. Messner, M. Kraihamer, **H. Schmitz**, S. Corradini, C. Belka, C. Kurz, M. Riboldi, G. Landry. "Cone-beam CT Artefaktreduzierung mittels Satteltrajektorien implementiert auf einem mobilen, robotergestützten CBCT Scanner". Oral presentation at the *53. Jahrestagung der DGMP* (2022) in Aachen

Acknowledgments

This thesis has solely one name on its cover, yet many if not all of the presented works, were only feasible through the great support of my colleagues, friends, and family. While there have been numerous people helping me throughout my studies, to who I owe gratitude, I will only list those, having a direct connection to this thesis.

First and foremost, it is my pleasure to thank my supervisors. I was lucky to be in an uncommon situation of having four supervisors. I would like to start by thanking Prof. Katia Parodi for supervising my thesis. Your impeccable work ethic and passion for medical physics make you an inspiring person.

Next, I would like to thank Prof. Guillaume Landry, who has given me the opportunity to be a part of his medical physics research group although I had no background in this field. In my recollection, Guillaume and I did not disagree on anything meaningful over the course of my PhD. However, I disagree with you describing yourself as impatient. Thank you for your generosity with your time and patience with your explanations. You have been a fantastic supervisor, maintaining overwhelming energy throughout your work and carrying that through to all around you. I am lucky to have had the chance to work with you so closely.

I have also been very fortunate to have had the chance to tap the fountain of knowledge that is PD Dr. Christopher Kurz. In countless hours you discussed numerous medical physics topics with me. You always challenged and encouraged me, which led me achieve better results.

Last, but definitely not least among my supervisors, I owe gratitude to Dr. Florian Kamp. By introducing me to the clinical physicists and physicians you bridged the gap for me to the clinic. During my PhD your own work brought you to the University Clinic in Cologne, which did not change the fact that you stayed fully involved with my work. Thanks for stretching and prodding me to work hard on this thesis.

Looking back, I will not miss abstract deadlines, but I will miss the weekly Monday morning meetings with Guillaume, Christopher, and Florian. I always enjoyed starting the week with everyone sharing some personal notes about their weekends. Besides sharing nice personal moments, a key attribute that links all of my supervisors is the fact that they are tireless campaigners for the cause of scientific rigour. I hope that all of you stay exactly like you are. Thank you for all your valuable advice including those on anything and everything that is not related to medical physics.

The term medical physics already reveals the interdisciplinary environment I had the opportunity to work in. With the student office located in the Department of Radiation Oncology at the University Hospital, LMU Munich, I was in close contact with physicians under the leadership of Prof. Claus Belka and clinical medical physicists of Dr. Michael Reiner's group. Numerous coffee breaks - with me never ever drinking a single coffee - established a wonderful working environment. In particular, I would like to thank Roel Shpani, Amra Mekic-Krejovic, Dr. Katrin Straub, Dr. Jan Hofmaier, Vanessa Filipa da Silva Mendes, Catrin Rodenberg, Dr. Mohammad Safari, and Dr. Vasiliki Anagnostatou for interesting chats as well as sometimes fooling around. On the same note, I would like to thank Dr. Christoph Losert, Dr. Helmut Weingandt, Dr. Sylvia Garny, Lukas Nierer, Tobias

Winderl, Robert Kießling, Winfried Hoischen, Sebastian Neppl and Dr. Philipp Freislederer, who all tried to explain Bavarian quirks to me.

In addition to all these clinical colleagues, I had fantastic colleagues in the research group with whom I worked closely together. Here I would like to thank my fellow PhD students Elia Lombardo, Maria Kawula, Ivy Chan, Jackie Xiong, Lili Huang, Rabea Klaar, Nikolaos Ntelopoulos, and Dr. Moritz Rabe. I want to thank especially Moritz as he started his PhD roughly a year before me and thus became my go-to guy for PhD-specific as well as all kinds of other questions. Besides many things, I will miss our times at butcheries and in general with Tosca. I would also like to thank the postdocs Dr. Yiling Wang and Adrian Thummerer. I am happy that Adrian will continue my work and I am convinced that he will lift it to new heights. Additionally, I would like to thank Dr. Jannis Dickmann with whom it was a pleasure to share an office when I was in Garching for a few weeks due to the construction work at our offices in the clinic. Last but not least among my colleagues I would like to thank PD Dr. Dr. Christian Thieke for doing extremely valuable work in the background as a research coordinator. Thanks for providing a fantastic research setting as well as for many funny conversations during lunch. In summary, my thanks go to all the colleagues I mentioned as well as those who I forgot. It has been a blast.

I look back with joy to many evenings with colleagues in beer gardens, restaurants, bars, and sometimes even clubs. I hope that I will be able to join occasionally a few of those events in the future although not being affiliated with LMU or the clinic anymore. The special situation due to the pandemic has unfortunately moved many other events to the virtual world. Nevertheless, I was fortunate enough to go on trips for conferences, and scientific collaborations to Krakow, Delft, Washington D.C., Aachen, Cologne, and Lyon. I enjoyed all of these trips and thus I am looking forward to going on my last scientific trip, which will be ESTRO 2023 in Vienna. Instead of listing many of the above-mentioned colleagues, who accompanied me on these journeys and thus made them more enjoyable, again, I will here just thank Johanna Albrecht, who put up with me in Washington D.C., Aachen, and Lyon.

In Lyon at CREATIS I met Dr. Simon Rit, whose framework RTK was the basis for all of the reconstructions done during my thesis. The positive image of Simon, which I purely had from email conversations, was directly confirmed when I met him. He was an important collaborator for the first two projects as he is incredibly knowledgeable when it comes to reconstructions. Thanks again for a very pleasant stay in Lyon. Another important collaborator for the first two projects was Dr. Guillaume Janssens, who came up with the virtual CT pipeline. Unfortunately, I never met Guillaume Janssens in person, yet I can only echo what I just said about Simon. Independently of how often I bugged him with complicated and probably also trivial questions via emails, he always replied quickly and thoroughly to them in a way so that I could not only continue my work but also understood what I was doing. Additionally, I want to thank Dr. David Bondesson for giving me a hands-on session on the 4DvCT pipeline and Prof. Julien Dinkel for lending us the porcine lung phantom for our measurements.

I want to thank Prof. Marco Riboldi, who agreed to be the second reviewer of this thesis. I owe gratitude to the German Research Foundation (DFG), which funded my research and I want to thank the graduate college group GRK 2274 for many inspiring seminars, block courses, and a nice retreat in Lenggries.

In addition to Guillaume, Christopher, Flo, and Katia, I want to acknowledge the help of my friends Dr. Agnes Bußmann, Dr. Max Busch, and Alexander Zeltinger for proofreading selected parts of this thesis. This thesis is readable because of your efforts. The remaining errors are entirely mine.

Most importantly, I owe gratitude to my family for their support and love. Thank you for encouraging me to excel in every aspect of life, not just academia. According to Johann

Wolfgang von Goethe, "Zwei Dinge sollen Kinder von ihren Eltern bekommen. Wurzeln, solange sie klein sind, und Flügel, wenn sie größer werden." Thank you for giving me both.